รายงานวิจัยฉบับสมบูรณ์

โครงการ

การใช้โฟมที่ปรับเสถียรด้วยอนุภาคแม่เหล็กนาโนร่วมกับการเหนี่ยวนำความร้อนทางแม่เหล็กไฟฟ้าในการเร่งการฟื้นฟูพื้นที่ปนเปื้อนสารอินทรีย์ระเหยด้วยวิธีสกัดไอดิน

โดย ดร.ธนพล เพ็ญรัตน์

ธันวาคม 2558

สัญญาเลขที่ MRG5680129

รายงานวิจัยฉบับสมบูรณ์

โครงการ

การใช้โฟมที่ปรับเสถียรด้วยอนุภาคแม่เหล็กนาโนร่วมกับการเหนี่ยวนำความร้อนทางแม่เหล็กไฟฟ้าในการเร่งการฟื้นฟูพื้นที่ปนเปื้อนสารอินทรีย์ระเหยด้วยวิธีสกัดไอดิน

ผู้วิจัย

ดร.ธนพล เพ็ญรัตน์

สังกัด

คณะวิศวกรรมศาสตร์ มหาวิทยาลัยนเรศวร

สนับสนุนโดยสำนักงานกองทุนสนับสนุนการวิจัย

(ความเห็นในรายงานนี้เป็นของผู้วิจัย สกว.ไม่จำเป็นต้องเห็นด้วยเสมอไป)

สารบัญ

สารบัญรูป

สารบัญรูป (ต่อ)

สารบัญรูป (ต่อ)

สารบัญตาราง

บทคัดย่อ

รหัสโครงการ : MRG5680129

ชื่อโครงการวิจัย : การใช้โฟมที่ปรับเสถียรภาพด้วยอนุภาคแม่เหล็กนาโนร่วมกับการเหนี่ยวนำความร้อนทางแม่เหล็กไฟฟ้าในการเร่งการฟื้นฟูพื้นที่ปนเปื้อนสารอินทรีย์ระเหยง่ายด้วยวิธีสกัดไอดิน

ผู้วิจัย: นายธนพล เพ็ญรัตน์

ตำแหน่งวิชาการ: อาจารย์ ดร.

E-mail Address : pomphenrat@gmail.com

ระยะเวลาดำเนินงาน : 2 ปี

บทคัดย่อ

อนุภาคนาโนของเหล็กประจุศูนย์ (NZVI) เป็นวัสดุสำหรับการฟื้นฟูการปนเปื้อนสารอินทรีย์ระเหยที่มีคลอรีนเป็นองค์ประกอบในน้ำใต้ดินที่มีศักยภาพสูง อย่างไรก็ดีวัสดุนวัตกรรมนี้ไม่สามารถใช้ในการฟื้นฟูการปนเปื้อนในชั้นดินที่ไม่อิ่มตัวด้วยน้ำได้อย่างมีประสิทธิภาพด้วยโมเลกุลของน้ำไม่พอในการทำปฏิกิริยาการปลดคลอรีนออก อย่างไรก็ดี NZVI เป็นอนุภาคแม่เหล็กที่สามารถสร้างความร้อนได้ภายใต้การเหนี่ยวนำทางแม่เหล็กไฟฟ้าด้วยสนามแม่เหล็กความถี่ต่ำ (LF-EMF) ซึ่งความร้อนนี้หากใช้ร่วมกับการสกัดไอดินจะสามารถเร่งการฟื้นฟูการปนเปื้อนสารอินทรีย์ระเหยที่มีคลอรีนเป็นองค์ประกอบในดินที่ไม่อิ่มตัวด้วยน้ำได้ ในงานวิจัยนี้เราศึกษาการใช้โฟมเป็นตัวส่ง NZVI เข้าไปในชั้นดินที่ไม่อิ่มตัวด้วยน้ำแล้วจึงใช้ LF-EMF ตามเพื่อเร่งการกำจัดสารอินทรีย์ระเหยที่มีคลอรีนเป็นองค์ประกอบในดินที่ไม่อิ่มตัวด้วยน้ำ โดยทำการทดลองในห้องปฏิบัติการ เราพบว่า sodium lauryl ether sulfate (SLES) (3% w/w) สามารถสร้างโฟมที่ส่ง NZVI ได้เสถียรที่สุด โดยโฟมของ NZVI ที่เสถียรด้วย SLES เรียกว่า SLES-F-NZVI มีค่าครึ่งชีวิต 173 นาที SLES-F-NZVI สามารถส่ง NZVI ในน้ำได้เข้มข้นถึง 41.31 กรัมต่อลิตร และสร้างความร้อนภายใต้ LF-EMF ได้เพิ่ม ΔT = 77ºC ใน 15 นาที หากส่งโฟมลงไปในชั้นดินที่ไม่อิ่มตัวด้วยน้ำที่ความเข้มข้น NZVI = 77 กรัมต่อกิโลกรัม ภายใต้สภาวะนี้การใช้ SLES-F-NZVI ร่วมกับ LF-EMF สามารถเร่งการระเหยของ TCE จาก แหล่งกำเนิดประเภทสารเคมีบริสุทธิ์ที่รั่วไหลในชั้นดินที่ไม่อิ่มตัวด้วยน้ำได้เพิ่มขึ้นถึง 39.51 ± 6.59 เมื่อเทียบกับกรณีที่ไม่มีการใช้ SLES-F-NZVI ร่วมกับ LF-EMF ด้วยเหตุนี้การใช้ SLES-F-NZVI ร่วมกับ LF-EMF จะเพิ่มประสิทธิภาพการฟื้นฟูด้วยการสกัดไอดินได้สูงถึง 40 เท่า

คำสำคัญ : อนุภาคแม่เหล็ก, โฟม, การฟื้นฟูพื้นที่ปนเปื้อนสารอันตราย, ชั้นดินที่ไม่อิ่มตัวด้วยน้ำ, สารอินทรีย์ระเหยอันตราย

Abstract

Project Code: MRG5680129

Project Title: Using Magnetic Nanoparticle-Stabilized Foam together with Magnetic Induction Heating to Enhance In Situ Remediation of Volatile Organic Contaminants (VOC) by Soil Vapor Extraction

Investigator: Tanapon Phenrat

Academic Position: Lecturer

E-mail Address: pomphenrat@gmail.com

Project Period: 2 years

Abstract

Nanoscale zerovalent iron (NZVI) is a promising remediation agent for volatile organic compound contamination in saturated subsurface but is rarely applied for vadose zone as there are not enough water molecules in the unsaturated zone to participate in reductive dechlorination. Nevertheless, NZVI is ferromagnetic, capable of inducing heat under an applied low frequency electromagnetic field (LF-EMF), offering an opportunity to serve as a thermally enhanced remediation when combined with soil vapor extraction. In this study, we evaluated the possibility of using foam as a carrying vehicle to emplace NZVI in unsaturated porous media followed by the application of LF-EMF in laboratory batch reactors. We found that sodium lauryl ether sulfate (SLES) (3% w/w) was the best candidate for generating stable foam-based NZVI. The half-life of SLES foam-based NZVI (SLES-F-NZVI) was 173 min. The SLES-F-NZVI carried as much as 41.31 g/L of NZVI in the liquid phase of the foam, and could generate heat to raise ΔT = 77ºC in 15 min at the deposited SLES-F-NZVI =77 g/kg. Under this condition, SLES-F-NZVI together with LF-EMF enhanced TCE evaporation from TCE dense non-aqueous phase liquid (DNAPL) in unsaturated sand by 39.51 ± 6.59 times in comparison to the reactors without SLF-EMF application.

Keywords : Magnetic Particles, Foam, Remediation, Vadose Zone Contamination, Volatile Organic Compound

Output จากโครงการวิจัยที่ได้รับทุนจาก สกว.

1. ผลงานตีพิมพ์ในวารสารวิชาการนานาชาติ

   <u>ได้รับการตีพิมพ์แล้ว</u>

   - <u>Phenrat, T.</u>; Thongboot,T.; Lowry, G.V. (2016). Electromagnetic Induction of Zerovalent Iron (ZVI) Powder and Nanoscale Zerovalent Iron (NZVI) Particles Enhances Dechlorination of Trichloroethylene in Contaminated Groundwater and Soil: Proof of Concept. *Environmental Science & Technology*, 50 (2), pp 872–880 (IF = 5.330)

   - Babakhani, P.; Fagerlund, F.; Shamsai, A.; Lowry, G. V.; and <u>Phenrat, T</u>.* (2015). Modified MODFLOW-Based Model for Simulating the Agglomeration and Transport of Polymer-Modified Fe0 Nanoparticles in Saturated Porous Media. *Environmental Science Pollution Research*, (In Press) (IF = 2.828)

   - <u>Phenrat, T*</u>.; Schoenfelder, D.; Kirschling, T. L.; Tilton, R. D.; Lowry, G. V.* (2015).Adsorbed poly(aspartate) coating limits the adverse effects of dissolved groundwater solutes on Fe0 nanoparticle reactivity with trichloroethylene. *Environmental Science Pollution Research* (In Press) (IF = 2.828)

   <u>อยู่ในระหว่างการพิจารณาบทความ</u>

   - Srirattana, S.; Piaowan, K.; Lowry, G. V.; Saenton, S.; Phenrat, T. Delivery and Electromagnetic Induction of Foam-based Nanoscale Zerovalent Iron (NZVI) Particles as a Combined Remediation Technique for Non-Aqueous Phase Liquid (NAPL) in Unsaturated Porous Media: Proof of Concept. Submitted to *Environmental Science & Technology* (IF =5.330)

2. การนำผลงานวิจัยไปใช้ประโยชน์
   - เชิงสาธารณะ (มีเครือข่ายความร่วมมือ/สร้างกระแสความสนใจในวงกว้าง)
     - งานวิจัยเป็นส่วนหนึ่งที่ทำให้ได้รับรางวัล The Best Entrepreneur Award 2014 of Takeda Foundation ที่กรุงโตเกียว ประเทศญี่ปุ่น
   - เชิงวิชาการ (มีการพัฒนาการเรียนการสอน/สร้างนักวิจัยใหม่)
     - มีนิสิตปริญญามหาบัณฑิต สาขาวิศวกรรมสิ่งแวดล้อม 2 ท่าน และปริญญาดุษฎีบัณฑิต สาขาวิศวกรรมสิ่งแวดล้อม คณะวิศวกรรมศาสตร์ ม.นเรศวร เข้าร่วมทำวิจัย 1 ท่าน คือ
       - นางสาวทิพย์วรรณ ทองบุศย์ (นิสิตปริญญามหาบัณฑิต)
       - Peyman Babakhani (นิสิตแรกเปลี่ยนระดับปริญญามหาบัณฑิตจากประเทศอิหร่าน)
       - นางสาวสุภาวรรณ ศรีรัตนา (นิสิตปริญญาดุษฎีบัณฑิต)

3. อื่นๆ (เช่น ผลงานตีพิมพ์ในวารสารวิชาการในประเทศ การเสนอผลงานในที่ประชุมวิชาการ หนังสือ การจดสิทธิบัตร)

<u>การนำเสนอผลงานระดับนานาชาติ</u>

- Phenrat, T.; Suk-in, J. (2014) Restoration of Cadmium-contaminated Paddy Soil by Ex-situ Magnetic-Assisted Soil Washing: Proof of Concept. Water Dynamics 11, 12-15 March, 2014, Sendai, Japan.
- Phenrat,T.; Kumloet,I.; Malem,F.; Soontorndecha,P.;Lowry,G.V.; Tilton, R.D. (2013) Electromagnetic Induction Heating of Polymer-Modified Nanoscale Zerovalent Iron (NZVI) Accelerates Remediation of Dense Non-aqueous Phase Liquid (DNAPL) Source Zone via Enhanced Dechlorination and NAPL Dissolution. International Conference on Environmental and Hazardous Substance Management (EHWM 2013), Bangkok, Thailand.
- Phenrat, T. (2013) "Reactive Nanoscale Zerovalent Iron for In Situ Groundwater and Soil Remediation: Progress, Challenge, and Opportunity". Pure and Applied Chemistry International Conference 2013 "Global Chemical Sciences for Green Community" January 23-25, 2013, the Tide Resort, Bangsaen Beach, Chon Buri, Thailand.

<u>การนำเสนอผลงานระดับชาติ</u>

- อิสราพงษ์ คุ้มเลิศ และ ธนพล เพ็ญรัตน์ (2557) ก๊าซไฮโดรเจนจากอนุภาคนาโนเหล็กประจุศูนย์ช่วยเร่งการกำจัดแหล่งกำเนิดการปนเปื้อนสารไตรคลอโรเอทธิลีนในดินและน้ำใต้ดิน. การประชุมวิชาการสิ่งแวดล้อมแห่งชาติครั้งที่ 13 . วันที่ 26-28 มีนาคม 2557
- อิสราพงษ์ คุ้มเลิศ, นุชจรี อัมรักษ์, นุสราภรณ์ ธูปประดิษฐ์ และ ธนพล เพ็ญรัตน์ (2556) การใช้อนุภาคแม่เหล็กนาโนที่ถูกปรับปรุงด้วยโพลีเมอร์ร่วมกับสนามแม่เหล็กไฟฟ้ากระแสสลับในการเร่งการกำจัดแหล่งกำเนิดของสารอันตรายประเภทสารอินทรีย์ระเหยที่มีคลอรีนเป็นองค์ประกอบจากน้ำใต้ดินและดินที่ปนเปื้อนโดยการใช้ความร้อนที่สร้างด้วยการเหนี่ยวนำทางแม่เหล็กไฟฟ้า. นเรศวรวิจัยครั้งที่ 9 28-29 กรกฎาคม *2556* ณ มหาวิทยาลัยนเรศวร
- ทิพย์วรรณ ทองบุศย์; ธนพล เพ็ญรัตน์; แฟรดาซ์ มาเหล็ม; พีรพงษ์ สุนทรเดชะ (2556) การใช้เหล็กประจุศูนย์ร่วมกับการเหนี่ยวนำความร้อนทางแม่เหล็กไฟฟ้าในการเร่งการฟื้นฟูน้ำใต้ดินที่ปนเปื้อนด้วยสารไตรคลอโรเอทธิลีน, การประชุมวิชาการวิศวกรรมโยธาแห่งชาติ ครั้งที่ 18, วันที่ 8-10 พฤษภาคม 2556 ณ โรงแรมดิเอ็มเพลส เชียงใหม่

เนื้อหางานวิจัย

1. ความเป็นมาของปัญหา

ปัญหาจากการปนเปื้อนของดินและน้ำใต้ดินในปัจจุบัน จากมลสารอันตรายประเภทสารอินทรีย์ระเหย (ทั้งที่มีคลอรีนเป็นองค์ประกอบ เช่น สารไตรคลอโรเอทธิลีน (TCE) และสารเตตระคลอโรเอทธิลีน (PCE) และที่ไม่มีคลอรีนเป็นองค์ประกอบ เช่น สารเบนซีน(Benzene) และ เอททิลเบนซีน(Ethylbenzene)) เป็นปัญหาใหญ่ที่พบได้ทั่วโลกรวมทั้งประเทศไทย (เช่น นิคมอุตสาหกรรมมาบตาพุด จังหวัดระยอง, อำเภอปากช่อง จังหวัดนครราชสีมา, นิคมอุตสาหกรรมภาคเหนือ จังหวัดลำพูน (รูปที่ 1) ซึ่งสารปนเปื้อนเหล่านี้ส่วนมากมักเป็นสารปนเปื้อนที่ไม่ละลายน้ำ (Non-aqueous Phase Liquids ; NAPLs) ทำให้เมื่อเกิดการปนเปื้อนในสิ่งแวดล้อมแล้วสามารถก่อให้เกิดปัญหาหาขึ้นหลายประการ อาทิเช่น ต่อชั้นดินและน้ำใต้ดิน โดยเฉพาะอย่างยิ่งปัญหาทางสิ่งแวดล้อมต่อสิ่งมีชีวิตในระบบนิเวศ และผลกระทบต่อสุขภาพอนามัยของมนุษย์ เนื่องจากสารปนเปื้อนเหล่านี้ มีความสามารถในการละลายน้ำได้น้อยมาก จึงส่งผลให้เกิดการปนเปื้อนอยู่ในชั้นดินและน้ำใต้ดินได้เป็นเวลายาวนาน ส่งผลต่อการใช้น้ำเพื่อการอุปโภคและบริโรค รวมไปถึงการเกษตรกรรม ประกอบกับสารเหล่านี้จัดเป็นสารอินทรีย์ระเหย ที่สามารถระเหยออกสู่บรรยากาศ มีผลทำให้เกิดพิษทั้งเฉียบพลันและเรื้อรัง บางชนิดก่อให้เกิดมะเร็งต่อมนุษย์ ดังนั้นจึงมีความจำเป็นต้องมีการฟื้นฟูพื้นที่ที่เกิดการปนเปื้อนเปื้อน และบำบัดให้สารปนเปื้อนเหล่านี้อยู่ในเกณฑ์ที่ยอมรับได้

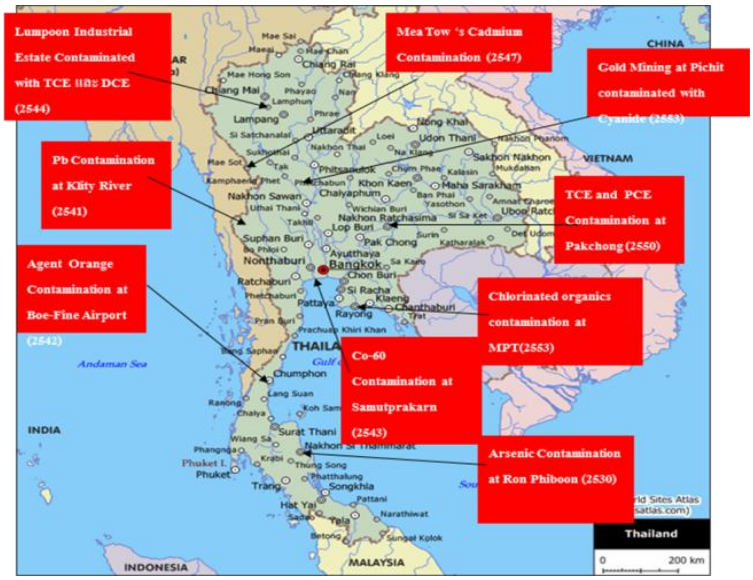

รูปที่ 1 พื้นที่ปนเปื้อนสารอันตรายในประเทศไทย อย่างน้อย 3 พื้นที่ปนเปื้อนด้วยสารอันตรายประเภทสารอินทรีย์ระเหย

การปนเปื้อนเหล่านี้มักจะเกิดจากการรั่วไหลของสารอันตรายผ่านชั้นดินเหนือระดับน้ำใต้ดินก่อนจะเคลื่อนที่โดยแรงโน้มถ่วงและโดยการชะพาโดยน้ำฝนลงสู่น้ำใต้ดิน (รูปที่ 2) สารปนเปื้อนบางส่วนจะยังคงติดค้างอยู่ในดินเหนือระดับน้ำใต้ดิน ดินที่ปนเปื้อนจะดูดซับสารปนเปื้อนเอาไว้ ทั้งสารพิษที่ตกค้างและดินที่ดูดซับสารพิษไว้เป็นเสมือนแหล่งกำเนิดการปนเปื้อนที่เติมสารปนเปื้อนลงสู่น้ำใต้ดินเรื่อยๆ ด้วยเหตุนี้เพื่อการลดผลกระทบต่อสุขภาพและสิ่งแวดล้อมจากการปนเปื้อน วิศวกรรมการฟื้นฟูพื้นที่ปนเปื้อนจึงมีความจำเป็นสำหรับประเทศไทย ซึ่งในปัจจุบันวิธีการจัดการของเสียอันตรายมีหลากหลายประเภท ได้แก่ การบำบัดในพื้นที่ (in situ remediation) และการบำบัดนอกพื้นที่ (ex situ remediation) โดยเทคโนโลยีที่ใช้ในการฟื้นฟูมีทั้งวิธีทางกายเคมี และชีวภาพ เช่น Soil washing , Pump and treat, Bio remediation, chemical oxidation และ soil vapor extraction เป็นต้น ซึ่งวิธีการหนึ่ง ที่สามารถปฏิบัติได้จริงและเริ่มได้รับความนิยมอย่างมาก คือ วิธีการ soil vapor extraction ที่ใช้หลักการในการดูดสารอันตรายที่ระเหยในรูปไอ อาศัยการสูบสารอินทรีย์ระเหยออกมาจากดิน และส่งไปยังระบบบำบัดสารพิษที่ติดตั้งไว้เหนือพื้นดิน เช่น เตาเผา เป็นต้น โดย ดร.ธนพล เพ็ญรัตน์ ในฐานะที่ปรึกษาโครงการวิจัย ได้ทำการออกแบบและติดตั้งระบบสกัดไอดิน (รูปที่ 3(b)) เครื่องแรกในประเทศไทย และสาธิตการฟื้นฟูในพื้นที่ปนเปื้อนบริเวณนิคมอุตสาหกรรมมาบตาพุด จังหวัดระยอง โดยเทคนิคการสกัดไอดินสามารถกำจัดสารอินทรีย์ระเหยที่ตกค้างในช่องว่างของดินได้ดี (ในรูปของสารบริสุทธิ์ซึ่งมีลักษณะคล้ายน้ำมัน) แต่ไม่สามารถกำจัดสารปนเปื้อนที่ถูกดูดซับอยู่ในช่องว่างของเม็ดดินได้ดีนัก จึงทำให้ไม่สามารถบำบัดและฟื้นฟูได้อย่างเต็มประสิทธิภาพ จึงจำเป็นต้องใช้ความร้อนร่วมกับการสกัดไอดิน โดยการส่งไอร้อนลงไปใต้ดินเพื่อเร่งการชะละลายสารปนเปื้อนออกมาจากดินก่อนการสกัดออกมาเพื่อบำบัด

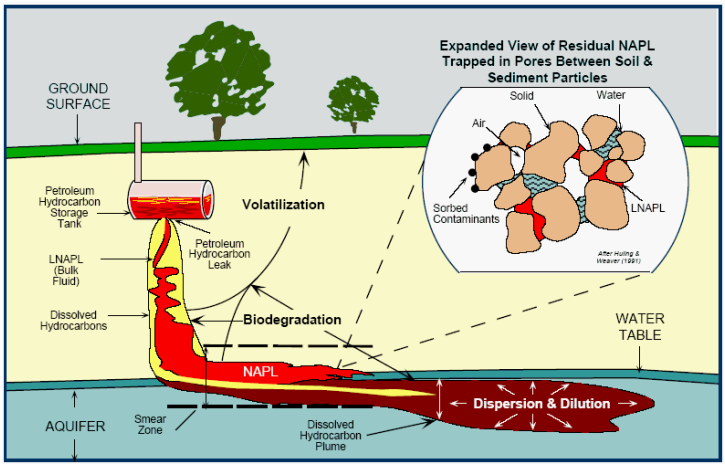

รูปที่ 2 การรั่วไหลของสารอินทรีย์ระเหยจากชั้นดินเหนือระดับน้ำใต้ดินสู่ชั้นน้ำใต้ดิน (สารปนเปื้อนที่คงค้างอยู่ในชั้นดินเหนือน้ำใต้ดิน มีพฤติกรรมเป็นแหล่งกำเนิดการปนเปื้อนน้ำใต้ดินระยะยาว จำเป็นต้องได้รับการกำจัดก่อนการฟื้นฟูน้ำใต้ดิน)

งานวิจัยนี้เสนอนวัตกรรมการใช้โฟมที่ปรับเสถียรด้วยอนุภาคแม่เหล็กนาโนร่วมกับสนามแม่เหล็กไฟฟ้ากระแสสลับในการสร้างความร้อนใต้ดินเพื่อเร่งการฟื้นฟูดินปนเปื้อนสารอินทรีย์ระเหยร่วมกับการสกัดไอดิน โดยมีแนวคิด คือ การส่งโฟมที่ปรับเสถียรด้วยอนุภาคแม่เหล็กนาโนลงไปในชั้นดินที่ปนเปื้อน จากนั้นจึงส่งสนามแม่เหล็กไฟฟ้ากระแสสลับลงไปพร้อมกับทำการสกัดไอดิน สนามแม่เหล็กไฟฟ้ากระแสสลับจะเหนี่ยวนำอนุภาคแม่เหล็กให้เกิดความร้อน ซึ่งจะส่งผ่านสู่ดินและเร่งการระเหยของสารปนปื้อนออกมาจากดินทำให้สามารถสกัดสารอินทรีย์ระเหยออกมาได้เร็วขึ้น ดังแสดงรูปที่ 4

(a)

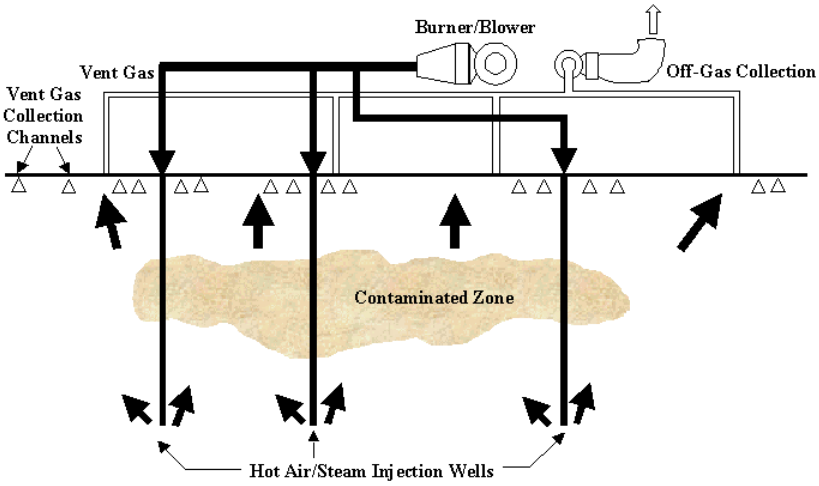

(b)

รูปที่ 3 (a) ระบบสกัดไอดินทั่วไป ประกอบด้วยบ่อสกัด เครื่องสูบไอดิน และ ระบบบำบัดไอดินปนเปื้อน (b) ระบบสกัดไอดินเครื่องแรกของประเทศไทยที่สร้างโดยกรมส่งเสริมคุณภาพสิ่งแวดล้อม โดยมีดร.ธนพล เพ็ญรัตน์ ในฐานะที่ปรึกษาและคณะทำงานวิจัย

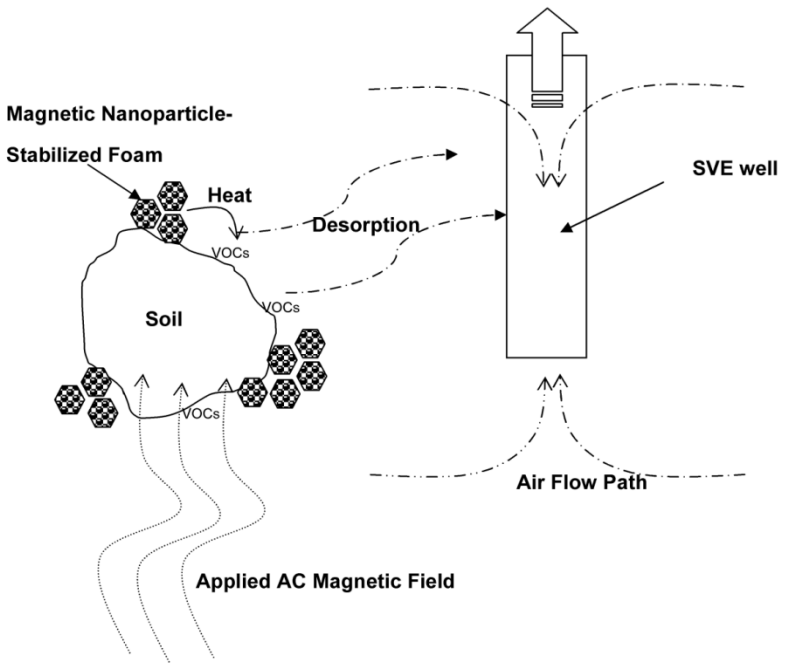

รูปที่ 4 การใช้โฟมที่ปรับเสถียรด้วยอนุภาคแม่เหล็กนาโนร่วมกับสนามแม่เหล็กไฟฟ้ากระแสสลับในการสร้างความร้อนใต้ดินเพื่อเร่งการฟื้นฟูดินปนเปื้อนสารอินทรีย์ระเหยโดยการสกัดไอดิน

2. วัตถุประสงค์ของการศึกษา

1. เพื่อสังเคราะห์โฟมที่ปรับเสถียรด้วยอนุภาคแม่เหล็กนาโน

2. เพื่อประเมินความสามารถของโฟมที่ปรับเสถียรด้วยอนุภาคแม่เหล็กนาโนในการสร้างความร้อน ภายใต้การเหนี่ยวนำความร้อนทางแม่เหล็กไฟฟ้ากระแสสลับ

3. เพื่อประเมินความสามารถของโฟม ต่อการเคลื่อนที่ของอนุภาคนาโนของเหล็กประจุศูนย์ผ่านตัวกลางทราย

4. เพื่อสาธิตการเร่งการบำบัดฟื้นฟูดินที่ปนเปื่อนสาร TCE โดยความสามารถในการบำบัดสาร TCE จะถูกแทนด้วยปริมาณการละลายหรือระเหยกลายเป็นไอของสาร TCE ในรูปของการเปรียบเทียบความแตกต่างระหว่างเมื่อได้รับความร้อน และไม่ได้รับความร้อน (โดยใช้การทดลองแบบ Batch ในห้องปฏิบัติการ)

3. สมมติฐานของการวิจัย

1. อนุภาคนาโนของเหล็กประจุศูนย์เป็นอนุภาคแม่เหล็กนาโนแบบ Ferromagnetic สามารถสร้างความร้อนโดยการเหนี่ยวนำทางแม่เหล็กไฟฟ้าภายใต้สนามแม่เหล็กกระแสสลับ

2. ความร้อนที่สร้างจากเหนี่ยวนำทางแม่เหล็กไฟฟ้าภายใต้สนามแม่เหล็กกระแสสลับช่วยในการดึงเอาสารพิษประเภทสารอินทรีย์ระเหยที่มีคลอรีนเป็นองค์ที่ถูกดูดซับอยู่กับดินให้ละลายออกมา (Desorption หรือ Back Diffusion)

3. การใช้อนุภาคนาโนของเหล็กประจุศูนย์ร่วมกับการเหนี่ยวนำทางแม่เหล็กไฟฟ้าภายใต้สนามแม่เหล็กกระแสสลับสามารถนำไปประยุกต์ ใช้ได้จริงในพื้นที่ปนเปื้อน

4. วิธีดำเนินงานวิจัย

4.1 กรอบแนวคิดการวิจัย

การประยุกต์ใช้เทคโนโลยีนี้ประกอบด้วยการส่งอนุภาคนาโนของเหล็กประจุศูนย์ที่ถูกปรับเสถียรภาพด้วยโฟม ลงไปใต้ดินเพื่อทำปฏิกิริยาทางเคมี (Dechlorination) ร่วมกับการใช้ความร้อนที่สร้างจากการเหนี่ยวนำทางแม่เหล็กไฟฟ้าของอนุภาคนาโนของเหล็กประจุศูนย์เพื่อเร่งการสลายสารปนเปื้อนประเภทสารอินทรีย์ระเหยที่มีคลอรีนเป็นองค์ประกอบที่ปนเปื้อนดินและน้ำใต้ดิน เพื่อให้สามารถส่งอนุภาคนาโนของเหล็กประจุศูนย์ลงไปยังใต้ดิน จำเป็นต้องมีการทำการปรับปรุงอนุภาคนาโนของเหล็กประจุศูนย์ด้วยสารโพลีเมอร์ และต้องมีขั้นตอนการทดสอบความสามารถในการเคลื่อนที่ได้ใต้ดิน อย่างไรก็ดีประเด็นเหล่านี้ได้ถูกวิจัยโดยละเอียดแล้วในงานวิจัยที่ผ่านมาของ ดร. ธนพล (Phenrat et al. 2010a; Phenrat et al. 2010b; Phenrat et al. 2009a; Phenrat et al. 2008; Phenrat et al. 2010d) และ ของนักวิจัยท่านอื่นๆ (He et al. 2007; Hong et al. 2009; Johnson et al. 2009; Kanel et al. 2008; Saleh et al. 2008) ดังนั้นสิ่งที่จะถูกให้ความสำคัญในงานวิจัยนี้ คือ กลไกการเร่งอัตราการสลายมลสารโดยใช้ความร้อนที่สร้างจากการเหนี่ยวนำทางแม่เหล็กไฟฟ้าของอนุภาคนาโนของเหล็กประจุศูนย์ร่วมกับการทำปฏิกริยาทางเคมีเพื่อสลายสารปนเปื้อนประเภทสารอินทรีย์ระเหยที่มีคลอรีนเป็นองค์ประกอบซึ่งเป็นเรื่องใหม่และเป็นนวัตกรรมที่จะได้จากงานวิจัยนี้

จากการศึกษาค้นคว้าพบว่าว่าขั้นตอนการถูกปลดปล่อย (Desorption) ออกจากดินเป็นขั้นที่กำหนดอัตรารวมของการเกิดปฏิกิริยา(Rate-Limited Step) ด้วยเหตุนี้ถึงแม้ว่าอนุภาคนาโนของเหล็กประจุศูนย์จะสามารถทำปฏิกิริยาการปลดคลอรีนออกได้อย่างรวดเร็วก็ไม่เป็นประโยชน์เท่าที่ควร เนื่องจากขั้นที่ช้าและกำหนดอัตราการเกิดปฏิกิริยารวม คือ การถูกปลดปล่อย (Desorption) ของTCEออกมาจากดิน งานวิจัยนี้เสนอกรอบแนวคิดเพื่อแก้ไขปัญหานี้ได้โดยการเพิ่มอุณหภูมิของดินข้างเคียง เพื่อเร่งอัตราการถูกปลดปล่อยของมลสารที่ถูกดูดซับอยู่ในดิน การเพิ่มอุณหภูมิสามารถทำได้โดยใช้ความร้อนที่เกิดจากการเหนี่ยวนำความร้อนทางแม่เหล็กไฟฟ้าของอนุภาคนาโนของเหล็กประจุศูนย์ที่ถูกส่งลงไปในชั้นดิน โดยอาศัยการส่งสนามแม่เหล็กกระแสสลับลงไปใต้ดินที่ต้องการฟื้นฟู

อนุภาคนาโนของเหล็กประจุศูนย์เป็นอนุภาคแม่เหล็กนาโนแบบ Ferromagnetite (Phenrat et al., 2007) ซึ่งสามารถสร้างความร้อนโดยการเหนี่ยวนำทางแม่เหล็กไฟฟ้าภายใต้สนามแม่เหล็กกระแสสลับผ่านปรากฏการณ์ Hysteresis Losses ที่เกิดขึ้นในวัฏจักร Magnetization /Demagnetization ของอนุภาคแม่เหล็ก(Li et al., 2010) ดังแสดงในสมการที่ 1

$$P = f\Delta U \tag{1}$$

เมื่อ P คือ อัตราการเกิดความร้อน *f* คือความถี่สนามแม่เหล็กไฟฟ้ากระแสสลับ

ΔU คือ พื้นที่ใต้ Hysteresis Loop ของอนุภาคแม่เหล็กนาโนภายใต้สนามแม่เหล็ก

อุณหภูมิสูงสุดของการเหนี่ยวนำด้วยวิธีนี้ขึ้นอยู่กับค่า Curie Temperature (T_C) ซึ่งขึ้นอยู่กับองค์ประกอบทางเคมีของอนุภาคแม่เหล็กนาโน(Zhang et al., 2003) โดยทั่วไปแล้ว T_C ของอนุภาคแม่เหล็กนาโนมีค่าตั้งแต่ 100 ถึง ~400 ^{o}C ซึ่งมากเกินพอสำหรับการให้ความร้อนเพื่อเร่งการบำบัดการปนเปื้อนใต้ดิน การสร้างความร้อนโดยการเหนี่ยวนำทางแม่เหล็กไฟฟ้าของอนุภาคแม่เหล็กนาโนได้มีการศึกษากันอย่างแพร่หลาย เพื่อการประยุกต์ใช้ในการรักษาโรคมะเร็งแบบ Hyperthermia (Li et al., 2010) อย่างไรก็ดีการประยุกต์ใช้กับ Hyperthermia ต้องการสร้างความร้อนถึงแค่ประมาณ 41-46 ^{o}C เท่านั้น เพื่อกำจัดเซลล์มะเร็ง และไม่ทำอันตรายกับเซลล์ข้างเคียง ดังนั้นการศึกษาเพื่อ Hyperthermia ส่วนใหญ่จึงทำที่ความถี่ต่ำๆ(Li et al., 2010) ในขณะที่ความถี่สูงๆ อนุภาคแม่เหล็กนาโนสามารถสร้างความร้อนได้มากพอสำหรับการประยุกต์ใช้ในการฟื้นฟูพื้นที่ปนเปื้อน ยกตัวอย่างเช่นที่ความถี่ 5.85 เมกะเฮิร์ซ ภายใต้สนามแม่เหล็กไฟฟ้ากระแสสลับที่ความเข้มข้น 21.83 Oe อนุภาคแม่เหล็กนาโนเฟอร์ไรท์จะสร้างความร้อนจนถึงค่า T_C (344 ^{o}C) ในเวลาแค่ 4 นาทีเท่านั้น (Zhang et al., 2003)

ด้วยเหตุนี้เราจึงสามารถใช้ประโยชน์จากการเหนี่ยวนำทางแม่เหล็กไฟฟ้าของอนุภาคนาโนของเหล็กประจุศูนย์เมื่อมีการส่งสนามแม่เหล็กกระแสสลับลงไปใต้ดินร่วมกับการทำปฏิกิริยาทางเคมีเพื่อเร่งอัตราการสลายสารสารอินทรีย์ระเหยที่มีคลอรีนเป็นองค์ประกอบในดินและน้ำใต้ดินที่ปนเปื้อนได้ (รูปที่ 5)

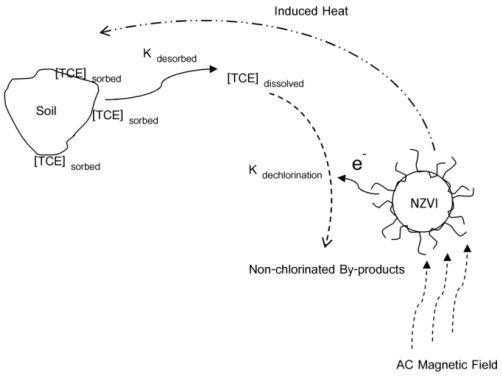

รูปที่ 5 กระบวนการทางเคมี-ฟิสิกส์ ที่เกิดขึ้นในระดับโมเลกุลที่เกี่ยวข้องกับการใช้อนุภาคนาโนของเหล็กประจุศูนย์เพื่อฟื้นฟูดินและน้ำใต้ดินที่ปนเปื้อนด้วย TCE สำหรับการบำบัดโดยเทคนิคที่ถูกนำเสนอในข้อเสนอโครงการนี้ซึ่งใช้ความร้อนที่สร้างจากการเหนี่ยวนำทางแม่เหล็กไฟฟ้าของอนุภาคนาโนของเหล็กประจุศูนย์ร่วมกับการทำปฏิกิริยาทางเคมีเพื่อสลาย TCE การเหนี่ยวนำทางแม่เหล็กไฟฟ้าของอนุภาคนาโนจะเร่งอัตราการการถูกปลดปล่อย (Desorption) ของTCE ออกมาจากดินซึ่งทำให้อัตราการบำบัดเร็วขึ้นและถูกกำหนดโดยอัตราการเกิดปฏิกิริยาทางเคมี(Dechlorination reaction)

4.2 ขอบเขตของงานวิจัย

- ทำการสังเคราะห์โฟมที่ปรับเสถียรด้วยอนุภาคแม่เหล็กนาโนโดยใช้อนุภาคนาโนของเหล็กประจุศูนย์ร่วมกับ สารลดแรงตึงผิว 5 ชนิด ประกอบด้วย Sodium Lauryl Ether Sulfate (*SLES*), PEG-20 Sorbitan monostearate (Tween 60) , Sorbitan monooleate(Span 80), Vertex Type 1 (Foaming Agent for Lightweight Cellular Concrete)และ Vertex Type 2 (Foaming Agent for Lightweight Cellular Concrete) เพื่อหาชนิดของสารลดแรงตึงผิว และปริมาณ %ความเข้,ข้น ที่เหมาะสมต่อการทดลอง
- ทำการประเมินประสิทธิภาพของการเหนี่ยวนำความร้อนทางแม่เหล็กไฟฟ้าของอนุภาคเหล็กนาโนของเหล็กประจุศูนย์ ที่เกิดขึ้นเมื่ออยู่ในตัวกลาง และสภาวะที่แตกต่างกัน
- การประเมินความสามารถของโฟม ที่มีต่อการนำพาให้อนุภาคเหล็กนาโนสามารถเคลื่อนที่ขณะผ่านตัวกลางทราย (Pack Column) ตลอดจนปริมาณคงค้าง (Sorbed) ที่สามารถเหนี่ยวนำให้เกิดความร้อนขึ้นในทราย ที่อุณหภูมิมากกว่า 80 ^{o}C
- การประเมินความสารถในบำบัดสาร TCE โดยความสามารถในการบำบัดสาร TCE จะถูกแทนด้วยปริมาณการละลายหรือระเหยกลายเป็นไอของสาร TCE ในรูปของการเปรียบเทียบความแตกต่างระหว่างเมื่อได้รับความร้อน และไม่ได้รับความร้อน (โดยใช้การทดลองแบบ Batch เพื่อให้ง่ายต่อการควบคุม) ซึ่งรูปแบบของการทดลองที่มีจลศาสตร์ของการสลายตัวของสาร TCE เร็วกว่า แปลว่าลักษณะทางกายภาพนั้นเอื้อต่อการน้ำไปใช้ในการฟื้นฟูการปนเปื้อน โดยรูปแบบการทดลองถูกแสดงดังในรูปที่ 6 และ 7

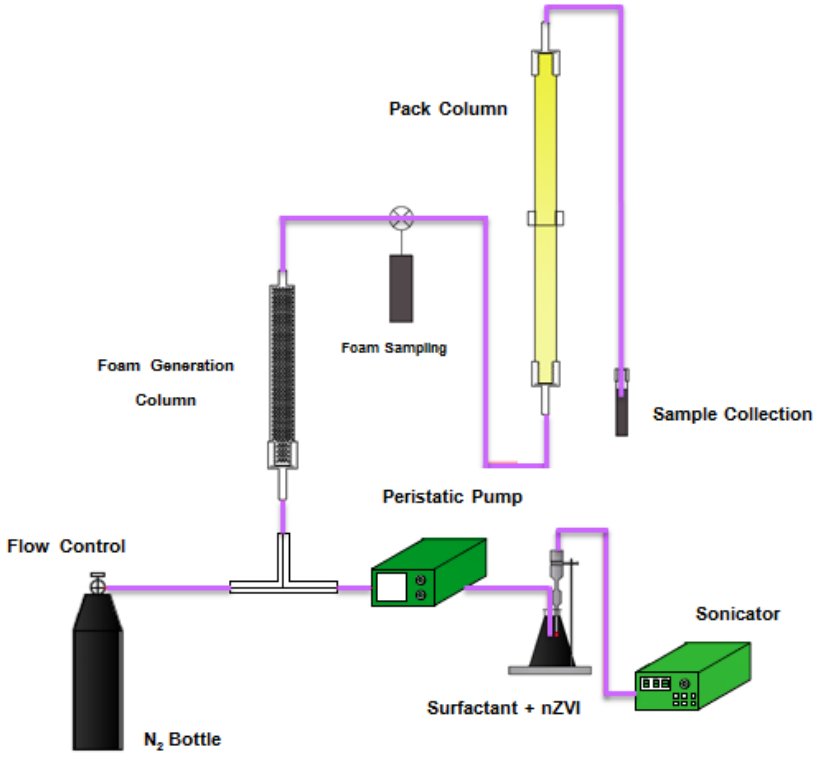

รูปที่ 6 แผนภาพผังการทดลอง

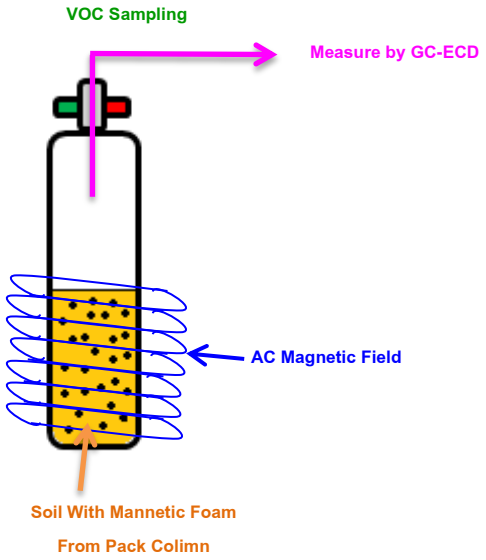

รูปที่ 7 การทดลองการสาธิตการเร่งการฟื้นฟูดินที่ปนเปื้อนสารอินทรีย์ระเหยโดยใช้การสกัดไอดินร่วมกับการเหนี่ยวนำความร้อนทางแม่เหล็กไฟฟ้าของโฟมที่ปรับเสถียรด้วยอนุภาคแม่เหล็กนาโนโดยการทดลองในห้องปฏิบัติการ

4.3 อุปกรณ์และเครื่องมือที่ใช้ในการศึกษาวิจัย

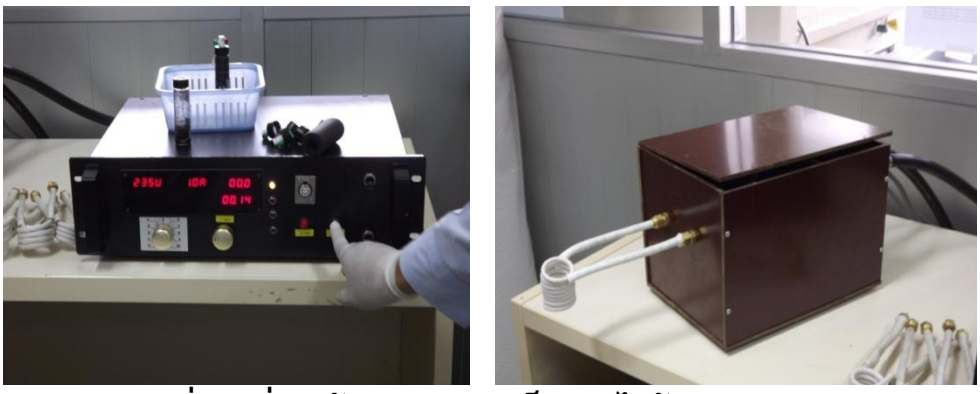

รูปที่ 8 เครื่องสร้างสนามแม่เหล็ก จากไฟฟ้ากระแสสลับ

รูปที่ 9 กล้องถ่ายภาพความร้อน (FLIR i3 Infrared Camera)

รูปที่ 10 เครื่องวัดอุณหภูมิโดยใช้แสงอินฟาเรด (Digital Infrared Thermometer)

รูปที่ 11 เครื่องชั่ง ความละเอียดทศนิยม 4 ตำแหน่ง

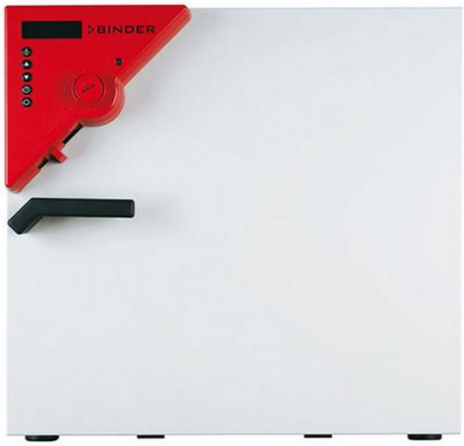

รูปที่ 12 ตู้อบไล่ความชื้น (อุณหภูมิ 105 °C)

รูปที่ 13 แก๊สโครมาโทรกราฟี (Gas Chromatography)

รูปที่ 14 เครื่อง Sonicator

รูปที่ 15 Peristaltic Pump

รูปที่ 16 เข็มสำหรับเก็บตัวอย่างก๊าซ แบบมีวาล์วเปิด-ปิด

รูปที่ 17 กล้องจุลทรรศน์ (microscope)

4.4 รายละเอียดการทดลอง

4.4.1 การวางแผนการทดลอง

การทดลองที่ 1 : การหาชนิดของสารลดแรงตึงผิว (Surfactant) และปริมาณ %ความเข้มข้น ตลอดจนอัตราการไหลของสารลดแรงตึงผิว ที่มีความเหมาะสมต่อการทดลอง

การทดลองที่ 2 : การประเมินประสิทธิภาพของการเหนี่ยวนำความร้อนทางแม่เหล็กไฟฟ้าโดยอนุภาคนาโนของเหล็กประจุศูนย์ ที่เกิดขึ้นจากเหล็กในตัวกลางโฟม น้ำ และสารลดแรงตึงผิว

การทดลองที่ 3 : การประเมินความสามารถของโฟม ที่มีต่อการนำพาการเคลื่อนที่ของอนุภาค NZVI

การทดลองที่ 4 : การประเมินความสามารถของอนุภาค NZVI ที่ถูกปรับเสถียรภาพด้วยโฟมในการบำบัดสาร TCE โดยการใช้ความร้อนจากการเหนี่ยวนำทางแม่เหล็กไฟฟ้าในการทดลองแบบ Batch

4.4.2 ขั้นตอนการทดลอง

<u>การทดลองที่ 1 : การหาชนิดของสารลดแรงตึงผิว (Surfactant) และปริมาณ %ความเข้มข้น ตลอดจนอัตราการไหลของสารลดแรงตึงผิว ที่มีความเหมาะสมต่อการทดลอง</u>

1.1 การเปรียบเทียบเสถียรภาพของสารลดแรงตึงผิว

ทำการศึกษาทดลองโดยใช้สารลดแรงตึงผิว (Surfactant) ทั้งหมด 5 ชนิด เพื่อนำมาสังเคราะห์เป็นสารตั้งต้นทำโฟม อันประกอบด้วย

1) Sodium Lauryl Ether Sulfate (SLES)
2) Sorbitanmonooleate (Span 80)
3) PolyoxyethyleneSorbitanMonostearate (Tween 60)
4) Vertex Type 1 (Foaming Agent for Lightweight Cellular Concrete)
5) Vertex Type 2 (Foaming Agent for Lightweight Cellular Concrete)

รูปที่ 18 สารลดแรงตึงผิว (Surfactant)

ทำการสร้างโฟม โดยใช้คอลัมน์ทรงกระบอกขนาดเส้นผ่านศูนย์กลาง 1.9 ซม. ยาว 16 ซม. บริเวณส่วนปลายปิดด้วยตะแรงเบอร์ 200 ใช้อัตราการไหลของสาร Surfactant ผ่านปั๊มสุญญากาศแบบรีดท่อ (Peristaltic Pump) เท่ากับ 1.50 มล./นาที และอัตราการไหลของแก๊สไนโตรเจน เท่ากับ 500 มล./นาที

รูปที่ 19 Foam Generation Column

การทดลองนี้ ได้ทำการเปรียบเทียบเสถียรภาพของโฟมที่ถูกสร้างขึ้น แบบโฟมเปล่าๆ และโฟมที่ผสมอนุภาคนาโนของเหล็กประจุศูนย์ (Nano-Zero Valent Iron ; NZVI) จากนั้นทำการเก็บตัวอย่างโฟมที่ถูกสร้างผ่านคอลัมน์ด้วยขวดแก้ว ขนาดเส้นผ่านศูนย์กลาง 2 ซม. และมีความยาว 7 ซม. จำนวน 2 ขวด

รูปที่ 20 โฟมที่ไม่ผสม NZVI

รูปที่ 21 โฟมที่ผสม NZVI (ความเข้มข้น 50 กรัม/ลิตร)

1.2 การเปรียบเทียบการกระจายตัวของขนาดอนุภาค (Particle Size Distribution)

การหาขนาดของอนุภาคโฟมด้วยกล้องจุลทรรศน์ (microscope) กำลังขยาย 4x/0.01 ที่ต่อเชื่อมกับกล้องดิจิตอลความละเอียด 3.0 MP เพื่อทำการบันทึกภาพแล้วทำการวัดขนาดและนับจำนวนอนุภาค (รูปที่ 17)

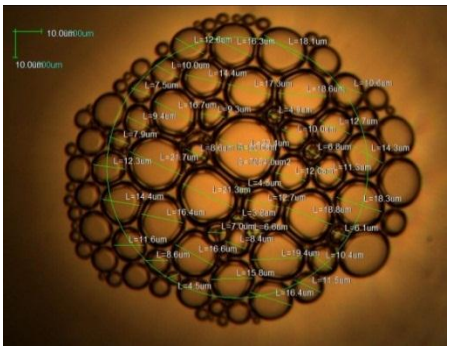

รูปที่ 22 อนุภาคโฟม จากกล้องจุลทรรศน์อิเล็กตรอน (microscope)

1.3 ปริมาณ %ความเข้มข้น ที่มีความเสถียรภาพและเหมาะสม

นำสาร Surfactant ชนิด SLES ซึ่งมีความสามารถในการคงเสถียรภาพได้มากที่สุด มาทำการทดลองที่ความเข้มข้นแตกต่างกัน เพื่อหาความเข้มข้นที่เหมาะสม และสามารถคงเสถียรภาพได้นานที่สุด โดยได้ทำการทดลองทั้งหมด 5 ความเข้มข้น ประกอบด้วย 1% 3% 5% 7% และ 9% ตามลำดับ

<u>การทดลองที่ 2 การประเมินประสิทธิภาพของการเหนี่ยวนำความร้อนทางแม่เหล็กไฟฟ้าโดยอนุภาคนาโนของเหล็กประจุศูนย์ ที่เกิดขึ้นจากเหล็กในตัวกลางโฟม น้ำ และสารลดแรงตึงผิว</u>

ทำการทดลองเปรียบเทียบค่าเฉลี่ยความร้อน (°C) ที่เกิดขึ้นจากเหล็กในตัวกลางโฟมน้ำ และสารลดแรงตึงผิว (SLES) โดยทำการใส่น้ำ สารลดแรงตึงผิว และโฟม ลงไปในขวดทดลองในปริมาตรที่เท่ากัน คือ 12.5 มล. (ครึ่งขวด) แล้วนำไปเหนี่ยวนำให้เกิดความร้อนทางแม่เหล็กไฟฟ้า ที่เวลา 5 10 และ15 นาที แล้วนำขวดทดลองไปอบที่ตู้อุณหภูมิ 105 °C (รูปที่ 12) เพื่อหาน้ำหนักเหล็กที่อยู่ในขวด จากนั้นนำไปทำการคำนวณเปรียบเทียบ ค่าอุณหภูมิที่เกิดการเปลี่ยนแปลงไป (ΔT) จากเดิม โดยคำนวณจากค่าอุณหภูมิที่เปลี่ยนแปลงไป (°C) ต่อปริมาณเหล็ก (กรัม) ที่มีอยู่ในตัวกลางทั้ง 3 ชนิด

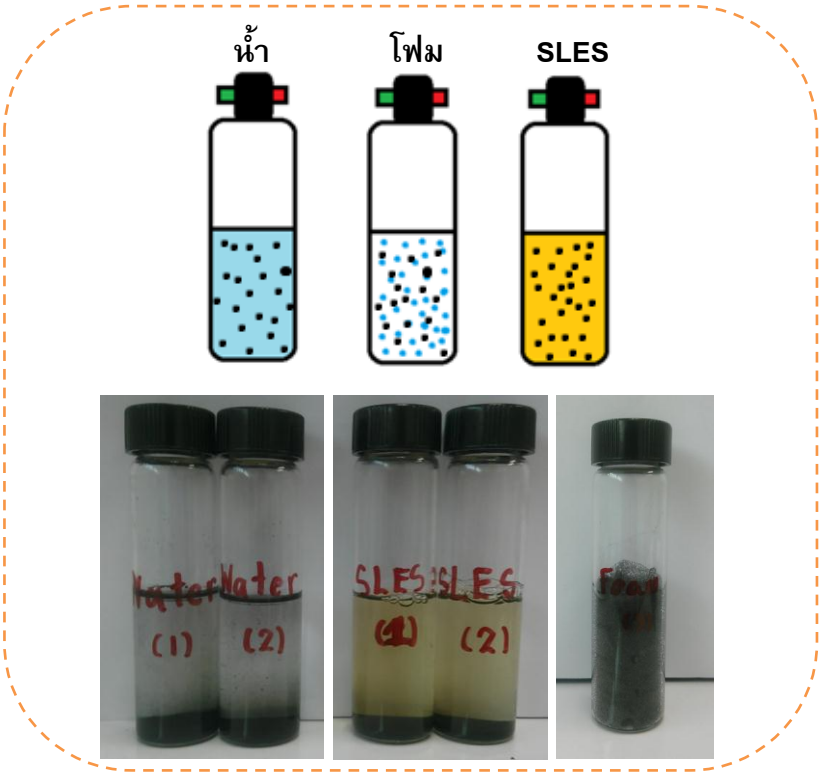

รูปที่ 23 ตัวกลางน้ำ สารลดแรงตึงผิว และโฟม

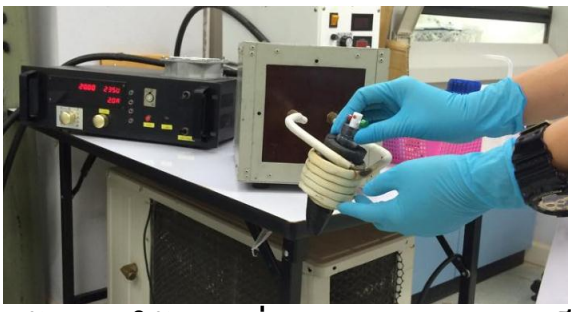

รูปที่ 24 การให้ความร้อนภายใต้การเหนี่ยวนำ ผ่านสนามแม่เหล็กไฟฟ้ากระแสสลับ

<u>การทดลองที่ 3 การประเมินความสามารถของโฟม ที่มีต่อการนำพาการเคลื่อนที่ของอนุภาค NZVI</u>

3.1 ค่าความสามารถของโฟม ต่อความสามารถในการการเคลื่อนที่ของอนุภาค NZVI

ทำการเป่าสร้างโฟมใช้อัตราการไหลของสาร SLES-NZVI เท่ากับ 1.5 มล./นาที ใช้ความเข้มข้นของอนุภาค NZVI เท่ากันในทุกการทดลอง เท่ากับ 50 กรัม/ลิตร และใช้อัตราการไหลของแก๊สไนโตรเจน เท่ากับ 125, 300 และ 500 มล./นาที ตามลำดับ โดยรอจนฟองโฟมมีเสถียรภาพ และมีขนาดอนุภาคคงที่ (ประมาณ 3 นาที) จึงทำการเก็บตัวอย่างโฟมใส่ในขวดแก้วรูปชมพู่ขนาด 50 มล. โดยภายในขวดเก็บตัวอย่างรูปชมพู่บรรจุเมทานอลจำนวน 10 มล. เพื่อให้สารเมทานอลเป็นตัวสลายอนุภาคฟองโฟมให้อยู่ในสถานะของเหลว ทำการเก็บตัวอย่างเป็นเวลา 5 นาที/ตัวอย่าง โดยเก็บตังอย่างจำนวน 3 ตัวอย่าง เพื่อนำมาหาค่าเฉลี่ยของปริมาณความเข้มข้นของอนุภาค NZVI ที่สามารถเคลื่อนที่มาพร้อมกับโฟม โดยระหว่างที่ทำการสร้างโฟม ได้มีการกระตุ้นด้วยเครื่อง Sonicator ตลอดเวลา (รูปที่ 14) เพื่อไม่ให้อนุภาคเหล็กเกิดการตกตะกอนอยู่บริเวณด้านล่างของบีกเกอร์

อนุภาค NZVI ที่อยู่ในขวดแก้วรูปชมพู่ จะถูกแยกโดยใช้แท่งแม่เหล็กทำการดูดเหล็กติดไว้ในขวดแก้ว ที่ทำการชั่งน้ำหนักไว้แล้ว เพื่อเปรียบเทียบปริมาณเหล็กที่อยู่ในขวดต่อไป

รูปที่ 25 Ability of Foam to Carry NZVI

ในส่วนของการทดลองเพื่อหาปริมารการคงค้าง (Sorbed) ของอนุภาค NZVI ในทรายตามระยะทางในการเคลื่อนที่ สามารถแสดงได้ดังต่อไปนี้

1. ใช้คอลัมน์ทรงกระบอก ทำจากอะคริลิก ขนาดเส้นผ่านศูนย์กลาง 1.9 ซม. สูง 16 ซม. (ปริมาตร 49.30 ลบ.ซม.)ที่บริเวณส่วนปลาย ทั้งส่วนหัวและท้าย ปิดด้วยตะแกรงขนาดเบอร์ 60

2. ใช้ทรายขนาด 0.85 มม. แล้วทำการชั่งน้ำหนักทรายพร้อมคอลัมน์ก่อนทำการทดลอง (น้ำหนักแห้ง)

3. ทำการคำนวณค่าความพรุน (porosity) จากปริมาณของเหลวที่ถูกใส่ลงไปในคอลัมน์ขณะที่บรรจุทรายอยู่ภายใน(มล.) หารด้วยปริมาตรคอลัมน์ทั้งหมด (มล.)

4. ทำการฝลัดสารละลาย 0.02 M Nacl จำนวน 3 pore volume เพื่อทำการปรับสภาพให้ทรายที่อยู่ในคอลัมน์มีลักษณะประจุ หรืออิออนใกล้เคียงกับทรายธรรมชาติ จากนั้นปล่อยให้น้ำไหลออกจากคอลัมน์ ภายใต้แรงโน้มถ่วง รอจนน้ำหยุดไหลแล้วนำไปชั่งน้ำหนัก (น้ำหนักทรายเปียก) เพื่อหา %Saturation (นน.ทรายเปียก-นน.ทรายแห้ง)

5. ทำการฝลัดด้วย SLES (โฟมเปล่าๆ) จำนวน 1 pore volume

6. ทำการฝลัด SLES + NZVI ผ่านคอลัมน์ทราย จำนวน 60 pore volume

7. นำทรายออกจากคอลัมน์ โดยแบ่งเป็นทุก 2 ซม. (0-2, 2-4 ,4-8, 8-10, 10-12,12-14 และ 14-16 ซม.) ใส่ลงในบีกเกอร์ที่บรรจุด้วยน้ำ DI แล้วนำไปทำการกระตุ้นด้วยเสียง (Sonicator) เป็นเวลา 1 นาที แล้วตามด้วยการเขย่าเบาๆ ด้วยมือ เพื่อให้เหล็กที่ติดอยู่กับทราย หลุดออกมา

8. เหล็กที่หลุดออกมาถูกแยกโดยใช้แท่งแม่เหล็กทำการดูดเหล็กติดไว้ในขวดแก้ว ที่ทำการชั่งน้ำหนักไว้แล้ว เพื่อเปรียบเทียบปริมาณเหล็กที่อยู่ในขวด ส่วนทรายก็นำไปทำการชั่งน้ำหนัก เพื่อนำไปคำนวณหาปริมาณเหล็กที่อยู่ในทรายต่อไป (กรัม$_{เหล็ก}$/กรัม$_{ทราย}$)

รูปที่ 26 ความสามารถของโฟม ที่มีต่อการนำพาการเคลื่อนที่ของอนุภาค NZVI

3.2 ปริมารการคงค้าง (Sorbed) ของอนุภาค NZVI ในทรายที่สามารถเหนี่ยวนำให้เกิดความร้อน ที่อุณหภูมิมากกว่า 80 °C

วัตถุประสงค์ในการทดลองนี้ คือ เพื่อหาปริมาณการสะสมตัวของอนุภาค NZVI ที่อยู่ในทราย เมื่อผ่านการเหนี่ยวนำความร้อนทางแม่เหล็กไฟฟ้า แล้วสามารถเหนี่ยวนำให้เกิดความร้อนที่อุณหภูมิมากกว่า 80 °C โดยทำการเป่าสร้างโฟมใช้อัตราการไหลของสาร SLES-NZVI เท่ากับ 1.5 มล./นาที ใช้อัตราการไหลของแก๊สไนโตรเจน เท่ากับ 500 มล./นาที (Condition ที่ดีที่สุดจากการทดลองที่ 3.1) และทดลองใช้ความเข้มข้นของอนุภาค NZVI ที่ต่างกัน โดยเพิ่มความเข้มข้นของ NZVI ขึ้นทีละ 20 กรัม/ลิตร โดยเริ่มทำการทดลองจากความเข้มข้น 60 กรัม/ลิตร ทำการฝลัดโฟมผ่านคอลัมน์ที่บรรจุทราย จำนวน 60 pore volume จากนั้นนำทรายออกจากคอลัมน์ โดยแบ่งเป็นทุก 2 ซม. ใส่ลงในขวด Vail ขนาดเส้นผ่านศูนย์กลาง 2 ซม. และมีความยาว 7 ซม. (รูปที่ 27) แล้วนำไปเหนี่ยวนำผ่านสนามแม่เหล็ก เป็นเวลา 5,10 และ 15 นาที ตามลำดับ จากนั้นนำทรายที่อยู่ในขวด vial เทใส่ลงในบีกเกอร์ที่บรรจุด้วยน้ำ DI แล้วนำไปกระตุ้นด้วยเสียง (Sonicate) เป็นเวลา 1 นาที แล้วตามด้วยการเขย่าเบาๆ ด้วยมือ เพื่อให้เหล็กที่ติดอยู่กับทรายหลุดออกมา

เหล็กที่หลุดออกมาถูกแยกโดยใช้แท่งแม่เหล็กทำการดูดเหล็กติดไว้ในขวดแก้ว ที่ทำการชั่งน้ำหนักไว้แล้ว เพื่อเปรียบเทียบปริมาณเหล็กที่อยู่ในขวด ส่วนทรายนำไปทำการชั่งน้ำหนัก เพื่อนำไปคำนวณหาปริมาณเหล็กที่อยู่ในทรายต่อไป (กรัม$_{เหล็ก}$/กรัม$_{ทราย}$)

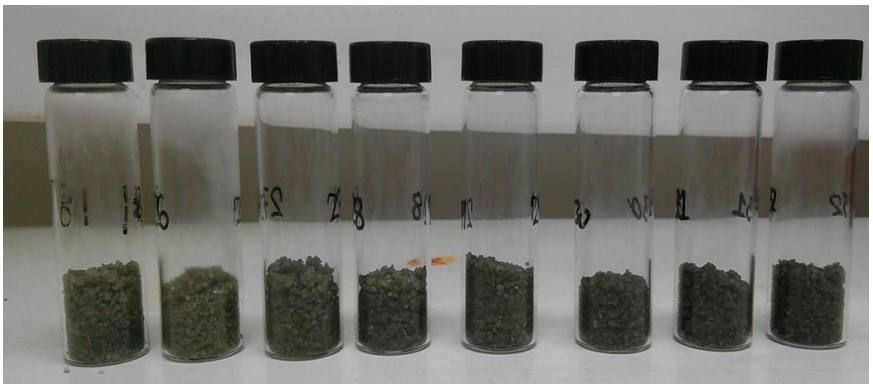

รูปที่ 27 ปริมารการคงค้าง (Sorbed) ของอนุภาค NZVI ในทราย

<u>การทดลองที่ 4 การประเมินความสามารถของอนุภาค NZVI ที่ถูกปรับเสถียรภาพด้วยโฟมในการบำบัดสาร TCE โดยการใช้ความร้อนจากการเหนี่ยวนำทางแม่เหล็กไฟฟ้าในการทดลองแบบ Batch (การทดลองที่ 4)</u>

การทดลองในขั้นตอนนี้ ได้ทำการทดลงเพื่อประเมินความสามารถของอนุภาค NZVI ที่ถูกปรับเสถียรภาพด้วยโฟมในการกำจัดสาร TCE โดยการใช้ความร้อนจากการเหนี่ยวนำทางแม่เหล็กไฟฟ้า โดยใช้การทดลองแบบ Batch

เมื่อทราบถึงปริมาณการสะสมตัวของ NZVI ที่อยู่ในทราย ว่าควรมีปริมาณเท่าใด(กรัม$_{เหล็ก}$/กรัม$_{ทราย}$) เมื่อผ่านการเหนี่ยวนำความร้อนทางแม่เหล็กไฟฟ้า แล้วสามารถทำให้เกิดความร้อนที่อุณหภูมิมากกว่า 80 $^{\circ}$C (จากผลการทดลองที่ 3.2) จึงนำค่าดังกล่าวมาใช้ในการเตรียมการทดลองในการทดลองที่ 4 จากนั้นเติมสาร TCE (Pure phase) ที่มีความเข้มข้นสูงเข้าไปในขวดทดลองจำนวน 2 มิลลิลิตร (ทำการย้อมสี TCE จากลักษณะใส ไม่มีสีให้มีสีแดงด้วย Sudan IV (รูปที่ 29) เพื่อให้ง่ายต่อการสังเกตเห็น ขณะทำการทดลอง) โดยทำการเปลี่ยนฝาขวดทดลองจากฝาพลาสติกสีดำ เป็นฝาสำหรับป้องกันก๊าซเข้าและออกจากขวด (รูปที่ 30) จากนั้นขวดทดลองจะถูกเขย่าด้วยมือเป็นเวลา 2 นาที แล้วตั้งทิ้งไว้อีก 20 นาที ก่อนที่จะนำไปใส่เครื่องกำเนิดสนามแม่เหล็กไฟฟ้ากระแสสลับ เพื่อเหนี่ยวนำให้เกิดความร้อน แล้วทำการเก็บตัวอย่างก๊าซด้วยเข็มเก็บก๊าซ ทุกๆ 5 10 15 30 และ 60 นาที (รูปที่ 31) ตามลำดับ

การวัดปริมาณการสลายตัวของสาร TCE จะนำก๊าซที่เก็บได้จากขวดตัวอย่างไปทำการวิเคราะห์ด้วยเครื่อง Gas Chromatography ที่ต่อพ่วงเข้ากับหัววัดชนิด Electron Capture Detector (GC – ECD) ตัวอย่างก๊าซจำนวน 50 ไมโครลิตร จะถูกฉีดเข้าเครื่อง GC ในโหมด Splitless ที่อุณหภูมิ 280 $^{\circ}$C ผ่านคอลัมน์ ชนิด J&W 121-1324 : 20 เมตร × 180 ไมโครเมตร × 1 ไมโครเมตร ที่มีก๊าซไนโตรเจนเป็นตัวพาที่อัตราการไหลคงที่ (25 มล./นาที) ภายใต้อุณหภูมิเตาอบ (Oven) ที่กำหนดไว้ คือ เริ่มต้นที่อุณหภูมิ 135 $^{\circ}$C จากนั้นเพิ่มขึ้นในอัตรา 43 $^{\circ}$C ต่อนาที จนถึง 220 $^{\circ}$C ทำการวิเคราะห์ข้อมูลโดยใช้โปรแกรมที่ติดตั้งมาพร้อมกับเครื่อง GC โดยพื้นที่ใต้พีคจะแสดงถึงปริมาณสารที่ต้องการตรวจวิเคราะห์

และเพื่อประเมินว่าวิธีการทดลองนี้สามารถกำจัดสารมลพิษออกจากดินได้จริงหรือไม่ จึงได้ทำการทดลองคู่ขนานกัน คือ การทดลองการบำบัดโดยการใช้อนุภาคนา NZVI ที่ถูกปรับเสถียรภาพด้วยโฟม แต่ไม่ใช้การเหนี่ยวนำทางแม่เหล็กไฟฟ้า และการทดลองในทรายเปล่าๆ ที่ถูกทำให้มีค่า %Saturation ใกล้เคียงกับการทดลองที่ 3.2 ประสิทธิภาพของทั้งสามวิธีจะถูกนำมาเปรียบเทียบกัน

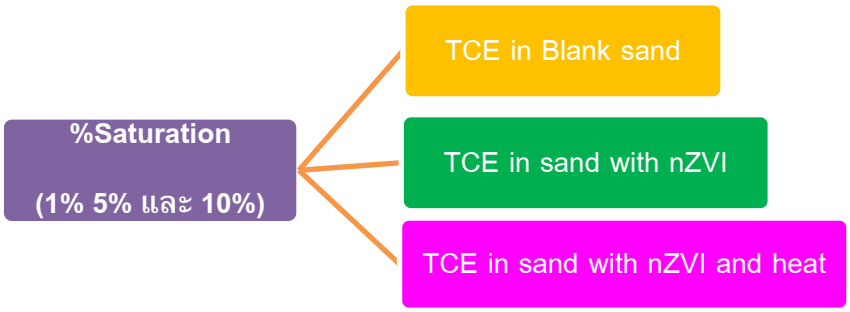

รูปที่ 28 แผนการทดลองเพื่อประเมินความสามารถในการกำจัด TCE ในการทดลองแบบ Batch

ตาราง 1 สภาวะของเครื่อง GC ที่ใช้ในการทดลอง

พารามิเตอร์	สภาวะ
1. คอลัมน์	J&W 121-1324 : 20m × 180 μm × 1 μm
2. อุณหภูมิจุดฉีดสาร	135°C
3. อุณหภูมิคอลัมน์	280 °C
4. อุณหภูมิเครื่องตรวจวัด	เป็นโปรแกรมอุณหภูมิ คือ เริ่มที่ 135°C มีอัตราการเพิ่ม 43 °C/min จนถึง 220 °C
3. อัตราการไหลแก๊สตัวพา	ไนโตรเจน 25 mL/min
4. เครื่องตรวจวัด	Electron Capture Detector (ECD)
5. ปริมาณสาร	50 μL

รูปที่ 29 Sudan IV

รูปที่ 30 ขวดการทดลองสำหรับการประเมินความสามารถของอนุภาค NZVI ที่ถูกปรับเสถียรภาพด้วยโฟมในการกำจัดสาร TCE

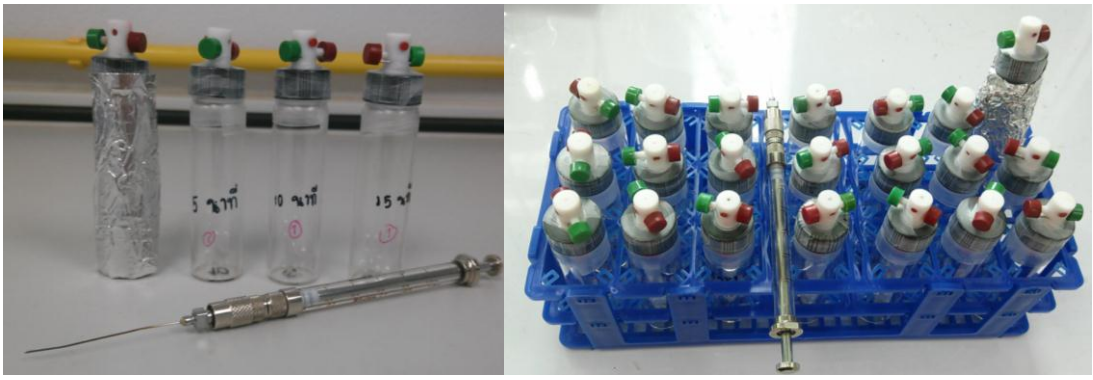

รูปที่ 31 การเก็บตัวอย่างก๊าซด้วยเข็มเก็บก๊าซทุก ๆ 5 10 15 30 และ 60 นาที

5. ผลการศึกษาวิจัย

5.1 การหาชนิดของสารลดแรงตึงผิว (Surfactant) และปริมาณ %ความเข้มข้น ตลอดจนอัตราการไหลของสารลดแรงตึงผิว ที่มีความเหมาะสมต่อการทดลอง

5.1.1 การเปรียบเทียบเสถียรภาพของสารลดแรงตึงผิว

ทำการศึกษาทดลองเพื่อคัดเลือกสารลดแรงตึงผิว ชนิดที่สามารถคงเสถียรภาพได้ดีที่สุดเมื่อถูกทำให้เป็นโฟม โดยใช้ความเข้มข้นตั้งต้นที่เท่ากัน คือ 1% w/w ซึ่งสารลดแรงตึงผิวที่นำมาใช้มีทั้งหมด 5 ชนิด ดังนี้

- Sodium Lauryl Ether Sulfate (*SLES*)
- Sorbitanmonooleate (Span 80)
- Polyoxyethylene SorbitanMonostearate (Tween 60)
- Vertex Type 1 (Foaming Agent for Lightweight Cellular Concrete)
- Vertex Type 2 (Foaming Agent for Lightweight Cellular Concrete)

เมื่อนำสารลดแรงตึงผิว มาทำการเตรียมความเข้มข้นที่เท่ากัน คือ 1% w/w โดยการใช้น้ำในการเจือจางพบว่ามีสารลดแรงตึงผิว เพียง 3 ชนิด ที่สามารถนำมาทำการทดลองได้ คือ SLES, Vertex Type 1 และ Vertex Type 2 ส่วนสารลดแรงตึงผิวอีกสองชนิด คือ Span 80 มีคุณสมบัติละลายน้ำได้เพียงเล็กน้อย หรือเพียงบางส่วนเท่านั้น แต่สามารถละลายได้ในน้ำมันเช่นเดียวกันกับ Tween 60 จึงไม่สามารถนำมาทำการทดลองในลำดับต่อไปได้ แสงดังรูปที่ 32

จากนั้นจึงได้นำสารลดแรงตึงผิวทั้ง 3 ชนิด ทำการสร้างโฟม โดยใช้คอลัมน์ทรงกระบอกขนาดเส้นผ่านศูนย์กลาง 2 ซม. ยาว 20 ซม. บริเวณส่วนปลายปิดด้วยตะแรงเบอร์ 200 ใช้อัตราการไหลของสารลดแรงตึงผิว ผ่านปั๊มสุญญากาศแบบรีดท่อ (Peristaltic Pump) ทั้งหมด 6 อัตราการไหล โดยเริ่มทำการทดลองที่ 0.5 มล./นาที แล้วค่อยๆ เพิ่มอัตราการไหลขึ้นทีละ 0.5 มล./นาที พบว่าที่อัตราการไหลสาร SLES เริ่มต้น คือ 0.5 มล./นาที โฟมมีขนาดใหญ่ที่สุด มีความหนาแน่นน้อยที่สุด จากนั้นเมื่อเพิ่มอัตราการไหลเป็น 1 มล./นาที โฟมเริ่มมีขนาดเล็กลง แล้วเริ่มมีขนาดและความหนาแน่นคงที่ตั้งแต่ 1.5 ไปจนถึง 3.0 มล./นาที โดยใช้อัตราการไหลของแก๊สไนโตรเจนคงที่ เท่ากับ 500 มล./นาที (รูปที่ 33) แต่พบว่าแม้ขนาด และความหนาแน่นของโฟมจะมีลักษณะใกล้เคียงกัน แต่จะสังเกตได้ว่าเริ่มมีน้ำ เกิดขึ้นอยู่บริเวณช่วงท้ายของ Column เนื่องจากอัตราการไหลที่เริ่มมากเกินพอกับความต้องการ

ดังนั้นจึงได้เลือกใช้อัตราการไหลของสารลดแรงตึงผิวเท่ากับ 1.5 มล./นาที เป็นค่าอัตราการไหลที่เหมาะสม อีกทั้งยังได้ลองทำการทดลองเพิ่มโดยการนำอนุภาค NZVI มาผสมกับสารลดแรงตึงผิว ก็ยังมีค่าสอดคล้องกันกับการสร้างโฟมเปล่า โดยไม่ผสมเหล็ก

รูปที่ 32 สารลดแรงตึงผิว 5 ชนิด

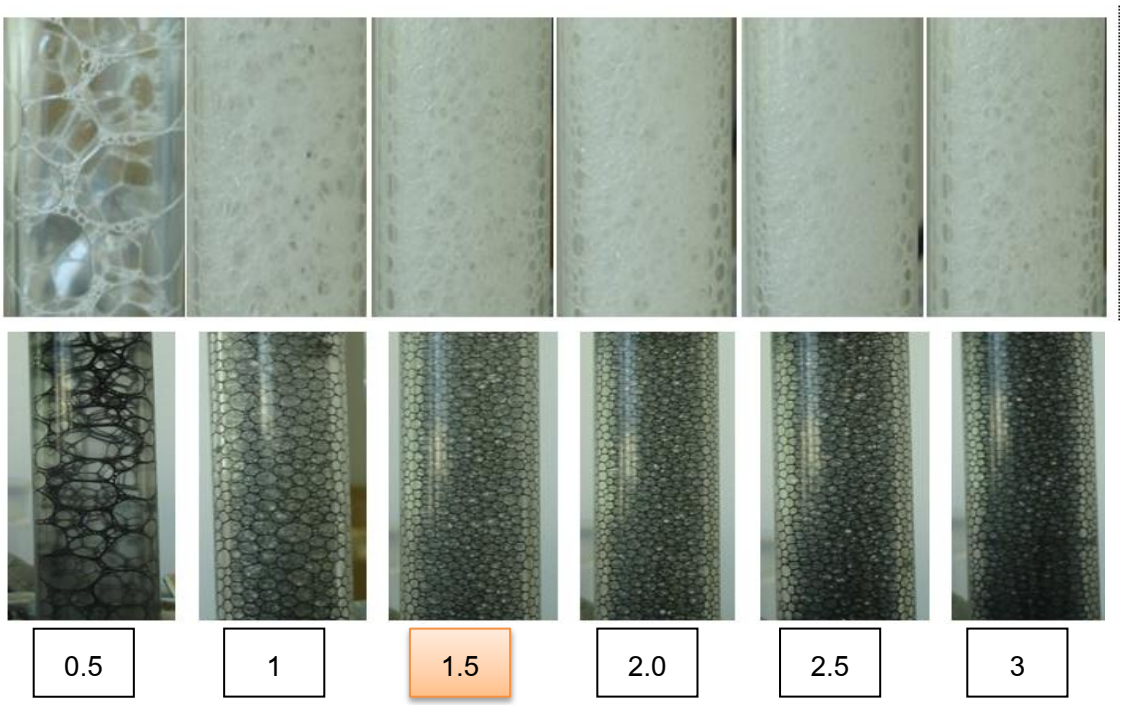

รูปที่ 33 อัตราการไหลของสารลดแรงตึงผิวที่มีความเหมาะสมต่อการทดลอง

ผลการทดลองเพื่อเปรียบเทียบเสถียรภาพของของโฟม ได้ทำการแปลผลแบ่งออกเป็น 3 ส่วน แสดงดังต่อไปนี้

1) วัดจากค่าประสิทธิภาพของโฟม (Foam Quality)

ค่าประสิทธิภาพของโฟม(Foam Quality) คำนวณโดยใช้สมการของ (Mulligan and Eftekhari, 2003)

$$\textbf{Foam Quality (f)} = \frac{\textbf{Gas Volume (Vg)}}{\textbf{Total foam Volume (V l+ Vg)}} \times 100\%$$

โดย F คือ Foam Quality

Vg คือ Volume of gas in foam (มล.)

Vl คือ Volume of liquid in foam (มล.)

ค่าประสิทธิภาพของโฟม(Foam Quality) นับได้ว่าโฟมที่ถูกสร้างขึ้นมีประสิทธิภาพสูงถึง 99% พบว่าสารลดแรงตึงผิวทุกชนิดมีความใกล้เคียงกันมาก มีความต่างกันเพียงระดับตำแหน่งทิศยมเท่านั้น สารลดแรงตึงผิวชนิด SLES มีค่าประสิทธิภาพของโฟมสูงที่สุดเท่ากับ 99.67% สำหรับโฟมที่ไม่ผสมอนุภาค NZVI และ 99.69% สำหรับโฟมที่ผสมอนุภาค NZVI รองลงมาคือVertex Type 2 และ Vertex Type 1 ตามลำดับ

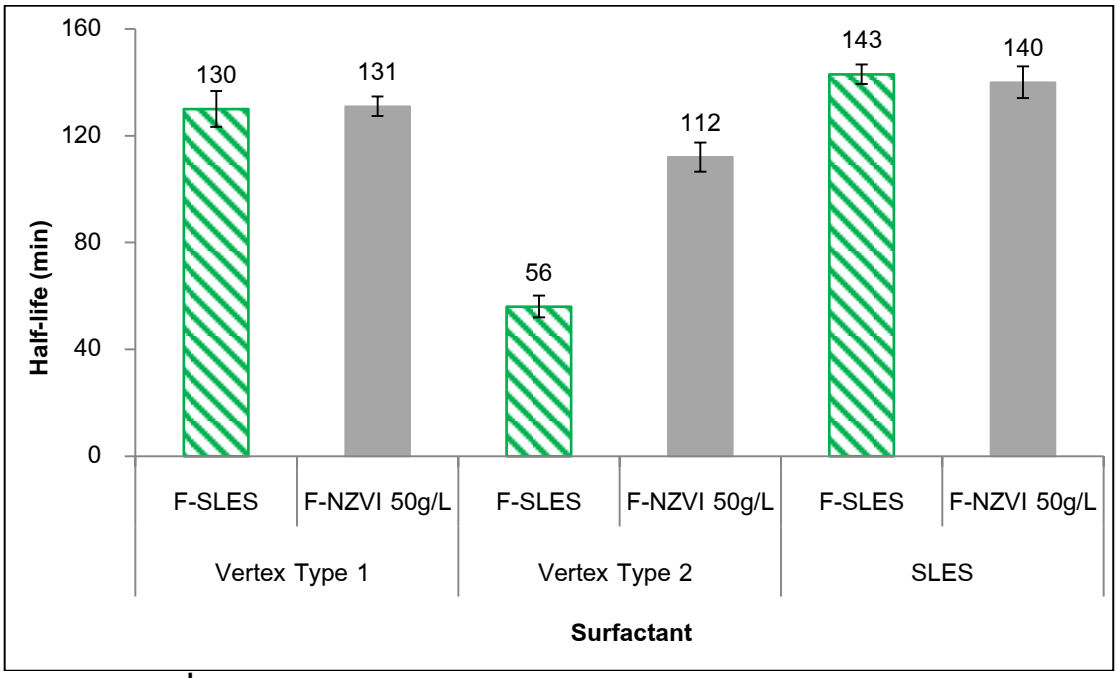

รูปที่ 34 การเปรียบเทียบค่าเสถียรภาพของสารลดแรงตึงผิว 3 ชนิด

2) วัดจากค่าครึ่งชีวิต (half-life) และการสลายตัวเปลี่ยนสถานะ จากโฟมกลายเป็นสถานะของเหลว

ทำการเก็บตัวอย่างโฟมใส่ขวดแก้ว ขนาด 100 มิลลิลิตร จำนวน 2 ขวด/ตัวอย่าง แล้วสังเกตดูลักษณะการเปลี่ยนแปลง การสูญเสียเสถียรภาพของโฟม เริ่มทำการจับเวลาตั้งแต่ที่โฟมเริ่มมีการยุบสลายตัวจากปริมาณเต็มขวด จนเหลือครึ่งขวด (half-life) พร้อมทำการถ่ายภาพ และจดบันทึกระดับน้ำที่เกิดขึ้นจากการเปลี่ยนสถานะของโฟม กลายเป็นของเหลว ทุกๆ 3 นาที จนครบ 60 นาที แสดงในรูปที่ 35

พบว่าสารลดแรงตึงผิว ชนิด SLES มีความสามารถในการคงเสถียรภาพ (Stability) ได้มากที่สุด รองลงมา คือ Vertex Type 1 และ Vertex Type 2 ตามลำดับ(ตาราง 2) และในส่วนของการเปลี่ยนสถานะจากโฟม กลายเป็นของเหลว สามารถสรุปได้ดังต่อไปนี้

- Vertex Type 1 : ในการทำฟองโฟมจะทำให้การสูญเสียเสถียรภาพของฟองโฟมนั้นรวดเร็วที่สุด แต่มีการตกตะกอนของ NZVI เร็วเป็นอันดับที่ 2 เมื่อฟองโฟมสูญเสียเสถียรภาพจนหมดปริมาณของเหลวที่ผสมกับ NZVI จะมีปริมาตรเป็นอันดับที่ 2 จากทั้งสามตัวอย่าง

- Vertex Type 2 : ในการทำฟองโฟมจะทำให้การสูญเสียเสถียรภาพของฟองโฟมลดลงเร็วเป็นอันดับที่ 2 ลองมาจาก S1 แต่มีการตกตะกอนของ NZVI เร็วเป็นอันดับแรก เมื่อฟองโฟมสูญเสียเสถียรภาพจนหมดปริมาณของเหลวที่ผสมกับ NZVI จะมีปริมาตรมากที่สุด จากทั้งสามตัวอย่าง

- SLES : เมื่อผสม NZVI ในการทำฟองโฟมจะทำให้การสูญเสียเสถียรภาพของฟองโฟมลดลงช้าที่สุด และการตกตะกอนของ NZVI ก็เกิดขึ้นช้าที่สุด เมื่อฟองโฟมสูญเสียเสถียรภาพจนหมดปริมาณของเหลวที่ผสมกับ NZVI จะมีปริมาตรน้อยที่สุด จากทั้งสามตัวอย่าง

จากผลการทดลองพบว่าโฟมที่ถูกสร้างจากสารลดแรงตึงผิวทั้ง 3 ชนิด ที่พบปริมาณของของเหลวที่เกิดขึ้นจากการเสียเสถียรภาพของเนื้อโฟมมากที่สุดเรียงลำดับจากมากไปน้อย คือVertex type 2, Vertex type 1 และ SLES ตามลำดับ

ตาราง 2 แสดงค่าเสถียรภาพและประสิทธิภาพของโฟม ที่สร้างขึ้นจากสารลดแรงตึงผิว 3 ชนิด (Vertex Type 1,2 และSLES) ที่ความเข้มข้น 1%

Surfactant (1% w/w)	Foam Stability (นาที)	Foam Quality
Vertex Type 1	130	99.60 %
Vertex Type 2	56	99.65 %
SLES	143	99.67 %
Vertex Type 1 + NZVI (50 กรัม/ลิตร)	131	99.68%
Vertex Type 2 + NZVI (50 กรัม/ลิตร)	112	99.68%
SLES (1%)+ NZVI (50 กรัม/ลิตร)	140	99.69%

รูปที่ 35 การวัดการสลายตัวเปลี่ยนสถานะ จากสถานะโฟมกลายเป็นสถานะของเหลว ที่ระยะเวลา 30 นาที

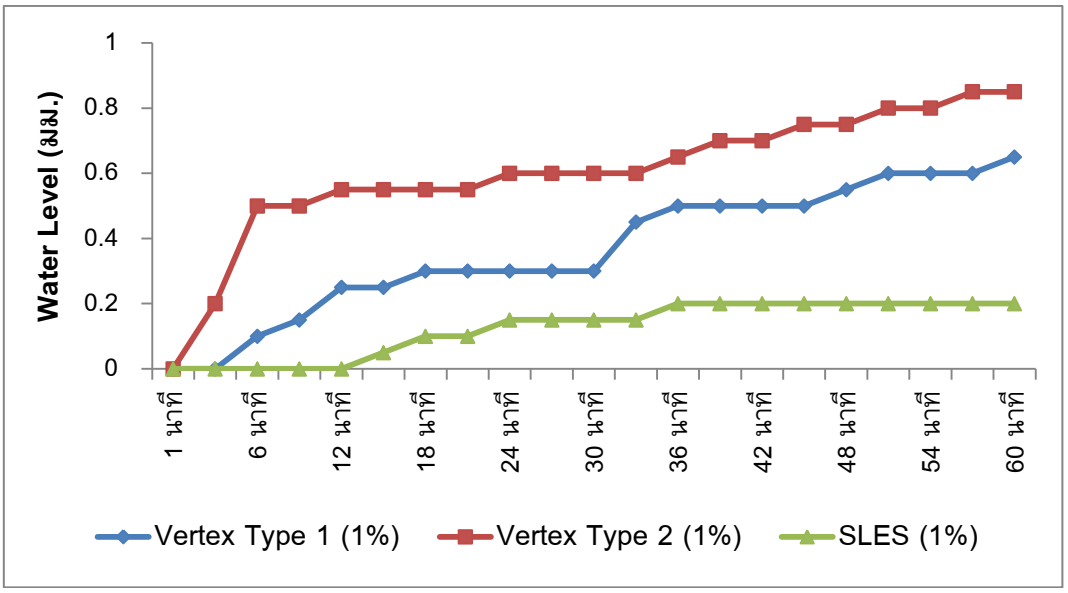

รูปที่ 36 การสลายตัวเปลี่ยนสถานะ จากสถานะโฟมกลายเป็นสถานะของเหลว ของสารลดแรงตึงผิว 3 ชนิด

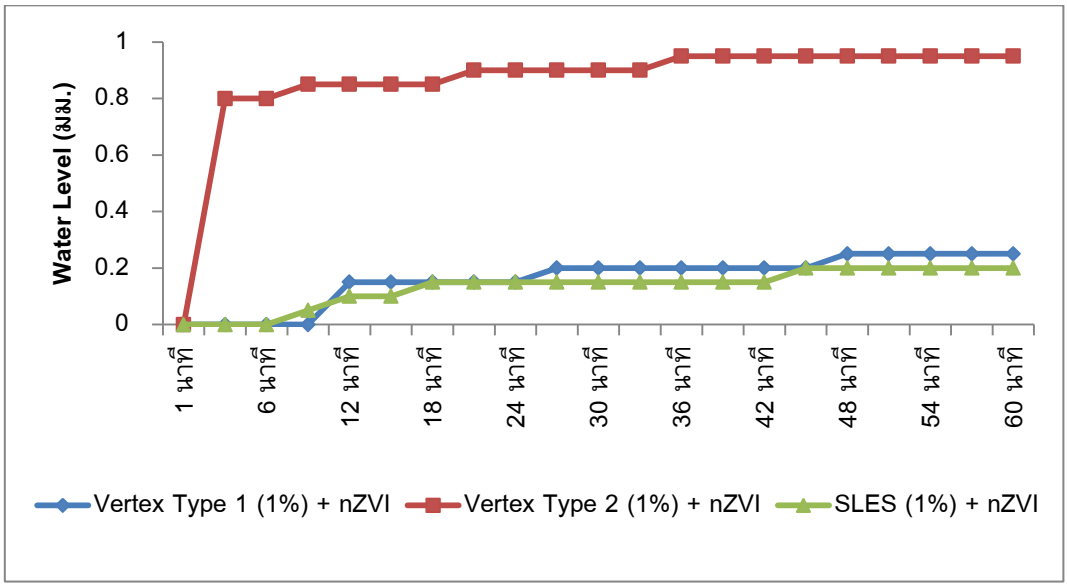

รูปที่ 37 การสลายตัวเปลี่ยนสถานะ จากสถานะโฟมกลายเป็นสถานะของเหลว ของสารลดแรงตึงผิว 3 ชนิด รวมกับ NZVI

5.1.2 การเปรียบเทียบการกระจายตัวของขนาดอนุภาค (Particle Size Distribution)

ขนาดของอนุภาคโฟมที่ถูกสร้างขึ้น สามารถส่งผลโดยตรงต่อช่องว่างระหว่างเม็ดโฟม กล่าวคือหากยิ่งโฟมมีขนาดเล็ก พื้นที่ช่องว่างระหว่างเม็ดโฟมย่อมเพิ่มมากขึ้นตามไปด้วย การหาขนาดของอนุภาคโฟมด้วยกล้องจุลทรรศน์ (microscope) กำลังขยาย 4x/0.01 ที่ต่อเชื่อมกับกล้องดิจิตอลความละเอียด 3.0 MP เพื่อทำการบันทึกภาพ แล้วทำการวัดขนาด และนับจำนวนอนุภาคแยกตามขนาด (รูปที่ 39) ผลการทดลองพบว่าอนุภาคโฟมมีขนาดตั้งแต่ 1.9-30.5 ไมโครเมตร สารลดแรงตึงผิวชนิด Vertex Type 1 มีขนาดอนุภาคโฟมอยู่ในช่วง 11-15 ไมโครเมตร มากที่สุด และสารลดแรงตึงผิว Vertex Type 2 และ SLES มีขนาดอนุภาคโฟมอยู่ในช่วง 6-10 ไมโครเมตร มากที่สุด แม้ว่าสารลดแรงตึงผิวชนิด Vertex Type 2 จะมีประมาณอนุภาคโฟมอยู่ในช่วง 6-10 ไมโครเมตร มากกว่า SLES แต่เมื่อมองในภาพรวม พบว่า SLES มีแนวโน้มการกระจายตัวของอนุภาคในช่วงขนาดที่เล็กกว่า (รูปที่ 38)

5.1.3 ปริมาณ %ความเข้มข้น ที่มีความเสถียรภาพและเหมาะสม

จากผลการทดลองที่ 4.1.1-4.1.2 พบว่าสารลดแรงตึงผิวชนิด SLES มีความสามารถในการคงเสถียรภาพได้นานที่สุด สลายตัวช้าที่สุด จึงได้นำมาทำการทดลองเพิ่มโดยการใช้สัดส่วนโดยน้ำหนักที่แตกต่างกัน (% w/w) เพื่อให้ได้ค่าที่มีความเหมาะสมที่ที่สุด โดยทำการทดลองทั้งหมด 5 การทดลอง ประกอบด้วย 1% 3% 5% 7% และ 9% w/w ตามลำดับ ผลการทดลองพบว่าที่ความเข้มข้น 3% w/w มีค่าเสถียรภาพมากที่สุด เท่ากับ 173 นาที รองลงมา คือ 1% 9% 7% และ 5% w/w ตามลำดับ (รูปที่ 40 และตาราง 4)

ตาราง 3 แสดงค่าร้อยละการกระจายตัวของของอนุภาค(Particle Size Distribution)

Size of particle (ไมโครเมตร)	สารลดแรงตึงผิว (1% w/w)		
	Vertex Type 1	Vertex Type 2	SLES
0-5	15.1%	22.1%	13.5%
6-10	24.4%	41.9%	33.7%
11-15	37.2%	24.4%	25.8%
16-20	9.3%	11.6%	21.3%
21-25	7.0%	7.0%	5.6%
26-30	2.3%	1.2%	0%
31-35	3.5%	0%	0%

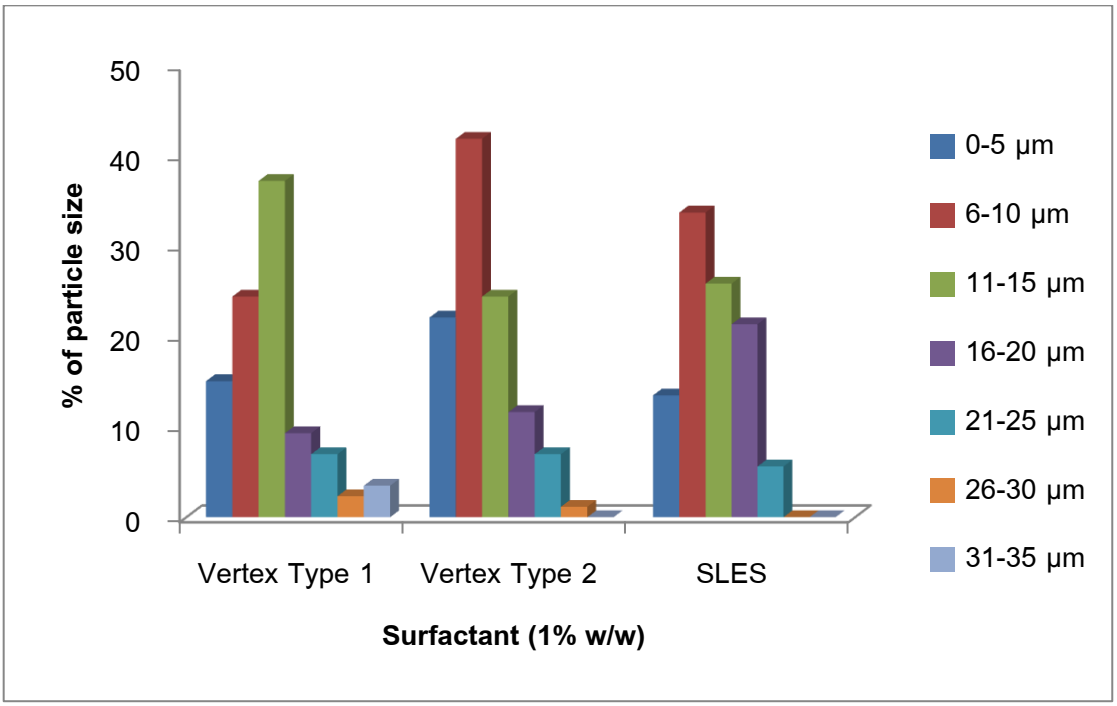

รูปที่ 38 ร้อยละการกระจายตัวของขนาดอนุภาค (Particle Size Distribution)

Vertex Type 1

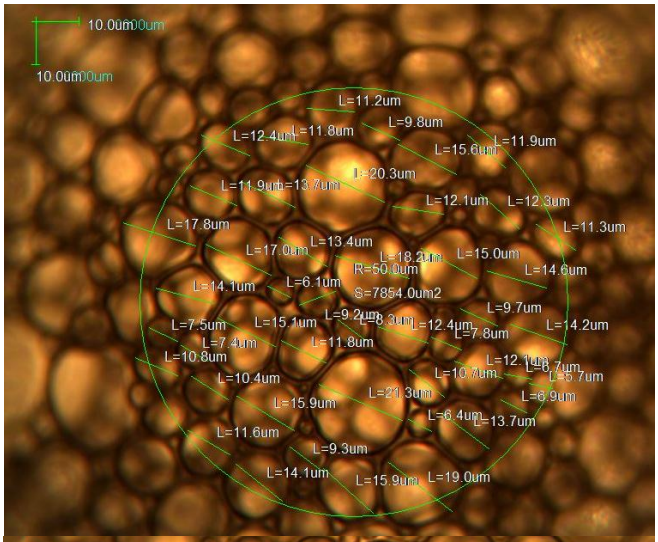

Vertex Type 2

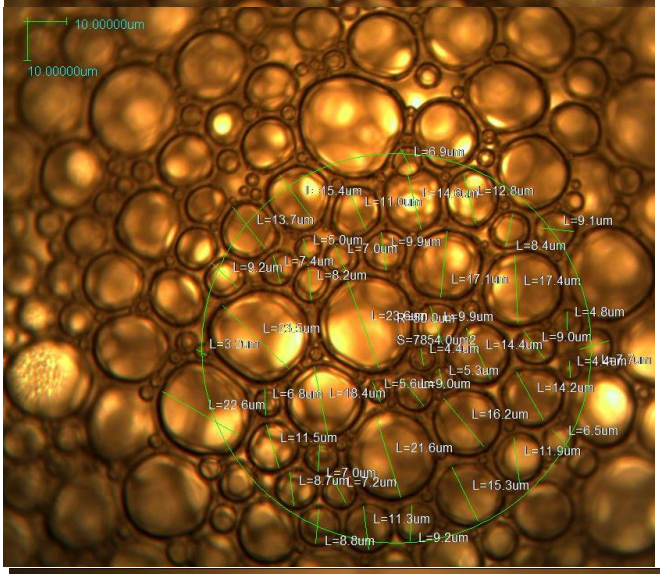

SLES

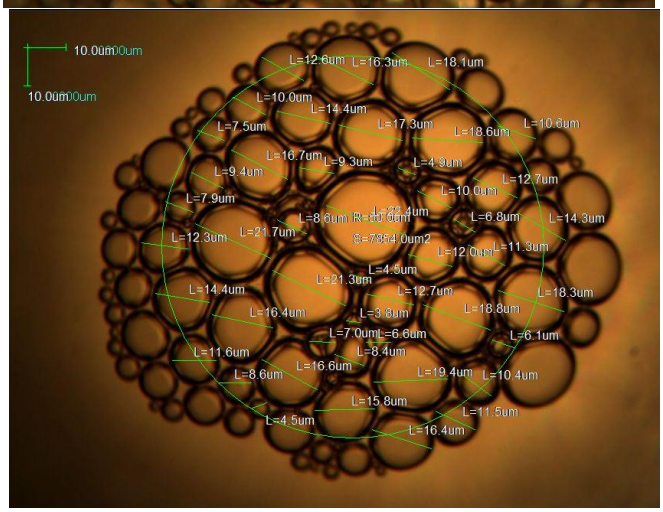

รูปที่ 39 อนุภาคโฟม จากกล้องจุลทรรศน์อิเล็กตรอน (microscope)

ตาราง 4 แสดงค่าเสถียรภาพและประสิทธิภาพของโฟม ที่สร้างขึ้นจากสารลดแรงตึงผิว ชนิด SLES ที่ความเข้มข้น 1% 3% 5% 7% และ 9% w/w

Surfactant	Foam Stability (นาที)	Foam Quality
SLES (1% w/w)	143	99.67 %
SLES (3% w/w)	173	99.61 %
SLES (5% w/w)	101	99.65 %
SLES (7% w/w)	108	99.61 %
SLES (9% w/w)	115	99.64 %

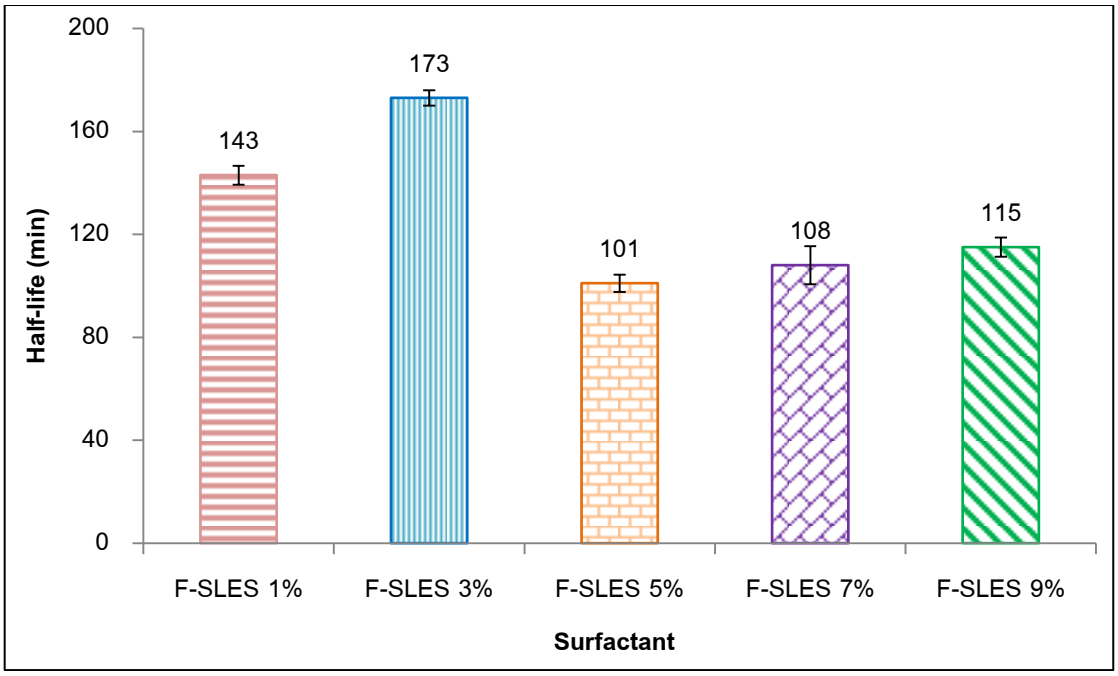

รูปที่ 40 ค่าเสถียรภาพของสารลดแรงตึงผิว ชนิด SLES ที่ความเข้มข้น 1% 3% 5% 7% และ 9% w/w

5.2 การประเมินประสิทธิภาพของการเหนี่ยวนำความร้อนทางแม่เหล็กไฟฟ้าโดยอนุภาคนาโนของเหล็กประจุศูนย์เกิดขึ้นจากเหล็กในตัวกลางโฟม น้ำ และสารลดแรงตึงผิว

ทำการทดลองเปรียบเทียบค่าเฉลี่ยความร้อน (°C) ที่เกิดขึ้นจากเหล็กในตัวกลางโฟมน้ำ และสารลดแรงตึงผิ โดยได้ทำการทดลองให้ความร้อนผ่านสนามแม่เหล็กที่ 5 10 และ 15 นาที ทำการคำนวณเปรียบเทียบโดยเทียบจากอุณหภูมิที่เปลี่ยนแปลงไป (ΔT) ต่อปริมาณเหล็ก (กรัม) ได้ผลการทดลองดังนี้

พบว่าค่าเฉลี่ยความร้อน (°C) ที่เกิดขึ้นจากเหล็กในตัวกลางต่าง เรียงลำดับจากมากไปน้อย คือ โฟมมีค่าสูงที่สุด รองลงมาคือ น้ำ และสารลดแรงตึงผิว โดยมีค่าเท่ากับ 289.22 , 377.67 และ 364.21 °C ส่วนในตัวกลางที่เป็นของเหลว คือ น้ำมีค่าเท่ากับ 78.01, 112.98 และ 147.99 °C และใน SLES มีค่าเท่ากับ 41.31, 66.54 และ 66.54 °C ตามลำดับ (รูปที่ 41) ซึ่งสาเหตุที่ค่าความร้อนในตัวกลาง SLES มีค่าความร้อนต่ำที่สุด เนื่องจาก SLES มีค่าจุดเดือดสูงกว่าน้ำ คือ มีค่าเท่ากับ 657 °C (US EPA, 2006)

สามารถกล่าวโดยสรุปว่า ปริมาณเหล็กที่เท่ากัน 1 กรัม สามารถก่อให้เกิดความร้อนในตัวกลางที่เป็นโฟมสูงกว่าตัวกลางที่เป็นน้ำ 3 เท่า และสารลดแรงตึงผิว 5 เท่า

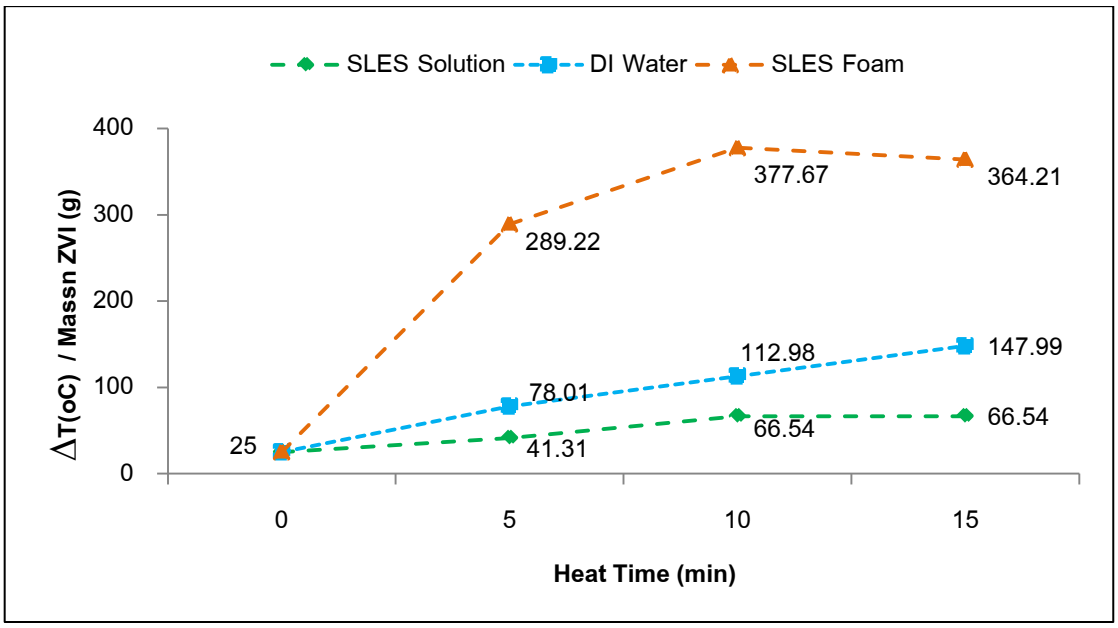

รูปที่ 41 ปริมาณค่าเฉลี่ยความร้อน (°C) ที่เกิดขึ้นจากเหล็กในตัวกลางโฟม น้ำ และสารลดแรงตึงผิว

ตาราง 5 ปริมาณค่าเฉลี่ยความร้อน (°C) ที่เกิดขึ้นจากการเหนี่ยวนำความร้อนทางแม่เหล็กไฟฟ้า ของอนุภาค NZVI ที่อยู่ในตัวกลางน้ำ SLES และโฟม

Heat time (นาที)	**ΔT(°C) / Mass$_{NZVI}$(กรัม)**		
	SLES	Water	Foam
0	25.00	25.00	25.00
5	41.31	78.01	289.2
10	66.54	112.98	377.7
15	66.54	147.99	364.2
30	105.6	209.83	272.7
Mass$_{NZVI}$ (กรัม)	**0.242**	**0.2065**	**0.041**

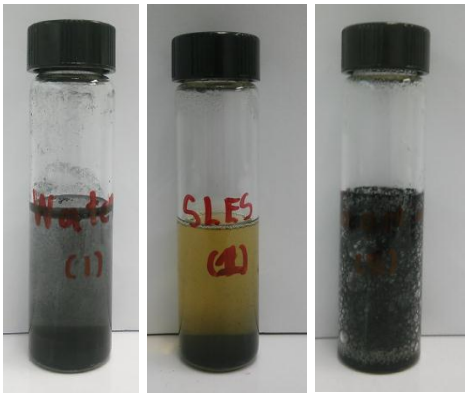

รูปที่ 42 อนุภาค NZVI ที่อยู่ในตัวกลางน้ำ SLES และโฟม หลังจากผ่านการเหนี่ยวนำความร้อนทางแม่เหล็กไฟฟ้า เป็นเวลา 15 นาที

5.3 การประเมินความสามารถของโฟม ที่มีต่อการนำพาการเคลื่อนที่ของอนุภาค NZVI

การศึกษาความสามารถของโฟม ต่อความสามารถในการที่จะนำพาอนุภาค NZVI ให้เคลื่อนที่ไปยังพื้นที่เป้าหมาย โดยได้ทำการเป่าสร้างโฟมที่ผสมด้วยอนุภาค NZVI โดยใช้อัตราการไหลของสารลดแรงตึงผิวและความเข้มเข้มข้นของอนุภาค NZVI เท่ากันในทุกการทดลอง เท่ากับ 1.5 มล./นาที และ 50 กรัม/ลิตร ตามลำดับ แต่เปลี่ยนอัตราการไหลของแก๊สไนโตรเจนให้มีค่าที่แตกต่างกันไป คือ 125, 300 และ 500 มล./นาที ตามลำดับ เพื่อเปรียบเทียบว่าอัตราการไหลของแก๊สที่ปริมาณเท่าใด มีความสามารถในการที่จะนำพาอนุภาค NZVI ให้เคลื่อนที่ไปยังพื้นที่เป้าหมายได้ดีที่สุด

<u>5.3.1 ค่าความสามารถของโฟม ต่อความสามารถในการการเคลื่อนที่ของอนุภาค NZVI</u>

ผลการทดลองพบว่าที่อัตราการไหลของแก๊สไนโตรเจนเท่ากับ 500 มล./นาที มีค่าความ สามารถในการนำพาอนุภาค NZVI เคลื่อนที่ได้มากที่สุด เท่ากับ 66.98 % (รูปที่ 43) โดยมีค่าเปอร์เซ็นความแตกต่างของความเข้มข้นของอนุภาค NZVI ในสารละลายตั้งต้น (Stock solution) น้อยที่สุด คือ 16.51 กรัม/ลิตร (รูปที่ 44) รองลงมาคือ 300 และ 125 มล./นาที โดยมีค่าเท่ากับ 42.15 % และ 27.32 % ตามลำดับ

ผลการทดลองยังแสดงให้เห็นว่า เมื่อใช้อัตราการไหลของแก๊สไนโตรเจนเท่ากับ 500 มล./นาที มีการสะสมตัวของอนุภาค NZVI ในทรายมากที่สุด คือ 1.3315 มก.$_{เหล็ก}$/กรัม$_{ทราย}$ รองลงมา คือ 300 มล./นาที และ 125 มล./นาที ตามลำดับ (รูปที่ 45 และตาราง 6) และจากการสังเกตจากการทดลอง พบว่าที่อัตราการไหลแก๊สไนโตรเจน 125มล./นาที เมื่อนำมาต่อเข้ากับ Pack Column แล้วพบว่ามีปริมาณของเหลวกองอยู่บริเวณช่วงท้ายของ Column จำนวนมาก โดยเริ่มมีน้ำเกิดขึ้นเมื่อเวลาผ่านไปเพียง 5 นาที นับจากเริ่มต้นการทดลอง (รูปที่ 46 และตาราง 6) จึงอาจเป็นสาเหตุของการที่อนุภาค NZVI ส่วนใหญ่จะตกตะกอนอยู่บริเวณส่วนท้ายของ Gereration Column ส่วนที่อัตราการไหลแก๊สไนโตรเจน 500 มล./นาที มีน้ำเกิดขึ้นที่ Gereration Column น้อยที่สุด โฟม และอนุภาค NZVI สามารถเคลื่อนที่ได้ดีกว่า จึงทำให้สามารถพาอนุภาค NZVI เคลื่อนที่ได้ดีกว่า จึงเป็นเหตุให้เกิดการสะสมอยู่ที่ Pack Column ได้มากกว่า

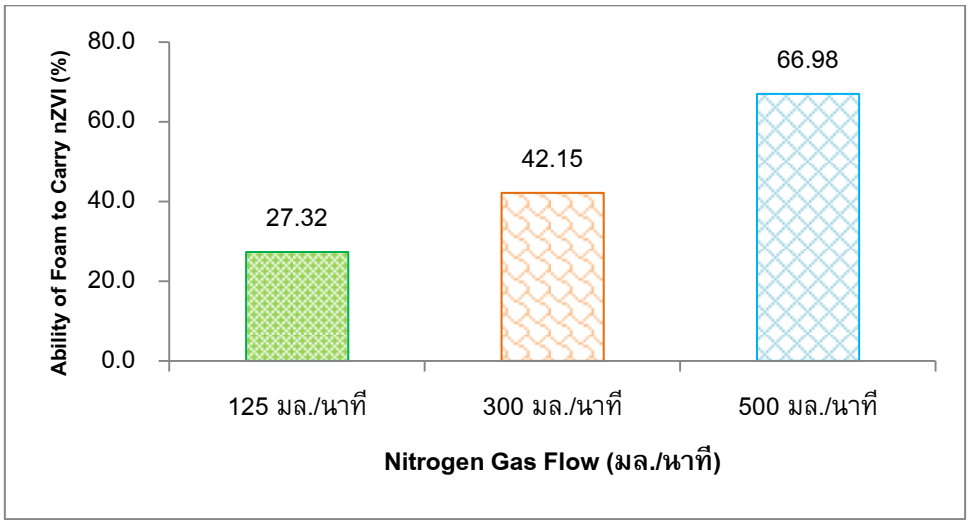

รูปที่ 43 Ability of Foam to Carry NZVI (%)

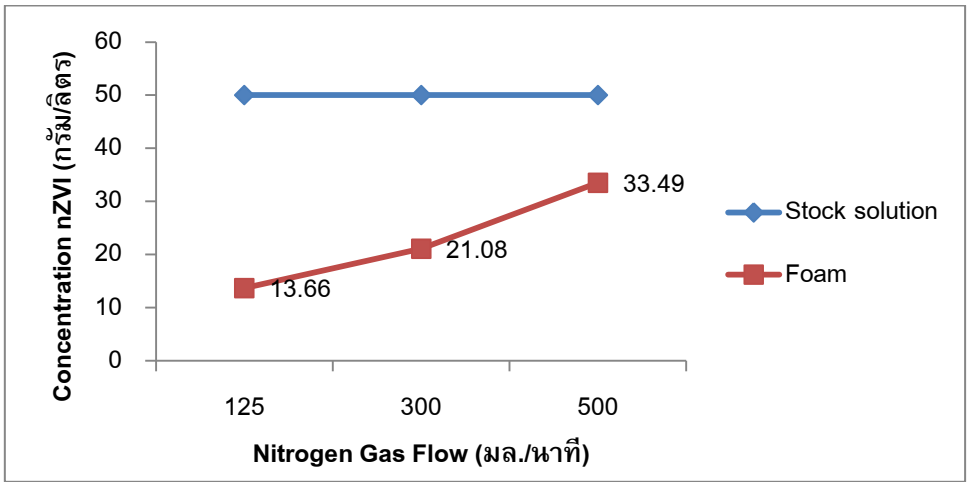

รูปที่ 44 Ability of Foam to Carry NZVI (กรัม/ลิตร)

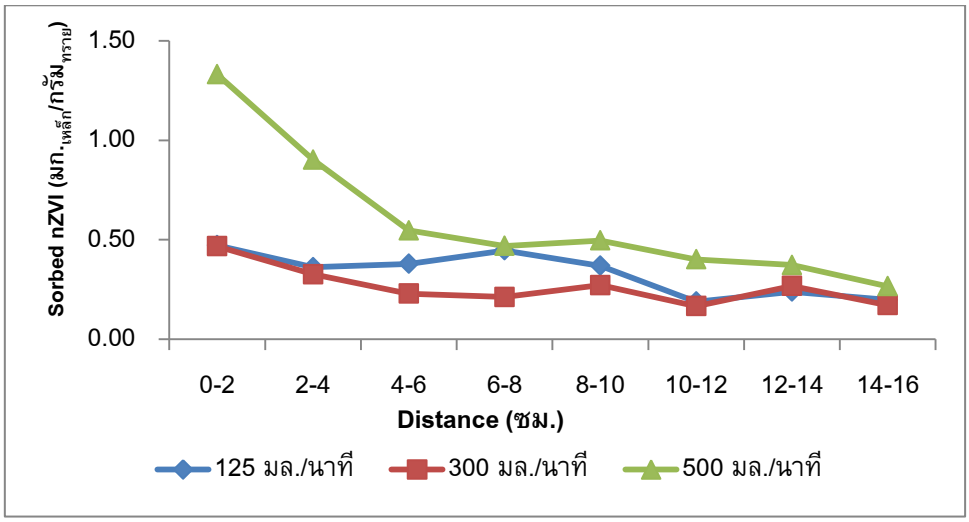

รูปที่ 45 แสดงปริมารการคงค้าง (Sorbed) ของอนุภาค NZVI ในทราย

ตาราง 6 แสดงปริมารการคงค้าง (Sorbed) ของอนุภาค NZVI ในทราย

Distance (ซม.)	NZVI in Sand (มก.$_{เหล็ก}$/กรัม$_{ทราย}$)		
	125 มล./นาที	300 มล./นาที	500 มล./นาที
0-2	0.472	0.467	**1.3315**
2-4	0.362	0.327	0.9027
4-6	0.379	0.229	0.5470
6-8	0.447	0.212	0.4693
8-10	0.369	0.272	0.4962
10-12	0.189	0.166	0.4010
12-14	0.239	0.268	0.3734
14-16	0.198	0.171	0.2660

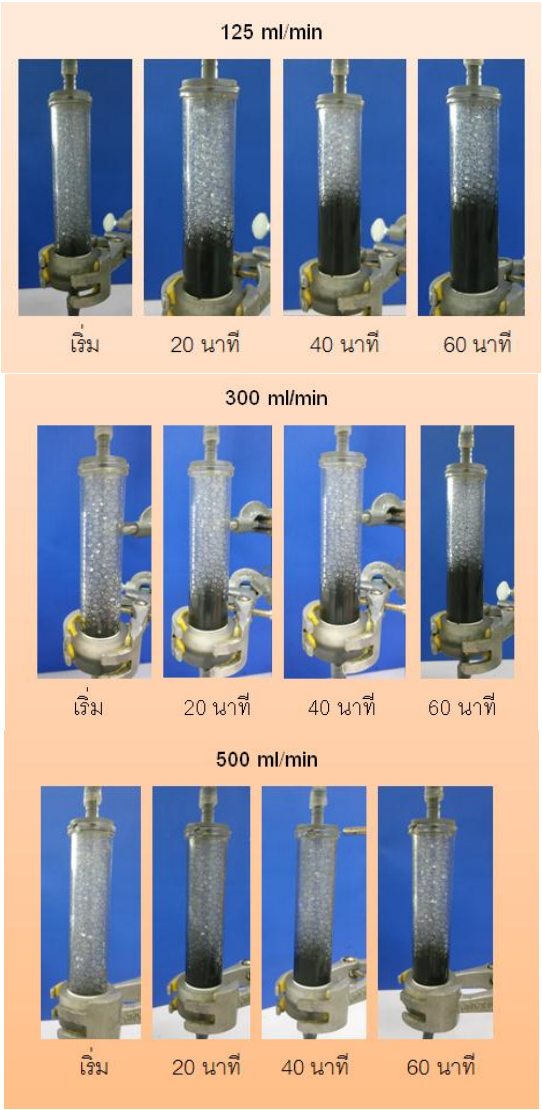

รูปที่ 46 การเป่าสร้างโฟมที่อัตราการไหลแก๊สออกซิเจน 125 300 และ 500 มล./นาที

5.3.2 ปริมารการคงค้าง (Sorbed) ของอนุภาค NZVI ในทรายที่สามารถเหนี่ยวนำให้เกิดความร้อน ที่อุณหภูมิมากกว่า 70 °C

สืบเนื่องจากผลการทดลองที่ 5.3.1 ที่พบว่าการใช้อัตราการไหลของแก๊สไนโตรเจน เท่ากับ 500 มล./นาที เป็นอัตราการไหลที่ดีที่สุด โดยมีวัตถุประสงค์หลักเพื่อศึกษาถึงปริมาณการสะสมตัวของอนุภาค NZVI เมื่ออยู่ในทราย แล้วสามารถเหนี่ยวนำให้เกิดความร้อนได้ที่อุณหภูมิมากกว่า 80 °C โดยทำการใช้อนุภาค NZVI ที่ความเข้มข้นเริ่มต้นที่ 60 กรัม/ลิตร แล้วเพิ่มขึ้นทีละ 20 กรัม/ลิตร จนพบว่าที่อัตราความเข้มข้นของอนุภาค NZVI ที่ 100 กรัม/ลิตร สามารถเหนี่ยวนำให้เกิดความร้อนจึงถึงอุณหภูมิที่มากกว่า 80 °C และพบว่าปริมาณการสะสมตัวของอนุภาค NZVI ที่ถูกส่งผ่านเข้าไปใน Pack Column นั้นจะเกิดการสะสมตัวสูงที่สุดที่บริเวณช่วงต้นของ Pack Column คือ ช่วง 0-2 ซม. และลดระดับความเข้มข้นลงจนเหลือน้อยที่สุดบริเวณส่วนปลายที่ทางออกของ Pack Column (รูปที่ 47) เมื่อนำไปเข้าสนามแม่เหล็ก ก็พบว่ามีเพียงบริเวณช่วง 0-2 ซม. เท่านั้นที่สามารถให้ความร้อนได้สูงกว่า 80 °C (รูปที่ 48) คือ สามารถให้ความร้อนได้มากถึง 82.22 °C (5 นาที) , 97.22 °C (10 นาที) และ 100.00 °C (15 นาที) มีปริมาณการสะสมตัวของเหล็กเท่ากับ 0.0422 **(กรัม$_{เหล็ก}$/กรัม$_{ทราย}$)** (ตาราง 7) และในช่วงถัดไปจนถึงปลายคอลัมน์ ไม่สามารถให้ความร้อนได้จนถึงระดับที่ต้องการ ส่วนที่ความเข้มข้น 60 และ 80 กรัม/ลิตร มีค่าปริมาณความร้อนที่เกิดขึ้นมากที่สุดเพียง 33.89 และ 36.11 °C ตามลำดับ

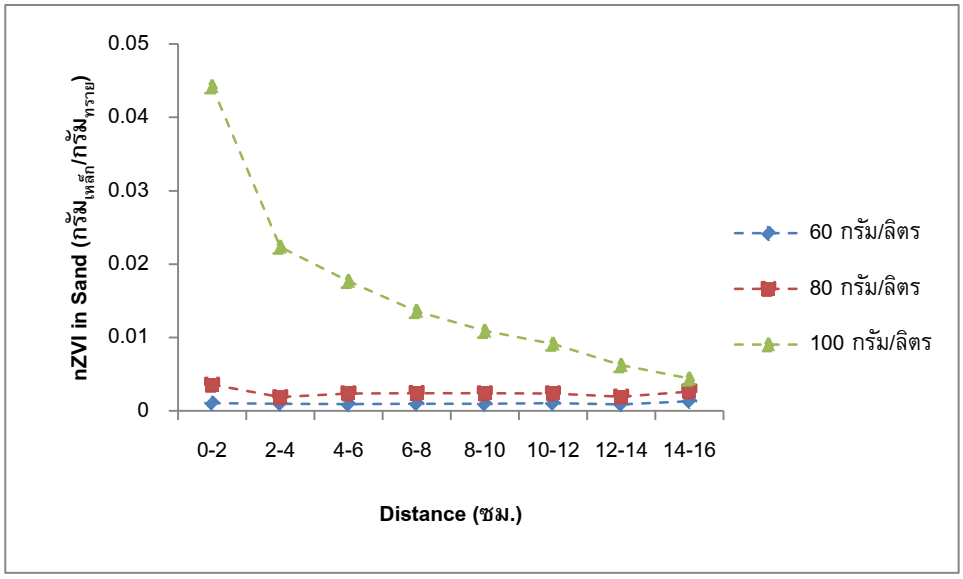

รูปที่ 47 แสดงการสะสมตัวของเหล็กในทราย

ตาราง 7 แสดงปริมาณความร้อนที่เกิดขึ้นของเหล็กที่ความเข้มข้น 60 80 และ 100 กรัม/ลิตร

Distance (ซม.)	Heat Time (นาที)	Temperature (°C)		
		60 กรัม/ลิตร	80 กรัม/ลิตร	100 กรัม/ลิตร
0-2	5	30.00	29.44	**82.22**
	10	32.22	33.88	**97.22**
	15	33.89	36.11	**100.00**
NZVI in Sand (กรัม$_{เหล็ก}$/กรัม$_{ทราย}$)		0.0011	0.0036	**0.0442**
2-4	5	30.00	30.00	53.89
	10	32.22	30.56	58.33
	15	33.33	32.22	64.44
NZVI in Sand (กรัม$_{เหล็ก}$/กรัม$_{ทราย}$)		0.0010	0.0019	0.0224
4-6	5	30.00	31.12	46.66
	10	32.22	33.89	54.44
	15	33.34	35.56	59.44
NZVI in Sand (กรัม$_{เหล็ก}$/กรัม$_{ทราย}$)		0.0009	0.0024	0.0177
6-8	5	30.56	34.45	41.11
	10	32.22	35.56	48.34
	15	33.34	36.11	50.56
NZVI in Sand (กรัม$_{เหล็ก}$/กรัม$_{ทราย}$)		0.0010	0.0024	0.0136
8-10	5	30.00	32.22	40.00
	10	32.22	34.45	45.00
	15	33.33	35.56	47.78
NZVI in Sand (กรัม$_{เหล็ก}$/กรัม$_{ทราย}$)		0.0010	0.0024	0.0109
10-12	5	30.56	31.11	38.89
	10	32.78	33.33	43.33
	15	33.34	33.89	45.56
NZVI in Sand (กรัม$_{เหล็ก}$/กรัม$_{ทราย}$)		0.0011	0.0024	0.0091
12-14	5	30.00	31.11	35.00
	10	30.01	32.22	40.00
	15	33.34	33.33	41.11
NZVI in Sand (กรัม$_{เหล็ก}$/กรัม$_{ทราย}$)		0.0009	0.0019	0.0062
14-16	5	30.00	31.11	32.22
	10	30.00	33.33	35.00
	15	33.33	35.00	36.66
NZVI in Sand (กรัม$_{เหล็ก}$/กรัม$_{ทราย}$)		0.0013	0.0026	0.0044

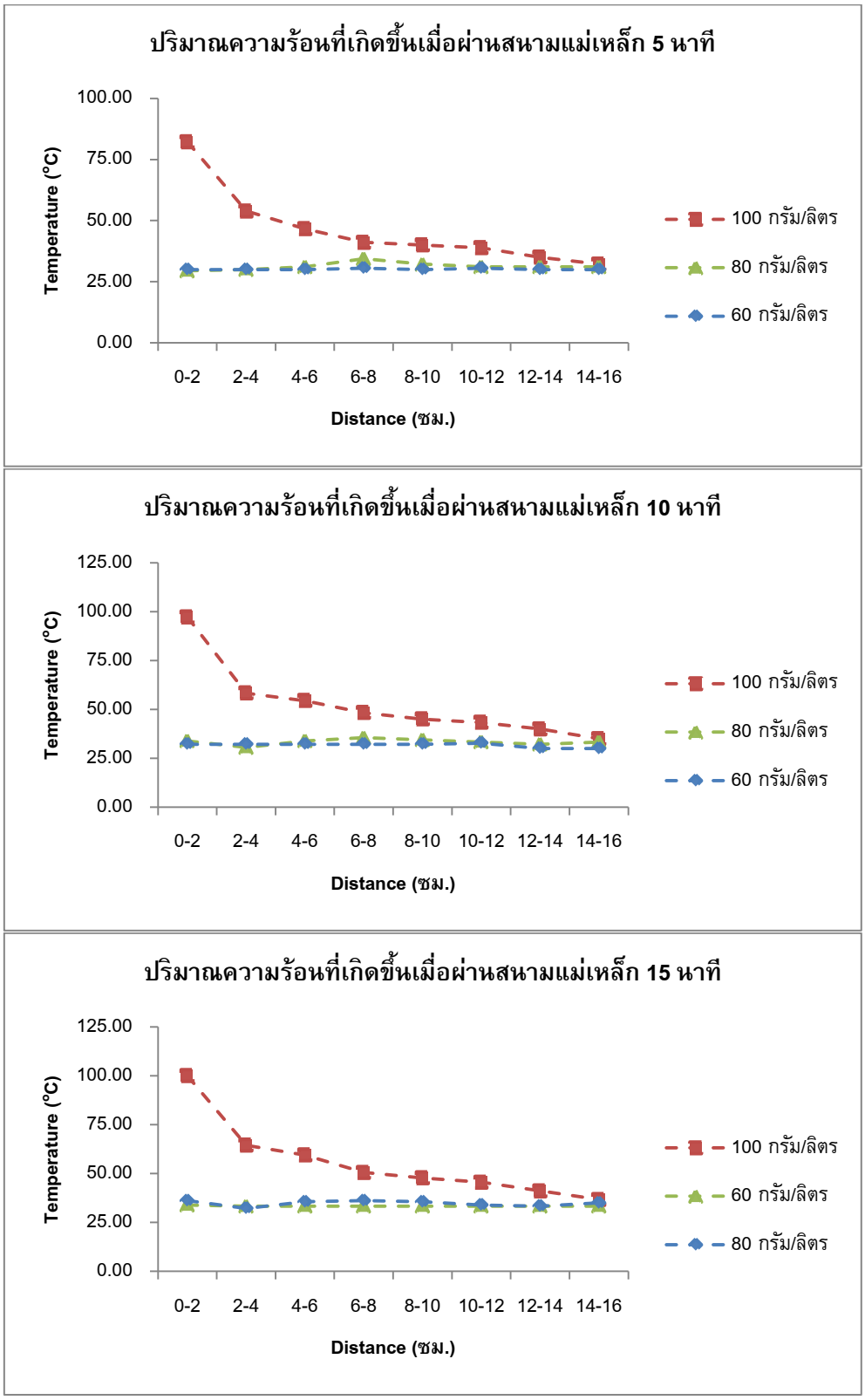

รูปที่ 48 ปริมาณความร้อนที่เกิดขึ้นจากเหล็ก ที่ผ่านการเหนี่ยวนำโดยใช้สนามแม่เหล็ก

ตาราง 8 ค่าพารามิเตอร์ที่ใช้ในการทดลองการสะสมตัวของเหล็กในทราย

พารามิเตอร์	1	2	3	หมายเหตุ
Stock Solution (กรัม/ลิตร)	60	80	100	
Flow N_2 (มล./นาที)	500			
Flow SLES (มล./นาที)	1.5			
น้ำหนัก Pack Column เปล่า (กรัม)	88.81			
Sand Size (มม.)	0.85			
น้ำหนัก Column + ทรายแห้ง	161.07	161.16	161.44	A
น้ำหนัก Column + โฟม	161.62	161.81	162.13	B
ปริมาตรน้ำ 1 pore volume (มล.)	21	19	19.5	C
ปริมาตร pack column เปล่า (มล.)	49.298			D
%saturation	0.34	0.40	0.43	
Porosity	0.42	0.39	0.40	

หมายเหตุ : %saturation = ((B – A) / A) × 100

Porosity = C / D

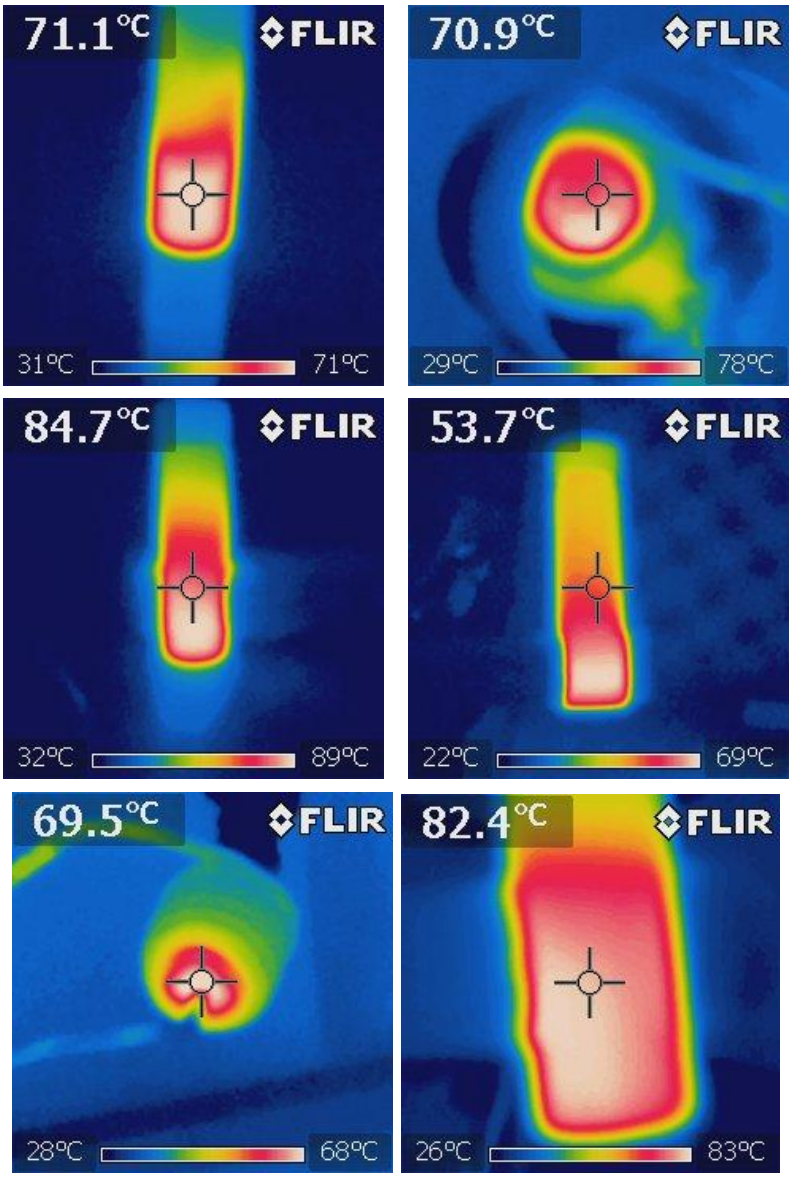

รูปที่ 49 แสดงตัวอย่างภาพ ที่ถ่ายได้จากกล้องถ่ายภาพความร้อน

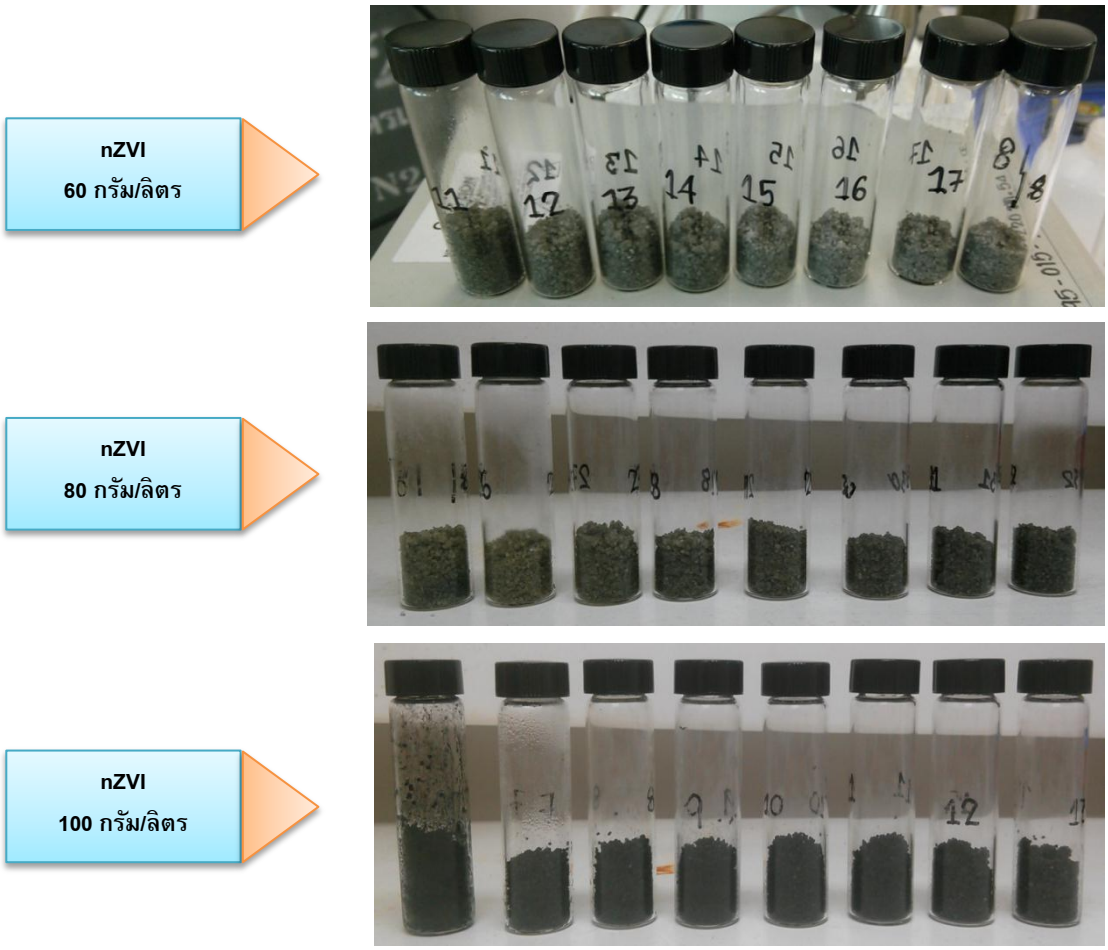

รูปที่ 50 ทรายที่ถูกแกะออกจาก Pack Column ภายหลังจากฝลัดโฟม 60 pore volume (0-2, 2-4, 4-6, 6-8, 8-10, 10-12, 12-14, 14-16 และ 16-18 ซม. (เรียงลำดับจากซ้ายไปขวา))

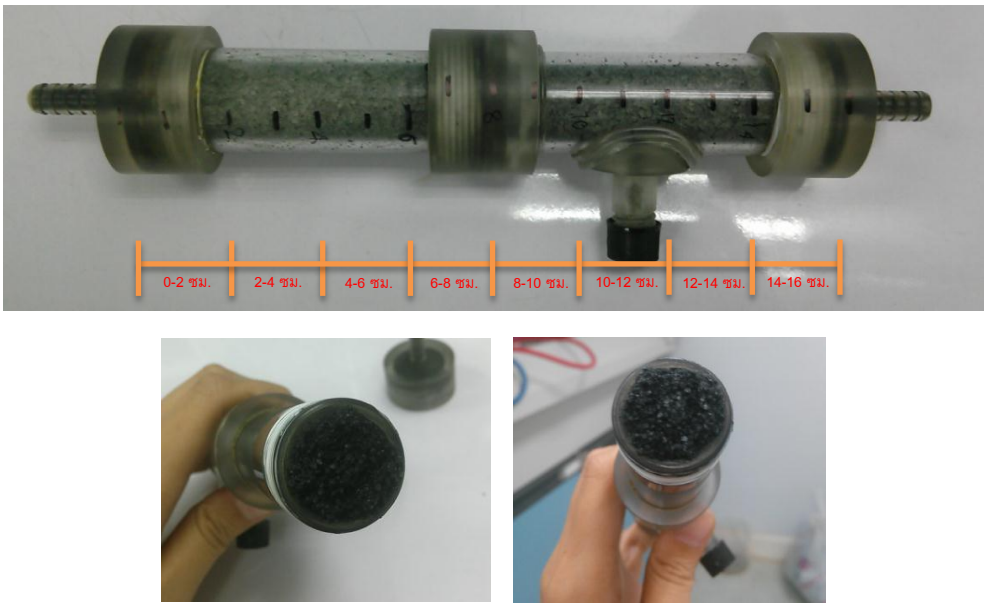

รูปที่ 51 Pack Column ภายหลังจากฝลัดโฟม 60 pore volume

5.4 การประเมินความสามารถของอนุภาค NZVI ที่ถูกปรับเสถียรภาพด้วยโฟม ในการบำบัดสาร TCE ด้วยการเหนี่ยวนำความร้อนทางแม่เหล็กไฟฟ้า ในการทดลองแบบ Batch

จากผลการทดลองที่ 5.3.2 และตารางที่ 8 ทำให้ทราบว่า %Saturation ที่ได้จากการฝลัดอนุภาค NZVI ที่ถูกปรับเสถียรภาพด้วยโฟม จำนวน 60 pore volume ซึ่งมีค่าเท่ากับ 0.43 (เป็น Condition ที่สามารถทำให้เหนี่ยวนำแล้วเกิดความร้อนมากกว่า 80 $^{\circ}$C) ผู้ศึกษาวิจัยได้มุ่งเน้นเล็งเห็นถึงความสำคัญของ %Saturation ที่มีต่อประสิทธิภาพในการบำบัดสาร TCE (เนื่องจากลักษณะ %Saturation ของดินในพื้นที่จริงมีความแตกต่างกัน) จึงได้ทำการทดลองโดยใช้ %Saturation เท่ากับ 1% 5% และ 10% ตามลำดับ (ปรับ %Saturation ในทราย โดยใช้สารลดแรงตึงผิว) โดยอาศัยการทดลองแบบ Batch เพื่อให้ง่ายต่อการควบคุม และแม่นยำขณะเก็บตัวอย่างก๊าซ TCE

โดยตัวอย่างที่มีจลศาสตร์ของการสลายตัวของสาร TCE เร็วกว่า แปลว่าลักษณะทางกายภาพนั้นเอื้อต่อการใช้อนุภาคนาโนของเหล็กประจุศูนย์ร่วมกับการเหนี่ยวนำความร้อนทางแม่เหล็กไฟฟ้าในการฟื้นฟูการปนเปื้อน ความสามารถในการกำจัดสาร TCE จะถูกแทนด้วยปริมาณการละลายหรือระเหยกลายเป็นไอของสาร TCE ในรูปของการได้รับความร้อน และการไม่ได้รับความร้อน

รูปที่ 52 ทราย ก่อนทำการทดลอง (%Saturation เท่ากับ 1% 5% และ 10%)

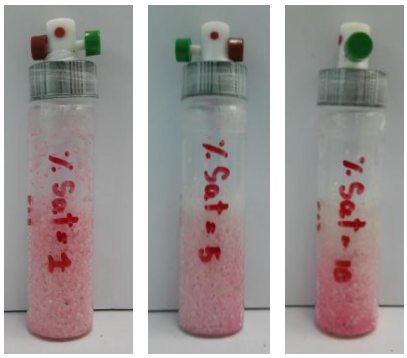

รูปที่ 53 สาร TCE ในทราย ที่มี %Saturation เท่ากับ 1% 5% และ 10%

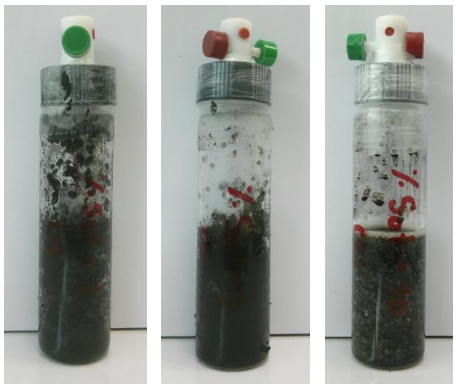

รูปที่ 54 สาร TCE ในทรายที่ผสม NZVI ที่มี %Saturation เท่ากับ 1% 5% และ 10% หลังจากผ่านการเหนี่ยวนำความร้อนทางแม่เหล็กไฟฟ้า เป็นเวลา 60 นาที

5.4.1 ปริมาณค่าเฉลี่ยความร้อน (°C) ที่เกิดขึ้นจากการเหนี่ยวนำความร้อนทางแม่เหล็กไฟฟ้าเหล็กของอนุภาค NZVI ที่อยู่ในตัวกลางกลางทราย ที่มี %Saturation แตกต่างกัน

ผลจากการทำการทดลอง โดยการนำอนุภาค NZVI ผสมลงไปในทรายที่มี %Saturation เท่ากับ 1% 5% และ 10% ตามลำดับ พบว่าทุก %Saturation สามารถเหนี่ยวนำให้เกิดความร้อนได้เกิน 80 °C โดยใช้เวลาเพียง 5 นาที ซึ่งในช่วงแรกของการทดลอง คือ 10 นาทีแรก มีอุณหภูมิใกล้เคียงกัน คือ อยู่ในช่วง 90.0-94.44 °C (มากที่สุดที่ %Saturation เท่ากับ 10) และเมื่อทำการให้ความร้อนนานขึ้น ค่าความร้อนจะเพิ่มขึ้นเรื่อยๆ ตามเวลาที่ให้ความร้อน ที่เวลา 30 นาที เป็นเวลาที่ทุก %Saturation สามารถเกิดความร้อนได้สูงที่สุด คือ 92.22(1%), 117.22(5%) และ 111.67(10%) °C ตามลำดับ แต่เมื่อใช้เวลาในการให้ความร้อนไปเรื่อย จนถึง 60 นาที กลับพบว่าค่าความร้อนไม่เพิ่มขึ้น แต่กลับลดลงเล็กน้อย

สามารถสรุปผลการทดลองได้ว่า ที่เวลาในการให้ความร้อน 5 นาที เป็นเวลาที่เพียงพอต่อค่าความร้อนที่ต้องการ คือ มากกว่า 80 °C เป็นการประหยัดพลังงานไฟฟ้าที่ใช้ในการเหนี่ยวนำ ตลอดจนเป็นการประหยัดเวลาอีกด้วย และค่า %Saturation ในทราย ไม่ส่งผลกระทบต่อการเหนี่ยวนำให้เกิดความร้อนอย่างมีนัยสำคัญ

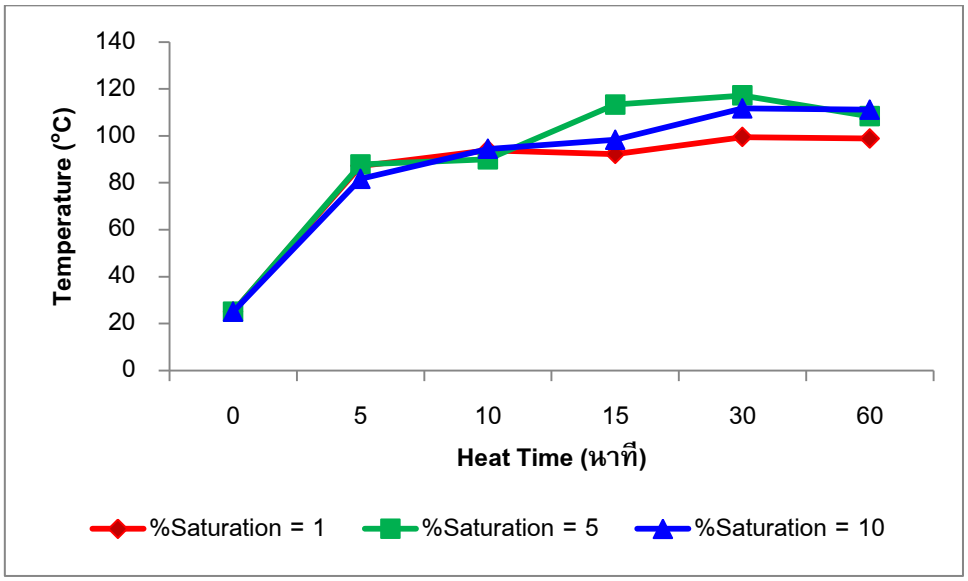

รูปที่ 55 ปริมาณค่าเฉลี่ยความร้อน (˚C) ที่เกิดขึ้นจากการเหนี่ยวนำความร้อนทางแม่เหล็กไฟฟ้าเหล็กของอนุภาค NZVI ที่อยู่ในตัวกลางกลางทราย ที่มี %Saturation เท่ากับ 1% 5% และ 10%

ตาราง 9 ปริมาณค่าเฉลี่ยความร้อน (˚C) ที่เกิดขึ้นจากการเหนี่ยวนำความร้อนทางแม่เหล็กไฟฟ้าเหล็กของอนุภาค NZVI ที่อยู่ในตัวกลางกลางทราย ที่มี %Saturation แตกต่างกัน

Heat time (นาที)	**Temperature (˚C)**		
	%Saturation = 1	%Saturation = 5	%Saturation = 10
0	25	25	25
5	87.22	87.78	81.67
10	93.89	90.00	94.44
15	92.22	113.33	98.33
30	99.44	117.22	111.67
60	98.89	108.33	111.11
$Mass_{NZVI}$ (กรัม)	0.2454	0.2452	0.2542
$Mass_{ทราย}$ (กรัม)	17.2049	17.2055	17.2039
NZVI in Sand (กรัม$_{เหล็ก}$/กรัม$_{ทราย}$)	**0.0143**	**0.0143**	**0.0148**

4.4.2 ลักษณะของสาร TCE เมื่อเกิดการปนเปื้อนลงสู่ดินและน้ำใต้ดิน

สาร TCE เมื่อใส่ลงไปในขวดทดลองจะค่อยๆ ไหลซึมผ่านทราย ลงไปกองอยู่บริเวณก้นขวดทดลอง โดยเฉพาะอย่างยิ่ง ที่ %Saturation เท่ากับ 10 จะซึมลงไปได้ไวที่สุด จากนั้นเมื่อเวลาผ่านไป ไอระเหยของสาร TCE จะค่อยๆ ดันน้ำที่อยู่ในชั้นทราย ให้ขึ้นมากองอยู่ด้านบน (รูปที่ 56) ซึ่งตรงกับงานวิจัยที่ต่างๆ ที่ได้เคยทำการศึกษาค้นคว้าว่าหากสารในกลุ่ม Dense non-aqueous phase liquid (DNAPL) เกิดการปนเปื้อนลงสู่ดินและน้ำใต้ดิน จะก่อให้เกิดกระบวนการต่างๆ ได้หลากหลายประการ อาทิเช่น 1)การละลายลงสู่ดิน หรือน้ำใต้ดิน (Dissolution) 2) เกิดการระเหยของสารเคมีที่ละลายอยู่ในน้ำสู่อากาศ(Vaporization) และ การดูดซับหรือดูดซึมลงสู่ดิน (Sorption) Pankow and Cherry, 1996)

เมื่อ DNAPL ปนเปื้อนลงสู่ดินจะเกิดการเคลื่อนที่ลงตามแรงโน้มถ่วงของโลก โดยปริมาณของ DNAPL ที่เคลื่อนได้จะมีบางส่วนตกค้างอยู่ในโพรงหรือรูระหว่างเม็ดดิน อีกทั้งบริเวณชั้นดินไม่อิ่มตัวด้วยน้ำ (Vadose Zone) DNAPL มีความสามารถที่จะซึมผ่านได้ดีกว่าน้ำ เนื่องจาก DNAPL เป็น non-wetting fluid จึงสามารถเคลื่อนที่ผ่านรูหรือโพรงได้ดีกว่าน้ำที่เป็น wetting fluid (Fitter, 1993) อีกปัจจัยที่ DNAPL เคลื่อนที่ในชั้นใต้ดินได้ดี เพราะมีความหนาแน่นสูง ความหนืดต่ำ และความสามารถในการละลายน้ำได้ต่ำ (Hasan, 1996) DNAPL เคลื่อนที่ได้ดีจนถึงชั้นที่อิ่มตัวด้วยน้ำ โดยขณะเคลื่อนที่ DNAPL จะไปแทรกตัว แทนที่น้ำที่มีความหนาแน่นน้อยกว่า โดยขณะที่สารปนเปื้อนเคลื่อนที่ลงนั้นจะเกิดการระเหยเป็นไอบางส่วน การเคลื่อนที่ของ DNAPL จะหยุดเมื่อถูกกักเก็บไว้ในโพรงระหว่างเม็ดดินจนหมด ส่วน DNAPL อาจสามารถเคลื่อนที่ต่อไป จนถึงชั้นระดับน้ำใต้ดิน ทำให้เกิดการละลายของสารเคมีลงสู่ชั้นอิ่มตัวด้วยน้ำได้ต่อไป

รูปที่ 56 ลักษณะของสาร TCE เมื่อเกิดการปนเปื้อนลงสู่ดินและน้ำใต้ดิน

4.4.3 ปริมาณการละลายหรือระเหยกลายเป็นไอของสาร TCE

ในการศึกษาทดลองในครั้งนี้ ได้ทำการทดลองที่ %Saturation ที่แตกต่างกันเพียงช่วงแคบๆ ปริมาณการละลายหรือระเลยกลายเป็นไอของสาร TCE จึงมีค่าที่ใกล้เคียงกัน เมื่ออยู่ในสภาวะปกติ คือ ไม่ได้เหนี่ยวนำให้เกิดความร้อนผ่านสนามแม่เหล็ก ทั้งในส่วนของการทดลองที่ทำการใส่สาร TCE ลงไปในทรายเปล่า และใส่สาร TCE ลงไปในทรายที่ผสมกับอนุภาค NZVI แต่เมื่อทำการให้ความร้อนกับอนุภาค NZVI พบว่าสาร TCE สามารถชะละลายออกมาได้มากกว่าเดิม

จากผลการศึกษาพบว่าที่ %Saturation เท่ากับ 5 มีแนวโน้มของการระเหยของสาร TCE ออกมาได้มากที่สูง โดยหากพิจารณาที่เวลาการให้ความร้อนเพียง 5 นาที พบว่าสาร TCE สามารถระเหยออกมาได้มากที่สุด เท่ากับ 62,968.52 มก./ลิตร จากเดิมก่อนที่จะให้ความร้อน คือ 1,488.98 มก./ลิตร กว่าเดิมถึง 40 เท่า และปริมาณการระเหยของสาร TCE ยังมีแนวโน้มที่เพิ่มมากขึ้นเรื่อย จนถึงนาทีที่ 15 ที่พบว่ามีการระเหยของสาร TCE มากถึง 84,463.63 มก./ลิตร และคงที่ไปจนจบการให้ความร้อนที่ 60 นาที ส่วนที่ %Saturation เท่ากับ 10 TCE ก็สามารถระเหยออกมาในปริมาณมากเท่ากับ 5% ได้เช่นกัน หากแต่ต้องใช้เวลาในการให้ความร้อนที่มากกว่า คือ 30 นาที (รูปที่ 57)

จึงสามารถสรุปได้ว่าที่ %Saturation เท่ากับ 5 มีปริมาณการระเหยของสาร TCE เมื่อถูกให้ความร้อนได้มากที่สุด รองลงมาคือ 10% และ 1% ตามลำดับ ส่วนการระเหยของสาร TCE เมื่ออยู่ในสภาวะปกติ มีปริมาณการระเหยของสาร TCE ใกล้เคียงกัน อยู่ในช่วง 1,786.21 ถึง 2,804.10 มก./ลิตร ตามลำดับ

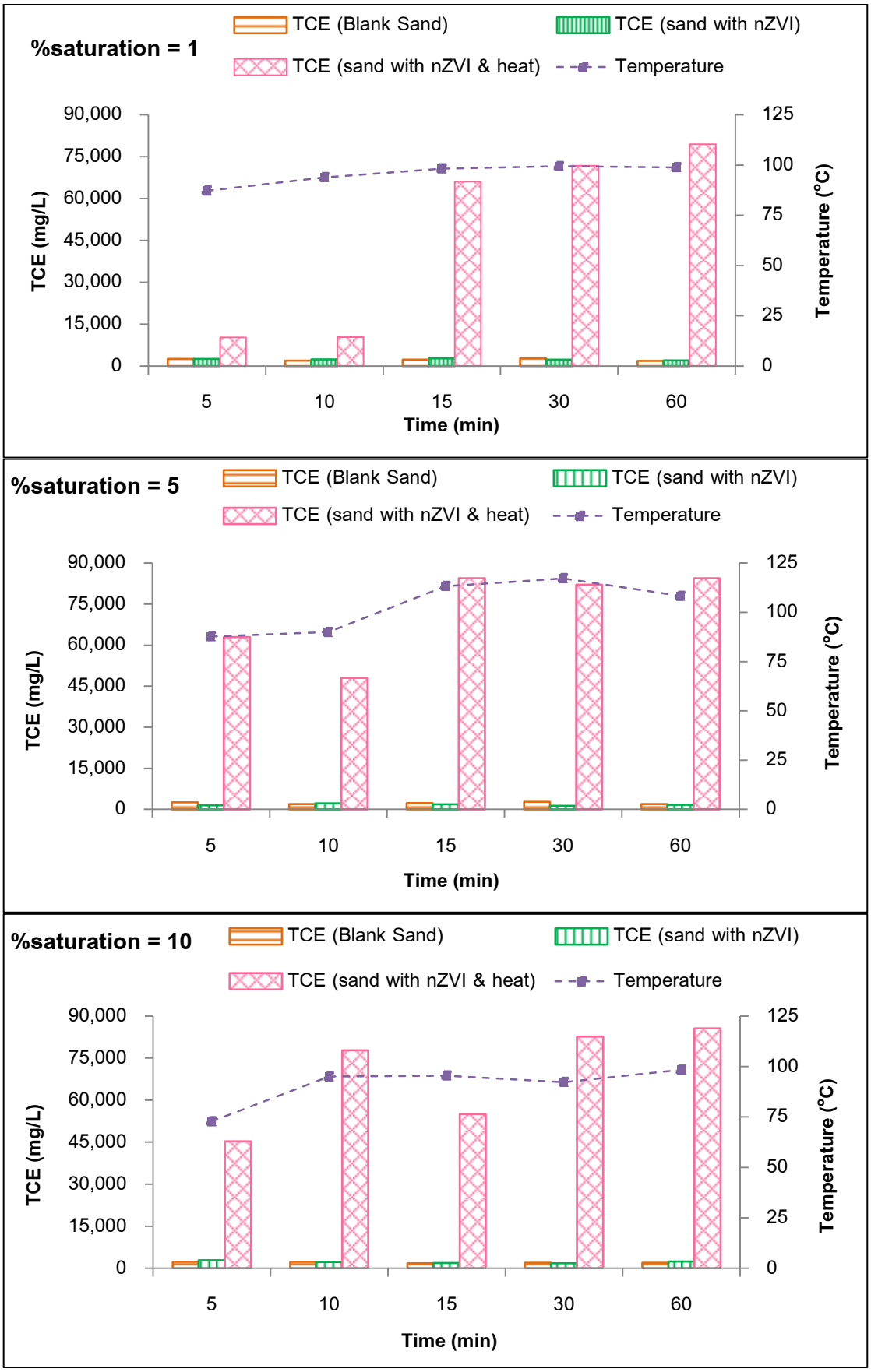

รูปที่ 57 ปริมาณการละลายหรือระเหยกลายเป็นไอของสาร TCE เมื่อได้รับความร้อน และไม่ได้รับความร้อน

ตาราง 10 ปริมาณความเข้มข้นของสาร TCE ที่ %Saturation เท่ากับ 1 5 และ 10%

n	% Saturation	Conc. TCE (มก./ลิตร)		
		Blank and	Sand With ZVI	Sand with NZVI & heat
5	1	2,611.66	2,553.48	10,231.38
	5	2,611.66	1,488.98	62,968.52
	10	2,349.78	2,868.08	45,278.05
10	1	1,963.02	2,403.43	10,342.36
	5	1,963.02	2,243.71	48,027.09
	10	2,347.34	2,260.06	77,772.97
15	1	2,298.96	2,804.10	66,076.48
	5	2,298.96	1,831.18	84,463.63
	10	1,786.21	1,858.60	54,989.02
30	1	2,746.38	2,285.65	71,742.65
	5	2,746.38	1,268.62	82,139.91
	10	2,006.58	1,802.37	82,650.03
60	1	1,911.98	2,024.40	79,471.33
	5	1,911.98	1,651.77	84,441.29
	10	1,985.96	2,366.70	85,615.96

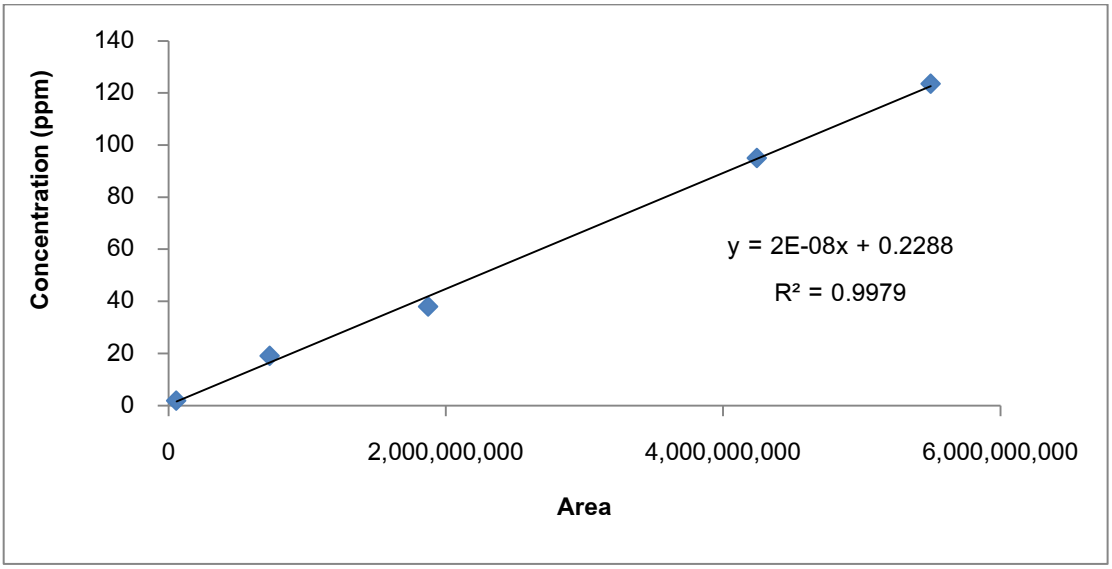

รูปที่ 58 Standard Calibration Curve ของสาร TCE

ตาราง 11 ปริมาณการละลายหรือระเหยกลายเป็นไอของสาร TCE (Blank Sand)

Time (นาที)	Area	Dilution Factor	Conc. TCE (มก./ลิตร)
% Saturation = 1			
5	40,793,209	2,500	2,611.66
10	27,820,417		1,963.02
15	34,539,283		2,298.96
30	43,487,664		2,746.38
60	26,799,698		1,911.98
% Saturation = 5			
5	40,793,209	2,500	2,611.66
10	27,820,417		1,963.02
15	34,539,283		2,298.96
30	43,487,664		2,746.38
60	26,799,698		1,911.98
% Saturation = 10			
5	71,111,021	2,500	2,349.78
10	71,013,432		2,347.34
15	48,568,413		1,786.21
30	57,383,178		2,006.58
60	56,558,368		1,985.96

ตาราง 12 ปริมาณการละลายหรือระเหยกลายเป็นไอของสาร TCE (Sand With NZVI)

Time (นาที)	Area	Dilution Factor	Conc. TCE (มก./ลิตร)
%Saturation = 1			
5	79,259,187	2500	2,553.48
10	73,257,361		2,403.43
15	89,283,873		2,804.10
30	68,546,154		2,285.65
60	58,095,884		2,024.40
%Saturation = 5			
5	36,679,170	2500	1,488.98
10	66,868,203		2,243.71
15	50,367,209		1,831.18
30	27,864,748		1,268.62
60	43,190,717		1,651.77
%Saturation = 10			
5	91,843,395	2500	2,868.08
10	67,522,386		2,260.06
15	51,463,940		1,858.60
30	49,214,627		1,802.37
60	71,788,099		2,366.70

ตาราง 13 ปริมาณการละลายหรือระเหยกลายเป็นไอของสาร TCE (sand with NZVI & heat)

Time (นาที)	Area	Dilution Factor	Conc. TCE (มก./ลิตร)
%Saturation = 1			
5	193,187,531	2,500	10,231.38
10	195,407,109		10,342.36
15	1,310,089,669		66,076.48
30	1,423,413,039		71,742.65
60	1,577,986,578		79,471.33
%Saturation = 5			
5	1,247,930,472	2,500	62,968.52
10	949,101,834		48,027.09
15	1,677,832,605		84,463.63
30	1,631,358,131		82,139.91
60	1,677,385,821		84,441.29
%Saturation = 10			
5	894,121,035	2,500	45,278.05
10	1,544,019,340		77,772.97
15	1,088,340,446		54,989.02
30	1,641,560,587		82,650.03
60	1,700,879,169		85,615.96

6. สรุปและวิจารณ์ผลการทดลอง

จากผลการศึกษาถึงประสิทธิภาพของโฟมที่ปรับเสถียรภาพด้วยอนุภาคเหล็กนาโน ร่วมกับการเหนี่ยวนำความร้อนทางแม่เหล็กไฟฟ้า เพื่อใช้ในการบำบัดสาร TCE ที่ปนเปื้อนอยู่ในดินและน้ำใต้ดิน โดยเฉพาะอย่างยิ่งบริเวณพื้นที่ไม่อิ่มตัวด้วยน้ำ (Vadose Zone) พบว่าโฟมที่ถูกสร้างขึ้น สามารถคงเสถียรภาพได้นานมากกว่า 120 นาที และมีคุณภาพของโฟม (Quality) สูงถึง 99% ขนาดอนุภาคของโฟมเมื่อส่องผ่านกล้องจุลทรรศน์พบว่ามีขนาดอยู่ในช่วง 5-15 ไมโครเมตร โฟมมีความสามารถที่จะนำพาอนุภาค NZVI ให้เคลื่อนที่ได้อย่างมีประสิทธิภาพ ที่ 66.98% แต่เมื่อทดลองนำโฟมที่ปรับเสถียรภาพด้วยอนุภาคเหล็กนาโน เคลื่อนที่ผ่านชั้นทราย จะพบว่าอนุภาค NZVI จะเกิดการสะสมอยู่มากเพียงช่วงแรกของ Pack Column และมีค่าการสะสมลดน้อยลงเรื่อยๆ จนถึงช่วงปลาย Pack Column จึงได้นำทรายเฉพาะบริเวณช่วงแรกของ Pack Column ไปทำการเหนี่ยวนำความร้อนทางแม่เหล็กไฟฟ้า พบสามารถก่อให้เกิดความร้อนขึ้นได้มากกว่า 80 $^{\circ}$C โดยใช้เวลาเพียง 5 นาที โดยที่ค่า %Saturation ในทราย ไม่ส่งผลกระทบต่อการเหนี่ยวนำให้เกิดความร้อนอย่างมีนัยสำคัญ ซึ่งสามารถเพิ่มประสิทธิภาพในการบำบัดสาร TCE ได้มากกว่าเดิมถึง 40 เท่า (เปรียบเทียบจากการทดลองควบคุม ที่ไม่ผ่านการให้ความร้อนปล่อยให้สาร TCE ค่อยๆระเหยออกมาเองตามธรรมชาติ)

7. ข้อเสนอแนะ

ปัจจุบันมีการศึกษาวิจัยเกี่ยวกับการฟื้นดิน หรือน้ำใต้ดินที่มีการปนเปื้อนของสารอันตรายต่างๆ มากมาย แต่การศึกษาวิจัยเกี่ยวกับแนวทางในการดำเนินการตรวจสอบ และจัดการพื้นที่ปนเปื้อน หรือการฟื้นฟูดินและน้ำใต้ดิน ที่เกิดจากการปนเปื้อนสารอินทรีย์ระเหยที่มีคลอรีนเป็นองค์ประกอบ ยังมีไม่มากนัก โดยเฉพาะอย่างยิ่งในประเทศไทยหรือประเทศที่กำลังพัฒนา ดังนั้นการศึกษาวิจัยที่เกี่ยวข้องกับแนวทางในการดำเนินการตรวจสอบและจัดการพื้นที่ปนเปื้อน หรือการฟื้นฟูดิน และน้ำใต้ดินที่ปนเปื้อนสารอินทรีย์ระเหย จึงมีความจำเป็นอย่างยิ่งเพื่อเป็นประโยชน์ต่อหน่วยงายภาครัฐ และบริษัทเอกชน รวมไปถึงประชาชนที่เกี่ยวข้อง เพื่อให้ทราบถึงโอกาสในการเกิดความเสี่ยง ทั้งต่อสุขภาพและต่อระบบนิเวศที่มีสาเหตุจากการปนเปื้อนสารพิษเหล่านี้ งานวิจัยฉบับนี้จึงอาจเป็นอีกหนึ่งวิศวกรรมทางเลือกสำหรับการบำบัดฟื้นฟูดินและน้ำใต้ดินที่ปนเปื้อนจากสาร TCE ที่ผ่านการศึกษาแล้วว่าสามารถทำได้จริงในห้องปฏิบัติการ ทำให้มีโอกาสก่อให้เกิดประโยชน์ได้อย่างมากต่อการบำบัดฟื้นฟูพื้นที่ปนเปื้อนจากสารอินทรีย์ระเหย และควรมีการศึกษาเพิ่มเติมต่อยอดให้มีองค์ความรู้ที่เพิ่มมากขึ้น

8. บรรณานุกรม

กิจการ พรหม. (2547). **อุทกธรณีวิทยาสิ่งแวดล้อม**. พิษณุโลก: มหาวิทยาลัยนเรศวร.

กำหนดมาตรฐานคุณภาพน้ำใต้ดิน. (15 กันยายน 2543). **ราชกิจจานุเบกษา ฉบับ20** เล่ม 117(ตอนพิเศษ 95 ง). หน้า 263-267.

ฉลอง บัวผัน. (2528). **น้ำบาดาล**. (1). กรุงเทพฯ: โอ.เอสพริ้นติง เฮาส์.

ชูโชค อายุพงศ์. (2535). **อุทกวิทยา**. เชียงใหม่: มหาวิทยาลัยเชียงใหม่.

แฟรดาซ์ มาเหล็ม, พีรพงษ์ สุนทรเดชะ, สีหนาถ ชาญณรงค์, อ่อนจันทร์ โคตรพงษ์, โครงการศึกษาการปนเปื้อนของสารประกอบอินทรีย์ระเหยง่ายในน้ำใต้ดินบริเวณนิคมอุตสาหกรรม ภาคเหนือจังหวัดลำพูน, รายงานผลงานวิจัยศูนย์วิจัยและฝึกอบรมด้านสิ่งแวดล้อมปี 2549 – 2550.

มีศักดิ์ มิลินทวิสมัย และ คณะ. (2544). **การปนเปื้อนของสาร Chlorinated Ethylene ในดินและน้ำใต้ดินและกรณีศึกษาของประเทศไทย**. ปทุมธานี: กลุ่มงานวิจัยและพัฒนาเทคโนโลยีสิ่งแวดล้อมด้านน้ำ ศูนย์วิจัยและฝึกอบรมด้านสิ่งแวดล้อม กรมส่งเสริมคุณภาพสิ่งแวดล้อม.

วีระพล แต้สมบัติ. (2528). **หลักอุทกวิทยา**. กรุงเทพฯ: มหาวิทยาลัยเกษตรศาสตร์.

ไสว พงศ์สุวรรณ. (ม.ป.ป). **น้ำใต้ดิน**. กรุงเทพฯ: มหาวิทยาลัยเกตษรศาสตร์.

Domenico, P.A and F.W. Schwartz. (1990). **Physical and Chemical Hydrogeology**. New York: John Wiley & Sons Inc.

Environmental Remediation Problems Company. New York: McGraw-Hill Book.

Fawell, J. K., and Gowers, A. M. (2010). **Hot Spots and Local Priorities: Chlorinated Solvents**. สืบค้นเมื่อ 20 ,April215, จาก http://www.bvsde.paho.org/muwww/fulltext/aguabas/europa/Water5.pdf.

Fetter, C.W. (1999). Contaminant Hydrogeology. (2). New York: Macmillan Publishing Company.

Freeze, R.A. and J.A. Cherry. (1979). Groundwater. New Jersey: Prentice-Hall, Inc.

Harr, M.E. (1962). **Groundwater and Seepage**. New York: McGraw-hill Inc.

Hasan, Syed E. (1996). **Geology and Hazardous Waste Management**. New Jersey: PrenticeHall, Inc.

Jo, Y.-J., Lee, J.-Y., Yi, M.-J., Kim, H.-S., and Lee, K.-K. (2010). Soil contamination with TCE in an industrial complex: contamination levels and implication for groundwater contamination. **Geosciences Journal**. 14(3), 313-320.

LaGrega, M., Buckingham, P., and Evans, J. (2000). **Hazardous Waste Management**. (2). New York: McGraw-Hill Science/Engineering/Math.

Lehr, J., M.; Hyman. T.E. Gass. and W. Seevers. (2001). Handbook of Complex

Li, Z., Kawashita, M., Araki, N., Mitsumori, M., Hiraoka, M., and Doi, M. (2010). Magnetite nanoparticles with high heating efficiencies for application in the hyperthermia of cancer. **Materials Science and Engineering C**. 30, 990-996.

Ma, H.-W., Wu, K.-Y., and Ton, C.-D. (2002). Setting information priorities for remediaition decisions at a contaminated-groundwater site. **Chemosphere**. 46, 75-81.

Mel Environmental Solutions. (2006). **Remediation Method**. Retrieved Apirl 12, 2015, from http://www.melltd.com/nhvsoil.htm.

Molson, J.W., E.O. Frind, D.R. Van Stempvoort and S. Lesage. (2002). Humic Acid Enhanced Remediation of an Emplaced Diesel Source in Groundwater. **Journal of Contaminant Hydrology**. 54(3-4), 277-305.

Phenrat, T., Saleh, N., Sirk, K., Tilton, R., D., and Lowry, G., V. (2007). Aggregation and sedimentation of aqueous nanoscale zerovalent iron dispersions. **Environ. Sci. Technol**. 41(1), 184-290.

Stroo, H., Unger, M., Ward, C. H., Kavanaugh, M., Vogel, C., Leeson, A., Marquesee, J., and Smith, B. (2003). Remediating chlorinated solvent source zones. **Environ. Sci. Technol**. 37, 193a-232a.

US Environmental Protection Agency. (May 2006). **SODIUM 2-(2-DODECYLOXYETHOXY) ETHYL SULPHATE(SODIUM LAURETH SULFATE; CAS NO. 3088-3 l-l):TEST PLAN**. สืบค้นเมื่อ 18 สิงหาคม 2558, จาก http://www.epa.gov/hpv/pubs/summaries/sodium22/c16316tp.pdf.

Younger, paul L. (2007). **Groundwater In The Environment: An Introduction**. oxford: Blackwell Publising.

Zhang, X. K., Li, Y. F., and Xiao, J. Q. (2003). Theoretical and experimental analysis of magnetic inductive heating in ferrite materials. **Journal of Applied Physics**. 93(10), 7124-7126.

Zhang, W. (2003). Nanoscale iron particles for environmental remediation: An overview. **J. Nanopart. Res**. 5, 323-332.

ภาคผนวก 1

Environ Sci Pollut Res
DOI 10.1007/s11356-015-5092-4

ADVANCES IN ENVIRONMENTAL CHEMISTRY OF POLLUTANTS

Adsorbed poly(aspartate) coating limits the adverse effects of dissolved groundwater solutes on Fe^0 nanoparticle reactivity with trichloroethylene

Tanapon Phenrat[1,2] · **Daniel Schoenfelder**[3] · **Teresa L. Kirschling**[3,4,5] · **Robert D. Tilton**[3,4,5] · **Gregory V. Lowry**[3,4,5]

Received: 3 April 2015 / Accepted: 16 July 2015

Abstract For in situ groundwater remediation, polyelectrolyte-modified nanoscale zerovalent iron particles (NZVIs) have to be delivered into the subsurface, where they degrade pollutants such as trichloroethylene (TCE). The effect of groundwater organic and ionic solutes on TCE dechlorination using polyelectrolyte-modified NZVIs is unexplored, but is required for an effective remediation design. This study evaluates the TCE dechlorination rate and reaction by-products using poly(aspartate) (PAP)-modified and bare NZVIs in groundwater samples from actual TCE-contaminated sites in Florida, South Carolina, and Michigan. The effects of groundwater solutes on short- and intermediate-term dechlorination rates were evaluated. An adsorbed PAP layer on the NZVIs appeared to limit the adverse effect of groundwater solutes on the TCE dechlorination rate in the first TCE dechlorination cycle (short-term effect). Presumably, the pre-adsorption of PAP "trains" and the Donnan potential in the adsorbed PAP layer prevented groundwater solutes from further blocking NZVI reactive sites, which appeared to substantially decrease the TCE dechlorination rate of bare NZVIs. In the second and third TCE dechlorination cycles (intermediate-term effect), TCE dechlorination rates using PAP-modified NZVIs increased substantially (~100 and 200%, respectively, from the rate of the first spike). The desorption of PAP from the surface of NZVIs over time due to salt-induced desorption is hypothesized to restore NZVI reactivity with TCE. This study suggests that NZVI surface modification with small, charged macromolecules, such as PAP, helps to restore NZVI reactivity due to gradual PAP desorption in groundwater.

Keywords Nanoscale zerovalent iron (NZVI) · Chlorinated organics · Dechlorination kinetics · Remediation · Groundwater · Polyelectrolyte · Poly(aspartate) · Desorption

Responsible editor: Philippe Garrigues

Electronic supplementary material The online version of this article (doi:10.1007/s11356-015-5092-4) contains supplementary material, which is available to authorized users.

✉ Tanapon Phenrat
pomphenrat@gmail.com

✉ Gregory V. Lowry
glowry@cmu.edu

[1] Research Unit for Integrated Natural Resources Remediation and Reclamation (IN3R), Department of Civil Engineering, Faculty of Engineering, Naresuan University, Phitsanulok 65000, Thailand

[2] Center of Excellence for Sustainability of Health, Environment and Industry (SHEI), Faculty of Engineering, Naresuan University, Phitsanulok 65000, Thailand

[3] Center for Environmental Implications of Nanotechnology (CEINT) and Department of Civil and Environmental Engineering, Carnegie Mellon University, Pittsburgh, PA 15213-3890, USA

[4] Department of Chemical Engineering, Carnegie Mellon University, Pittsburgh, PA 15213-3890, USA

[5] Department of Biomedical Engineering, Carnegie Mellon University, Pittsburgh, PA 15213-3890, USA

Introduction

Nanoscale zerovalent iron particles (NZVIs) have rapidly received much attention as a novel, in situ subsurface remediation agent to treat various kinds of vexing environmental contaminants, including chlorinated organics such as trichloroethylene (TCE) (Lowry 2007; Tratnyek and Johnson 2006; Zhang 2003). Various organic macromolecule surface modifiers, such as xanthane, guar gum, poly(aspartate) (PAP), poly(styrene sulfonate), carboxymethyl cellulose (CMC), poly(methyl methacrylate), poly(acrylic acid), and tri-block copolymers, are used to engineer NZVIs to inhibit their aggregation (Golas et al. 2010;

Published online: 02 August 2015

Phenrat et al. 2008; Sakulchaicharoen et al. 2010; Saleh et al. 2005; Wang et al. 2010), increase their mobility in the subsurface (Kim et al. 2009; Phenrat et al. 2009a, 2010; Saleh et al. 2008; Vecchia et al. 2009), and provide pollutant selectivity (Bishop et al. 2010; Phenrat et al. 2011; Saleh et al. 2005; Wang and Zhou 2010), all of which are necessary for effective in situ remediation. Several promising pilot- and field-scale tests using surface-modified NZVIs have been reported (Bennett et al. 2010; He et al. 2010; Henn and Waddill 2006; Kocur et al. 2014).

From the materials science point of view, significant research progress has been made in understanding the important properties of bare and polymeric-modified NZVIs that affect NZVI reactivity with chlorinated organics (Liu et al. 2005a, 2007; Liu and Lowry 2006; Nurmi et al. 2005; Phenrat et al. 2009a; Sarathy et al. 2008). Different dechlorination rates (Liu et al. 2005a, b; Nurmi et al. 2005; Sakulchaicharoen et al. 2010; Song and Carraway 2008; Zhang et al. 1998), dechlorination pathways (Liu et al. 2005a, b; Nurmi et al. 2005; Song and Carraway 2008; Zhang et al. 1998), electron utilization efficiencies (Liu et al. 2005a, b; Song and Carraway 2008), and longevities (Liu et al. 2005a; Sarathy et al. 2008) have been attributed to the crystallinity and chemical composition of bare NZVIs (i.e., the presence of noble metals, such as Pd and Ni, on the NZVI surfaces). As for polymer-modified NZVIs, Phenrat et al. (2009b) revealed that when the surfaces of pre-synthesized NZVIs were modified by the physisorption of polyelectrolytes, the TCE dechlorination rate constant decreased nonlinearly with increasing adsorbed mass of the polyelectrolytes, with a maximum 24-fold decrease in reactivity, due to reactive site blocking and a decrease in the aqueous TCE concentration at the surfaces of the NZVIs due to the partitioning of TCE to the adsorbed polyelectrolytes. A similar finding was also reported by Wang and Zhou (2010) using solvent-responsive, polymer-coated NZVIs to degrade TCE. Nevertheless, increases in TCE reactivity with polymer-modified Fe-Pd bimetallic nanoparticles at low polyelectrolyte concentrations compared with bare Fe-Pd bimetallic nanoparticles were also observed (He and Zhao 2008; Sakulchaicharoen et al. 2010). This difference is probably because the Fe-Pd bimetallic nanoparticles were synthesized in the presence of polymers such as CMC, guar gum, and polyvinylpyrrolidone (PVP), thereby yielding smaller particles that were resistant to aggregation and, thus, more reactive than larger, non-stabilized Fe-Pd particles (He and Zhao 2008; Sakulchaicharoen et al. 2010).

However, in addition to the properties of the particles themselves, the interaction between NZVIs and other (non-target) inorganic ions and dissolved natural organic matter (NOM) in groundwater can affect the reactivity, longevity, and, thus, the performance of NZVIs. Because of geochemical cycles (dissolution and precipitation) of minerals in the subsurface, groundwater normally consists of various cationic and anionic species, such as Na^+, Ca^{2+}, Mg^{2+}, NO_3^-, Cl^-, SO_4^{2-}, HCO_3^-, and HPO_4^{-2}. Groundwater chemistry is known to affect the performance of the ZVI permeable reactive barrier (PRB) by controlling the Fe^0 corrosion rate (El-Naggar 2006; Scherer et al. 2000), dechlorination rate (Klausen et al. 2003; Kohn et al. 2005; Su and Puls 2004), H_2 production (Scherer et al. 2000), microbial activity (Scherer et al. 2000; Van Nooten et al. 2008), the formation of mineral precipitates on the surfaces of iron filings (Agrawal et al. 2002; Kohn et al. 2005), and the dissolution of the iron oxide layer on Fe^0 (Agrawal et al. 2002). Some similar effects of anionic species on the performances of bare and bimetallic NZVIs were experimentally observed (Lim and Zhu 2008; Liu et al. 2007). At low concentrations (0.2–1 mM), reducible solutes, such as NO_3^-, did not significantly affect the NZVI-mediated TCE dechlorination rate. However, at high concentrations (~5 mM), NO_3^- reduced the reactivity of NZVIs with TCE after 3 days, even though Fe^0 remained in the NZVIs. Presumably, at high NO_3^- concentrations, the surface reaction was shifted from cathodic control (i.e., the reduction of TCE) to anodic control (i.e., the release of Fe^{2+} and electrons) and, thus, facilitated the formation of a passivating FeOOH layer (Liu et al. 2007). In the presence of high NO_3^- and NO_2^- concentrations, a similar decrease in reactivity and particle passivation was also observed for trichlorobenzene (TCB) dechlorination using bimetallic Fe-Pd nanoparticles (Lim and Zhu 2008).

In contrast, anions such as Cl^-, SO_4^{2-}, HCO_3^-, and HPO_4^{-2} are not reducible by Fe^0. Their effects on dechlorination using iron filings varied with their concentration. Several studies (Agrawal et al. 2002; Devlin and Allin 2005; Johnson et al. 1998) reported that high concentrations of non-reducible ionic species decreased ZVI reactivity through the formation of a passivating oxide layer. In contrast, other studies (Agrawal et al. 2002; Johnson et al. 1998) reported the opposite, i.e., that these ions promoted the dissolution of the iron oxide layer, leading to increased reactivity at low concentrations. As for NZVIs, a recent study (Liu et al. 2007) revealed that non-reducible ionic species decreased the TCE dechlorination rate by up to a factor of seven compared with deionized (DI) water, and the order of their effect followed their affinity for hydrous ferric oxide, i.e., $Cl^- < SO_4^{2-} < HCO_3^- < HPO_4^{2-}$ at pH 8.9 (Liu et al. 2007). This implies that the inhibitory effect of these solutes on TCE degradation may be caused by reactive site blocking due to the formation of Fe-anion complexes on the NZVI surface.

The effect of non-catalytic cations, such as Na^+, Ca^{2+}, and Mg^{2+}, on TCE dechlorination using NZVIs has not been systematically studied, although these cations, which normally coexist with anions in groundwater, are likely to accumulate more closely to the surfaces of NZVIs than anions according to the Boltzmann distribution of ions in a solution that contains negatively charged surfaces (Israelachvili 1992). At a neutral pH, the electrostatic interaction between the negatively charged NZVI surface and cations might exhibit reactive site blocking, which might affect the TCE dechlorination rate.

Field applications of NZVIs for in situ remediation cannot avoid interactions with a mixture of non-target,

dissolved ionic and organic species that are commonly present in the subsurface, as mentioned previously. Understanding the effects of these dissolved species on the short- and intermediate-term TCE dechlorination rates of NZVIs is essential to determine the amount of NZVIs that should be injected into the subsurface to achieve a particular clean-up goal. While such effects on bare NZVIs are known, the effects on polymer-modified NZVIs, which are more practical for field applications, are not (He and Zhao 2008; Karn et al. 2009; Sakulchaicharoen et al. 2010). Dechlorination using NZVIs is an interfacial phenomenon that is substantially affected by the presence of adsorbed polymer layers (Phenrat et al. 2009b). Therefore, it is not appropriate to assume that the effects of groundwater solutes on TCE dechlorination using polymer-modified NZVIs will be similar to those using bare NZVIs.

The objective of this study was to experimentally examine the short- and intermediate-term effects of a mixture of dissolved ionic and organic species in natural groundwater on TCE dechlorination using polymer-modified NZVIs. Poly(aspartate) (PAP), a bio-polyelectrolyte, was used as a representative polymeric modifier in this study (Phenrat et al. 2009b, c). The three cycles of TCE dechlorination using PAP-modified and bare NZVIs were conducted in three different natural groundwater samples from Florida (FL), South Carolina (SC), and Michigan (MI). The difference between TCE dechlorination rates using bare and PAP-modified NZVIs in the same groundwater sample was discussed and attributed to the presence of adsorbed PAP layers. An initial spike of TCE was used to evaluate short-term TCE dechlorination, while the second and third spikes of TCE were used to evaluate intermediate-term TCE dechlorination. The presence of a Donnan potential inside the adsorbed polyelectrolyte layers was used to mechanistically explain the altered distributions of ionic species surrounding the NZVI surfaces that might hypothetically contribute to decreasing the adverse effects of dissolved ionic species on TCE dechlorination rates using polymer-modified NZVIs in comparison with bare NZVIs. A conceptual model that explains the decrease in solute concentrations at the NZVI surface, as well as the decrease in site blocking by (ionic and organic) solutes, due to the presence of adsorbed polyelectrolyte layers was proposed to illustrate how a polymeric surface coating limits the adverse effects of groundwater solutes on NZVI reactivity. In addition, the desorption of PAP from the surface of NZVIs in the presence of groundwater solutes was indirectly observed using electrophoretic mobility measurements and was attributed to the experimentally observed improvement in the intermediate-term TCE dechlorination rate for PAP-modified NZVIs.

Materials and methods

Chemicals

TCE (99.5+%) was from Sigma-Aldrich (St. Louis, MO, USA). Acetylene (1000 ppm and 1 %), ethylene (1 %), ethane (1 %), vinyl chloride (VC) (10 ppm), and hydrogen (1.08 %) standards were from Alltech Chemicals (Subiaco, Australia). The balance gas standard was N_2. Ultra high-purity argon, hydrogen (5.18 %), and N_2 were from Butler Gas products (Pittsburgh, PA, USA).

Bare NZVIs

Reactive nanoscale iron particles (RNIPs), consisting of reactive Fe^0/Fe_3O_4 core-shelled NZVI particles, were obtained from Toda Kogyo (Onada, Japan). The physical and chemical properties of the RNIPs have been previously reported (Liu et al. 2005b; Nurmi et al. 2005; Phenrat et al. 2007). Prior to use, RNIPs were stored as an aqueous slurry (pH 10.6) at approximately 300 g/L in an anaerobic chamber. From this slurry, a stock dispersion (10 mL at ~120 g/L) was prepared in 1 mM $NaHCO_3$, followed by ultrasonication for 30 min to break up any aggregates that formed during storage. The N_2-BET specific surface area of the RNIPs was ~15 m^2/g. The Fe^0 content of the particles determined from acid digestion and monitoring hydrogen evolution as previously described (Liu et al. 2005b) was ~15 % by mass.

Poly(aspartate)-modified NZVIs

Sodium PAP (MW 2000–3000 g/mol) stabilized NZVIs (MRNIP) were obtained from Toda Kogyo. The physical and chemical properties of the PAP-modified NZVIs have been previously reported (Phenrat et al. 2008; Saleh et al. 2007; 2008). The PAP monomer unit is aspartate, one of the 20 natural amino acid building blocks of proteins, making PAP of potential interest as an environmentally benign modifier. Prior to use, MRNIPs were stored as an aqueous slurry (pH 10.6) at approximately 180 g/L in an anaerobic chamber. From this slurry, a stock dispersion (10 mL at ~30 g/L) was prepared in DI water followed by ultrasonication for 30 min to break up any aggregates that formed during storage. The excess PAP in the MRNIP dispersion was removed by ultracentrifugation prior to redispersion by ultrasonication for 3 min before the TCE dechlorination study. The N_2-BET specific surface area of MRNIP was found to be similar to that of bare RNIPs, i.e., ~15 m^2/g. The Fe^0 content of the particles determined as described above was similar to the bare particles, i.e., ~15 % by mass.

Zeta potential of bare NZVIs

The electrophoretic mobility of bare RNIPs was measured for dilute dispersions (~30 mg/L) in 1 mM NaCl (pH 8) with a Malvern Zetasizer (Southborough, MA, USA). The measured electrophoretic mobilities were converted to apparent ζ-potentials using the Helmholtz-Smoluchowski relationship (Israelachvili 1992).

Adsorbed PAP layer characterization

The adsorbed polymer layer properties of polymer-modified NZVIs govern the TCE dechlorination rate (Phenrat et al. 2009b). The adsorbed PAP layer on the MRNIPs was characterized using electrophoretic mobility (EPM) measurements and Ohshima's soft particle theory (Ohshima 1995) as previously described (Phenrat et al. 2008). Details of Ohshima's method can be found in Ohshima (1995) and Phenrat et al. (2008)), as well as in the Additional file 1. Briefly, EPM was measured for 10 mg/L solutions of the washed, PAP-modified NZVIs at NaCl concentrations ranging from 1 to 61 mM (pH 8.0±0.1). EPM was measured in triplicate (25 °C) using a Malvern Zetasizer. The mean and standard deviation (σ) of the measured EPM (u_e) were calculated. The procedure for extracting the adsorbed polyelectrolyte layer properties from the EPM data involves fitting Ohshima's model to obtain the best fit layer properties, including the charge density in the adsorbed polyelectrolyte layer (N), the softness parameter (λ), the adsorbed layer thickness (d) for the mean u_e, and the mean $u_e \pm \sigma$ as a function of ionic strength using a MATLAB (the Mathworks, Novi, MI, USA) code employing an iterative least-squares minimization.

Groundwater

Three different groundwater samples from three actual TCE-contaminated sites in FL, SC, and MI were used in this study. Groundwater samples were stored at 4 °C and deoxygenated by N_2 sparging prior to use. All VOCs were also purged from the groundwater samples by N_2 sparging prior to the addition of known concentration of TCE for dechlorination study described next. The pH of the solution was measured after N_2 sparging. Concentrations of dissolved anions and cations were determined by a commercial laboratory (Severn Trent Laboratories, Pittsburgh, PA, USA) for the FL and SC groundwater samples, and they were provided by the Michigan Department of Environmental Quality Environmental Laboratory (Lansing, MI) for the MI groundwater samples. Total organic carbon (TOC) was measured using UV/persulfate wet oxidation (OI Analytical Model 1100). Table 1 summarizes the solute concentrations in the three groundwater samples.

Table 1 Dissolved solutes in FL, MI, and SC groundwater

Solute	FL (mM)	MI (mM)	SC (mM)
Na^+	0.54	0.13	6.09
K^+	0.04	0.01	0.04
Ca^{2+}	0.42	1.44	0.89
Mg^{2+}	0.1	0.5	0.45
HCO_3^-	0.92	2.72	1.18
Cl^-	0.6	0.31	5.32
NO_3^-	ND	0.26	ND
SO_4^{2-}	0.06	0.06	1.23
TOC	1.0 mg/L	0.8 mg/L	9.6 mg/L
pH	7.2	7.9	6.0

ND not detected

TCE dechlorination

TCE dechlorination rates and by-products were measured in 70-mL serum bottles containing 40 mL of headspace, 30 mL of liquid, and a Mininert™ closure. All reactors were prepared in an anaerobic glove box (argon-filled) and contained 3 g/L of either bare or PAP-modified NZVIs in one of the three groundwater samples. An aliquot of 0.15 mL of saturated TCE solution (8.4 mM) was added to provide an initial TCE concentration of 40 μM. Experiments were performed in duplicate. The reactors were rotated on an end-over-end rotator at 30 rpm at 23±2 °C. In control experiments without NZVIs, it was demonstrated that the TCE loss by mechanisms (e.g., photodegradation, adsorption, leakage) other than degradation by Fe^0 was negligible. Mass transfer resistance at the vapor/liquid interface was not considered, as these phases are assumed to be in equilibrium (Burris et al. 1996). Kinetically, a series of 100-μL headspace samples were withdrawn from the reactors and analyzed for TCE and its products using a 30-m GSQ PLOT capillary column on a HP 6890 GC/FID. Following the complete degradation of the first spike of TCE, the reactors were sparged with nitrogen, purged in a glove box, and then an additional spike of TCE was added right away. This process was repeated to achieve three cycles of TCE dechlorination or until the NZVIs were no longer reactive.

A previously reported model of the TCE degradation pathway by bare (Liu et al. 2007) (Additional file 1: Fig. S1a) and PAP-modified NZVIs (Phenrat et al. 2009a) was used to interpret the dechlorination kinetics in this study. It was assumed that all TCE reduction was via β-elimination to form acetylene, and that both ethane and ethene resulted from the reduction of acetylene. The reaction rate constants, k_{TCE} (TCE dechlorination to acetylene), k_2 (ethene formation from acetylene), and k_3 (ethane formation from acetylene), were determined using a kinetic modeling software package, Scientist,

v.2.01 (Micromath, St. Louis, MO, USA), in which the loss of TCE and the formation of products (acetylene, ethane, and ethane) were fit concurrently to determine the rate constants and 95 % confidence intervals for the fits. The observed reaction rate constants determined from headspace measurements, $k_{obs\text{-}h}$, were converted to the observed rate constants without headspace, k_{obs}, to compare TCE and acetylene, which have different Henry's law constants (Additional file 1: Fig. S1b) (Liu and Lowry 2006).

Quantifying the change of adsorbed PAP layers on NZVIs after TCE dechlorination

To determine the change in the adsorbed PAP layers on NZVIs due to a possible interaction with organic and inorganic solutes in groundwater samples during the dechlorination process, PAP-modified and bare NZVIs were recovered from the TCE dechlorination reactors using magnetic separation and washed with N_2-purged DI water several times to remove solutes that were attached to the NZVI surfaces. Then, EPM measurements were conducted on the recovered particles. To compare the influence of groundwater solutes on the adsorbed PAP layer on the NZVIs, the EPM of the recovered PAP-modified NZVIs was compared to that of PAP-modified NZVIs aged in DI water for the same period of time.

Acridine orange counting of microorganisms

To evaluate if the change of adsorbed biomacromolecules, such as PAP, can be driven by microbial activity, microorganisms were enumerated by acridine orange counting according to the methods of Kepner and Pratt (1994). Briefly, sample aliquots were dispersed in 0.01 M tetrasodium pyrophosphate (Na4PP-i) (Sigma-Aldrich). Ten milliliters of dispersed sample was stained in the dark for 5 min in a 100 μg/mL acridine orange solution (Sigma-Aldrich). The suspension was filtered onto a 0.22-μm black polycarbonate track-etched membrane (Millipore, Billerica, MA, USA) and visualized by epi-fluorescent microscopy using a Zeiss Observer Z1 microscope. Twenty random view fields were counted for each measurement to obtain total cell counts.

Results and discussion

Charge density of bare NZVIs and adsorbed layer properties of PAP-modified NZVIs

The EPM of bare RNIPs in 1 mM NaCl at pH 8 was −3.3 μm V^{-1} s^{-1} cm, which corresponds to a zeta potential (ζ) of −42.5 mV using the Helmholtz-Smoluchowski relationship. The apparent bare NZVI charge density (σ) of -3×10^{-4} C/m^2 was obtained from the apparent ζ-potentials using Eq. 1 (Evans and Wennerstrom 1999).

$$\sigma = \frac{2\varepsilon_r\varepsilon_0\kappa k_B T}{ze}\sinh\left(\frac{ze\zeta}{2k_B T}\right) \quad (1)$$

where e is the electron charge, z is the valence of the ionic species of interest, k_B is Boltzmann's constant, T is absolute temperature, ε_0 is the permittivity of a vacuum, and ε_r is the relative permittivity. κ is the Debye-Hückel parameter of the solution (Eq. 2).

$$\kappa = \left(\frac{2\sum_{i=1}^{J} e^2 C_i^* z_i^2}{\varepsilon_r\varepsilon_0 k_B T}\right)^{1/2} \quad (2)$$

The adsorbed PAP layer properties for PAP-modified NZVIs, based on Ohshima's soft particle analysis and EPM (Fig. 1), are as follows: $N=-2.1\times10^{23}/m^3$, d=~40 nm, and $1/\lambda$=~24 nm. These adsorbed layer properties are in good agreement with the properties of PAP-modified NZVIs that were reported in recent papers (Phenrat et al. 2008, 2009b).

Effect of groundwater solutes on TCE dechlorination using bare NZVIs

Figure 2 illustrates the TCE degradation kinetics and by-product formation kinetics using bare and PAP-modified

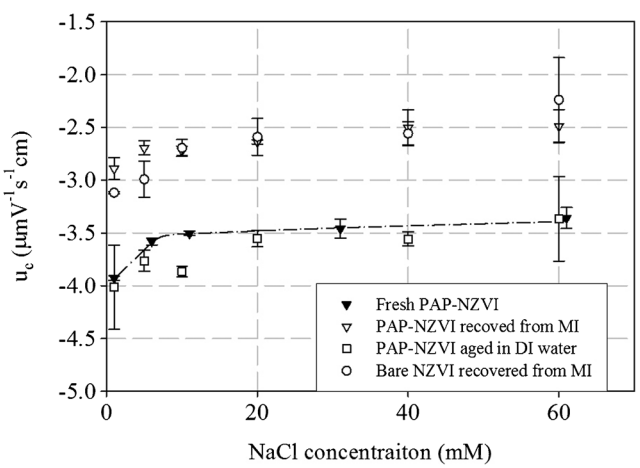

Fig. 1 Electrophoretic mobility of fresh PAP-modified NZVIs (*filled triangles*), PAP-modified NZVIs recovered from MI groundwater after TCE dechlorination (*open triangles*), bare NZVIs recovered from MI groundwater after TCE dechlorination (*open circles*), and PAP-modified NZVI aged in DI water for the same period of time (*open squares*) as a function of the NaCl concentration (mM) at pH 8.0±0.1. The *lines* represent the best-fit theoretical curves obtained using Ohshima's soft particle analysis.

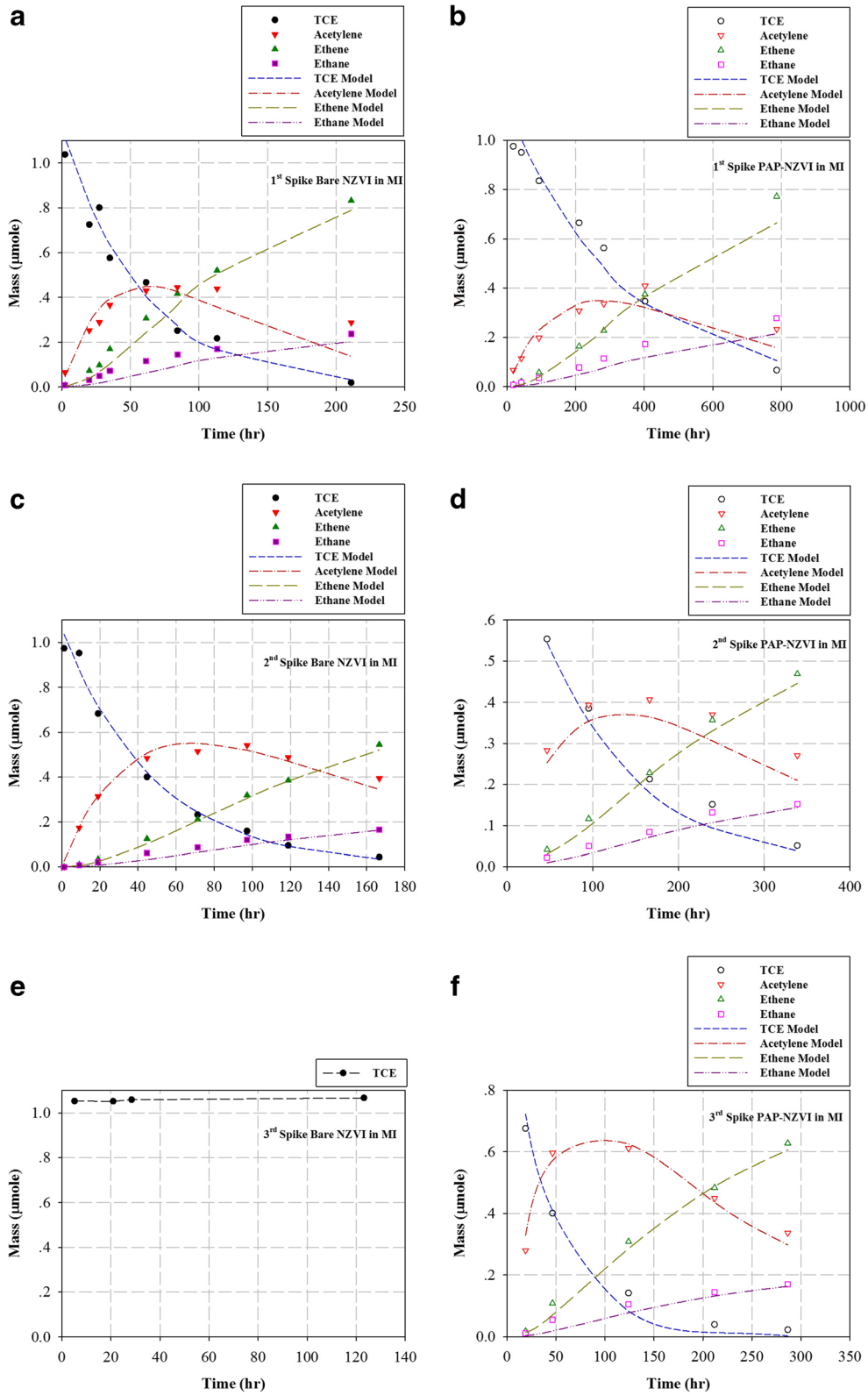

Fig. 2 TCE degradation kinetics and by-product formation kinetics using bare NZVIs for the **a** first, **c** second, and **e** third TCE degradation cycles, and using PAP-modified NZVIs for the **b** first, **d** second, and **f** third TCE degradation cycles in MI groundwater

NZVIs in MI groundwater as a representative example of the groundwater samples evaluated in this study. Acetylene was the intermediate, while ethane and ethene were the main by-products. Mass balance of TCE and dechlorination by-products was from 96 to 127 % for all the cases (Additional file 1: Fig. S2). The experimental rate constants are also reported in Table 2 for bare NZVIs and in Table 3 for PAP-modified NZVIs. The presence of ionic and organic solutes

Table 2 TCE degradation rate constants and by-product formation rate constants for bare NZVIs (reported as an average± 95 % CI)

Groundwater	k_{TCE} (10^{-3} L m^{-2} h^{-1})	k_2 (10^{-3} L m^{-2} h^{-1})	k_3 (10^{-3} L m^{-2} h^{-1})
First spike			
FL	0.485±0.087	0.181±0.064	0.063±0.055
MI	0.833±0.162	0.402±0.124	0.101±0.080
SC	0.794±0.135	0.497±0.124	0.126±0.077
Second spike			
FL	0.566±0.044	0.175±0.024	0.058±0.022
MI	0.742±0.040	0.205±0.013	0.058±0.066
SC	0.499±0.037	0.191±0.022	0.056±0.059

in natural groundwater decreased the TCE dechlorination rates using bare NZVIs to a similar extent as that previously reported by Liu et al. (2007). We found that the TCE dechlorination rates in the SC and MI groundwater samples for the first TCE spike were around ~22 % of the TCE dechlorination rate using bare NZVIs in DI water (Fig. 3a). Similarly, the TCE dechlorination rate using bare NZVIs in FL groundwater, in which the solute concentrations were in the range of those for the SC and MI groundwater, was around 13 % of the TCE dechlorination rate in DI water. Presumably, the decline in the TCE dechlorination rate in groundwater is attributed to the surface complexation of the NZVIs by cationic and anionic solutes (Liu et al. 2007) and reactive site blocking via the adsorption of natural organic matter onto the surface of the NZVIs.

The TCE dechlorination rates in the second TCE spike for MI and FL groundwater were similar to the dechlorination rates of the first spike, which is in good agreement with Liu and Lowry's observation that TCE dechlorination rates remained constant over the life time of NZVIs under a particular solution chemistry (i.e., pH) (Liu and Lowry 2006). However, the TCE dechlorination rate of bare NZVIs in SC groundwater declined in the second spike. In the third TCE spike (around 30 days after the first TCE spike), bare NZVIs stopped reacting with TCE in all three groundwater samples, presumably due to the depletion of Fe^0 at the end of the particles' life time (Fe^0 content <3 % by mass for all the cases).

Effect of groundwater solutes on TCE dechlorination using PAP-modified NZVIs

Groundwater solutes did not alter TCE dechlorination pathways using PAP-modified NZVI. Similar to PAP-modified NZVIs in DI water (Phenrat et al. 2009b), for TCE dechlorination using PAP-modified NZVIs in the groundwater samples, acetylene was the intermediate and ethane and ethene were the main by-products (Fig. 2). For the first TCE spike, the TCE dechlorination rate using PAP-modified NZVIs was less than that of bare NZVIs in all the groundwater samples. This is because the adsorbed PAP blocks the NZVI reactive sites and decreases the aqueous TCE concentration at the NZVI surface due to the partitioning of TCE to the adsorbed

Table 3 TCE degradation rate constants and by-product formation rate constants for PAP-modified NZVIs (reported as an average±95 % CI)

Groundwater	k_{TCE} (10^{-3} L m^{-2} h^{-1})	k_2 (10^{-3} L m^{-2} h^{-1})	k_3 (10^{-3} L m^{-2} h^{-1})
First spike			
FL	0.226±0.022	0.124±0.021	0.045±0.017
MI	0.103±0.012	0.081±0.017	0.026±0.028
SC	0.126±0.012	0.078±0.013	0.020±0.024
Second spike			
FL	0.566±0.044	0.175±0.024	0.058±0.022
MI	0.325±0.027	0.103±0.011	0.032±0.033
SC	0.357±0.023	0.102±0.008	0.026±0.031
Third spike			
FL	1.254±0.094	0.181±0.016	0.046±0.013
MI	0.697±0.067	0.118±0.013	0.029±0.032
SC	0.613±0.054	0.091±0.010	0.021±0.029

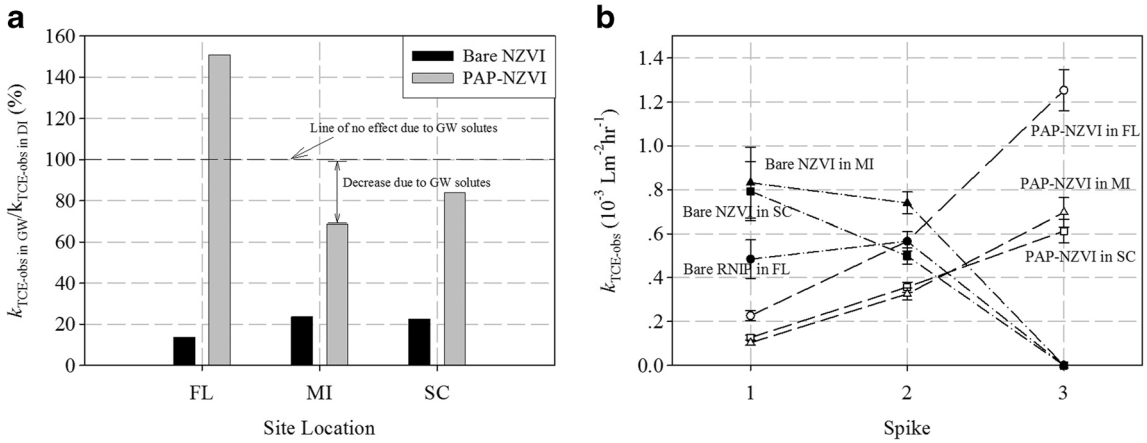

Fig. 3 **a** TCE dechlorination of bare and PAP-modified NZVIs in FL, SC, and MI groundwater standardized by TCE dechlorination in DI water. **b** Change in TCE dechlorination rates of bare and PAP-modified NZVIs in FL, SC, and MI groundwater from the first to the third TCE spike

PAP layer. This observation is in good agreement with our recent study (Phenrat et al. 2009b).

However, the adsorbed PAP layer on the NZVI surface limited the adverse effect of groundwater solutes on TCE dechlorination rates. As shown in Fig. 3a, for the first TCE spike, TCE dechlorination rates using PAP-modified NZVIs in the MI and SC groundwater samples were 70 and 85 % of the TCE dechlorination rate using PAP-modified NZVIs in DI water (Phenrat et al. 2009b). Moreover, the TCE dechlorination rate using MRNIPs in FL groundwater was even greater than that of PAP-modified NZVIs in DI water; a possible explanation for this observation will be discussed in the last section regarding the desorption of PAP from the surfaces of the NZVIs. Overall, the TCE dechlorination rate using PAP-modified NZVIs in the groundwater samples was much less affected by the presence of groundwater solutes than that using bare NZVIs. A possible explanation, the effect of the Donnan potential in the PAP layer on solute distributions, for this finding is discussed in the next section.

Interestingly, unlike bare NZVIs, for which the TCE dechlorination rates in the second spike either decreased or remained the same, the TCE dechlorination rates of PAP-modified NZVIs in all groundwater samples increased substantially (~100 % greater than that in the first spike). The TCE dechlorination rates of PAP-modified NZVIs kept increasing in the third TCE spike (~200 % greater than that of the first spike). PAP-modified NZVIs did not become non-reactive, as occurred for the bare NZVIs, after two cycles of TCE dechlorination. A possible explanation for the increase in the TCE dechlorination rates following the second and third spikes will be discussed in the last section on the desorption of PAP from the surfaces of the NZVIs.

Conceptual model: Donnan potential in the adsorbed PAP layer and NZVI site blocking by PAP trains limit the adverse effect of dissolved solutes in groundwater on TCE dechlorination

The pre-adsorbed PAP layer on the surfaces of NZVIs behaves as a barrier that prevents organic and ionic solutes from effectively blocking and passivating the reactive sites of the NZVIs. The adsorbed PAP layer consists of trains, loops, and tails (Phenrat et al. 2009b). The loops and tails exhibit an extended polymeric layer surrounding the surfaces of the NZVIs, while the trains adsorb directly onto the surfaces of the NZVIs, i.e., they block the NZVI reactive sites. Because of volume exclusion and osmotic pressure effects, the extended PAP layer on the NZVIs decreases the subsequent adsorption of charged macromolecules, such as NOM, onto the surfaces of the NZVIs and, thus, decreases the reactive site blocking by NOM. Similarly, the charged PAP layer exhibits a negative Donnan potential (Phenrat et al. 2008) (Fig. 4), which can decrease the concentration of cationic solutes at the surfaces of NZVIs and possibly reduce their blocking effect compared with that for bare NZVIs. This hypothesis can be theoretically supported by considering the distribution of ionic species with and without the presence of the adsorbed PAP layer (Fig. 5) as discussed below.

The adverse effect of ionic species on dechlorination using bare NZVIs is an interfacial phenomenon (Liu et al. 2007) that should be substantially affected by the interfacial concentrations, rather than the bulk concentrations, of ionic species at the surfaces of NZVIs. The interfacial concentration of an ionic species is a function of its valence, its bulk concentration, and the electrical potential in the electrostatic double layer of bare NZVIs (Israelachvili 1992). The concentration

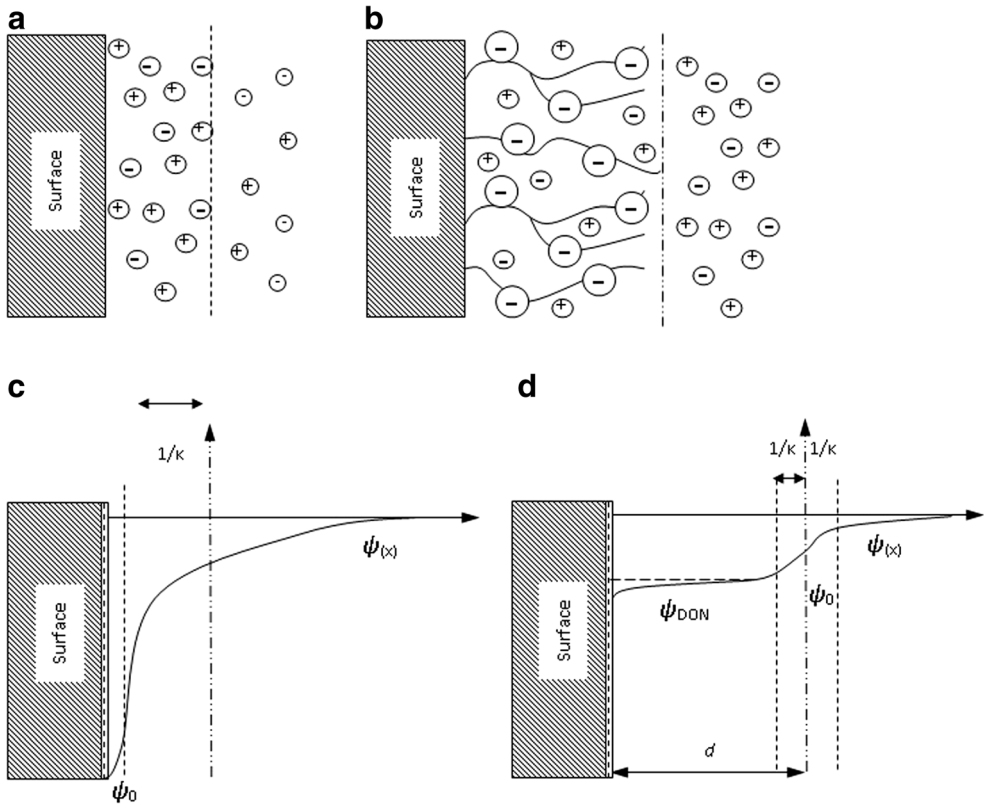

Fig. 4 Schematic illustrating the ion distribution surrounding **a** bare and **b** PAP-modified NZVIs focusing on the effect of the adsorbed PAP layer on ion distribution. Schematic illustrating the electrical potentials surrounding **c** bare and **d** PAP-modified NZVIs focusing on the presence of a Donnan potential in the adsorbed PAP layer

of the ionic species (C_i*) as a function of distance (x) from the surfaces of the NZVIs can be calculated from the Boltzmann distribution (Israelachvili 1992) (Eq. 3).

$$C_i^*(x) = C_{i0}^* \exp\left(\frac{-z_i e\phi(x)}{k_B T}\right) \quad (3)$$

where C_{i0}* is the bulk concentration of ionic species i and z_i is its valence. For a solution chemistry of interest, the electrical potential ($\Phi(x)$) as a function of the distance (x) from the bare NZVI surface can be approximated using Eq. 4 if the zeta potential of the NZVIs (ζ) and the solution chemistry (which controls the Debye-Hückel parameter (κ)) (Eq. 2) are known.

$$\varphi(x) = \frac{4k_B T}{ze} \tanh\left(\frac{ze\zeta}{4k_B T}\right) \exp(-\kappa x) \quad (4)$$

As shown in Figs. 4a, c and 5a, following the Boltzmann distribution (Eq. 3), cationic species accumulated near the surface of negatively charged NZVIs and their bulk concentration gradually decreases as the distance increases due to the exponential decrease in the electrical potential ($\Phi(x)$). In the Stern layer very close to the surface, an excess of cations

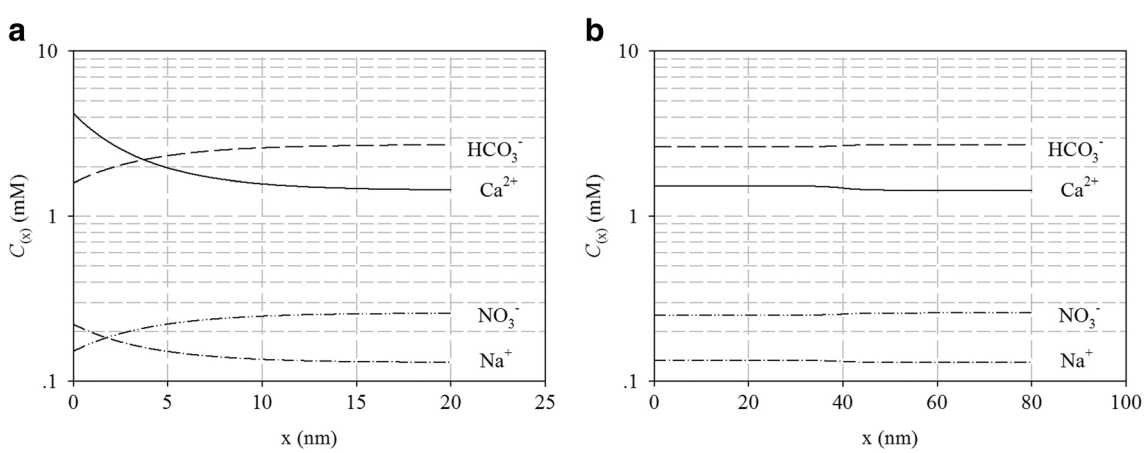

Fig. 5 Representative distributions of anionic and cation species from the surfaces of **a** bare and **b** PAP-modified NZVIs in MI groundwater using the Boltzmann distribution

neutralizes the surface charge of NZVIs, which might block reactive sites. The degree of cationic accumulation increases with their bulk concentration and valence (i.e., a divalent cation accumulates at the surface to a greater degree than a monovalent cation). In contrast, anionic species are depleted close to the surface in comparison to their bulk concentration (Fig. 5a).

Similar to the case of the bare NZVIs mentioned previously, the adverse effect of ionic species on dechlorination using PAP-modified NZVIs should be governed by the interfacial concentration of ionic species, which is a function of the valence of the ionic species of interest, their bulk concentrations, and the electrical potential in the adsorbed PAP layer on the NZVIs according to the Boltzmann distribution (Eq. 3) (Israelachvili 1992). However, unlike the bare NZVIs, the electrical potential in the adsorbed PAP layer on NZVIs ($\psi(x)$) is substantially affected by the Donnan potential (ψ_{DON}), which is mostly controlled by the adsorbed layer thickness (d) and charge density in the layer (N) (Phenrat et al. 2008) as shown in Eq. 5 (Fig. 4b, d). The zeta potential of bare NZVIs (ζ) plays only a minor role in the case of polyelectrolyte-modified NZVIs (Eq. 5) in comparison to bare NZVIs (Eq. 4).

$$\Psi(x) = \Psi_{\mathrm{DON}} + (\Psi_0 - \Psi_{\mathrm{DON}})e^{\kappa_m x} + \frac{2k_{\mathrm{B}}T}{ze}\ln\left(\frac{1+\tanh\left(\frac{ze\zeta}{4k_{\mathrm{B}}T}\right)\cdot e^{-\kappa_m(x+d)}}{1\text{-}\tanh\left(\frac{ze\zeta}{4k_{\mathrm{B}}T}\right)\cdot e^{-\kappa_m(x+d)}}\right), -d \le x \le 0 \quad (5)$$

The effective Debye-Hückel parameter (κ_m) is expressed in Eq. 6. The corresponding ψ_{DON} and the surface potential (ψ_0) at the boundary between the adsorbed layer and the surrounding solution (not the same as zeta potential) (Fig. 4b, d) are as shown in Eqs. 7 and 8, respectively.

$$\kappa_m = \kappa\left[\cosh\left(\frac{ze\psi_{\mathrm{DON}}}{k_{\mathrm{B}}T}\right)\right]^{1/2} \quad (6)$$

$$\psi_{\mathrm{DON}} = \frac{k_{\mathrm{B}}T}{ze}\sinh^{-1}\left(\frac{ZN}{2zn}\right) \quad (7)$$

$$\psi_0 = \psi_{\mathrm{DON}} - \frac{k_{\mathrm{B}}T}{ze}\tanh\left(\frac{ze\psi_{\mathrm{DON}}}{2k_{\mathrm{B}}T}\right) + \frac{4k_{\mathrm{B}}T}{ze}.e^{-\kappa_m d}\tanh\frac{ze\zeta}{4k_{\mathrm{B}}T} \quad (8)$$

where Z is the valence of the ionized groups on the polyelectrolyte, which is −1 for PAP.

Because of the weak polyelectrolyte nature of PAP (i.e., the relatively low charge density (N) as determined by Ohshima's soft particle analysis) and its relatively extended layer thickness (d), the electrical potential in the adsorbed PAP layer on the NZVIs ($\psi(x)$) is low in magnitude but extended (i.e., it has a longer range than the electrical potential of bare NZVIs). As shown in Fig. 5b, according to the distribution (Eq. 3), the ion distribution in the adsorbed PAP layer was relatively unaltered compared with the bulk concentration. Cationic species did not accumulate near the surface of PAP-modified NZVIs as in the case of bare NZVIs. Thus, the site blocking of PAP-modified RNIPs due to cationic species should be less than that of bare NZVIs.

While the loops and tails in the extended PAP layer reduce the adverse effects of groundwater solutes on TCE dechlorination by decreasing the availability of NOM and cationic species at the surfaces of the NZVIs as discussed above, the PAP trains also decrease the blocking effect of NOM or cationic species that reach the surfaces of the NZVIs. Sorption of organic molecules to iron oxide surfaces is typically driven by specific interactions between iron oxide surfaces and carboxylic ligands (Edwards et al. 1996). Since both PAP and NOM have carboxylic groups, the sorption of both macromolecules to iron oxide surfaces of NZVIs is promoted by such oxide surface-ligand complexation. Consequently, the pre-sorption of PAP to NZVIs limits further reactive site blocking of NZVIs by further sorption of NOM and ionic species. For these reasons, NOM and ionic species that reach the reactive sites of bare NZVIs will have a greater impact in blocking the pristine (bare) NZVI reactive sites in comparison to the case of PAP-modified NZVIs, of which substantial amount of sites are already pre-blocked by adsorbed PAP trains.

Desorption of PAP from PAP-modified NZVIs increases the TCE dechlorination rate over time

While the decreases in the adverse effects of groundwater solutes on TCE dechlorination using PAP-modified NZVIs are attributed to the extended, absorbed PAP layers and the adsorbed PAP trains, they cannot explain the observation that the TCE dechlorination rates using PAP-modified NZVIs increased over time from the first to the third spike (Fig. 3b). A possible explanation is that, over time, during the TCE dechlorination in the presence of groundwater solutes, PAP gradually desorbed from the surfaces of the NZVIs, and the PAP-modified NZVIs behaved more similarly to the bare NZVIs in terms of their reactions with TCE. This desorption hypothesis is supported by the EPM of PAP-modified NZVIs recovered from the groundwater samples after the three TCE dechlorination cycles. The EPM of polymer-modified particles as a function of the NaCl concentration provides information on the characteristics of the adsorbed polymer layer (Phenrat et al. 2008). The greater negative charge on the PAP-modified NZVIs, in comparison to bare NZVIs, comes from the charged layers of PAP on the RNIP surface. Figure 1 suggests that the desorption of PAP from the surface of PAP-modified

NZVIs after three cycles of TCE dechlorination occurs because the response of the EPM as a function of the NaCl concentration for the PAP-modified NZVIs recovered from MI groundwater is similar to the EPM of bare RNIPs (no polymer on its surface) recovered from MI groundwater, although it is very different from the EPM of fresh PAP-modified NZVIs (fully covered with PAP). The EPM of fresh PAP-modified NZVIs is greater than that of PAP-modified NZVIs or the bare NZVIs recovered from MI groundwater at all NaCl concentrations.

The evidence suggests that PAP desorption is only observed when PAP-modified NZVIs were aged in the presence of groundwater solutes. As shown in Fig. 1, the EPM as a function of the NaCl concentration for PAP-modified NZVIs aged in DI water for the same period of time is similar to that of fresh PAP-modified NZVIs, suggesting that PAP is not desorbed from the NZVI surface in the presence of DI water alone. The relatively insignificant desorption of PAP from NZVIs in DI water is in agreement with the results of a recent study (Kim et al. 2009). In natural groundwater, the desorption of biomacromolecules, such as PAP, can be driven by biotic or abiotic reactions due to microorganisms and abiotic solutes, respectively. Microorganisms might use macromolecules as their carbon source (He et al. 2010; Kirschling et al. 2010, 2011; Xiu et al. 2010), resulting in the removal of macromolecules from the surfaces of NZVIs (Kirschling et al. 2011). However, according to acridine orange counting of bacteria, we observed a low population of bacteria (~10^4 cells/mL) in all groundwater samples, both for bare and PAP-modified NZVIs. This suggests that there is no biostimulation due to the presence of PAP-modified NZVIs in groundwater, which is in good agreement with the fact that we did not observe any chlorinated by-products, as indicators of biotic dechlorination, during TCE degradation in this study (Xiu et al. 2010). Thus, biodegradation of PAP by microorganisms was unlikely. Consequently, the desorption of PAP was likely driven by either ionic or organic solutes. Normally, under a particular solution chemistry, the adsorption of macromolecules on a substrate is considered to be irreversible due to their multiple-segment attachment nature (Holmberg et al. 2003; Kim et al. 2009). For a macromolecule to desorb from a surface, all polymer segments attached to the surface must be detached at approximately the same time. If only a few segments are detached, there is a high probability that other available segments will occupy the available adsorption sites before the whole polymer desorbs (Holmberg et al. 2003). However, when the solution chemistry is changed due to an increase in ionic concentrations, polyelectrolyte desorption is theoretically possible due to the change in polyelectrolyte confirmation that is induced by the ionic species (de Carvalho 2010; Man et al. 2008). The salt-induced desorption transition of charged macromolecules is an entropically driven phenomenon (de Carvalho 2010). High ionic concentrations cause an electrostatic screening of charged groups in polyelectrolytes, which subsequently decrease the electrostatic volume exclusion of the polyelectrolytes. This leads to an entropic penalty for adsorbed macromolecules, i.e., polyelectrolytes in a desorbed configuration have a lower conformational entropy than polyelectrolytes in an adsorbed configuration. As a result, when a few segments of polyelectrolytes are detached, because of the entropic penalty, other segments might not reattach at the available sites, gradually leading to desorption of the entire polymer. This is hypothesized to occur when mixing polymer-modified NZVIs prepared in a low ionic strength solution (1 mM $NaHCO_3$) with natural groundwater samples (which have a high ionic concentration, as shown in Table 1). This is coupled with the fact that the PAP used in this study is a small macromolecule (MW of 25 kg/mol and 16 monomers per chain), making desorption easier. For this reason, over time, an increasing number of segments of PAP became detached from the NZVI surface and resulted in gradual desorption, as suggested by the increase in the TCE dechlorination rates over time (Fig. 3b). It should be noted that the increase in the TCE dechlorination rates over time was not observed for NZVIs encapsulated in an alginate biopolymer (Bezbaruah et al. 2011). Instead, a gradual decrease of TCE dechlorination rates was evident over time, i.e., a 5–7 % decrease over 5–6 months. Presumably, a relatively thick skin (0.2736± 0.0036 mm) of cross-linked Ca-alginate gel, compared with the adsorbed PAP layer in this study (d=40 nm), makes alginate desorption from NZVIs unlikely.

Implications for applications of NZVIs

The physisorption of polyelectrolytes on NZVI is necessary for effective in situ remediation. However, polymeric surface modification comes with two drawbacks. Firstly, it decreases NZVI reactivity with chlorinated organics such as TCE; adsorbed PAP on the surfaces of NZVIs is reported to decrease the TCE dechlorination rate by 24-fold compared with that of bare NZVIs in DI water (Phenrat et al. 2009b). Secondly, it raises a concern regarding the risk of NZVIs leaching from a treatment zone in the subsurface, which might have unintended ecological effects (Karn et al. 2009; Phenrat et al. 2009c). This study found that although surface modification with PAP decreases NZVI reactivity due to reactive site blocking and decreases the aqueous TCE concentration at the NZVI surface because of the partitioning of TCE to the adsorbed polyelectrolytes (Phenrat et al. 2009a), it subsequently reduces the interaction of NZVIs with non-target groundwater solutes (organic and ionic species), which has been shown to substantially decrease the reactivity of bare NZVIs (Liu et al. 2007). In addition, over an intermediate period of time (30 days), in the presence of groundwater solutes, PAP desorbed, thus restoring the reactivity of NZVIs with TCE. In addition, the desorption of PAP from NZVIs also decreases the chance that

NZVIs can leach from the treatment zones to other ecological sites. This suggests that the modification of the NZVI surface with small charged macromolecules, such as PAP, helps to deliver NZVIs to the subsurface, restores NZVI reactivity over time due to a gradual PAP desorption in groundwater, and should not cause a significant, unacceptable risk due to uncontrollable particle migration (Phenrat et al. 2009c).

Acknowledgments The authors are thankful for financial support from (1) the Thailand Research Fund (TRF) (MRG5680129), (2) the National Nanotechnology Centre (Thailand), a member of the National Science and Technology Development Agency, through grant number P-11-00989, (3) the National Research Council of Thailand (grant no. R2556B070 and R2555C010), and (4) the U.S. EPA (R830898 and R833326), NSF (BES-068646 and EF-0830093), and Department of Defense through the Strategic Environmental Research and Development Program (W912HQ-06-C-0038).

References

Agrawal A, Ferguson WJ, Gardner BO, Christ JA, Bandstra JZ, Tratnyek PG (2002) Effects of carbonate species on kinetics of dechlorination of 1,1,1-trichloroethane by zero-valent iron. Environ Sci Technol 36:4326–4333

Bennett P, He F, Zhao D, Aiken B, Feldman L (2010) In situ testing of metallic iron nanoparticle mobility and reactivity in a shallow granular aquifer. J Contam Hydrol 116:35–46

Bezbaruah AN, Shanbhogue SS, Simsek S, Khan E (2011) Encapsulation of iron nanoparticles in alginate biopolymer for trichloroethylene remediation. J Nanopart Res 13:6673–6681

Bishop EJ, Fowler DE, Skluzacek JM, Seibel E, Mallouk TE (2010) Anionic homopolymers efficiently target zerovalent iron particles to hydrophobic contaminants in sand columns. Environ Sci Technol 44:9069–9074

Burris DR, Delcomyn CA, Smith MH, Roberts AL (1996) Reductive dechlorination of tetrachloroethylene and trichloroethylene catalyzed by vitamin B12 in homogeneous and heterogeneous systems. Environ Sci Technol 30:3047–3052

de Carvalho SJ (2010) First-order–like transition in salt-induced macroion-polyelectrolyte desorption. EPL 92:18001

Devlin JF, Allin KO (2005) Major anion effects on the kinetics and reactivity of granular iron in glass-encased magnet batch reactor experiments. Environ Sci Technol 39:1868–1874

Edwards M, Benjamin MM, Ryan JN (1996) Role of organic acidity in sorption of natural organic matter (NOM) to oxide surfaces. Colloid Surface A 107:297–307

El-Naggar MM (2006) Effects of Cl^-, NO_3^-, and SO_4^{2-} anions on the anodic behavior of carbon steel in deaerated 0.50 M $NaHCO_3$ solutions. Appl Surf Sci 252:6179–6194

Evans DF, Wennerstrom H (1999) The colloidal domain; where physics, chemistry, biology, and technology meet. Wiley-VCH, New York

Golas PL, Louie S, Lowry GV, Matyjaszewski K, Tilton RD (2010) Comparative study of polymeric stabilizers for magnetite nanoparticles using ATRP. Langmuir 26:16890–16900

He F, Zhao D (2008) Hydrodechlorination of trichloroethene using stabilized Fe-Pd nanoparticles: reaction mechanism and effects of stabilizers, catalysts, and reaction conditions. Appl Catal B Environ 84: 533–540

He F, Zhao D, Paul C (2010) Field assessment of carboxymethyl cellulose stabilized iron nanoparticles for in situ destruction of chlorinated solvents in source zones. Water Res 44:2360–2370

Henn KW, Waddill DW (2006) Utilization of nanoscale zero-valent iron for source remediation—a case study. Remediation J 16:57–77

Holmberg K, Jonsson B, Kronberg B, Lindman B (2003) Surfactants and polymers in aqueous solution, 2nd edn. John Wiley & Sons, Ltd., Chichester, West Sussex, England

Israelachvili JN (1992) Intermolecular and surface forces: with applications to colloidal and biological systems, 2nd edn. Academic Press, New York

Johnson TL, Fish W, Gorby YA, Tratnyek PG (1998) Degradation of carbon tetrachloride by iron metal: complexation effects on the oxide surface. J Contam Hydrol 29:379–398

Karn B, Kuiken T, Otto M (2009) Nanotechnology and in situ remediation: a review of the benefits and potential risks. Environ Health Perspect 117:1823–1831

Kepner RL Jr, Pratt JR (1994) Use of fluorochromes for direct enumeration of total bacteria in environmental samples: past and present. Microbiol Mol Biol R 58:603–615

Kim H-J, Phenrat T, Tilton RD, Lowry GV (2009) Fe^0 nanoparticles remain mobile in porous media after aging due to slow desorption of polymeric surface modifiers. Environ Sci Technol 43:3824–3830

Kirschling TL, Gregory KB, Minkley EGJ, Lowry GV, Tilton RD (2010) Impact of nanoscale zero valent iron on geochemistry and microbial populations in trichloroethylene contaminated aquifer materials. Environ Sci Technol 44:3474–3480

Kirschling TL, Golas PL, Unrine JM, Matyjaszewski K, Gregory KB, Lowry GV, Tilton RD (2011) Microbial bioavailability of covalently bound polymer coatings on model engineered nanomaterials. Environ Sci Technol 45:5253–5259

Klausen J, Vikesland PJ, Kohn T, Burris DR, Ball WP, Roberts AL (2003) Longevity of granular iron in groundwater treatment processes: solution composition effects on reduction of organohalides and nitroaromatic compounds. Environ Sci Technol 37:1208–1218

Kocur CM et al (2014) Characterization of nZVI mobility in a field scale test. Environ Sci Technol 48:2862–2869

Kohn T, Livi KJT, Roberts AL, Vikesland PJ (2005) Longevity of granular iron in groundwater treatment processes: corrosion product development. Environ Sci Technol 39:2867–2879

Lim T-T, Zhu B-W (2008) Effects of anions on the kinetics and reactivity of nanoscale Pd/Fe in trichlorobenzene dechlorination. Chemosphere 73:1471–1477

Liu Y, Lowry GV (2006) Effect of particle age (Fe^0 content) and solution pH on NZVI reactivity: H_2 evolution and TCE dechlorination. Environ Sci Technol 40:6085–6090

Liu Y, Choi H, Dionysiou D, Lowry GV (2005a) Trichloroethene hydrodechlorination in water by highly disordered monometallic nanoiron. Chem Mater 17:5315–5322

Liu Y, Majetich SA, Tilton RD, Sholl DS, Lowry GV (2005b) TCE dechlorination rates, pathways, and efficiency of nanoscale iron particles with different properties. Environ Sci Technol 39:1338–1345

Liu Y, Phenrat T, Lowry GV (2007) Effect of TCE concentration and dissolved groundwater solutes on NZVI-promoted TCE dechlorination and H_2 evolution. Environ Sci Technol 41:7881–7887

Lowry GV (2007) Nanomaterials for groundwater remediation. In: Wiesner MR, Bottero J-Y (eds) Environmental nanotechnology: applications and impacts of nanomaterials. McGraw-Hill, New York

Man X, Yang S, Yan D, Shi A-C (2008) Adsorption and depletion of polyelectrolytes in charged cylindrical system within self-consistent field theory. Macromolecules 41:5451–5456

Nurmi JT et al (2005) Characterization and properties of metallic iron nanoparticles: spectroscopy, electrochemistry, and kinetics. Environ Sci Technol 39:1221–1230

Ohshima H (1995) Electrophoresis of soft particles. Adv Colloid Interface Sci 62:189–235

Phenrat T, Saleh N, Sirk K, Tilton R, Lowry GV (2007) Aggregation and sedimentation of aqueous nanoscale zerovalent iron dispersions. Environ Sci Technol 41:284–290

Phenrat T, Saleh N, Sirk K, Kim H-J, Tilton RD, Lowry GV (2008) Stabilization of aqueous nanoscale zerovalent iron dispersions by anionic polyelectrolytes: adsorbed anionic polyelectrolyte layer properties and their effect on aggregation and sedimentation. J Nanopart Res 10:795–814

Phenrat T, Kim H-J, Fagerlund F, Illangasekare T, Tilton RD, Lowry GV (2009a) Particle size distribution, concentration, and magnetic attraction affect transport of polymer-modified Fe^0 nanoparticles in sand columns. Environ Sci Technol 43:5079–5085

Phenrat T, Liu Y, Tilton R, Lowry GV (2009b) Adsorbed polyelectrolyte coatings decrease Fe^0 nanoparticle reactivity with TCE in water: conceptual model and mechanisms. Environ Sci Technol 43:1507–1514

Phenrat T, Long TC, Lowry GV, Veronesi B (2009c) Partial oxidation ("aging") and surface modification decrease the toxicity of nanosized zerovalent iron. Environ Sci Technol 43:195–200

Phenrat T, Cihan A, Kim H-J, Mital M, Illangasekare T, Lowry GV (2010) Transport and deposition of polymer-modified Fe^0 nanoparticles in 2-D heterogeneous porous media: effects of particle concentration, Fe^0 content, and coatings. Environ Sci Technol 44:9086–9093

Phenrat T, Fagerlund F, Illanagasekare T, Lowry GV, Tilton RD (2011) Polymer-modified Fe^0 nanoparticles target entrapped NAPL in two dimensional porous media: effect of particle concentration, NAPL saturation, and injection strategy. Environ Sci Technol 45:6102–6109

Sakulchaicharoen N, O'Carroll DM, Herrera JE (2010) Enhanced stability and dechlorination activity of pre-synthesis stabilized nanoscale FePd particles. J Contam Hydrol 118:117–127

Saleh N, Phenrat T, Sirk K, Dufour B, Matyjaszewski K, Tilton RD, Lowry GV (2005) Adsorbed triblock copolymers deliver reactive iron nanoparticles to the oil/water interface. Nano Lett 12:2489–2494

Saleh N et al (2007) Surface modifications enhance nanoiron transport and NAPL targeting in saturated porous media. Environ Eng Sci 24: 45–57

Saleh N, Kim H-J, Phenrat T, Matyjaszewski K, Tilton RD, Lowry GV (2008) Ionic strength and composition affect the mobility of surface-modified Fe^0 nanoparticles in water-saturated sand columns. Environ Sci Technol 42:3349–3355

Sarathy V et al (2008) Aging of iron nanoparticles in aqueous solution: effects on structure and reactivity. J Phys Chem C 112:2286–2293

Scherer MM, Richter S, Valentine RL, Alvarez PJJ (2000) Chemistry and microbiology of permeable reactive barriers for in situ groundwater clean up. Crit Rev Microbiol 26:221–264

Song H, Carraway ER (2008) Catalytic hydrodechlorination of chlorinated ethenes by nanoscale zero-valent iron. Appl Catal B Environ 78: 53–60

Su CM, Puls RW (2004) Nitrate reduction by zerovalent iron: effects of formate, oxalate, citrate, chloride, sulfate, borate, and phosphate. Environ Sci Technol 38:2715–2720

Tratnyek PG, Johnson RL (2006) Nanotechnologies for environmental cleanup. Nano Today 1:44–48

Van Nooten T, Springael D, Bastiaens L (2008) Positive impact of microorganisms on the performance of laboratory-scale permeable reactive iron barriers. Environ Sci Technol 42:1680–1686

Vecchia ED, Luna M, Sethi R (2009) Transport in porous media of highly concentrated iron micro- and nanoparticles in the presence of xanthan gum. Environ Sci Technol 43:8942–8947

Wang W, Zhou M (2010) Degradation of trichloroethylene using solvent-responsive polymer coated Fe nanoparticles. Colloid Surface A 369: 232–239

Wang W, Zhou M, Jin Z, Li T (2010) Reactivity characteristics of poly(methyl methacrylate) coated nanoscale iron particles for trichloroethylene remediation. J Hazard Mater 173:724–730

Xiu ZM, Gregory KB, Lowry GV, Alvarez PJ (2010) Effect of bare and coated nanoscale zerovalent iron on tceA and vcrA gene expression in *Dehalococcoides* spp. Environ Sci Technol 44:7647–7651

Zhang W (2003) Nanoscale iron particles for environmental remediation: an overview. J Nanopart Res 5:323–332

Zhang W-X, Wang C-B, Lien H-L (1998) Treatment of chlorinated organic contaminants with nanoscale bimetallic particles. Catal Today 40:387–395

Supporting Information for "Adsorbed Poly(aspartate) Coating Limits Adverse Effect of Dissolved Groundwater Solutes on Fe0 Nanoparticle Reactivity with TCE"

Tanapon Phenrat[1,2]*, Daniel Schoenfelder[3], Teresa L. Kirschling[3,4], Robert D. Tilton[3,4], Gregory V. Lowry[3,4*]

[1]Research Unit for Integrated Natural Resources Remediation and Reclamation (IN3R), Department of Civil Engineering, Faculty of Engineering, Naresuan University, Phitsanulok, Thailand, 65000

[2]Center of Excellence for Sustainability of Health, Environment and Industry (SHEI), Faculty of Engineering, Naresuan University, Phitsanulok, Thailand, 65000

[3]Center for Environmental Implications of Nanotechnology (CEINT) and Department of Civil & Environmental Engineering, Carnegie Mellon University, Pittsburgh, PA 15213-3890, USA.

[4] Department of Chemical Engineering and Department of Biomedical Engineering, Carnegie Mellon University, Pittsburgh, PA 15213-3890, USA.

(a)

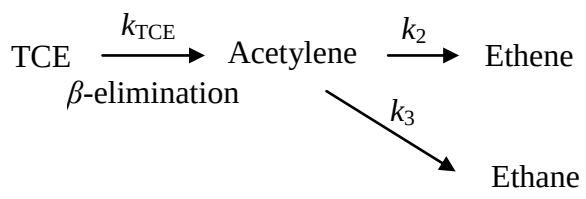

(b)

$$k_{obs} = k_{obs-h} \frac{K_H V_h + V_w + K_p V_p}{V_w}$$

FIGURE S1. (a) Proposed TCE reduction pathways by bare and surface-modified RNIP *(1)*. (b) The relationship between the observed reaction rate constants determined from headspace measurements, $k_{obs\text{-}h}$, and the corresponding rate constant without headspace, k_{obs} *(1)*.

Fe^0 Content Determination via Acid Digestion

The Fe^0 content of RNIP can be determined (separately from total iron) by acid digestion in a closed container with headspace as described in our previous study *(1, 2)*. H_2 produced from the oxidation of Fe^0 in RNIP by H^+ is measured by GC-TCD and used to quantify the Fe^0 content of the particles (eqn S1) *(3)*. The RNIP concentration was calculated assuming a Fe^0(core)/Fe_3O_4(shell) morphology, and using the measured Fe^0

content, α' (eqns S2 and S3). The factor 1.38 in Eq. S3 is to convert the mass of iron (Fe) to magnetite (Fe_3O_4).

$$Fe^0 + 2H^+ \rightarrow Fe^{2+} + H_2 \uparrow \quad \text{(S1)}$$

$$[Fe]_{total} = [Fe]_{Fe_3O_4} + [Fe]_{Fe^0} \quad \text{(S2)}$$

$$[RNIP] = 1.38(1-\alpha')[Fe]_{total} + \alpha'[Fe]_{total} \quad \text{(S3)}$$

Applying Ohshima's Soft Particle Analysis to Estimate Adsorbed Polyelectrolyte Layer Properties on NZVI

The procedure for extracting the characteristics of the polyelectrolyte layer from electrophoretic mobility (EM) data involves fitting Ohshima's model, eqn. S4, with terms defined as in eqns. S5-S8 to the experimental electrophoretic mobility vs. concentration of a symmetrical electrolyte (NaCl in this study) to obtain the best fit *N*, *λ*, and *d (1, 4-9).* All other parameters in equations S5 to S8 are fixed for a given salt concentration.

$$u_e = \frac{\varepsilon}{\eta}\frac{\psi_0/\kappa_m + \psi_{DON}/\lambda}{1/\kappa_m + 1/\lambda} f\left(\frac{d}{a}\right) + \frac{ZeN}{\eta\lambda^2} + \frac{8\varepsilon k_B T}{\eta\lambda ze}.\tanh\frac{ze\zeta}{4k_B T}.\frac{e^{-\lambda d}/\lambda - e^{-\kappa_m d}/\kappa_m}{1/\lambda^2 - 1/\kappa_m{}^2}$$

(S4)

where ε is the electric permittivity of the liquid medium, η is its viscosity, λ is a frictional parameter given by $(\gamma/\eta)^{1/2}$, and κ_m is the effective Debye-Hückel parameter of the surface hydrogel layer, which includes the contribution of the fixed charge *ZeN (5)*. ζ is the apparent zeta potential of the bare particles calculated from EM measurements using Smoluchowski's formula. The function *f*(d/a) varies between 1 for a thin adsorbed layer relative to radius of the core particle (*a*), to 2/3 for a thick layer. Eqn. S4 is valid when λd and $\kappa d > 1$ *(4)*. The corresponding expressions for ψ_{DON}, ψ_0, *f*(d/a), and κ_m are given in eqn S5 to S8 *(4, 5, 10, 11),*

$$\psi_{DON} = \frac{k_B T}{ze} \sinh^{-1}\left(\frac{ZN}{2zn}\right) \tag{S5}$$

$$\psi_0 = \psi_{DON} - \frac{k_B T}{ze} \tanh\left(\frac{ze\psi_{DON}}{2k_B T}\right) + \frac{4k_B T}{ze} . e^{-\kappa_m d} \tanh \frac{ze\zeta}{4k_B T} \tag{S6}$$

$$f\left(\frac{d}{a}\right) = \frac{2}{3}\left[1 + \frac{1}{2(1+d/a)^3}\right] \tag{S7}$$

$$\kappa_m = \kappa\left[\cosh\left(\frac{ze\psi_{DON}}{k_B T}\right)\right]^{1/2} \tag{S8}$$

where k_B is Boltzmann's constant, T is absolute temperature, and κ is the Debye-Hückel parameter of the solution. Use of the Ohshima method requires data for the electrophoretic mobility for both the bare particles and for the polyelectrolyte-coated particles as a function of the bulk solution ionic strength.

A MATLAB (the Mathworks, Novi, MI) code employing iterative least squares minimization was used for this fitting the EM data. Ohshima's model was used to fit the mean u_e, mean $u_e+\sigma$, and mean $u_e-\sigma$ as a function of ionic strength to obtain three best-fit values of each fitting parameter ($1/\lambda$, N, and d). The average and standard deviation of the fitting parameters determined for the mean u_e, mean $u_e+\sigma$, and mean $u_e-\sigma$ was calculated and reported in Table S1. It should be noted that this procedure is not meant to convey the goodness of fit of the data, rather it is used to bound the range of the magnitude of each parameter *(12-14)*.

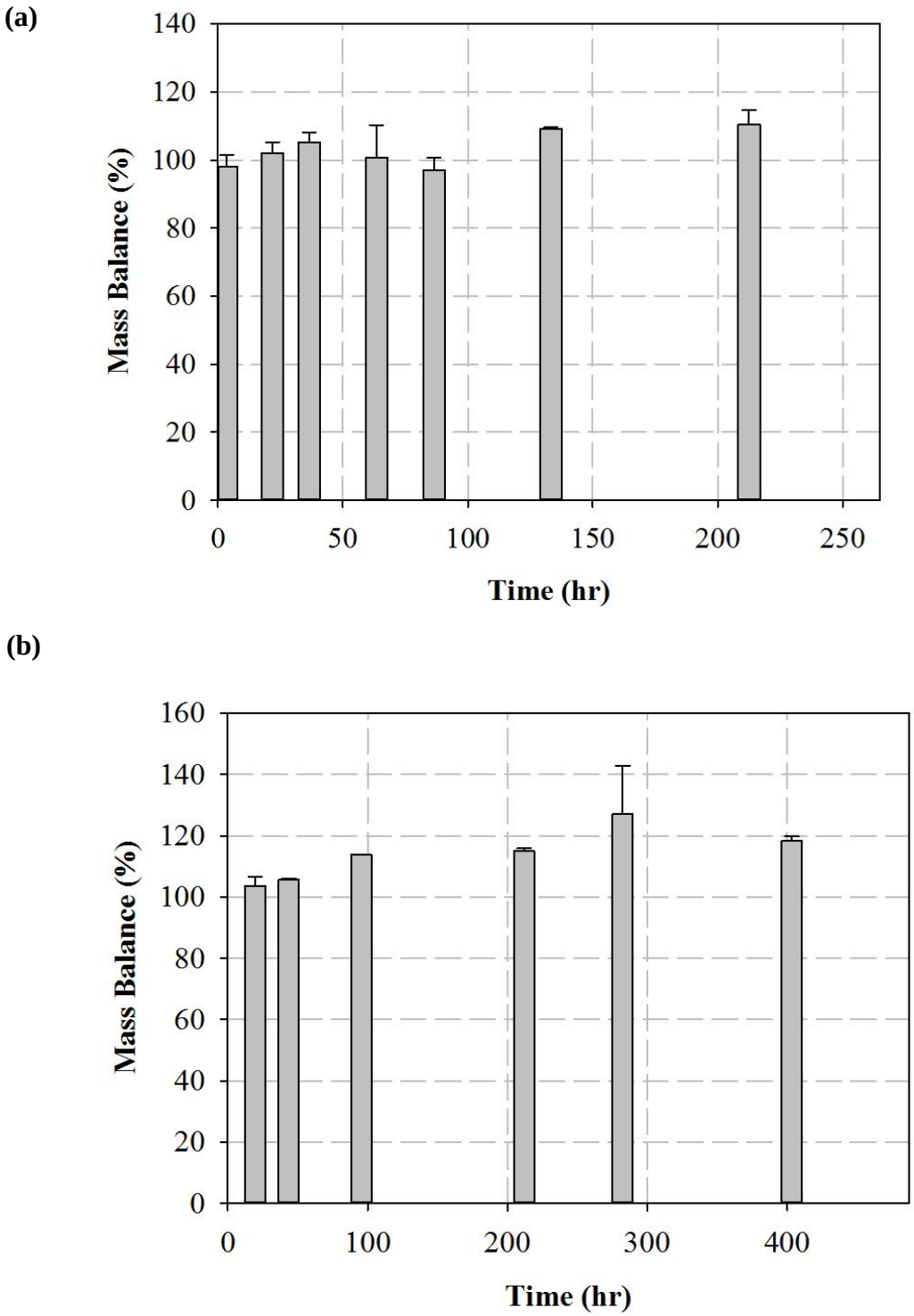

FIGURE S2. Representative mass balance of TCE dechlorination studies for (a) bare NZVI in FL and (b) PAP-NZVI in FL.

Environ Sci Pollut Res
DOI 10.1007/s11356-015-5193-0

ADVANCES IN ENVIRONMENTAL CHEMISTRY OF POLLUTANTS

Modified MODFLOW-based model for simulating the agglomeration and transport of polymer-modified Fe^0 nanoparticles in saturated porous media

Peyman Babakhani[1] · **Fritjof Fagerlund**[2,3] · **Abolfazl Shamsai**[1,4] · **Gregory V. Lowry**[5] · **Tanapon Phenrat**[6,7]

Received: 19 March 2015 / Accepted: 10 August 2015

Abstract The solute transport model MODFLOW has become a standard tool in risk assessment and remediation design. However, particle transport models that take into account both particle agglomeration and deposition phenomena are far less developed. The main objective of the present study was to evaluate the feasibility of adapting the standard code MODFLOW/MT3D to simulate the agglomeration and transport of three different types of polymer-modified nanoscale zerovalent iron (NZVI) in one-dimensional (1-D) and two-dimensional (2-D) saturated porous media. A first-order decay of the particle population was used to account for the agglomeration of particles. An iterative technique was used to optimize the model parameters. The model provided good matches to 1-D NZVI-breakthrough data sets, with R^2 values ranging from 0.96 to 0.99, and mass recovery differences between the experimental results and simulations ranged from 0.1 to 1.8 %. Similarly, simulations of NZVI transport in the heterogeneous 2-D model demonstrated that the model can be applied to more complicated heterogeneous domains. However, the fits were less good, with the R^2 values in the 2-D modeling cases ranging from 0.75 to 0.95, while the mass recovery differences ranged from 0.7 to 6.5 %. Nevertheless, the predicted NZVI concentration contours during transport were in good agreement with the 2-D experimental observations. The model provides insights into NZVI transport in porous media by mathematically decoupling agglomeration, attachment, and detachment, and it illustrates the importance of each phenomenon in various situations.

Responsible editor: Marcus Schulz

Highlights
- The standard code MODFLOW/MT3D was adapted to simulate the agglomeration and transport of polymer-modified NZVI.
- Simulations accurately predicted the transport and deposition patterns in both one-dimensional homogeneous and two-dimensional heterogeneous saturated porous media.
- All of the mechanisms incorporated in the model, i.e., agglomeration, attachment, detachment, and irreversible deposition, corresponded to the model results quantitatively and qualitatively.
- The model conserved the mass and predicted the sizes of the aggregates.

Electronic supplementary material The online version of this article (doi:10.1007/s11356-015-5193-0) contains supplementary material, which is available to authorized users.

✉ Tanapon Phenrat
pomphenrat@gmail.com

[1] Department of Hydrology Engineering, Tehran Science and Research Branch, Islamic Azad University, Tehran, Iran

[2] Department of Earth Sciences, Uppsala University, Villavägen 16, 75236 Uppsala, Sweden

[3] Center for Experimental Study of Subsurface Environmental Processes, Colorado School of Mines, Golden, CO, USA

[4] Department of Civil Engineering, Sharif University of Technology, Tehran, Iran

[5] Center for Environmental Implications of Nanotechnology (CEINT) and Department of Civil and Environmental Engineering, Department of Chemical Engineering, Carnegie Mellon University, Pittsburgh, PA 15213-3890, USA

[6] Research Unit for Integrated Natural Resources Remediation and Reclamation (IN3R), Department of Civil Engineering, Faculty of Engineering, Naresuan University, Phitsanulok 65000, Thailand

[7] Center of Excellence for Sustainability of Health, Environment and Industry (SHE&I), Faculty of Engineering, Naresuan University, Phitsanulok 65000, Thailand

Published online: 25 August 2015

Keywords NZVI · Transport · Aggregation · Numerical simulation · MODFLOW · Saturated porous media

Introduction

Groundwater and soil remediation can benefit from the use of nanotechnology. In situ chemical reduction (ISCR) using polymer-modified nanoscale zerovalent iron (NZVI) has been used to rapidly dechlorinate organic contaminants (He et al. 2010; Phenrat et al. 2009b) and to immobilize heavy metals (Boparai et al. 2011; Li et al. 2008) in contaminated soils and aquifers. According to the US Environmental Protection Agency (EPA) (U.S. EPA 2011), by the end of 2011, nanotechnology-enabled remediation alternatives were employed in 36 pilot and full-scale remediation projects. Of these sites, 85 % used NZVI-based technologies, such as polymer-modified NZVI, emulsified zerovalent iron, and bimetallic nanoparticles (NPs). For field-scale applications, attaining a thorough understanding of the fate and transport of the Fe^0-based NPs prior to performing remediation is necessary to determine how best to deliver the Fe^0-based NPs to the targeted treatment area. Such an understanding is also required to evaluate the possibility of the unintended migration of Fe^0-based NPs to nearby drinking water resources (Keane 2009). Thus, the research community has conducted many experimental studies on NZVI transport in porous media, ranging in scale from laboratory (Kim et al. 2009; Phenrat et al. 2009a, 2010a; Sirk et al. 2009) to pilot-scale demonstrations (Johnson et al. 2013; Su et al. 2012). Nevertheless, there remains a need for a comprehensive three dimensional (3-D) model that captures all of the important characteristics of NZVI transport (including agglomeration, deposition/re-entrainment, advection, and dispersion).

To date, most of the studies concerned with NP transport simulations have modified conventional colloid filtration theory (CFT) to incorporate the site-blocking effects (Bradford et al. 2003, 2006, 2007) of NPs, such as NZVI (Hosseini and Tosco 2013; Raychoudhury et al. 2014; Tosco and Sethi 2010), fullerene (Wang et al. 2008, 2010), carbon nanotubes (Cullen et al. 2010; Mattison et al. 2011; Wang et al. 2012b), silver NPs (Taghavy et al. 2013), and silica NPs (Wang et al. 2012a). However, the agglomeration of particles during transport has not typically been considered extensively in transport simulations, even though it is a critical mechanism that affects the transport and fate of NPs, such as NZVI (Kocur et al. 2013; Krol et al. 2013; O'Carroll et al. 2013; Petosa et al. 2010; Phenrat et al. 2007, 2009a, 2010b; Tosco and Sethi 2010), TiO_2 (Chen et al. 2011, 2012; Chowdhury et al. 2012b), CeO_2 (Quik et al. 2014, 2015; Velzeboer et al. 2014) and other iron-based NPs (Hong et al. 2009) that are subject to magnetic interaction forces. Including agglomeration in an NZVI transport model is necessary because despite numerous attempts to prevent the agglomeration of NZVI by, for instance, entrapping NZVI in a silica matrix (Zhan et al. 2008, 2011) or modifying the surfaces (e.g., using a polymer coating) (Phenrat et al. 2008; Saleh et al. 2005), the largest NZVI aggregates are not stabilized by any modifier, resulting in agglomeration during transport in porous media (Phenrat et al. 2008, 2009a).

Very few studies have attempted to simulate NZVI agglomeration during its transport in porous media. Initially, Phenrat et al. (2010b) developed an empirical correlation based on a wide range of one-dimensional (1-D) column transport data to predict the sizes of aggregates, and they also modified the attachment and contact efficiencies to take account of the subsequent deposition of aggregates. Raychoudhury et al. (2012) combined the Smoluchowski equation for aggregation along with the CFT in an advection–dispersion equation to simulate the aggregation and transport of polymer-modified NZVI. However, they did not explicitly obtain the particle–particle attachment efficiency in flow-through porous media. Instead, they determined aggregation kinetic parameters from static batch experiments and used them for fitting the model to the breakthrough data. In flow-through porous media, however, several other hydrodynamic phenomena including advection, shear force, and re-entainment can also affect agglomeration, whereas in batch experiments designed to fit the Smoluchowski model, only particle–particle collision frequency and efficiency in a static environment govern agglomeration (Phenrat et al. 2007). The significance of the difference between static laboratory-based studies with those conducted in a real dynamic environment was highlighted by Dale et al. (2015). In addition, Raychoudhury et al. (2012) used the Smoluchowski approach (Smoluchowski 1917), which is only applicable for the initial stage of the aggregation process when the collisions can be considered as binary (Elimelech et al. 1998). Following that paper, Taghavy et al. (2015) recently used the Smoluchowski equation and CFT in a completely Lagrangian approach based on random-walk particle tracking to simulate the concurrent aggregation and transport of NZVI. Although they tackled the problem of binary collision in their probabilistic modeling approach, the aggregation in that study was still limited to perikinetic aggregation, which is only the case when the particles are very small (only valid in the initial stage of aggregation) (Elimelech et al. 1998; Taghavy et al. 2015). However, other mechanisms of aggregation, e.g., orthokinetic aggregation and differential sedimentation, can be significant in environmentally relevant conditions (Quik et al. 2014; Risovic and Martinis 1994). It should be clarified that the perikinetic mechanism of aggregation is caused by the Brownian

motion of particles. Any motion or flow in a fluid can cause shear force in the fluid and thus lead to orthokinetic aggregation. Differential sedimentation is another mechanism of aggregation that occurs when the particle sizes are different. Because larger particles settle faster than the smaller ones, they will collide with small particles in their paths and induce aggregation (Elimelech et al. 1998). Especially in porous media, an orthokinetic mechanism cannot be neglected because pore water velocity always exists. However, the solution to a particle–balance model for all the mechanisms of aggregation together with the sedimentation or deposition simultaneously, as a partial integro-differential equation, has long been known to be difficult (Hunt 1982; Risovic and Martinis 1994). Thus, either simplifying assumptions, such as single mechanism operation at a time or self-similarity or other techniques such as dimension analysis or Monte Carlo method (Friedlander 1960a, b; Hunt 1982; Jeffrey 1981; Liu et al. 2011; Risovic and Martinis 1994; Sobkowicz 2006) have been adopted to cope with this problem.

Additionally, a Lagrangian approach, used in the study by Taghavy et al. (2015), poses a limitation on using an inverse model (auto-calibration model). Moreover, the Smoluchowski aggregation model used in the two aforementioned studies classifies the population of aggregates into a series of families based on their sizes. This kind of model can be computationally challenging for a simple 1-D homogeneous medium, and it is potentially intractable for 2-D and 3-D simulations in heterogeneous domains (Cornelis 2015; Dale et al. 2015). Recognition of the agglomeration phenomena in porous media has thus far been problematic from both experimental and modeling perspectives. From the experimental perspective, the problem originates from the lack of an appropriate sampling protocol for observing the extent of growth in particle size inside the porous media (Phenrat et al. 2009a). Moreover, from the modeling perspective, a special algorithm is needed to optimize the agglomeration parameter together with the parameters of nanoparticle transport in porous media simultaneously; to the best of our knowledge, this has not been performed in the literature.

In addition to neglecting agglomeration, the detachment of NPs is assumed to be negligible in most of the modeling studies of NP transport in porous media (Chowdhury et al. 2012a; Kocur et al. 2013; Krol et al. 2013; Mattison et al. 2011; Wang et al. 2008, 2010, 2012a, b). Many of these studies ignored detachment by observing a lack of breakthrough curve tailing (Krol et al. 2013; Wang et al. 2012a). However, detachment was reported to be an operative mechanism in the transport of polymer-modified NZVI (Phenrat et al. 2009a, 2010b; Raychoudhury et al. 2012, 2014; Tosco and Sethi 2010) as well as other colloids (Grolimund and Borkovec 2001, 2006; Johnson et al. 2007; Landkamer et al. 2013; Schijven and Hassanizadeh 2000).

NZVI transport modeling is needed for effective remediation design and implementation. Nevertheless, particle transport models are far less developed and much less available to remediation researchers and practitioners than solute transport models such as MODFLOW, which has become an effective tool for risk assessment and remediation design. The goal of the present study was to evaluate whether a MODFLOW-based model, with a generic advection-dispersion-reaction (ADR) equation, can be modified to account for all the processes affecting the transport of polymer-modified NZVI, including advection, dispersion, attachment, detachment, and agglomeration. If applicable, this approach, owing to the use of standard MODFLOW modules, can potentially provide simplified NZVI modeling to remediation practitioners and researchers who are already familiar with MODFLOW. Although MODLFOW, MT3DMS, and SEAWAT have all been modified to account for nanoparticle transport, attachment, and detachment in both constant and variable density flow scenarios (Bai and Li 2012; Becker et al. 2015a, b), none of the these studies have considered agglomeration phenomena together with other mechanisms of transport.

The proposed model was tested against a wide range of experimental data from 1-D and 2-D transport studies to illustrate the applicability of the model at various scales and conditions. Our model does not explicitly consider the interfacial forces acting on the surface of particles, i.e., forces related to the extended DLVO theory described previously (Phenrat et al. 2009a); however, it considers the change in the population and size of particles in addition to the tendency of particles and aggregates to agglomerate and deposition under different conditions. We analyzed whether the numerical values of the fitting parameters representing transport phenomena made physical sense according to the transport conditions and the concept of NZVI agglomeration and its subsequent deposition. The model's benefits and limitations are also discussed.

Theoretical and conceptual model

This section describes the modification of MOFLOW for NZVI transport simulation. The advection-dispersion-reaction (ADR) equation is used to simulate common mechanisms of solute and colloid transport in porous media. Simulation of NZVI transport needs to account for three more mechanisms as described as follows: (1) the attachment/detachment process, that is, the exchange between the fluid and deposited phases; (2) the agglomeration of particles in the fluid phase; and (3) the irreversible deposition of aggregates. The attachment/detachment processes (mechanism #1) are represented by a first-order, reversible, kinetic-reaction

(FRK) equation. The agglomeration of particles in the fluid phase (mechanism #2), which leads to a decay in the particle population, is introduced in the ADR equation using a pseudo first-order irreversible reaction term on the condition that the concentration variable in the ADR equation is expressed in terms of the particle number concentration instead of the mass concentration. Finally, the irreversible deposition of particles (mechanism #3) is accounted for by adding another sink term for the solid-phase concentration of the ADR equation to diminish the population of the deposited, detachable particles. According to the thorough extended DLVO analysis that considered the electrosteric repulsive forces (a combination of steric repulsion and electrostatic repulsion), as well as the magnetic forces and other DLVO forces investigated in former studies (Phenrat et al. 2009a, b), irreversible deposition can occur as a result of an increase in the size of the particles due to agglomeration. For example, an increase in size from 25 to 367 nm resulted in an increase in the secondary minimum well by four orders of magnitude (Phenrat et al. 2009a). This caused an increase in the tendency toward attachment at the primary minimum or deep secondary minimum; particle re-entrainment is less likely for such deposition (Johnson et al. 2007; Landkamer et al. 2013; Phenrat et al. 2009a).

Overall, the model for NZVI transport and agglomeration has the capability to consider the attachment—either reversible or irreversible—for any particle of any size to the porous media surfaces. It should be mentioned that from the three mechanisms described previously, mechanisms 1 and 3 have already been added to the MODFLOW/MT3DMS simulator in a different way in the literature (Bai and Li 2012; Becker et al. 2015a, b). Notably, most of the modeling studies on NP transport (e.g., Bai and Li 2012; Becker et al. 2015a; Li et al. 2008; Wang et al. 2008, 2014) have considered a site-blocking formulation along with the CFT model to take account of the limited capacity of available sites for retention of NPs. However, we did not consider this type of formulation in our model for several reasons. First, site-blocking phenomena have not been commonly observed for NZVI in the literature (see, e.g., Phenrat et al. 2010a). Second, a long and low slope shape of the left side (rising limb) of a breakthrough curve that is noticeable in most of the breakthrough curves of the related literature cited previously is not discernible in NZVI breakthrough curves. Third, a recent study (Goldberg et al. 2014) comparing seven types of particle transport models for breakthrough and retention curve simulations recommended that incorporating the site-blocking mechanism in the model should be performed only when the experimental evidence of this mechanism within the column test has been provided. Further discussion of the conceptual model is presented after the mathematical introduction of the model and in the Supplementary Materials (SM). The following modified ADR and FRK equations are used to capture all of the aforementioned processes:

$$\frac{\partial N}{\partial t} + \frac{\rho_b}{\varepsilon}\frac{\partial \overline{N}}{\partial t} = D\frac{\partial^2 N}{\partial x^2} - V\frac{\partial N}{\partial x} - \lambda_1 N - \lambda_2 \frac{\rho_b}{\varepsilon}\overline{N} \tag{1}$$

$$\frac{\rho_b}{\varepsilon}\frac{\partial \overline{N}}{\partial t} = K_{att}N - \frac{\rho_b}{\varepsilon}K_{det}\overline{N} \tag{2}$$

where N [with a dimension of L^{-3}] and $\overline{N}$ [with a dimension of M^{-1}] are the particle number concentrations of fluid-phase particles and deposited particles, respectively, V is the interstitial particle velocity, D is the hydrodynamic dispersion coefficient; ε is the bed porosity, ρ_b is the porous medium bulk density, λ_1 is the pseudo-first-order reaction rate [T^{-1}], which stands for the decay in population of particles due to agglomeration (mechanism #2), λ_2 is the pseudo-first-order reaction rate [T^{-1}], which stands for the decay in the population of deposited, detachable particles and represents irreversible deposition (mechanism #3), and K_{att} and K_{det} are the attachment and detachment rate constants [T^{-1}], respectively (mechanism #1). It should be noted that, throughout this paper, the word particles refers to both primary particles and agglomerates (clusters), which are differentiated by size.

While the concentration variable in Eqs. (1) and (2) is expressed in terms of the particle number concentration, it may be more convenient in many situations to work with the mass concentration. Mass concentration data from laboratory and field measurements are typically more readily available than particle number concentration data. In addition, widely used flow and transport models, such as MODFLOW/MT3D, are also based on the mass concentration. Furthermore, a recent study of the transport of NPs (Wang et al. 2012a) implied that different interpretations can occur when either mass or particle number concentrations are used. Hence, it is useful to be able to convert the particle number concentration to the mass concentration. To accomplish this, the following two equations are used:

$$N = \frac{C}{\frac{4}{3}\pi r^3 \rho_{fe}} \tag{3}$$

$$\overline{N} = \frac{\overline{C}}{\frac{4}{3}\pi \overline{r}^3 \rho_{fe}} \tag{4}$$

where C is the mass concentration of fluid-phase particles [ML^{-2}], $\overline{C}$ is the mass concentration of deposited-phase particles [MM^{-1}], r and $\overline{r}$ are the average radii of particles in the fluid phase and deposited phase, respectively, and ρ_{fe} is the average density of the particles or aggregates. It should be noted that assuming the shape of the particles or agglomerates in Eqs. (3) and (4) to be spherical is a common assumption for

polymer-coated NZVI particles (Raychoudhury et al. 2012; Taghavy et al. 2015). Moreover, this assumption is expected to pose no significant effect on the modeling results of this study, as a recent study (Seymour et al. 2013) of the influence of colloid shape over transport behavior indicates that the reason for the marked difference between the attachment rate trends of spherical and rod-shaped particles is due to ripening and blocking phenomena (Pan and Xing 2012), which were not the subjects of the present modeling study. After inserting Eqs. (3) and (4) into Eqs. (1) and (2), there were four variables in the resulting equations: C, $\overline{C}$, r, and $\bar{r}$. To solve the equations for these unknowns, two additional equations were required, one of which was obtained by considering that the change in the particles' radii is governed by agglomeration. Since Eq. (1) assumes that the population of particles decays at a rate of λ_1 due to agglomeration, we considered a pseudo first-order reaction equation to represent the agglomeration process:

$$\frac{\partial N}{\partial t} = -\lambda_1 t \tag{5}$$

Integrating Eq. (5) with the initial condition that $N=N_0$ at $t=0$ yielded:

$$N = N_0 e^{-\lambda_1 t} \tag{6}$$

Then, by inserting Eq. (3) into Eq. (6), the following equation was obtained to account for the change in the average particle radius due to agglomeration:

$$r = r_0 \sqrt[3]{e^{\lambda_1 t} \frac{c}{c_0}} \tag{7}$$

where r_0 is the average radius of particles (or agglomerates) at $t=0$ and C and C_0 are the mass concentrations of fluid-phase particles at a given t and $t=0$, respectively. Similarly, a first-order formulation was suggested by Baalousha (2009) to disaggregate the aggregates. This formulation was subsequently modified by Kocur et al. (2013) to simulate the NZVI agglomeration in the inlet reservoir of their column experiment. It should be mentioned that Eq. (7) was developed solely based on agglomeration, and that the parameter C/C_0, which emerged in this equation, must be assumed to equal unity because the change in the mass concentration cannot reflect any agglomeration effect. Additional clarification of this assumption, together with an investigation of an alternative assumption, is introduced in the SM.

As for this second additional equation, it was assumed that the radius of the suspended particles is equal to the radius of the deposited, detachable particles. This simplified assumption is used because particles are continually being exchanged between the suspended phase and the deposited, detachable phase, considering the fact that those particles that are irreversibly attached behave as if they were eliminated from the system (a typical assumption of perfect sink models) (Ryan and Elimelech 1996).

Ultimately, three equations remaining to be solved simultaneously include the ADR and FRK equations and Eq. (7). In laboratory particle transport experiments, the transport parameters related to attachment and agglomeration (K_{att}, K_{det}, λ_1, and λ_2) are typically unknown. Therefore, an iterative procedure was developed to optimize these parameters with respect to the observed concentration data. Identifying these parameters provides information about the agglomeration and attachment/detachment processes in the system. Furthermore, if no conclusive values for the proposed model parameters can be found by this procedure, it implies that the model does not capture the complexity of the experimental system. Therefore, the parameter estimation also serves as an evaluation of the appropriateness of the model under different experimental conditions. In summary, the observation data initially are in terms of the mass concentration; thus, the model fits these data to obtain the parameters. However, among the obtained parameters, λ_1 is not correct yet because it still does not reflect aggregation. Therefore, Eq. (7) is used to calculate the size of aggregates, and subsequently, Eq. (3) is used to calculate the population of aggregates (transformation of the mass concentration to the particle number concentration). Then, these transformed observation data are employed to recalibrate λ_1 again. This procedure is iterated until the difference in λ_1 between two successive iterations is negligible (<1 %). The full details of the iterative procedure steps are presented in the "Model implementation" section.

Instead of the conventional Smoluchowski model of aggregation, which is based on a second-order rate mechanism (Elimelech et al. 1998), here, a pseudo-first-order model was applied. This approach was already used for modeling the heteroaggregation of nanoparticles with natural colloid (Praetorius et al. 2012) based on this assumption that the population of the large-size category of particles was almost constant during the aggregation process. Such an assumption is deemed to be reasonable for modeling homoaggregation of polymer-modified Fe^0 nanoparticles in porous media because of the local dynamic equilibrium (Friedlander 1960b) existing for these NPs in the porous media. Based on this assumption, the description of which follows in this paragraph, we consider the dispersion of polymer-modified NZVI to be dominated by one population of particles, either large, small, or medium, and this population remains almost constant during aggregation for every cases so that the assumption of pseudo-first-order model can always be applicable. Thus, we first consider two extreme cases in which the population is either dominated by small particles or by large particles, and eventually, we will develop this assumption to the intermediate cases. According to previous experimental investigations (Phenrat et al. 2009a, 2010a, b), when the population is dominated by small

particles but the collision number of small particles (both with each other and with porous media surfaces) is high because of Brownian diffusion, not all collisions of small particles lead to agglomeration (or deposition), owing to the electrosteric repulsion resulting from the polymer coating. Thus, the reduction in the population of small particles is not substantial. Therefore, in this spectrum of particle size distribution, agglomeration occurs owing to the collision of small particles with large existing particles, suggesting that the population of small particles is constant because of the high proportion of the small particle number compared to that of the large ones and also the vulnerability of the population of large particles caused by irreversible deposition. On the other hand, when the population is dominated by large particles, the agglomeration is much faster than the previous case because of the increase in the magnetic attractive force with the sixth power of size. This leads to an increase in the number of large-sized agglomerates. However, in this case, the irreversible deposition is also more pronounced, as shown previously (Phenrat et al. 2009a, 2010b), resulting in an almost constant population for large particles. This assumption of dynamic equilibrium, also known as self-similarity of the particle size distribution, was originally developed by Friedlander (1960a, b) for aerosol and later applied to hydrosol (Hunt 1982; Jeffrey 1981). It should be mentioned that for the case in which the population of medium-sized particles is dominant, a tradeoff between the two aforementioned cases exists, and the population of the medium-sized particles compared to smaller forming particles and larger removing ones is still constant.

It should also be mentioned that although typically a second-order model is used to describe the aggregation process in the colloid literature (Elimelech et al. 1998; Holthoff et al. 1996; Szilagyi et al. 2014), there have been several studies which used a first-order formulation for aggregation (Baalousha 2009; Birkner and Morgan 1968; Kocur et al. 2013; Logan et al. 1995; Swift and Friedlander 1964). Here, however, we use a pseudo-first-order equation to describe the aggregation process in porous media according to the aforementioned assumption. However, the comparison of the results of different models is beyond the scope of this paper.

In order to reduce the computational burden in this study, the average particles size is considered instead of the particle size distribution. However, previous paper (Phenrat et al. 2009a) revealed that dispersions with different degrees of polydispersity have different aggregation and deposition behaviors compared with a monodisperse dispersion. Therefore, in order to investigate the impact of polydispersity as well as to evaluate various aforementioned hypotheses, the model is fitted against different breakthrough data sets obtained for dispersions with various degrees of initial polydispersity.

In addition to the assumption of dynamic equilibrium, the common assumption of two-body interactions (binary) is still made in this model. However, the assumptions of typical Smoluchowski model solutions regarding its mechanistic approach such as considering the single perikinetic aggregation governing only in the early stage of aggregation (Taghavy et al. 2015) or initially monodisperse dispersion (Holthoff et al. 1996; Szilagyi et al. 2014) are not the case in this model since any kind of collision can occur as a result of various mechanisms.

Materials and methods

NZVI breakthrough data

The model was fit against data sets consisting of 15 series of 1-D breakthrough data (Phenrat et al. 2009a; Raychoudhury et al. 2012), as well as four series of 2-D breakthrough data (Phenrat et al. 2010a) selected from the literature of polymer-modified NZVI. A brief description of these experiments is presented in the following.

In the 1-D experiments, Phenrat et al. (2009a) prepared three dispersions of polystyrene sulfonate (PSS)-modified reactive nano-iron particles (RNIPs) with different degrees of polydispersity (different particle size distributions). One dispersion, called F1, contained the highest amount of intrinsic aggregates (>100 nm); another dispersion, called F3, contained no significant amount of initial aggregates (>100 nm), and the third dispersion, called F2, was intermediate between F1 and F3. F1 was polydisperse with one peak at 45 nm (~11 % by volume) and another at 328 nm (~38 % by volume). F2 also had a bimodal particle size distribution with one peak of hydrodynamic size at 25 nm (~27 % by volume) and another at 367 nm (~2 % by volume). F3 was monodisperse with a single peak at the hydrodynamic size of 25 nm (~31 % by volume). The column was 25.5 cm long with an inner diameter of 1.27 cm and was packed wet with spherical silica sand with d_{50}=300 μm. The average porosity of the packed column was 0.33 with a constant pore water velocity of 3.2×10^{-4} ms^{-1} (Phenrat et al. 2009a, b). In this reference, all the slurry injections were conducted with a single pore volume (PV), followed by at least three PVs of flushing with a particle-free solution (1 mM $NaHCO_3$). In contrast, in the study by Raychoudhury et al. (2012), carboxymethyl cellulose (CMC)-modified NZVI (CMC-NZVI) was introduced through the column with multiple PV injections. Other experimental characteristics of that paper comprised a column with a length of 9 cm and an internal diameter (i.d.) of 1 cm, packed with silica sand with an average size of 375 μm and a porosity of 0.32. CMC-NZVI slurries, were injected at concentrations of 0.07, 0.2, and 0.725 g/L with a pore water velocity of 0.445 cm/min.

Additionally, the 2-D experiments of Phenrat et al. (2010a) were conducted by transporting NZVI modified by an olefin maleic acid copolymer (MRNIP2) through a 2-D flow cell

(30×18×2.5 cm) containing five layers: three of which were packed with fine sand (d_{50}=99 μm), one with medium sand (d_{50}=300 μm), and the other with coarse sand (d_{50}=880 μm). In addition to supplying a background groundwater flow through three side ports (with a total flow rate of 0.9 mL/min), an injection well was used to inject NZVI at a flow rate of 20 mL/min. The 2-D model data sets simulated in this study were for the transport of tracer data, MRNIP2 (unwashed) at a low particle concentration of 0.3 g/L, washed MRNIP2 at a high particle concentration of 6 g/L, MRNIP2 with excess free polymer (unwashed MRNIP2) at 6 g/L, and oxidized (and washed) MRNIP2 at 3 g/L (Phenrat et al. 2010a). Before performing the simulation of the NZVI transport and agglomeration in the 2-D model, the tracer data were utilized to calibrate the dispersivity parameters in different layers of the 2-D cell, as discussed with detail in the SM. It should be mentioned that although several studies (Krol et al. 2013; Tosco and Sethi 2010) emphasized the effect of viscosity on NZVI mobility, the viscosity measurements of polymer-modified NZVI at the applied concentrations used in the studies by Phenrat et al. (2009a, 2010a) showed that there were infinitesimal changes in the viscosity of the dispersions due to the added polymer. Furthermore, the amount of free polymer in MRNIP2 dispersions used in the 2-D models was ~3 wt% (Phenrat et al. 2010a), and the ~0.2 % ratio of the CMC concentration to the Fe^{2+} concentration (Raychoudhury et al. 2012) was far less than the values that were expected to affect the dispersion viscosity (Raychoudhury et al. 2014). Thus, we did not evaluate the effect of viscosity on NZVI agglomeration and deposition in the modeling in this study.

Model implementation

The public domain code MT3DMS (US Army Corps of Engineers, Washington, DC) (Zheng and Wang 1999) was applied to solve the ADR and FRK equations, the flow data of which were obtained by MODFLOW 2000 (U.S. Geological Survey, Denver, CO 80225-0425) (Harbaugh et al. 2000). WinPEST (Watermark Numerical Computing & Waterloo Hydrogeologic, Inc., Ontario, Canada) was used to calibrate the parameters of the ADR and FRK equations (Watermark Numerical Computing and Waterloo Hydrogeologic 1999). A further description of the applied models and software and the simulation characteristics, together with the goodness-of-fit criteria, is presented in the SM. In brief, the 1-D model was configured to have one row, one layer, and 130 columns (Fig. S1). A constant-flux boundary was used at the inlet of this model, while a constant head boundary was used at the outlet. The 2-D model grid was built to contain 101 columns, 62 layers, and 1 row (Fig. S2). An injection well with three filters was set as the inflow boundary condition introducing the background flow. Another injection well was placed in the model to simulate the injection port of material in the experiment. Finally, the outflow boundary was simulated using the drain boundary condition.

The two parameters of the MT3DMS model for nonequilibrium sorption, namely first-order mass transfer rate parameter (β) and distribution coefficient (K_d), were transformed into our model parameters (k_{att} and k_{det}) via the following expressions (Becker et al. 2015a):

$$k_{att} = \beta / \varepsilon \tag{8}$$

and

$$k_{det} = \beta / (\rho_b K_d) \tag{9}$$

In addition, the initial concentration and the concentration of all inflow boundary conditions were transformed from mass concentration into particle number concentration via Eq. (3), and the output results were translated back to the mass concentration via Eqs. (3), (4), and (7). Nevertheless, the calibration of the model requires a specific iterative algorithm which is described in the next section.

Iterative procedure for optimization of the parameters

The steps of the iterative algorithm for calibrating the parameters of the model are as follows:

i. First, assume that there is neither NZVI agglomeration nor irreversible deposition in the model's porous media; thus, the value of r would be equal to the value of r_0, which is equal to the average radius of the particles at time zero. Then, fit the standard numerical code to the observations, which are in terms of mass concentration, and obtain the parameters of the model (k_{att}, k_{det}, λ_1, and λ_2).
ii. Use Eq. (7) to calculate r with the λ_1 value obtained in the previous step; assume that t is equal to the average retention time of the particles in the model domain, and C/C_0 is equal to unity (or in an alternative approach calculated based on Eq. (S8) in the SM).
iii. Convert the inflow concentration and the concentration data observed at the outlet(s) from mass concentration to number concentration using Eq. (3) and the radius of particles (aggregates) obtained from the previous step.
iv. Fit the model output data (in number concentration) to the observed data, and optimize the parameters of the model using the WinPEST model.
v. Beginning at step II, iterate with the new values of λ_1 through step IV, until the difference in the values of λ_1 for two successive iterations becomes negligible.

As a convergence criteria for λ_1, a value of 1 % was considered to be sufficient because it induced a similar amount of

error in the estimated size of agglomerates which is relatively minor in comparison to other possible uncertainties of typical experimental and modeling procedures. In addition to the convergence for λ_1, we investigated the closure between the observation data and the renewed observation data based on the new parameters determined in each step of the iterative procedure. In this way, we obtained one R^2 value as a goodness-of-fit between two sets of data—the model output data after calibration in each step and the observation data—as well as another R^2 value for two sets of data—the model output data when updated based on the parameters of the model in that step and the observation data. The former R^2 value was always the maximum possible value that could be fitted by the model, whereas the latter R^2 value was poor at the initial stages of the iterative procedure but improved during the iterative procedure to reach the former R^2 value. This convergence between the observation data was monitored for the case in which it is not feasible to use λ_1 as a criterion for convergence, e.g., the model is heterogeneous, and there are several λ_1 parameters in different zones involved as fitting parameters. In all the simulated cases throughout this paper, an obvious closure was achieved between the R^2 values calculated before and after each iteration of the iterative process (Figs. S3–S8).

The iterative procedure used in the cases of 2-D modeling involved averaging the observations in terms of the particle number concentration for different zones. Although we fitted the model to the original breakthrough data obtained in the outlet of the experiment, it should be noted that there was only a single outlet for the whole 2-D cell, and the outflows of all sand layers were collected in that single outlet. Therefore, for converting the observation concentrations from mass to particle number concentration, it was necessary to average the observations obtained for the three different zones or vice versa in order to convert the observation concentrations from particle number concentration to mass; thus, averaging the parameters in the three layers was required. This was accomplished simply by calculating a weight for each layer considering their contribution to the simulation results, e.g., based on the amount of flow or mass entering each layer. The details of the averaging method are presented in the SM.

Results and discussion

1-D simulations of PSS-modified NZVI

Simulation of the 1-D model at a low particle concentration

At a low particle concentration (0.03 g/L), the model fit the data well, with R^2 in the range of 0.93–0.99 and P values ranging from 0.43 to 1.00 (Fig. 1a and b and Tables 1, S1 and S2). Initially, simulations were performed by fitting all four parameters, i.e., k_{att}, k_{det}, λ_1, and λ_2. However, in these cases, both λ_1 and λ_2 declined to lower bounds of the parameter threshold in the parameter estimation process, suggesting that agglomeration and subsequent irreversible deposition do not occur at a low concentration of PSS-modified NZVI. Excluding λ_1 and λ_2 from the parameter estimation process resulted in slightly better R^2 values, increasing from 0.934, 0.962, and 0.983 to 0.935, 0.964, and 0.984 for F1, F2, and F3, respectively (Tables S1 and S2). This suggests that the model of this study is not overparameterized (Goldberg et al. 2014) because, in terms of fitting, it shows the best goodness-of-fit for the lowest number of parameters, which is the same number with a counterpart CFT model (Raychoudhury et al. 2012). However, in the cases where the initial aggregates were pre-formed (i.e., F1 and F2), the correlation between the modeled and observation data did not passed the significance test at the 95 % confidence interval, as the p values were 0.001 and 0.011 for F1 and F2, respectively (Table S2). Thus, we allowed the parameter λ_1 to decline below zero (Table S2). Interestingly, the results of the fitting were improved markedly, with R^2 increasing to 0.983 and 0.970 for the cases of F2 and F1, respectively, while the p values reached 0.94 and 1.00 for the respective cases (Table S2). In these cases, the negative values obtained for λ_1 and the still negligible value obtained for λ_2 indicated that the net result of the agglomeration-disagglomeration process during transport is dominated by disagglomeration. It should be noted that the agglomeration process in this paper and Phenrat et al. (2009a) is assumed to be the net result of continuous agglomeration/disagglomreation processes which, depending on the particle characteristics as well as the geophysical, geochemical, and geohydrology conditions of the media, can be dominated by either agglomeration or disagglomeration. Interestingly, in this paper, among 12 cases of simulation for various concentrations and polydispersity statuses, it was revealed that in two cases of polydisperse dispersions (F1 and F2) at low particle concentration, the process is dominated by disagglomeration because at low particle concentration the number of particles and consequently the number of collisions are not high enough to accelerate the rate of agglomeration compared to the rate of disagglomeration in the agglomeration/disagglomreation process. The disagglomeration for polydisperse suspensions (F1 and F2) at low particle concentration under flow conditions is possible because the agglomerates had been pre-formed in a static environment and, thus, might subsequently be subjected to breakage under sheer force as the particles moved through the porous media. In this set of modeling, the sensitivity to parameter λ_1 rose by four orders of magnitude compared with the previous set (data not shown). This emphasizes the importance of the disagglomeration process at low NP concentrations and suggests that the injection of NZVI at low particle concentrations, in which disagglomeration rather than agglomeration occurs, may produce longer migration distances for the particles in

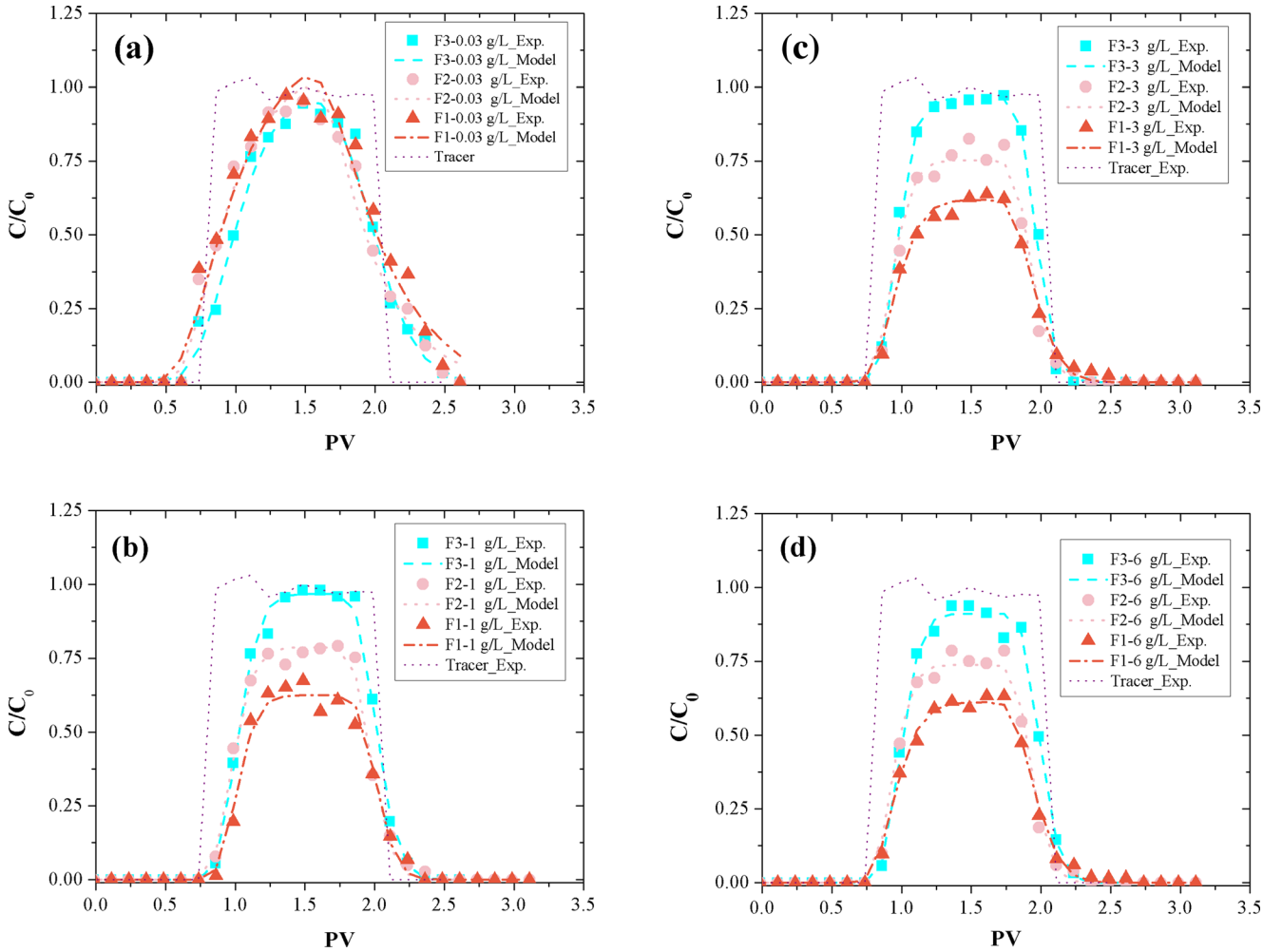

Fig. 1 Comparison of the experimental and modeled breakthrough curves of the 1-D model: **a** F3, F2, and F1 at the low concentration of 0.03 g/L; **b** F3, F2, and F1 at the high concentration of 1 g/L; **c** F3, F2, and F1 at the high concentration of 3 g/L; and **d** F3, F2, and F1 at the high concentration of 6 g/L. The *symbols* represent the experimental (Exp.) data, and the *lines* represent the modeled (Model) data. The experimental data were taken from Phenrat et al. (2009a), which had been conducted in columns (25.5 cm long with internal diameters of 1.02 cm) packed with spherical silica sand (d_{50}=300 μm) at a pore water velocity of 3.2× 10^{-4} m/s

field-scale projects, as demonstrated here by obtaining a negligible value for the irreversible deposition parameter, λ_2, in all cases. The greater mobility of small particles of polymer-modified NZVI in comparison with large aggregates was observed previously, which was attributed to the lower magnetic moment of the small particles relative to the larger ones (Phenrat et al. 2009a, 2010a, b). Overall, the modified model can, at a low NZVI concentration, effectively capture the major transport phenomena, deposition and detachment, and appropriately neglect agglomeration, as experimentally

Table 1 Simulation results for different cases of the 1-D model

	F3-0.03 g/L	F3-1 g/L	F3-3 g/L	F3-6 g/L	F2-0.03 g/L	F2-1 g/L	F2-3 g/L	F2-6 g/L	F1-0.03 g/L	F1-1 g/L	F1-3 g/L	F1-6 g/L
K_{att}	7.21E-03	2.08E-02	2.19E-02	2.29E-02	2.07E-03	1.80E-02	1.40E-02	1.60E-02	2.12E-03	2.46E-02	1.00E-02	1.05E-02
K_{det}	2.61E-02	6.65E-02	8.29E-02	7.87E-02	8.00E-03	6.38E-02	5.74E-02	6.65E-02	6.57E-03	7.59E-02	3.41E-02	3.61E-02
λ_1	–	2.62E-05	3.18E-05	6.96E-04	−1.28E-04	3.33E-04	5.24E-04	5.31E-04	−2.15E-04	8.66E-04	2.19E-03	9.11E-04
λ_2	–	1.31E-04	1.93E-04	3.98E-04	9.97E-06	1.10E-03	1.52E-03	1.64E-03	9.58E-06	1.89E-03	2.20E-03	2.27E-03
R^2	0.987	0.997	0.997	0.997	0.983	0.996	0.990	0.994	0.970	0.990	0.995	0.996
P-value	0.43	0.98	0.87	0.83	0.94	0.43	0.60	0.70	1.00	0.95	0.77	0.87

Parameter values for the high-concentration cases were obtained after satisfying the 1 %-convergence criterion for λ_1. The unit of all of the parameters is s^{-1}

observed. K_{att} and K_{det} were on the order of 10^{-3} s^{-1} and K_{det} was always around 3–4 times greater than K_{att}. This difference will be discussed later in this paper. Here, it should be noted that this is in accordance with previous experimental reports (Phenrat et al. 2009a, 2010b) in which the relative diluted mass from the column experiment (C/C_0) at low concentration of polymer-modified NZVI was always higher than 0.9.

1-D modeling simulations at high particle concentrations

According to Phenrat et al. (2009a), at low particle concentrations, F1, F2, and F3 dispersions are transported through porous media without particle agglomeration, whereas at high particle concentrations, agglomeration plays a substantial role in limiting NZVI transport. The degree of increase in particle deposition as a result of agglomeration was in the following order: F1 > F2 > F3, i.e., F1 was the greatest in aggregation and subsequent deposition followed by F2 and F3. The original study suggested that the limited NZVI transport was a combined effect of agglomeration, attachment, and irreversible deposition mechanisms. Nevertheless, it did not quantitatively analyze which mechanism played the greatest role.

The simulations for F1, F2, and F3 at high particle concentrations (1, 3, and 6 g/L) are presented in Fig. 1c–e and Table 1. The modified model effectively simulated the breakthrough curves in all cases. All of the fitting parameters were found to be significant, suggesting that agglomeration and subsequent deposition of the agglomerates was occurring, as expected for these higher particle concentrations. A convergence error criterion of 0.05 for the parameter λ_1 was satisfied after 3–11 iterations, and a convergence criterion of 0.01 was satisfied after 4–37 iterations (Table S3). Interestingly, K_{att} and K_{det} at high particle concentration cases were on the order of 10^{-2} s^{-1}, around one order of magnitude greater than they were at the low particle concentration (0.03 g/L). It is expected that the K_{att} and K_{det} values are proportional to the population of particles because there is a larger number of interactions with the sand surfaces as the number of particles increases (see the conceptual model description in the supplementary materials). K_{det} was around 3–4 times greater than K_{att} in every case, the same trend as observed at the low particle concentration. Noticeably, K_{att} and K_{det} decreased from F3 to F1 at the same particle concentration, suggesting that small monodisperse particles (F3) collided with and detached from the collectors more frequently than polydisperse particles (F2 and F1). This makes physical sense when considering the fact that F2 and F1 agglomerated at high particle concentrations and attached more irreversibly to sand grains, thereby reducing their total number concentration during the transport and resulting in less K_{att} and K_{det} values. On the other hand, F3 dispersion is less subjected to agglomeration and subsequent retention due to the existence of a less number of initial sintered aggregates in the dispersion (Phenrat et al. 2009a). This leads to the maintenance of the particle population during the transport of F3 dispersion, resulting in larger values for K_{att} and K_{det} because of larger number of interactions with sand surfaces.

Agglomeration (which results in decreases in the particle population) reduces the frequency of collisions, but every collision has a high attachment probability, as to be discussed subsequently when analyzing the λ_1 and λ_2 trends together with K_{att} and K_{det}. In "Deposition at high NZVI particle concentrations" and "Detachment at high particle concentrations" sections we will discuss each phenomenon (i.e., agglomeration, deposition, and detachment) separately. These analyses were not conducted in the study of Phenrat et al. (2009a) because it was not possible to quantitatively decouple the agglomeration, deposition, and detachment rates. Here, however, a distinctive parameter has been attributed to each phenomenon so that the role of each process can be quantified independently.

The impact of the agglomeration process at high NZVI concentrations λ_1 represents the agglomeration rate constant in each case. A comparison of the λ_1 values for F1, F2, and F3 at different particle concentrations indicates whether the modified model appropriately captures the agglomeration phenomenon. Noticeably, for each of the particle fractions (F1, F2, and F3), its λ_1 increased with the particle concentration (Table 1). This makes physical sense, as the agglomeration rate (λ_1) theoretically increases with the particle population. Furthermore, at the same particle concentration, the λ_1 trend was as follows: F1 > F2 > F3, which is in good agreement with the physicochemical properties of F1 dispersion, which has the greatest agglomeration tendency, followed by F2 and F3. This greatest agglomeration tendency is due to the fact that the increase in the magnetic force is proportional to the sixth power of the aggregate radius (Phenrat et al. 2009a). It should be noted that according to the initial particle size distribution (Phenrat et al. 2009a), the variation in the particle number concentration is not substantial among different dispersions of F1, F2, and F3 in comparison to that in the mass (volume) concentration—more than 98 % of the population in all the dispersions are related to the smaller peak in the number weighted particle size distribution (Phenrat et al. 2009a; see also Table S4 in the SM). The slight differences in particle number concentration between these cases even follow the order F3 > F2 > F1 (Phenrat et al. 2009a), which is in contrast with the trend obtained for λ_1, suggesting that the role of magnetic force in inducing the aggregation of NZVI in porous media is more pronounced than that of the particle number concentration.

Overall, for a given dispersion, e.g., F1, λ_1 decreases with decreasing concentration so that at very low concentration of 0.03 g/L, λ_1 becomes negative, showing that the process of

aggregation/disaggregation is governed by disaggregation. Furthermore, for a given concentration, e.g., 6 g/L—λ_1 decreases from dispersions with more initial large aggregates to dispersions with fewer initial large aggregates, even though the particle number concentrations of different dispersions are almost the same.

Deposition at high NZVI particle concentrations

K_{att} and λ_2 represent the characteristics of NZVI deposition. Discussing the K_{att} and λ_2 values for F1, F2, and F3 at different particle concentrations indicates how the model appropriately captures the deposition phenomenon.

When the concentrations were high, K_{att} ranged from 0.01 to 0.025 s^{-1} (Table 1), which is up to three orders of magnitude greater than the values reported in the literature (Johnson et al. 2007; Landkamer et al. 2013; Raychoudhury et al. 2014), which were typically estimated by CFT. The discrepancy between the results of the present study and the CFT values is presumably due to the fact that CFT does not model agglomeration and deposition. In the studies that have modified the CFT to capture the effect of agglomeration (Raychoudhury et al. 2012; Taghavy et al. 2015) or site-blocking phenomena (Bai and Li 2012; Becker et al. 2015a; Li et al. 2008; Wang et al. 2008, 2014), multiple values for the deposition parameter are obtained in various temporal and spatial points of model domain based on the variation of size with the growth of the particles, making it difficult to accurately compare their multiple deposition parameter values with our constant attachment and irreversible deposition parameters over the desired temporal period or spatial zone of the model domain. Moreover, this modified model separates the two major phenomena via the addition of λ_2 (see the verification of the necessity of λ_2 in the SM), which corresponds to the subsequent irreversible deposition of agglomerates. In effect, variations in the size of particles due to agglomeration account for the deviation from the CFT. CFT assumes that particles within porous media remain at a constant size and, therefore, it only considers one mode of deposition for all particles (Phenrat et al. 2009a). Meanwhile, in this study, relying on the extended DLVO analysis published previously (Phenrat et al. 2009a, b), we took into consideration the presence of two modes of deposition: one for the population of particles that reversibly attach to the collector surface (represented by K_{att} and K_{det}) and another for the population of particles that have grown sufficiently for irreversible deposition (represented by λ_2).

Conspicuously, at the same particle concentration, K_{att} values were in the following order: F3 > F2 > F1. However, this parameter only represents the collision of particles with the sand surfaces that either are going to rebound from or be temporarily retained on the porous material surfaces; this parameter does not account for permanent deposition. F1 had a lower number of interactions with porous media surfaces than F2 and F3 because after agglomeration, F1 had a smaller number of NZVI particles (aggregates) than F2 and F3, even though F1's clusters may have been larger in size. In contrast, at the same particle concentration, the trends for λ_2 values were in the following order: F1 > F2 > F3, indicating that although the total number of particles (aggregates) in the F1 dispersion during transport in the subsurface media is smaller than in F2 and F3, the number of large clusters that have a greater tendency for irreversible deposition (due to their deeper secondary minimum well; ~ −3500, −800, and −3 K_BT for larger aggregates in F1, F2, and F3, respectively) is larger than those in F2 and F3 (Phenrat et al. 2009a). This is in complete accordance with the conceptual model in the SM because when the number of particles is high, the K_{att} value is considerable (e.g., in the F3 dispersion), whereas when the tendencies for aggregation and irreversible retention due to the large size of aggregates are high, λ_1 and λ_2 values are significant (e.g., in the F2 and F1 dispersions).

Detachment at high particle concentrations

K_{det} represents the detachment rate constant in each case. The simulation results for K_{det} in the cases of high-concentration dispersions ranged from 0.034 to 0.083 s^{-1}. Similar to the trend observed for K_{att} at the same particle concentration, K_{det} values were predominately in the order: F3 > F2 > F1, in agreement with DLVO secondary minimum (particle collector) calculated for large particles in F1 and F2 dispersions to be 4 orders of magnitude larger than that in F3 dispersion (Phenrat et al. 2009a). This confirms that a larger number of interactions (attachment and release) occurs for the dispersions that contain a negligible number of large aggregates and predominately contain <100-nm particles. It is interesting to mention that by decreasing the size of particles, Brownian motion (considered both in CFT and the new modeling approach of this study) leads to higher particle mobility and transport to the collector surface. CFT considers this effect in the parameter contact efficiency (η_0) (Tufenkji and Elimelech 2004), while our modeling approach reflected this effect in K_{att} and K_{det} together. It should be noted that similar to our model, CFT also needs an additional parameter to take account of detachment (Raychoudhury et al. 2012, 2014); thus, it has a similar number of parameters with our model. Additionally, in CFT, the fraction of particles retained at the collector surfaces is accounted for by the attachment efficiency, whereas our model accounts for it via λ_2, a sink term in the population of already attached particles. The detachment mechanism has been neglected in a large number of NP transport studies (e.g., Chowdhury et al. 2012a; Cullen et al. 2010; Kanel et al. 2007; Kocur et al. 2013; Mattison et al. 2011; Wang et al. 2010, 2012b). However, this study reveals that detachment is an important mechanism in the transport of polymer-modified NZVI because the detachment rates are

higher than the attachment rates in all the cases of the simulation of Phenrat et al. A detachment rate greater than the attachment rate has been already observed for polymer-modified NZVI (Raychoudhury et al. 2014) and other colloids (Bradford et al. 2002, 2003; Schijven and Hassanizadeh 2000). However, the next section demonstrates that a detachment rate greater than the attachment rate is not always the case, as it is also governed by the physicochemical characteristics of the polymer-modified NZVI (Raychoudhury et al. 2012).

1-D Simulation of CMC-modified NZVI

To simulate another kind of polymer-modified NZVI with continuous injection condition, the transport data of carboxymethyl cellulose-modified NZVI (CMC-NZVI) through sand-packed columns were used (Raychoudhury et al. 2012). The results of this suite of simulations, presented in Fig. 2 and Table 2, are in overall agreement with the aggregation/deposition model of Raychoudhury et al., as well as with previous simulations in this study. In addition, in the case of low concentrations of CMC-NZVI, the model in this study performed even better than the modified CFT model of Raychoudhury et al. (Fig. 2). This indicates that the proposed rate equation-based model of our study is promising for a variety of polymer-modified NZVI types and injection conditions.

Although, as mentioned already, it is difficult to compare the parameters resulting from the current simulation with those of Raychoudhury et al. (2012) because of multiple values of K_{dep} parameters in the model of that study, we roughly calculated and averaged the values of the K_{dep} based

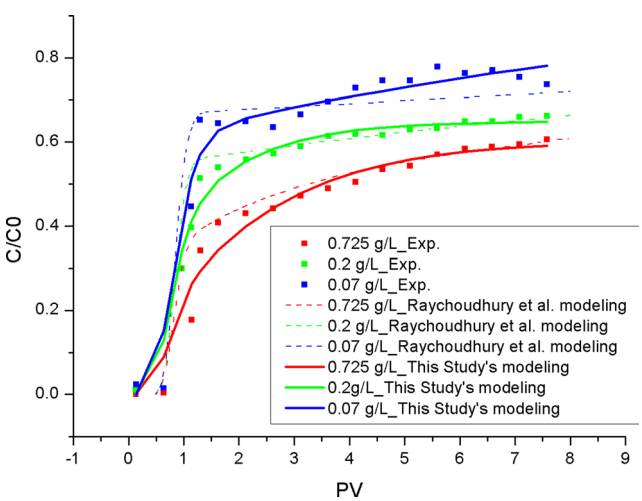

Fig. 2 Modeled breakthrough curves of CMC-NZVI transport data from Raychoudhury et al. (2012) at different concentrations (0.07, 0.2, and 0.725 g/L). *Points* represent experimental data, (Exp.), *dashed lines* show the simulation results of Raychoudhury et al., and the *solid lines* represent the simulation results of the current study. Data were obtained from Raychoudhury et al. (2012) with permission from Elsevier

Table 2 Simulation results for continuous injection of CMC-NZVI

	C0=0.725 g/L	C0=0.2 g/L	C0=0.07 g/L
K_{att}	1.50E-03	8.42E-04	4.29E-04
K_{det}	4.70E-04	3.84E-04	9.11E-05
λ_1	2.17E-04	2.11E-04	2.21E-08
λ_2	2.33E-04	3.95E-04	1.14E-05
R^2	0.961	0.971	0.959
P-value	0.61	0.54	0.69
Growth in size (nm)	9	8	–

Parameter values for the high-concentration cases were obtained after satisfying the 1 %-convergence criterion for λ_1. The unit of all the parameters is s^{-1}

on their modeling results in order to compare them with the K_{att} values in this study. This comparison showed that K_{att} values in our study are lower than the deposition rate coefficient (K_{dep}) from the CFT model by 10, 17, and 41 % at 0.725, 0.2, and 0.07 g/L, respectively. In contrast, the K_{det} values in this study are larger than those resulting from the CFT model by 82, 78, and 8 % at 0.725, 0.2, and 0.07 g/L, respectively. These differences may emanate from the existence of a distinct parameter, λ_2, in the current model, which accounts for permanent deposition, or different approaches used in modeling agglomeration in the two studies. It should be indicated that using a first-order rate model for attachment in our study and Raychoudhury et al. (2012) does not imply that the determined parameter values must be the same in the two models because a different applied approach in other phenomena results in two completely different models. However, we compared our results with the modeling results of that study because that was the most similar modeling approach to this study's approach. In the case of 0.07 g/L, the simulated and experimental data in Fig. 2 reveals that CFT overestimates the breakthrough curve from 1.3 to 3.1 PV and underestimates it from 3.1 to 8 PV. The current modeling study, however, ameliorates this discrepancy by using a lower value of K_{att} and a larger value of K_{det} so that more CMC-NZVI particles, on average, can be deposited before a 3-PV injection of NZVI, with a greater average release afterwards.

The λ_1 values in both cases of high concentrations, 0.725 and 0.2 g/L, are very similar (3 % different), and they are also similar to what was already obtained for RNIP at a concentration of 1 g/L for the case of F2 (36 % different). In this simulation, λ_1 at the concentration of 0.07 g/L tends toward the lower boundary of the parameter estimation limit, 1×10^{-8} S^{-1} which is considered as zero, and is in agreement with the simulation results of RNIP transport at the low concentration of 0.03 g/L. In contrast, the value of λ_2 at 0.07 g/L, although lower than that of the other cases, does not reach zero in the parameter estimation process, in contrast to the λ_2 value obtained for RNIP previously. It should be noted that the initial

hydrodynamic size of CMC-NZVI in the original paper (Raychoudhury et al. 2012) was 190 nm, which is 3–4 times larger than that of the polymer-modified RNIP (41 to 75 nm) in the study of Phenrat et al. (2009a). Thus, the larger size of injected CMC-NZVI might cause irreversible deposition even when the concentration is low and no aggregation occurs (a negligible value for λ_1). As already mentioned, the K_{det} values in this suite of simulations are not higher than the K_{att} values, in contrast to the RNIP simulation results. This lesser than expected detachment rate may be the result of the large initial size of the injected particles.

2-D simulations

Up-scaling of the model to 2-D simulations

In the previous sections, we verified that the model is applicable to simulating two types of polymer-modified NZVI transport through a 1-D homogeneous porous media. To evaluate the potential for applying the modified model in a more realistic 2-D flow within a heterogeneous porous media setting, we simulated the experimental breakthrough data from a multi-layered 2-D flow cell (variations in hydraulic conductivity) conducted by Phenrat et al. (2010a). The original study concluded that stratified heterogeneity in hydraulic conductivity had a significant impact on the deposition of NZVI. Obviously, polymer-modified NZVI followed preferential flow paths and deposited in the regions where fluid shear was insufficient to prevent NZVI agglomeration and deposition. Nevertheless, they did not explain the extent of agglomeration and deposition in each sand layer. Similar to their 1-D experimental study, Phenrat et al. (2010a) suggested that the limited NZVI transport was a combined effect of agglomeration, attachment, and irreversible deposition mechanisms. They did not, however, quantitatively analyze which mechanism played a greater role in each sand layer.

With the dispersivity values obtained from fitting the MT3DMS model to the nonreactive tracer data (see full details of the dispersivity determination in the SM), the MRNIP2 data at the low concentration were simulated using two parameters, K_{att} and K_{det}, in three zones of heterogeneity. Similar to the 1-D flow at the low particle concentration, both λ_1 and λ_2 were neglected from the modified model, as agglomeration is not relevant at a low particle concentration.

However, the other cases of MRNIP2, with high inflow concentrations, were simulated through an iterative procedure using all four parameters in each of the three zones to capture agglomeration and deposition. The results show no obvious convergence for the parameter λ_1 because each parameter produced different behaviors within different layers (Figs. S6a–S8a). However, after 3–5 iterations, all three cases demonstrated a noticeable closure for the observation data (as determined by the R^2 values before and after each iteration) (Figs. S6b–S8b). Satisfying these criteria (described in the "Iterative procedure for optimization of the parameters" section) confirms that the iterative procedure can be applied, even though the uncertainties induced by the averaging method and the zonal approach of the parameter estimation process were substantial.

The results of the 2-D simulations for all four cases are presented in Fig. 3 and Table 3. The best results were achieved for the washed MRNIP2 at the high concentration of 6 g/L, with an R^2 of 0.951 and a p value of 0.58. In the other cases, however, the R^2 coefficients were poorer (i.e., 0.787, 0.801, and 0.751 for low-concentration (unwashed), oxidized, and high concentration (unwashed) MRNIP2, respectively) despite passing the significance tests, with p values ranging from

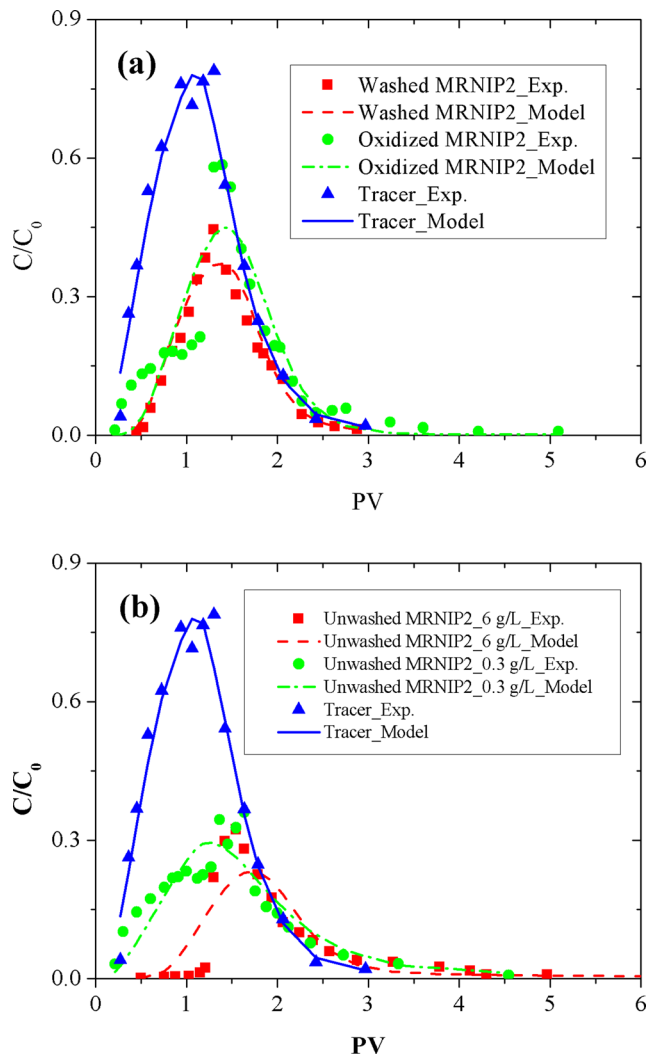

Fig. 3 Comparison of the experimental and modeled breakthrough curves of the 2-D model: **a** Washed MRNIP2 at the high concentration of 6 g/L, oxidized (and washed) MRNIP2 at the high concentration of 3 g/L, and tracer data. **b** Unwashed MRNIP2 at the high concentration of 6 g/L and at the low concentration of 0.3 g/L, together with the tracer data. *Symbols* represent the experimental (Exp.) data, and *lines* represent the modeled (Model) data

Table 3 Simulation results for different cases of the 2-D model

	Low-concentration	Washed	Oxidized	Unwashed
K_{att}−Fine	6.82E-03	2.34E-02	6.73E-03	3.33E-01
K_{att}−Medium	2.78E-03	3.67E-03	1.81E-03	8.35E-03
K_{att}−Coarse	3.90E-03	1.49E-01	8.18E-02	2.46E+00
K_{det}−Fine	4.88E-03	5.02E-02	1.46E-02	3.09E-01
K_{det}−Medium	1.69E-05	1.75E-04	6.32E-05	9.24E-05
K_{det}−Coarse	1.23E-03	2.83E-02	1.22E-02	2.86E-01
λ_1−Fine	–	1.46E-04	3.01E-05	1.25E-05
λ_1−Medium	–	2.27E-03	2.05E-03	2.99E-04
λ_1−Coarse	–	9.87E-05	1.08E-04	1.40E-04
λ_2−Fine	–	2.48E-04	1.20E-04	2.23E-04
λ_2−Medium	–	3.08E-04	6.02E-04	1.26E-04
λ_2−Coarse	–	1.27E-04	2.64E-05	3.23E-05
R^2	0.787	0.951	0.801	0.751
P-value	0.65	0.58	0.55	0.67

The unit of all the parameters is s^{-1}

0.55 to 0.67. Although the model of this study does not have specific parameters to distinguish different surface characteristics of NZVI such as oxidized shell properties, we tried to fit the model to the data of oxidized NZVI transported in the 2-D model. In spite of achieving an acceptable fitting, it was not as effective as non-oxidized NZVI. In the context of this modeling study, the reason behind the poorer fitting to this set of data is not exactly clear. Similarly, in spite of no specific consideration for the existence of free polymer in the dispersion of NZVI, the injected slurries of NZVI in two of the simulated data sets, i.e., at low concentration and high concentration (unwashed) MRNIP2, contained free polymer. The poorer fit in these cases compared to that of the washed MRNIP2 is due to the coexistence of free polymer and polymer-modified NZVI in the injecting dispersion combined with the complexity of the 2-D model, which was made apparent by the existence of multiple peaks in the experimental breakthrough curves produced by heterogeneous sand packing. Recently, several studies have shown that the free polymer in the nanoparticle dispersion can significantly affect the transport behavior of NPs (Becker et al. 2015a, b; Wang et al. 2014). Especially, Wang et al. (2014) found that the preferential adsorption behavior of free polymer near the column inlet hinders the attachment of NPs, whereas near the outlet, NPs attached to the solid surfaces without interference of free polymer. A more accurate modeling of this effect will be possible if a separated species is considered in the model formulation to represent the free polymer (Becker et al. 2015b), which is beyond the scope of this study.

At the high particle concentration, several interesting trends emerged when comparing K_{att}, K_{det}, λ_1, and λ_2 of the different experimental conditions and different porous media layers (Table 3). First, for the same type of NZVI particles, the λ_1 of the medium sand layer was always around 1 to 2 orders of magnitude greater than those of the fine and the coarse sand layers. This suggests that substantial agglomeration took place in the medium sand layer in comparison with the fine and the coarse sand layers. This makes physical sense because the NZVI that flowed through the coarse and fine sand layers encountered some unfavorable conditions for agglomeration. For example, most of the water flowed through the coarse sand layer, as evident in the flow field simulation (see the SM). Thus, the pore-water velocity through the coarse sand layer was relatively high (up to 0.54 cm s^{-1}), which might have prohibited NZVI agglomeration (Phenrat et al. 2009a, 2010a). Similarly, the pore size of the fine sand layer was significantly smaller than those of the medium and the coarse sand layers, resulting in a relatively high pore-water velocity (up to 0.65 cm.s^{-1}), which is unfavorable for agglomeration. In contrast, the flow velocity through the medium sand layer was lower than those of the other layers (up to 0.055 cm s^{-1}), making the medium sand layer the most favorable of all three layers for NZVI agglomeration. At the high particle concentration for all polymer-modified NZVI conditions, K_{att} in coarse-sand layer is larger than that in fine-sand layers which is in turn larger than K_{att} in medium-sand layer; moreover, K_{det} in coarse zone is almost similar to K_{det} in fine layers which is much greater than that in the medium layer. This matches very well with the flow field simulation (see the SM) for the 1-D simulation and CFT, in which the higher velocity induced more collision between the particles and the collector. Furthermore, for the same type of NZVI particles, the λ_2 of the coarse sand layer was around 5–10 times smaller than those of the fine and the medium sand, suggesting that attachment at the coarse sand layer was more reversible than that of the medium and fine sand layers. This also makes physical sense because the sheer forces from the flow field are supposed to be greatest in the coarse sand layer due to it having the highest flow rate among the three layers.

Comparison of the concentration contours in the 2-D simulations

To compare the NZVI concentration contours simulated based on the λ_1 values with the experimental observations (photos), the output concentrations from the simulation, in terms of the particle number concentration, were converted back to mass concentrations. To do so, in every spatial point of the model domain, the conversion was performed by calculating the radii of the agglomerates based on the λ_1 for the layer that contained a given point using the minimum time for agglomeration, t_{min}. The term t_{min} was defined as the minimum of the three times, including the time at which the photo was taken, the retention time of particles in each layer, and the particle transport time from the left-hand side of the model domain to the given point.

Figure 4 compares the resulting concentration contours based on the λ_1 values obtained in the initial iteration and the final iteration with the photos of the washed MRNIP2 plume (experimental results). These results show an overall improvement in the agreement between the experimental and simulated shapes of the NZVI plume after estimating λ_1

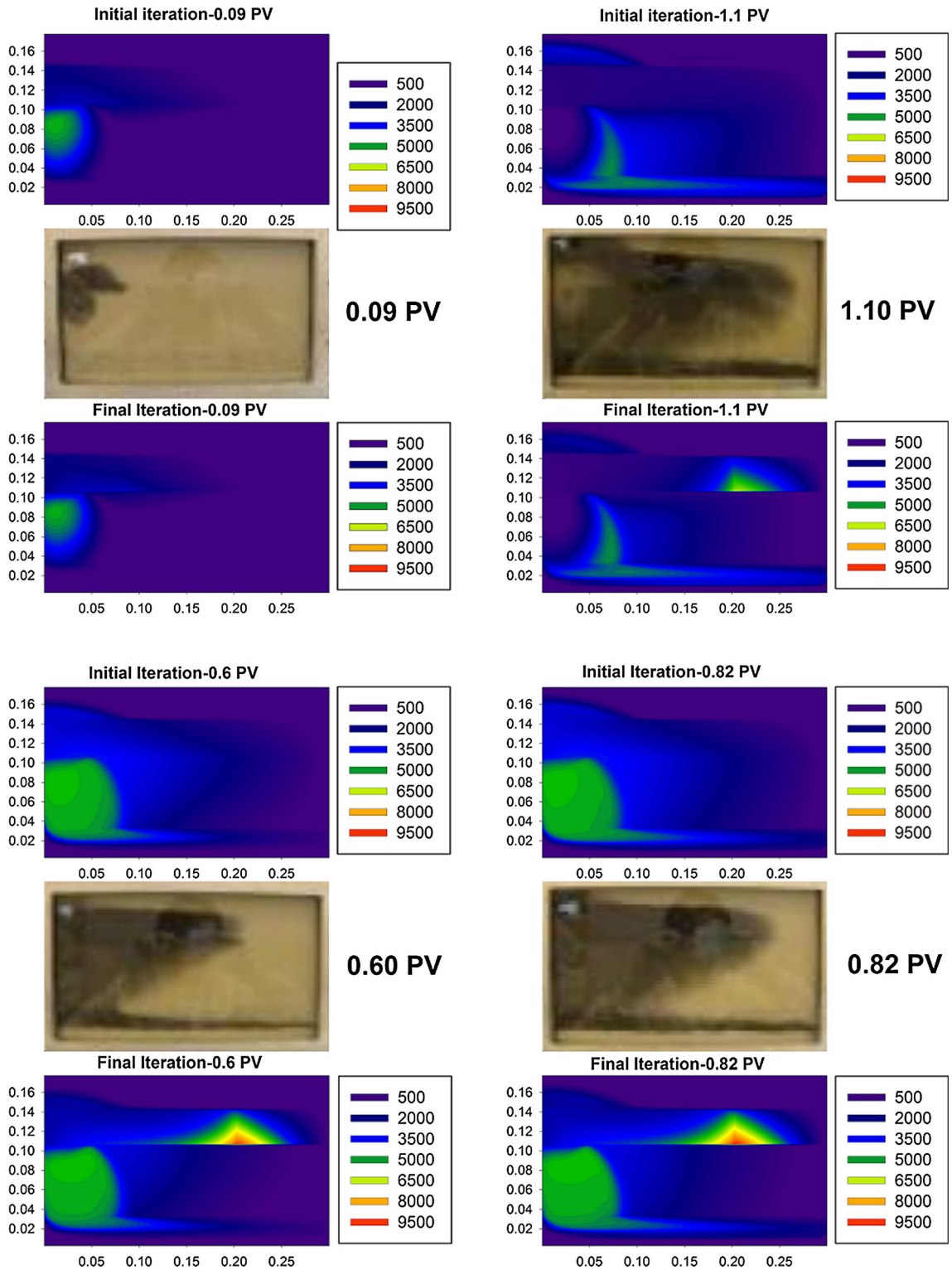

Fig. 4 Comparison of the experimental photos with the modeled, *color-shaded plots* for washed MRNIP2 at the high concentration of 6 g/L. The experimental photos were taken from Phenrat et al. (2010a). The *upper, color-shaded plots* of each photo were obtained in the initial iteration of the iterative procedure, while the *lower plots* were obtained in the final iteration

values through the iterative procedure. However, about a two-fold overestimation is obvious in the right side of the medium layer, which may have been due to the uncertainties found in this layer. In fact, low velocities obtained from the flow model in this area led to a large calculated t_{min}, which together with an order of magnitude greater value of λ_1 estimated in the medium layer in comparison to that of the other layers produced the largest-sized agglomerates. Accordingly, the largest calculated size of agglomerates resulted in the highest calculated mass concentration by Eq. (3). This suggests that to optimize the model parameters for real field remediation projects with NZVI, a thorough monitoring of the NZVI concentrations in every layer of the field area is necessary to resolve the uncertainties of the parameter estimation process caused by heterogeneity.

Mass conservation

We examined the mass conservative ability of the model with two approaches. In one approach, the cumulative mass budgets for all items involved in the modeling were checked at the end of each stress period or transient time step. These examinations showed that the discrepancies between the budgets of mass which entered the model domain and exited from, stored, or reacted in the model domain were far below 1 % in most of the simulation cases and, in very few cases, reached near 1 %. In another approach, the mass recovery results, i.e., the ratio of the sum of effluent mass exiting from the model to the sum of influent mass flowing into the model, were compared between modeling results and the experimental results. The results of this investigation for the final iterations of the various cases of the 1-D and 2-D simulations are reported in Tables S5 and S6, respectively. The average discrepancy of the mass recovery between the model results and the experimental results for 1-D modeling was 0.6 %, demonstrating that the proposed model is a mass-conserving model. The mass recovery discrepancy between the modeled and experimental results of the 2-D model was maximum for washed MRNIP2, 6.5 %. This is very close to 5 % of the effluent slurry that passed through the two upper ports in the 2-D experiment whereas in the modeling procedure we assumed the two upper outflow ports to be a no-flow boundary because the effluent passing through these ports was negligible (less than 5 %) according to the former study (Phenrat et al. 2010a). Therefore, the model's performance in such a heterogeneous and complicated model domain, which is reflective of field sites, is promising.

Prediction of the size of the agglomerate

The sizes of the agglomerates calculated based on the obtained λ_1 values were comparable to the results of the correlation equation developed by Phenrat et al. (2010b). The input parameters for these calculations are presented in Tables S7 and S8. A comparison was made for the cases of F1 and F2 at 6 g/L (available among the 1-D model cases) and washed MRNIP2 (available among the 2-D model cases). The discrepancy between the results of the current study based on the λ_1 values achieved in the initial stage of the iteration process and those of Phenrat et al. were 55, 46, and 42 % for F1 (6 g/L), F2 (6 g/L), and washed MRNIP2, respectively (Fig. 5). Interestingly, the agglomerate sizes obtained based on the λ_1 values in the final stage of the iteration process showed that the diminution of these errors to 47, 41, and 32 %, respectively, was statistically significant ($p<0.05$) (Figs. 5 and S9). This demonstrates that the proposed model is consistent with the existing model, and it furthermore suggests that the resulting λ_1 values from the proposed iteration algorithm can be useful for predicting the sizes of agglomerates formed during the transport of polymer-modified NZVI in subsurface environments, which has not been often considered in the literature (Areepitak and Ren 2011; Chatterjee and Gupta 2009; Grolimund et al. 2001; Petosa et al. 2010).

Similarly, the growth in particle due to agglomeration in porous media resulting from the current simulation is in close agreement with that measured by Raychoudhury et al. (2012) for CMC-NZVI suspensions in batch experiments. The results obtained at 0.725, 0.2, and 0.07 g/L show 18 nm, 16 nm, and zero increases, respectively, in the sizes of particles due to aggregation over the duration of the column experiment (~20 min) (Table 2). This is comparable with the results of Raychoudhury et al. (2012) for CMC-NZVI suspensions, where over the course of an ~1-h batch experiment, 76 nm, 28 nm, and negligible increases in the sizes of particles were

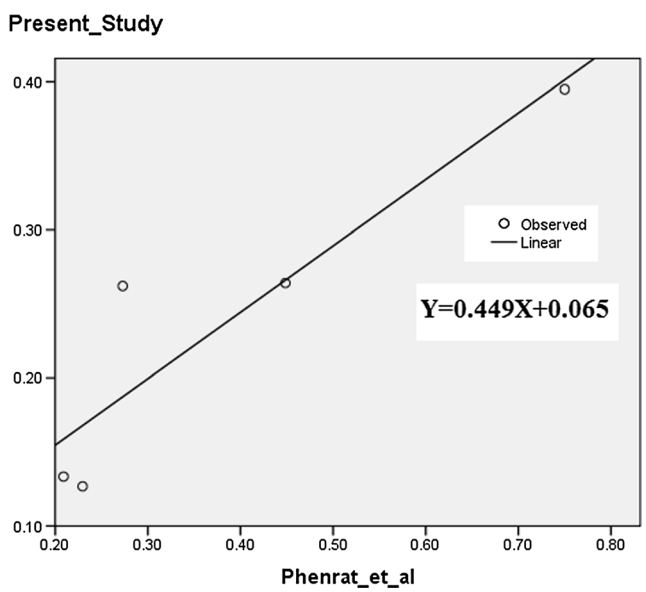

Fig. 5 Comparison of the sizes of the agglomerates obtained in the final iterations and by the empirical correlation of (Phenrat et al. (2010b)). Input parameters and the results of their empirical correlation are presented in Tables S7 and S8

observed for the cases of 0.725, 0.2, and 0.07 g/L, respectively.

Feasibility evaluation and limitation

This study shows that by implementing the proposed equations based on particle number concentration, the effect of agglomeration can be accounted for, and that by using an iterative procedure, the model parameters can be estimated and the sizes of the agglomerates at a given distance and time can be predicted in 1-D and 2-D heterogeneous porous media. Both agglomeration and detachment were found to be operative mechanisms in the transport of polymer-modified NZVI. This model needs to calibrate four parameters to capture the effects of attachment, detachment, agglomeration and irreversible deposition—similar to the CFT model which requires the estimation of the contact and attachment efficiencies for the attachment mechanism in addition to two more parameters for agglomeration and detachment mechanisms (Tufenkji and Elimelech 2004). However, CFT does not consider the irreversible deposition as a consequence of agglomeration whereas it has been considered in our model through one of the four aforementioned parameters. In addition, because no stochastic algorithm was used in the studied model, it benefits from the application of the inverse model (WinPEST) for the adjustment of parameters—a recent study that modeled the transport of NPs mentions the lack of this advantage for particle tracking-based numerical models (Taghavy et al. 2013). Further comparison of the proposed model with the CFT shows that CFT in combination with Smoluchowski model and using multiple values of K_{dep} is able to predict the particle size distribution whereas the proposed model of this study has the limitation of not being able to predict the particle size distribution although it can capture the effect of polydispersivity. However, the existence of multiple K_{att} values for various sizes in different spatial and temporal points of the model domain can increase the computational effort in CFT combined with the Smoluchowski model, even though it does not add to the number of parameters in the model. Furthermore, another drawback with the combination of CFT and the Smoluchowski model is that the calibration of the aggregation parameter ($\propto_{pp}$) with the deposition parameter ($\propto_{pc}$) at the same time has not been possible up to the time of this study. Thus, it requires conducting a static, batch experiment to obtain $\propto_{pp}$ for the given initial concentration of NPs and the same geochemical conditions (e.g., pH and ionic strength) but ignoring hydrodynamics of transport in porous media. Consequently, it is not clear how much the resulting $\propto_{pp}$ is reliable to be used for the simulation (Dale et al. 2015). On the other hand, in our modeling approach, the simultaneous calibration of agglomeration and transport parameters is facilitated via a novel iterative technique so that all the parameters of the model mechanisms including agglomeration, attachment/detachment, and irreversible deposition can be calibrated simultaneously even with the existence of different zones of heterogeneity in the model domain. Furthermore, to the best of our knowledge, this is the first time that the reversible and irreversible depositions of nanoparticles in porous media resulting from agglomeration are distinguished both mathematically and conceptually. This was accomplished in this study by considering a common first-order, reversible, kinetic-reaction equation for the attachment/detachment process as well as a sink term in the attached phase of particles.

The kinetic parameters obtained in this modeling study can be useful for the application of highly parameterized models of the fate and transport of NPs in the environment, which require a large number of input kinetic parameters, e.g., the recent multi-media model of Meesters et al. (Meesters et al. 2014). The results of the 2-D heterogeneous model suggest that monitoring the concentration in each layer of the model domain is necessary to minimize the uncertainties related to the estimated parameters. In field applications of NZVI, such monitoring has been performed via multi-level monitoring wells (Quinn et al. 2005; Su et al. 2012; Wei et al. 2010). Verifying the suitability of using this study's model with field data can be the subject of future studies.

Overall, our modeling procedure—thanks to employment of the PEST model for calibration of parameters in different zones of the model domain as well as utilizing the MODLFOW family models—is capable of simulating the transport and agglomeration of polymer-modified NZVI in the aquifers with various geological stratifications, in both steady state and transient modes. In this way, it not only considers heterogeneity in soil particle size and velocities but also can simulate preferential flow paths and thereby preferential paths of nanoparticle plume.

Acknowledgments The authors are thankful for the financial support from (1) the Thailand Research Fund (TRF) (MRG5680129), (2) the National Nanotechnology Center (Thailand), a member of the National Science and Technology Development Agency, through grant number P-11-00989, and (3) the National Research Council (Grant No. R2556B070 and R2555C010). We acknowledge the support of Naresuan University for the research fellowship it awarded to P.B. We thank Hamidreza Vosoughifar for his discussions about the *p*-value tests, Mohammad Elahi for his discussion about 2-D simulations, and Shahzad Kaviani for his English revision of the manuscript.

References

Areepitak T, Ren J (2011) Model simulations of particle aggregation effect on colloid exchange between streams and streambeds. Environ Sci Technol 45:5614–5621. doi:10.1021/es200586v

Baalousha M (2009) Aggregation and disaggregation of iron oxide nanoparticles: Influence of particle concentration, pH and natural organic

matter. Sci Total Environ 407:2093–2101. doi:10.1016/j.scitotenv.2008.11.022

Bai C, Li Y (2012) Modeling the transport and retention of nC 60 nanoparticles in the subsurface under different release scenarios. J Contam Hydrol 136:43–55

Becker MD, Wang Y, Paulsen JL, Song Y-Q, Abriola LM, Pennell KD (2015a) In situ measurement and simulation of nano-magnetite mobility in porous media subject to transient salinity. Nanoscale 7: 1047–1057

Becker MD, Wang Y, Pennell KD, Abriola LM (2015b) A multi-constituent site blocking model for nanoparticle and stabilizing agent transport in porous media. Environ Sci: Nano 2:155–166

Birkner FB, Morgan JJ (1968) Polymer flocculation kinetics of dilute colloidal suspensions. J Am Water Works Assoc 60:175–191

Boparai HK, Joseph M, O'Carroll DM (2011) Kinetics and thermodynamics of cadmium ion removal by adsorption onto nano zerovalent iron particles. J Hazard Mater 186:458–465. doi:10.1016/j.jhazmat.2010.11.029

Bradford SA, Yates SR, Bettahar M, Simunek J (2002) Physical factors affecting the transport and fate of colloids in saturated porous media. Water Resour Res 38(12). doi:10.1029/2002WR001340

Bradford SA, Simunek J, Bettahar M, van Genuchten MT, Yates SR (2003) Modeling colloid attachment, straining, and exclusion in saturated porous media. Environ Sci Technol 37:2242–2250. doi:10.1021/es025899u

Bradford SA, Simunek J, Bettahar M, van Genuchten MT, Yates SR (2006) Significance of straining in colloid deposition: evidence and implications. Water Resour Res 42:W12S15. doi:10.1029/2005WR004791

Bradford SA, Torkzaban S, Walker SL (2007) Coupling of physical and chemical mechanisms of colloid straining in saturated porous media. Water Res 41:3012–3024. doi:10.1016/j.watres.2007.03.030

Chatterjee J, Gupta SK (2009) An agglomeration-based model for colloid filtration. Environ Sci Technol 43:3694–3699. doi:10.1021/es8029973

Chen G, Liu X, Su C (2011) Transport and retention of tio2 rutile nanoparticles in saturated porous media under low-ionic-strength conditions: measurements and mechanisms. Langmuir 27:5393–5402. doi:10.1021/la200251v

Chen G, Liu X, Su C (2012) Distinct effects of humic acid on transport and retention of tio2 rutile nanoparticles in saturated sand columns. Environ Sci Technol 46:7142–7150. doi:10.1021/es204010g

Chowdhury AIA, O'Carroll DM, Xu Y, Sleep BE (2012a) Electrophoresis enhanced transport of nano-scale zero valent iron. Adv Water Resour 40:71–82. doi:10.1016/j.advwatres.2012.01.014

Chowdhury I, Cwiertny DM, Walker SL (2012b) Combined factors influencing the aggregation and deposition of nano-Tio_2 in the presence of humic acid and bacteria. Environ Sci Technol 46:6968–6976. doi:10.1021/es2034747

Cornelis G (2015) Fate descriptors for engineered nanoparticles: the good, the bad, and the ugly. Environ Sci: Nano 2:19–26

Cullen E, O'Carroll DM, Yanful EK, Sleep B (2010) Simulation of the subsurface mobility of carbon nanoparticles at the field scale. Adv Water Resour 33:361–371. doi:10.1016/j.advwatres.2009.12.001

Dale AL, Lowry GV, Casman EA (2015) Much ado about α: reframing the debate over appropriate fate descriptors in nanoparticle environmental risk modeling. Environ Sci: Nano 2:27–32

Elimelech M, Jia X, Gregory J, Williams R (1998) Particle deposition and aggregation: measurement, modelling and simulation. Elsevier, Amsterdam

Friedlander SK (1960a) On the particle-size spectrum of atmospheric aerosols. J Meteorol 17:373–374

Friedlander SK (1960b) Similarity considerations for the particle-size spectrum of a coagulating, sedimenting aerosol. J Meteorol 17: 479–483

Goldberg E, Scheringer M, Bucheli TD, Hungerbühler K (2014) Critical assessment of models for transport of engineered nanoparticles in saturated porous media. Environ Sci Technol 48:12732–12741

Grolimund D, Borkovec M (2001) Release and transport of colloidal particles in natural porous media: 1. Model Water Resour Res 37: 559–570. doi:10.1029/2000WR900285

Grolimund D, Borkovec M (2006) Release of colloidal particles in natural porous media by monovalent and divalent cations. J Contam Hydrol 87:155–175

Grolimund D, Elimelech M, Borkovec M (2001) Aggregation and deposition kinetics of mobile colloidal particles in natural porous media. Colloids Surf A Physicochem Eng Asp 191:179–188. doi:10.1016/S0927-7757(01)00773-7

Harbaugh AW, Banta ER, Hill MC, McDonald MG, U.S. Geological S (2000) MODFLOW-2000: the U.S. Geological Survey Modular Ground-water Model—user Guide to Modularization Concepts and the Ground-water Flow Process. U.S. Geological Survey open-file report 00-92. U.S. Department of the Interior, U.S. Geological Survey

He F, Zhao D, Paul C (2010) Field assessment of carboxymethyl cellulose stabilized iron nanoparticles for in situ destruction of chlorinated solvents in source zones. Water Res 44:2360–2370

Holthoff H, Egelhaaf SU, Borkovec M, Schurtenberger P, Sticher H (1996) Coagulation rate measurements of colloidal particles by simultaneous static and dynamic light scattering. Langmuir 12:5541–5549

Hong Y, Honda RJ, Myung NV, Walker SL (2009) Transport of iron-based nanoparticles: role of magnetic properties. Environ Sci Technol 43:8834–8839. doi:10.1021/es9015525

Hosseini SM, Tosco T (2013) Transport and retention of high concentrated nano-Fe/Cu particles through highly flow-rated packed sand column. Water Res 47:326–338

Hunt JR (1982) Self-similar particle-size distributions during coagulation: theory and experimental verification. J Fluid Mech 122:169–185

Jeffrey DJ (1981) Quasi-stationary approximations for the size distribution of aerosols. J Atmos Sci 38:2440–2443

Johnson WP, Li X, Assemi S (2007) Deposition and re-entrainment dynamics of microbes and non-biological colloids during non-perturbed transport in porous media in the presence of an energy barrier to deposition. Adv Water Resour 30:1432–1454

Johnson RL et al (2013) Field-scale transport and transformation of carboxymethylcellulose-stabilized nano zero-valent iron. Environ Sci Technol 47:1573–1580

Kanel SR, Goswami RR, Clement TP, Barnett MO, Zhao D (2007) Two dimensional transport characteristics of surface stabilized zero-valent iron nanoparticles in porous media. Environ Sci Technol 42:896–900

Keane E (2009) Fate, transport, and toxicity of nanoscale zero-valent iron (nZVI) used during superfund remediation US Environmental Protection Agency, Washington DC

Kim H-J, Phenrat T, Tilton RD, Lowry GV (2009) Fe0 nanoparticles remain mobile in porous media after aging due to slow desorption of polymeric surface modifiers. Environ Sci Technol 43:3824–3830

Kocur CM, O'Carroll DM, Sleep BE (2013) Impact of nZVI stability on mobility in porous media. J Contam Hydrol 145:17–25. doi:10.1016/j.jconhyd.2012.11.001

Krol MM, Oleniuk AJ, Kocur CM, Sleep BE, Bennett P, Xiong Z, O'Carroll DM (2013) A field-validated model for in situ transport of polymer-stabilized nZVI and implications for subsurface injection. Environ Sci Technol 47:7332–7340

Landkamer LL, Harvey RW, Scheibe TD, Ryan JN (2013) Colloid transport in saturated porous media: elimination of attachment efficiency in a new colloid transport model. Water Resour Res 49:2952–2965. doi:10.1002/wrcr.20195

Li X-Q, Cao J, Zhang W-X (2008) Stoichiometry of Cr (VI) immobilization using nanoscale zerovalent iron (nZVI): a study with high-

resolution X-ray photoelectron spectroscopy (HR-XPS). Ind Eng Chem Res 47:2131–2139

Liu HH, Surawanvijit S, Rallo R, Orkoulas G, Cohen Y (2011) Analysis of nanoparticle agglomeration in aqueous suspensions via constant-number Monte Carlo simulation. Environ Sci Technol 45:9284–9292

Logan BE, Passow U, Alldredge AL, Grossartt H-P, Simont M (1995) Rapid formation and sedimentation of large aggregates is predictable from coagulation rates (half-lives) of transparent exopolymer particles (TEP). Deep-Sea Res II Top Stud Oceanogr 42:203–214

Mattison NT, O'Carroll DM, Kerry Rowe R, Petersen EJ (2011) Impact of porous media grain size on the transport of multi-walled carbon nanotubes. Environ Sci Technol 45:9765–9775

Meesters JAJ, Koelmans AA, Quik JTK, Hendriks AJ, Van de Meent D (2014) Multimedia modeling of engineered nanoparticles with SimpleBox4nano: model definition and evaluation. Environ Sci Technol 48:5726–5736

O'Carroll D, Sleep B, Krol M, Boparai H, Kocur C (2013) Nanoscale zero valent iron and bimetallic particles for contaminated site remediation. Adv Water Resour 51:104–122

Pan B, Xing B (2012) Applications and implications of manufactured nanoparticles in soils: a review. Eur J Soil Sci 63:437–456

Petosa AR, Jaisi DP, Quevedo IR, Elimelech M, Tufenkji N (2010) Aggregation and deposition of engineered nanomaterials in aquatic environments: role of physicochemical interactions. Environ Sci Technol 44:6532–6549

Phenrat T, Saleh N, Sirk K, Tilton RD, Lowry GV (2007) Aggregation and sedimentation of aqueous nanoscale zerovalent iron dispersions. Environ Sci Technol 41:284–290

Phenrat T, Saleh N, Sirk K, Kim H-J, Tilton RD, Lowry GV (2008) Stabilization of aqueous nanoscale zerovalent iron dispersions by anionic polyelectrolytes: adsorbed anionic polyelectrolyte layer properties and their effect on aggregation and sedimentation. J Nanoparticle Res 10:795–814. doi:10.1007/s11051-007-9315-6

Phenrat T, Kim HJ, Fagerlund F, Illangasekare T, Tilton RD, Lowry GV (2009a) Particle size distribution, concentration, and magnetic attraction affect transport of polymer-modified Fe0 nanoparticles in sand columns. Environ Sci Technol 43:5079–5085

Phenrat T, Liu Y, Tilton RD, Lowry GV (2009b) Adsorbed polyelectrolyte coatings decrease Fe0 nanoparticle reactivity with TCE in water: conceptual model and mechanisms. Environ Sci Technol 43: 1507–1514

Phenrat T, Cihan A, Kim H-J, Mital M, Illangasekare T, Lowry GV (2010a) Transport and deposition of polymer-modified Fe0 nanoparticles in 2-D heterogeneous porous media: effects of particle concentration, Fe0 content, and coatings. Environ Sci Technol 44: 9086–9093

Phenrat T, Kim H-J, Fagerlund F, Illangasekare T, Lowry GV (2010b) Empirical correlations to estimate agglomerate size and deposition during injection of a polyelectrolyte-modified Fe0 nanoparticle at high particle concentration in saturated sand. J Contam Hydrol 118: 152–164. doi:10.1016/j.jconhyd.2010.09.002

Praetorius A, Scheringer M, Hungerbühler K (2012) Development of environmental fate models for engineered nanoparticles– a case study of tio2 nanoparticles in the Rhine river. Environ Sci Technol 46:6705–6713

Quik JTK, van De Meent D, Koelmans AA (2014) Simplifying modeling of nanoparticle aggregation–sedimentation behavior in environmental systems: a theoretical analysis. Water Res 62:193–201

Quik JTK, de Klein JJM, Koelmans AA (2015) Spatially explicit fate modelling of nanomaterials in natural waters. Water Res 80:200–208

Quinn J et al (2005) Field demonstration of DNAPL dehalogenation using emulsified zero-valent iron. Environ Sci Technol 39:1309–1318

Raychoudhury T, Tufenkji N, Ghoshal S (2012) Aggregation and deposition kinetics of carboxymethyl cellulose-modified zero-valent iron nanoparticles in porous media. Water Res 46:1735–1744

Raychoudhury T, Tufenkji N, Ghoshal S (2014) Straining of polyelectrolyte-stabilized nanoscale zero valent iron particles during transport through granular porous media. Water Res 50:80–90. doi: 10.1016/j.watres.2013.11.038

Risovic D, Martinis M (1994) The role of coagulation and sedimentation mechanisms in the two-component model of sea-particle size distribution. Fizika B 3:103–118

Ryan JN, Elimelech M (1996) Colloid mobilization and transport in groundwater. Colloids Surf A Physicochem Eng Asp 107:1–56

Saleh N et al (2005) Adsorbed triblock copolymers deliver reactive iron nanoparticles to the oil/water interface. Nano Lett 5:2489–2494

Schijven JK, Hassanizadeh SM (2000) Removal of viruses by soil passage: overview of modeling, processes, and parameters. Crit Rev Environ Sci Technol 30:49–127

Seymour MB, Chen G, Su C, Li Y (2013) Transport and retention of colloids in porous media: does shape really matter? Environ Sci Technol 47:8391–8398

Sirk KM et al (2009) Effect of adsorbed polyelectrolytes on nanoscale zero valent iron particle attachment to soil surface models. Environ Sci Technol 43:3803–3808

Smoluchowski M (1917) Versuch einer mathematischen Theorie der Koagulationskinetik kolloider Lösungen. Zeitschrift fuer Physikalische Chemie 92:129–168

Sobkowicz M (2006) Aggregation and equilibrium: a statistical model of the smoluchowski equation. Report for Class ChEN610, Statistical Thermodynamics, Colorado School of Mines.

Su C, Puls RW, Krug TA, Watling MT, O'Hara SK, Quinn JW, Ruiz NE (2012) A two and half-year-performance evaluation of a field test on treatment of source zone tetrachloroethene and its chlorinated daughter products using emulsified zero valent iron nanoparticles. Water Res 46:5071–5084. doi:10.1016/j.watres.2012.06.051

Swift DL, Friedlander SK (1964) The coagulation of hydrosols by Brownian motion and laminar shear flow. J Colloid Sci 19:621–647

Szilagyi I, Szabo T, Desert A, Trefalt G, Oncsik T, Borkovec M (2014) Particle aggregation mechanisms in ionic liquids. Phys Chem Chem Phys 16:9515–9524

Taghavy A, Mittelman A, Wang Y, Pennell KD, Abriola LM (2013) Mathematical modeling of the transport and dissolution of citrate-stabilized silver nanoparticles in porous media. Environ Sci Technol 47:8499–8507

Taghavy A, Pennell KD, Abriola LM (2015) Modeling coupled nanoparticle aggregation and transport in porous media: A Lagrangian approach. J Contam Hydrol 172:48–60

Tosco T, Sethi R (2010) Transport of non-Newtonian suspensions of highly concentrated micro-and nanoscale iron particles in porous media: a modeling approach. Environ Sci Technol 44:9062–9068

Tufenkji N, Elimelech M (2004) Correlation equation for predicting single-collector efficiency in physicochemical filtration in saturated porous media. Environ Sci Technol 38:529–536

U.S.EPA (2011) OSWER. Selected Sites Using or Testing Nanoparticles for Remediation. http://clu-in.org/download/remed/nano-site-list.pdf

Velzeboer I, Quik JTK, van de Meent D, Koelmans AA (2014) Rapid settling of nanoparticles due to heteroaggregation with suspended sediment. Environ Toxicol Chem 33:1766–1773

Wang Y, Li Y, Fortner JD, Hughes JB, Abriola LM, Pennell KD (2008) Transport and retention of nanoscale C60 aggregates in water-saturated porous media. Environ Sci Technol 42:3588–3594. doi: 10.1021/es800128m

Wang Y, Li Y, Kim H, Walker SL, Abriola LM, Pennell KD (2010) Transport and retention of fullerene nanoparticles in natural soils. J Environ Qual 39:1925–1933

Wang C, Bobba AD, Attinti R, Shen C, Lazouskaya V, Wang L-P, Jin Y (2012a) Retention and transport of silica nanoparticles in saturated porous media: effect of concentration and particle size. Environ Sci Technol 46:7151–7158. doi:10.1021/es300314n

Wang Y, Kim J-H, Baek J-B, Miller GW, Pennell KD (2012b) Transport behavior of functionalized multi-wall carbon nanotubes in water-saturated quartz sand as a function of tube length. Water Res 46: 4521–4531. doi:10.1016/j.watres.2012.05.036

Wang Y, Becker MD, Colvin VL, Abriola LM, Pennell KD (2014) Influence of residual polymer on nanoparticle deposition in porous media. Environ Sci Technol 48:10664–10671

Watermark Numerical Computing & Waterloo Hydrogeologic Inc. (1999) WinPEST User's Manual: Nonlinear Parameter Estimation and Predictive Analysis Program, Waterloo, Ontario, Canada

Wei Y-T, Wu S-C, Chou C-M, Che C-H, Tsai S-M, Lien H-L (2010) Influence of nanoscale zero-valent iron on geochemical properties of groundwater and vinyl chloride degradation: a field case study. Water Res 44:131–140

Zhan J et al (2008) Transport characteristics of nanoscale functional zerovalent iron/silica composites for in situ remediation of trichloroethylene. Environ Sci Technol 42:8871–8876

Zhan J, Kolesnichenko I, Sunkara B, He J, McPherson GL, Piringer G, John VT (2011) Multifunctional iron−carbon nanocomposites through an aerosol-based process for the in situ remediation of chlorinated hydrocarbons. Environ Sci Technol 45:1949–1954

Zheng C, Wang PP (1999) A modular three-dimensional multi-species transport model for simulation of advection, dispersion and chemical reactions of contaminants in groundwater systems; documentation and user's guide US Army Engineer Research and Development Center Contract Report SERDP-99-1, Vicksburg, Mississippi, USA

Supplementary Materials

Feasibility Evaluation of Using a Modified MODFLOW-Based Model for Simulating the Agglomeration and Transport of Polymer-Modified Fe^0 Nanoparticles in Saturated Porous Media

Peyman Babakhani[1], Fritjof Fagerlund[2, 3], Abolfazl Shamsai[1, 4].Gregory V. Lowry[5],

and Tanapon Phenrat[6, 7*]

[1]Department of Hydrology Engineering, Tehran Science and Research Branch, Islamic Azad University, Tehran, Iran.

[2]Department of Earth Sciences, Uppsala University, Villavägen 16, 75236 Uppsala, Sweden

[3]Center for Experimental Study of Subsurface Environmental Processes, Colorado School of Mines, Golden, CO, USA

[4]Department of Civil Engineering, Sharif University of Technology, Tehran, Iran

[5]Center for Environmental Implications of Nanotechnology (CEINT) and Department of Civil & Environmental Engineering, Department of Chemical Engineering, Carnegie Mellon University, Pittsburgh, PA 15213-3890, USA.

[6]Research Unit for Integrated Natural Resources Remediation and Reclamation (IN3R), Department of Civil Engineering, Faculty of Engineering, Naresuan University, Phitsanulok, Thailand, 65000

[7]Center of Excellence for Sustainability of Health, Environment and Industry (SHE&I), Faculty of Engineering, Naresuan University, Phitsanulok, Thailand, 65000

Submitted to

Environmental Science and Pollution Research

*Corresponding author: Tanapon Phenrat (pomphenrat@gmail.com)

(6655)964057(ph) (6655)964002(fax)

Contents.

1. Conceptual model. We based our conceptual model upon two principles of particle transport and agglomeration according to the litrature (Phenrat et al. 2010a; Phenrat et al. 2010b; Phenrat et al. 2009),. One of these principles is when there are initial aggregates in the dispersion, other individuals particles begin to be attracted to the aggregates and increase their sizes. Thus, the larger the population of aggregates is, the more agglomeration phenomena occurs. The second principle is that, the larger the sizes of agglomerates are, the more their tendency for deposition is. Accordingly, three scenarios are considered in the conceptual model as follows:

Scenario I. There is no inintial aggregates in the popualtion of particles. Thus, there is no agglomeration (Fig. S10a). The mathematical model for this case is expressed by Eqs. (S1) and (S2) as follows:

$$\frac{\partial N}{\partial t} + \frac{\rho_b}{\varepsilon}\frac{\partial \bar{N}}{\partial t} = D\frac{\partial^2 N}{\partial x^2} - V\frac{\partial N}{\partial x} \qquad \text{(S1)}$$

$$\frac{\rho_b}{\varepsilon}\frac{\partial \bar{N}}{\partial t} = K_{att}N - \frac{\rho_b}{\varepsilon}K_{det}\bar{N} \tag{S2}$$

here, attachment and detachment are expressed as first-order reaction rates. If the number of individual particles is high, the number of attached particles will be high, and subsequently the number of detached particles will be high too (because of the first-order reaction, the particles react proportional to their concentration or population). Eventually, the net result of deposition is zero as it has been shown by the experimental reports (Fig. S10a) (Phenrat et al. 2009).

Scenario II. There are initial aggregates in dispersion, yet we do not assume the tendency for deposition of aggregates is higher than that of individual particles (Fig. S10b). In other words, the first abovementioned principle is used but the second one is not applied yet. As a mathematical model, *a sink term* in Eq. (S1) should be added, in order to decay the population of aqueous-phase particles because of agglomeration:

$$\frac{\partial N}{\partial t} + \frac{\rho_b}{\varepsilon}\frac{\partial \bar{N}}{\partial t} = D\frac{\partial^2 N}{\partial x^2} - V\frac{\partial N}{\partial x} - \lambda_1 N \tag{S3}$$

$$\frac{\rho_b}{\varepsilon}\frac{\partial \bar{N}}{\partial t} = K_{att}N - \frac{\rho_b}{\varepsilon}K_{det}\bar{N} \tag{S4}$$

In this case, the population of particles (herein referred to all tiny particles and grown agglomerates) is less than the previous case because of the agglomeration. Therefore, the number of attached particles is less than the previous case and consequently the number of detached particles is also less due to the first-order reaction which indicates the particles react proportional to their concentration or population. The net result of deposition is zero after all, which is not consistent with the previous report (Phenrat et al. 2009). However, as the second principal is not incorporated yet in this scenario, this scenario is rejected.

Scenario III. A scenario similar to the previous one is considered but with the assumption that there is a difference between the attachment tendencies of individual particles and large grown clusters. In other words, as the tendency of agglomerates for deposition is higher than the individual ones, they attach to the collector surface greater than the individual particles (second principle) (Fig. S10c).

In this case there is less agglomeration in fluid phase than the previous scenario, because the number of agglomerates has decreased due to deposition. Consequently, the agglomeration is less than the previous case. Thus, the rate of attachment is between those of the two scenarios of (I) and (II). Nevertheless, as the detachment is in line with the population of attached particles and the model cannot identify whether the particles are small individual particles with shallow secondary minimum wells or a large clusters with deep secondary minimum wells, the net result of deposition is again zero. This is not in agreement with the previous paper (Phenrat et al. 2009) expressing that there should be retention in the system when the agglomeration occurs, i.e., the resulted, net deposition cannot be zero in case of agglomeration.

Hence, there is a need for another sink term to be added in the governing equation (Eq. (S3)) to decay the population of attached-phase agglomerates in order to have a less population of agglomerates in the attached phase, and subsequently reduce the return of the particles back to the fluid-phase (reduce the detachment). This final mathematical model is as follows:

$$\frac{\partial N}{\partial t} + \frac{\rho_b}{\varepsilon}\frac{\partial \bar{N}}{\partial t} = D\frac{\partial^2 N}{\partial x^2} - V\frac{\partial N}{\partial x} - \lambda_1 N - \lambda_2 \frac{\rho_b}{\varepsilon}\bar{N} \tag{S5}$$

$$\frac{\rho_b}{\varepsilon}\frac{\partial \bar{N}}{\partial t} = K_{att}N - \frac{\rho_b}{\varepsilon}K_{det}\bar{N} \tag{S6}$$

Based on this final mathematical model the net result of deposition is not zero, because some of the attached aggregates have been disappeared from the attached phase by the new sink term in the attached phase. It is interpreted as the subsequent deposition of agglomerates which are disappeared from the system. In other words, since they are "irreversibly" attached and are not able to return to the fluid phase any longer, their population is not counted as part of the population of the attached-phase particles. In fact, we have used a perfect sink model within a non-penetration model.

2. Unity assumption of C/C_0 in Eq. (7). C/C_0 in Eq. (7) was considered to be unity because the change in mass concentration theoretically cannot be reflected in an agglomeration equation, unless it is the effect of other phenomena, such as deposition, occurred for the particles in the system. Besides, since Eq. (7) is solved simultaneously with Eqs. (1) and (3), the effect of deposition may be introduced in C/C_0 and therefore it can influence the agglomeration. On the other hand, there are indications that this effect is negligible. One such indication is that, in estimating the size of the agglomerate in the empirical correlation equation developed by Phenrat et al. (Phenrat et al. 2010b), no parameter representing the effect of deposition on agglomeration has been found to be significant. Hence, it is assumed that C/C_0 in Eq. (7) is equal to unity. Moreover, during the parameter estimation process, which is performed via an iterative technique in this study, all the parameters of the model (λ_1, λ_2, K_{att}, and K_{det}) are optimizing together concurrently. Therefore, if there would be any effect of deposition on agglomeration, it can be excreted on the agglomeration parameter (λ_1) during parameter estimation procedure. Thus, the unity assumption of C/C_0 can conceptually be acceptable. To validate this assumption even further, the opposite hypothesis, i.e., C/C_0 in Eq. (7) can be affected by deposition, was

also tested by supposing that C/C_0 in Eq. (7) is calculated using the following equation (Bradford et al. 2006; Schijven and Hassanizadeh 2000):

$$\frac{C}{C_0} = \frac{K_{det} + K_{att}\, e^{-(K_{det}+K_{att})\times t}}{K_{det}+K_{att}} \tag{S8}$$

3. Applied models and graphical interfaces. In this study, the public-domain code of MT3DMS (U.S. Army Corps of Engineers, Washington, DC) (Zheng and Wang 1999) was applied for all the transport simulations. MT3DMS is a code from the MODFLOW family (U.S. Geological Survey, Denver, CO 80225-0425) (Harbaugh and U.S. Geological 2005) and it has been widely used to model the groundwater pollutant transport in recent decades (Zheng and Bennett 2002). The flow-field input data for MT3DMS was computed via MODFLOW 2000 (Harbaugh et al. 2000). The required files for running MT3DMS and MODFLOW2000 were translated by the graphical interface, Visual MODFLOW, version 2011.1 (Schlumberger Water Services Inc., Ontario, Canada) (Schlumberger Water Services 2011). Another software named WinPEST (Watermark Numerical Computing & Waterloo Hydrogeologic, Inc., Ontario, Canada) (Watermark Numerical Computing & Waterloo Hydrogeologic 1999) was used to calibrate the transport parameters. To validate model simulations and optimizations, the first-step of the iterative procedure for several cases of the 1-D model was conducted using a different graphical interface i.e., Groundwater Vistas, version 5 (Environmental Simulations, Inc., (ESI), PA) (Rumbaugh and Rumbaugh 2011) and through a manual calibration process described in the literature (Rumbaugh and Rumbaugh 2011). The results of these duplicate simulations are presented in this document.

4. Simulation characteristics. The 1-D model was simulated in a horizontal configuration, and with rectangular cross-section, the area of which was equivalent to the circular cross-section of experimental column. The horizontal assumption of vertical column cannot influence the simulation result since the variable density effect is not considered in this study as it cannot be accounted for by the MT3DMS model. Equal velocity between the flow model and the experiment was obtained. One row, one layer, and 130 columns configured the model grid. The model grid design involved the refinement of grid cells in areas around the inlet and outlet boundaries (Fig. S1). Refining and smoothing capabilities of Visual MODFLOW were incorporated to achieve this goal. A constant-flux boundary was used at the inlet of the model, and a constant-head boundary was used at the outlet. Other boundary conditions were selected as no-flow boundary. Such a selection of boundary conditions had been reported previously (Fagerlund et al. 2012). Longitudinal dispersivity was estimated through the calibration process of the case F3 at low concentration. This estimation resulted in a value of 0.015 cm which was consistent with the analytical values calculated based on the appropriate relationships from the literature (Illangasekare et al. 2010). Hence, in all of the 1-D simulations the dispersivity value of 0.015 cm was used, which was also consistent with the disperisvity values used in other studies (Pennell et al. 1993; Wang et al. 2008). Molecular diffusion coefficient in calculation of hydrodynamic dispersion tensor was assumed equal to zero in all of the simulations of this study, as it has been a common assumption in the literature (Zheng and Wang 1999). Hydraulic conductivity of the model was obtained from the experimental results published by Phenrat et al. (Phenrat et al. 2010a).

The 2-D simulations were firstly conducted by using the nonreactive tracer data to determine dispersivity parameters. In addition, other assumptions of flow model including

boundary condition setup and conductivity parameters were validated out of this simulation. After the refinement and smoothing of the grid in regions with high flow gradient, 101 columns, 62 layers, and 1 row built up the model grid (Fig. S2). An injection well with three filters was set as the inflow background flow through three side ports. Another injection well was represented as the real injection well. Finally, the outflow boundary conditions were simulated with a drain boundary condition which had flow only at lower port. In these boundary conditions the two upper outflow ports were assumed to have no flow, because the effluent through these ports were negligible according the previous paper (less than 5%) (Phenrat et al. 2010a). The conductance of the drain boundary was calculated so that the conductivity for each cell of this boundary was equal to the adjacent sand layer. The drain level, after adjustment in several calibrations conducted using the tracer data, was set at 9.95 cm from the bottom of model. Three stress periods were considered. The first stress period was specified for establishing a steady state background flow, prior to turning on the injection well of the NZVI or tracer. At the second stress period, the injection well of materials was turned on besides existing the background flow. Finally, the third stress period was applied as the rinsing stage of the experiments, i.e. it was similar to the second stress period except the injection concentration was zero.

In each calibration run of WinPEST three ASCII input files were manually prepared according to the model's documentation (Watermark Numerical Computing & Waterloo Hydrogeologic 1999). These files included a template file for identifying model parameters, an instruction file for identifying model-generated observations, and an input control file for supplying WinPEST with desired settings. In the parameter estimation process a zonal approach was applied, both in the tracer simulation for the dispersivitiy parameters and in the NZVI simulation for the parameters K_{att}, K_{det}, λ_1, and λ_2. This way, each parameter was considered

for each of the three zones including fine, medium, and coarse sand. However, only for the dispersivitiy parameters two upper and lower fine sand layers were considered as a separated zone of the middle fine sand layer. In other words, four zones were considered in the tracer simulation, while three zones were considered in the NZVI simulations. The ratio of the vertical to longitudinal dispersivity was assumed to be 0.01 which is a typical assumption in the literature (Schlumberger Water Services 2011; Zheng and Wang 1999).

It should be noted that the iterative parameter estimation process in this study, concurring with any common optimization technique (Parker et al. 1984), can be skipped in many applications in which the values of the applied parameters are ascertained by other methods, e.g., laboratory experiments. In this way, because the parameter values are already available, the simulation can be performed simply in one stage: solve Eqs. (1) and (2) in terms of the particle number concentration (the inflow and initial concentration values based on the mass concentration can be converted into the particle number concentration by inserting the initial size of aggregates into Eq. (3)). Then, using the available known value(s) of λ_1, the sizes of aggregates are obtained by Eq. (7). Finally, the spatial and temporal concentration data (resulting from the solutions of Eqs. (1) and (2)), which are in terms of particle number concentrations, can be converted into mass concentrations via Eq. (3).

5. Goodness-of-fit criteria. In order to assess the goodness of fit, a Nash–Sutcliffe (Nash and Sutcliffe 1970) model efficiency coefficient (a conservative R^2) was calculated for all of the simulations and for each step of the iterative procedure. Furthermore, a paired-samples T-Test (two tails) was conducted using SPSS Statistics (Version 17; IBM Inc., Armonk, NY), and the P-

value was assessed for a 95% confidence interval ($P \gg 0.05$ indicates that the *"correlation"* is significant). On the other hand, wherever the significance of the differences between two sets of data was needed to be proved, the same test but with the opposite null hypothesis was performed ($P < 0.05$ indicates that the "*difference"* is significant).

6. Averaging method used for the conversion of concentration in the 2-D model. In order to convert the observation concentrations from mass to particle number concentration, it was necessary to average the observations obtained for the three different zones or vice versa in order to convert the observation concentrations from particle number concentration to mass, averaging of parameters in the three layers was required.. The weights for the averaging technique can be selected based on any criteria that can result in the ratio of the flow in each layer to the total flow in the domain. In this study, we chose the weight for each layer as ratio of the number of particles passed through that layer to a number of virtual particles specified for the whole system. This was simply achieved by using the particle tracking model MODPATH which is built into the Visual MODFLOW software (Pollock 1994). This way, 40 particles were placed around the injection well of the suspensions and after running the model and obtaining a screenshot of the particle paths, a perpendicular line was drawn in the cross section of the model domain (Fig. S11). Then the ratio of the number of path-lines which pierced the perpendicular line in a specific layer to the entire number of the path-lines, i.e. 40, was considered as the weight for that specific layer. These weights were calculated as $26/40$ for the coarse sand layer, $12/40$ for the medium sand layer, and $2/40$ for the fine sand layer. It should be noted that for practical simulations in field applications, this procedure can be substituted by extracting the discharge of each layer of the model domain from output files of the MODLFOW model.

7. Transport of the low-concentration, NZVI dispersion containing no initial aggregates. In the case of F3 at low concentration, in which there are no apparent NZVI aggregates in the influent stream, both parameters of λ_1 and λ_2 declined to lower bounds of the parameter threshold in the parameter-estimation process (Table S1), consistent with the lack of agglomeration in this case. This is in accordance with previous experimental results (Phenrat et al. 2010b; Phenrat et al. 2009) suggesting that the agglomeration and subsequent deposition of agglomerates do not occur for low concentrations of polymer-modified NZVI. The best set of parameters for this case was achieved using both K_{att} and K_{det} with a goodness-of-fit criteria (R^2) of 0.987 and a P-value of 0.43 (Fig. 1a, Table S1). Fitting with only two parameters of K_{att} and K_{det} indicates that the transport of polymer-modified NZVI at low concentration and without initial aggregates is only affected by the exchange of particles between the mobile and deposited particle phases, and that no irreversible deposition occur.

8. Estimation of dispersivity parameters in the 2-D model. The dispersivity parameters in the different layers were obtained by fitting the MT3DMS model (by excluding reaction parameters and neglecting molecular diffusion) to nonreactive tracer data. This led to longitudinal dispersivity values as follows: $1.33 \times 10^{-4}\ m$ for the upper and lower fine sand layers; $8.46 \times 10^{-3}\ m$ for the middle fine sand layer; $0.2\ m$ for the medium sand layer; and $0.01\ m$ for the coarse sand layer (Fig. S2). The vertical transverse dispersivity of each layer was assumed to be one percent of the longitudinal dispersivity in that layer. R^2 and P-values of this fitting were 0.97 and 0.51, respectively (Fig. S12). In addition, the color-shaded maps of concentration contours at different times were in excellent agreement with the photos of tracer

plume (Fig. S13). The parameter sensitivities, calculated by WinPEST for dispersivity parameters at different zones, followed the order: coarse layer > medium layer > middle fine layer > upper and lower fine layers. However, uncertainty outcomes of WinPEST showed an order of magnitude higher value for the medium layer than for the other layers. This indicated that the reason for obtaining the higher value of the dispersivity for the medium sand layer than the expectation lies behind the lack of a monitoring point in this layer. This overestimation for vertical dispersivity in the medium sand layer in comparison to the study of Kanel et al., (Kanel et al. 2008) amounts to an order-of-magnitude.

9. Effect of deposition on agglomeration. Although the effect of agglomeration on the deposition of NPs had been emphasized in previous studies (Hotze et al. 2010; Phenrat et al. 2010a; Phenrat et al. 2010b; Phenrat et al. 2009), there had been no indication of the subsequent effect of deposition on agglomeration. In this study, we assumed that the latter effect was negligible and thus assumed that the C/C_0 in Eq. (7) was equal to unity. However, for the case of F1 at 6 g/L, some alternative assumptions were investigated. One hypothesis was to equate C/C_0 in Eq. (7) with the experimental C/C_0 (0.61). The result of this hypothesis, after conducting the iterative procedure, showed a sharp decline in the values of λ_1, and λ_2 within the iterative procedure (Fig. S14), and the calculated size of agglomerates after 10 iterations was almost equal to the size of the inflow particles (only 0.4% increase in the size of the agglomerates). Other hypothetical approaches, in which C/C_0 was considered as variable during the iterative procedure, led to similar results or did not converge at all (results not shown). In a final approach, C/C_0 was calculated via Eq. (S8). The resulted C/C_0 values in this approach ranged from 0.785 to 0.787 during the iterative procedure. Although a closure criterion of 1% for $\lambda_1$was

satisfied after five iterations, the size of the agglomerates that was calculated in the final iteration only increased by 1.3%. The recent approach was also tested with the 2-D model for the case of washed MRNIP2, and the results showed a sharp decline in all of the parameters, and the size of the aggregates in the outflow was smaller than that of the inflow (result not shown). These results demonstrated that assuming C/C_0 in Eq. (7) other than unity led to erroneous results. Therefore, considering any effect of deposition on agglomeration out of C/C_0 caused the model outcomes to be incorrect and the most reasonable results were achieved when this effect was cancelled.

10. Necessity for retaining the parameter, $\boldsymbol{\lambda_2}$. In order to show the necessity for the model parameter, λ_2 (the pseudo first-order reaction rate representing irreversible deposition), we eliminated this parameter from the modeling procedure, and then conducted the iteration procedure for the case of F1 at 6 g/L. The results showed that, in addition to slow convergence for λ_1 (a convergence criterion of 0.1 was satisfied after 10 iterations), there was a decline in the graph of R^2, calculated before the calibration stage of each iteration, versus the iteration number (Fig. S15-a). There was also a low average R^2 of 0.39 calculated based on the R^2 values before calibration stages of various iterations. All of these poor fitting results signify that the model cannot simulate the experimental data when λ_2 is eliminated, indicating the necessity for retaining the parameter λ_2 in the model. In other words, these results showed that the parameter, λ_2, was independent of other parameters of the model, because by eliminating it from the modeling procedure, the simulation grew wrong.

11. Results of different numerical methods. In order to find the most appropriate numerical method, two different methods of standard finite difference (FD) with central-in-space weighting and total variation diminishing (TVD) were investigated. Using the data of NZVI transport in 1-D columns, the results of all of the particle size distributions (F1, F2 and F3) at high particle concentration showed that the TVD method provided better R^2 values for the fits compared to the FD method ($P < 0.05$). However, at low particle concentration, F1, F2 and F3 were better fit when the FD method was used (Table S1 and Table S2), but the differences between the R^2 values were not significant ($\mathrm{P} > 0.05$). Thus, the TVD method was used in the numerical simulations of polymer-modified NZVI transport. This method was also selected to model NZVI transport by Kanel et al. (Kanel et al. 2007).

12. Results of replicated simulations. To validate the inverse modeling results and the software simulation results duplicate simulations were performed by Groundwater Vistas through a manual calibration for data sets in which the two parameters, K_{att} and K_{det}, were used. According to the results, there was not a significant discrepancy between the achieved parameters in the two types of simulations, i.e., between the simulations based on Groundwater Vistas through manual calibration and the simulations based on the combination of Visual MODFLOW and the automatic calibration model WinPEST. The correlation coefficients between the parameter results of the two sets of simulations were 0.30 and 0.33 for K_{att} and K_{det}, respectively, and the P-values were 0.34 and 0.27, respectively.

Table S1. Simulation results of the case F3 at 30 mg/L for different sets of parameters and two different numerical methods of finite difference (FD) and total variation diminishing (TVD).[a]

	FD-2par.	TVD-2par.	FD-4par.	TVD-4par.
$\mathbf{K_d}$ **or** $\mathbf{K_{att}}$	7.21E-03[c]	4.15E-03[c]	7.15E-03[c]	4.06E-03[c]
$\mathbf{K_{det}}$	2.61E-02	1.39E-02	2.59E-02	1.36E-02
$\boldsymbol{\lambda_1}$	-	-	1.19E-07	1.76E-07
$\boldsymbol{\lambda_2}$	-	-	4.32E-07	4.79E-07
$\mathbf{R^2}$	0.987	0.984	0.987	0.983
P-Value	0.43	0.45	0.43	0.44

[a]The unit of K_d is m^3/Kg and the units of other parameters are s^{-1}. [b]K_d. [c]K_{att}.

Table S2. Parameter values and fitting results for different sets of parameters and two different numerical methods for the cases F1 and F2 at 30 mg/L.[a]

		FD-2par.	TVD-2par.	FD-4par.	TVD-4par.	FD-4par.[b]	TVD-4par.[b]
F1-30 mg/L	$\mathbf{K_d}$ or $\mathbf{K_{att}}$	3.35E-03[d]	2.69E-03[d]	3.47E-03[d]	2.44E-03[d]	2.12E-03[d]	2.13E-03[d]
	$\mathbf{K_{det}}$	1.29E-02	9.14E-03	1.34E-02	8.18E-03	6.57E-03	6.28E-03
	$\boldsymbol{\lambda_1}$	-	-	1.00E-05	1.00E-07	-2.15E-04	-2.08E-04
	$\boldsymbol{\lambda_2}$	-	-	1.00E-05	3.34E-07	9.58E-06	9.99E-06
	$\mathbf{R^2}$	0.940	0.935	0.936	0.934	0.970	0.963
	P-Value	0.00	0.00	0.00	0.00	0.996	0.858
F2-30 mg/L	$\mathbf{K_d}$ or $\mathbf{K_{att}}$ *	2.39E-03[d]	2.27E-03[d]	2.45E-03[d]	2.29E-03[d]	2.07E-03[d]	1.94E-03[d]
	$\mathbf{K_{det}}$	9.84E-03	8.72E-03	1.02E-02	8.80E-03	8.00E-03	6.69E-03
	$\boldsymbol{\lambda_1}$	-	-	1.00E-05	1.00E-05	-1.28E-04	-1.14E-04
	$\boldsymbol{\lambda_2}$	-	-	1.00E-05	1.00E-05	9.97E-06	9.58E-06
	$\mathbf{R^2}$	0.970	0.964	0.968	0.962	0.983	0.974
	P-Value	0.01	0.02	0.01	0.01	0.94	0.69

[a] The unit of K_d is m^3/Kg and the units of other parameters are s^{-1}. [b] Allowing negative values for λ_1 and λ_2 in the calibration process. [c] K_d. [d] K_{att}.

Table S3. Number of the iterations in which 5% and 1% convergence were achieved for the parameter λ_1 in the iterative procedure, in different cases of the 1-D model.

	F3-1 g/L	**F3-3 g/L**	**F3-6 g/L**	**F2-1 g/L**	**F2-3 g/L**	**F2-6 g/L**	**F1-1 g/L**	**F1-3 g/L**	**F1-6 g/L**
5%	3	3	11	4	5	5	5	9	5
1%	4	4	37	6	9	8	9	22	9

Table S4. Mass recovery results at the final stage of the iteration procedure for each case of the1-D model.

	F1-6 g/L	**F1-3 g/L**	**F1-1 g/L**	**F2-6 g/L**	**F2-3 g/L**	**F2-1 g/L**	**F3-6**	**F3-3 g/L**	**F3-1 g/L**
Model M / M0	0.61	0.62	0.62	0.74	0.75	0.79	0.91	0.96	0.97
Experiment M / M0	0.61	0.61	0.62	0.73	0.74	0.80	0.91	0.96	0.97
Difference (%)	0.1	1.1	0.3	1.0	1.8	1.1	0.2	0.2	0.1

Table S5. Mass recovery results at the final stage of the iteration procedure for each case of the 2-D model.

	Washed MRNIP2	**Unwashed MRNIP2**	**Oxidized MRNIP2**
Model M/M0	0.43	0.32	0.55
Experiment M/M0	0.40	0.32	0.58
Difference (%)	6.5	0.7	4.4

Table S6. Input parameters and the results of calculating the agglomerate sizes based on Phenrat et al. (2010)(Phenrat et al. 2010b) for the cases of F1 and F2 of the 1-D model.

	d_p[a]	Q[b]	γ_s[c]	μ_0[d]	M_s[e]	M_W[f]	N_{avo}[g]	d_{MO}[h]	[NaCl][i]	d_{agg}[j]
F2	4.6E-07	9.85E-09	10.3	1.25E-06	400000	70	6.03E+23	7.5E-08	10	8.97E-07
F1	6.22E-07	9.85E-09	10.3	1.25E-06	400000	70	6.03E+23	6.3E-08	10	1.49E-06

[a]Particle diameter (m). [b]Total volumetric flow rate in the porous media (m^3/s). [c]Apparent shear rate (s^{-1}). [d]Magnetic permeability in vacuum (N/A^2). [e]NZVI saturation magnetization (A/m). [f]Molecular weight of polymeric surface modifier (kg/mol). [g]Avogadro's number (mol^{-1}). [h]Adsorbed polymer layer thickness determined from Ohshima's soft particle analysis (m). [i]NaCl concentration (mol/m^3). [j]Calculated agglomerate size (m) based on Phenrat et al. (2010).(Phenrat et al. 2010b)

Table S7. Input parameters and the results of calculating the agglomerate sizes based on Phenrat et al. (Phenrat et al. 2010b) for various layers in the case of the washed MRNIP2 of the 2-D model.

	d_p[a]	N_{Pore}[b]	V[c]	Q[d]	γ_s[e]	μ_0[f]	M_s[g]	M_W[h]	N_{avo}[i]	d_{MO}[j]	[NaCl][k]	d_{agg}[l]
Fine	2.53E-07	26708	2.48E-04	7.79E-05	53705	1.25E-06	711633	16	6.03E+23	7.0E-08	1	4.18E-07
Medium	2.53E-07	2909	3.09E-04	9.70E-05	22072	1.25E-06	711633	16	6.03E+23	7.0E-08	1	5.46E-07
Coarse	2.53E-07	263	1.25E-03	3.94E-04	39276	1.25E-06	711633	16	6.03E+23	7.0E-08	1	4.59E-07

[a]Particle diameter (m). [b]Number of pores in the column cross section. [c] Pore water velocity. [d]Total volumetric flow rate in the porous media (m^3/s). [e]Apparent shear rate (s^{-1}). [f]Magnetic permeability in vacuum (N/A^2). [g] NZVI saturation magnetization (A/m). [h]Molecular weight of polymeric surface modifier (kg/mol). [i]Avogadro's number (mol^{-1}). [j]Adsorbed polymer layer thickness determined from Ohshima's soft particle analysis (m). [k]NaCl concentration (mol/m^3). [l]Calculated agglomerate size (m) based on Phenrat et al. (2010b).

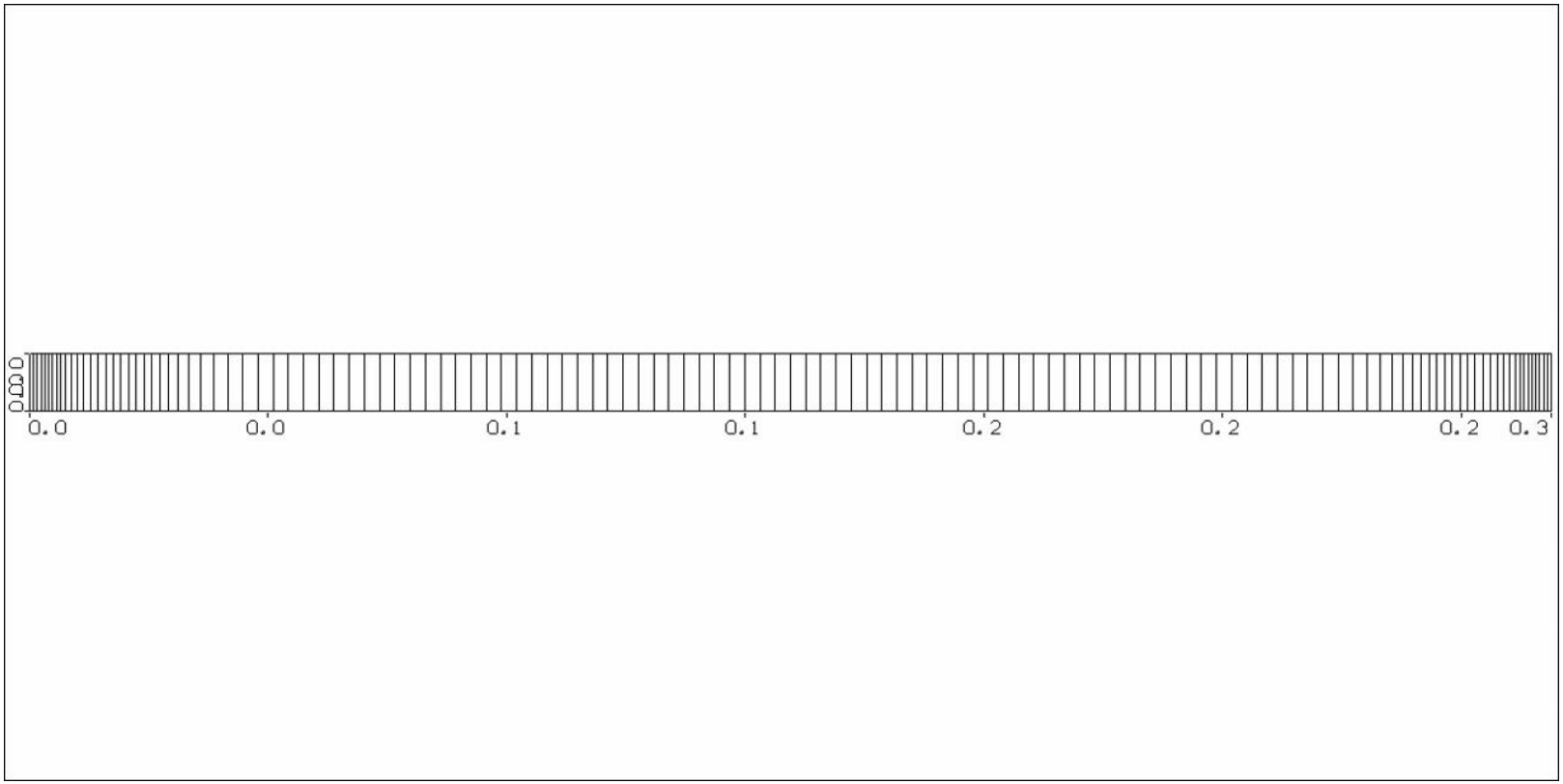

FIGURE S1. Display of the grid design for the 1-D model.

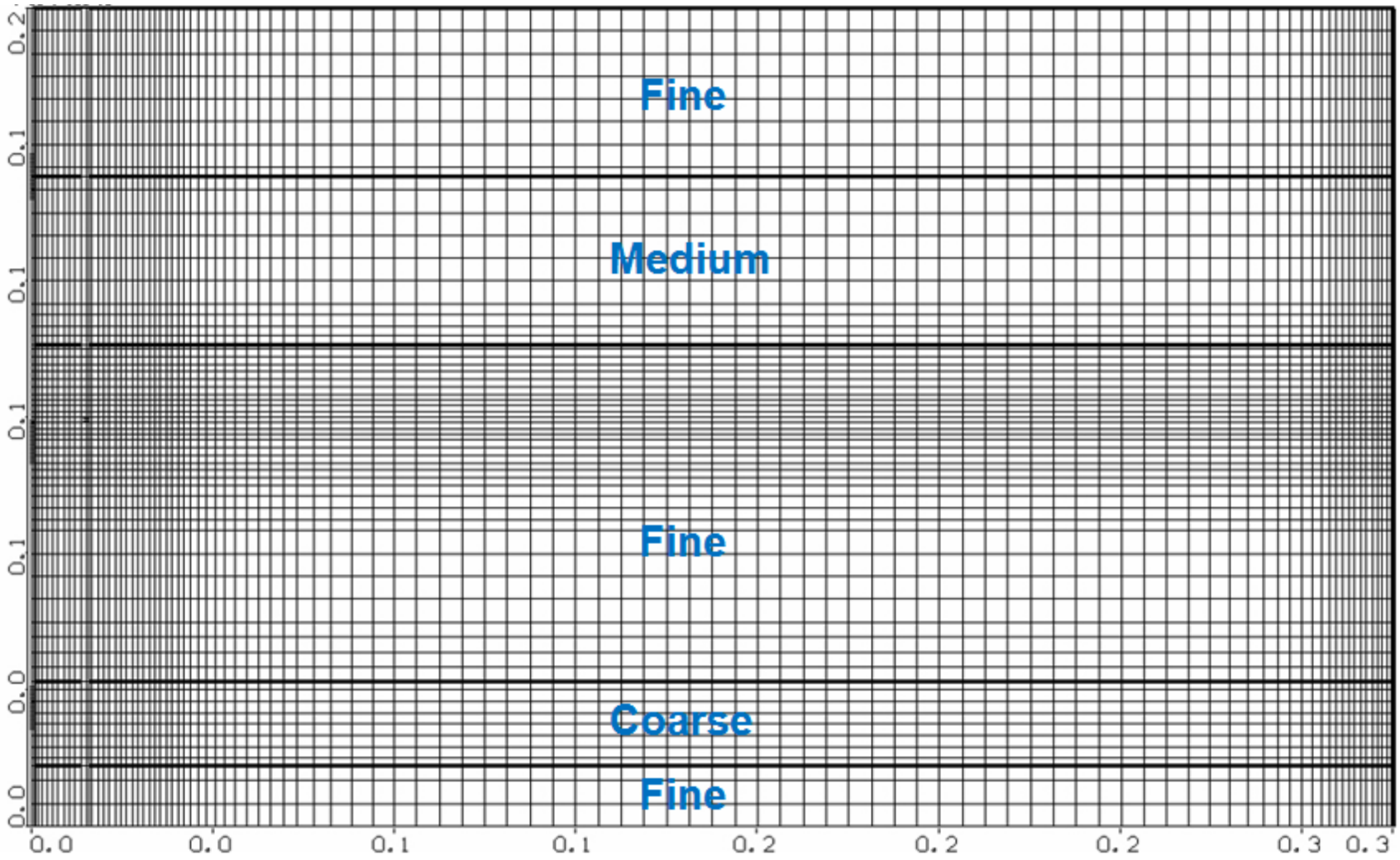

FIGURE S2. Display of the grid design for the 2-D model

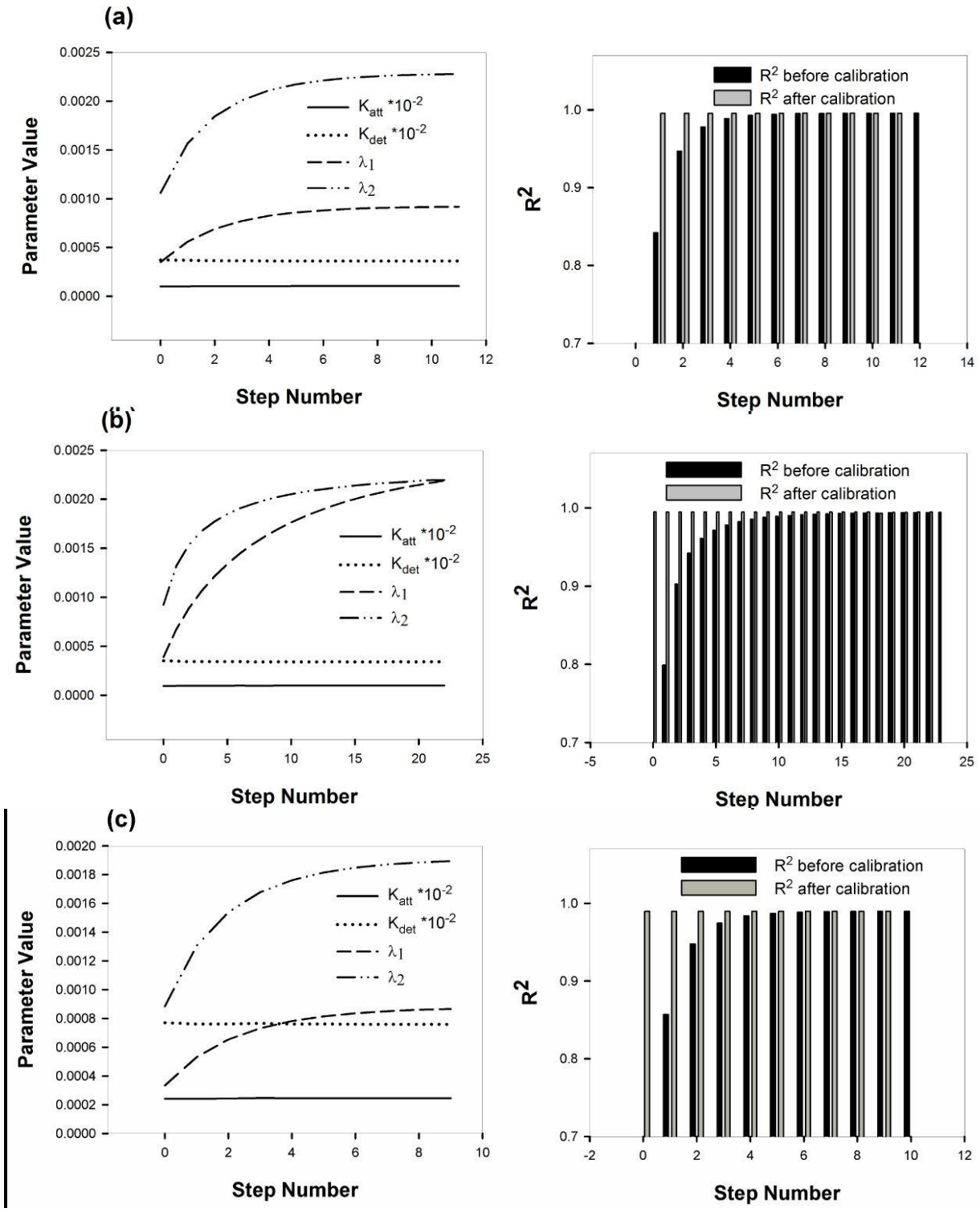

FIGURE S3. Variations in parameter values (left figures) and fitting results (right figures) during the iterative procedure for the case F1 at (a) 6 g/l, (b) 3 g/L, and (c) 1 g/L of the 1–D model.

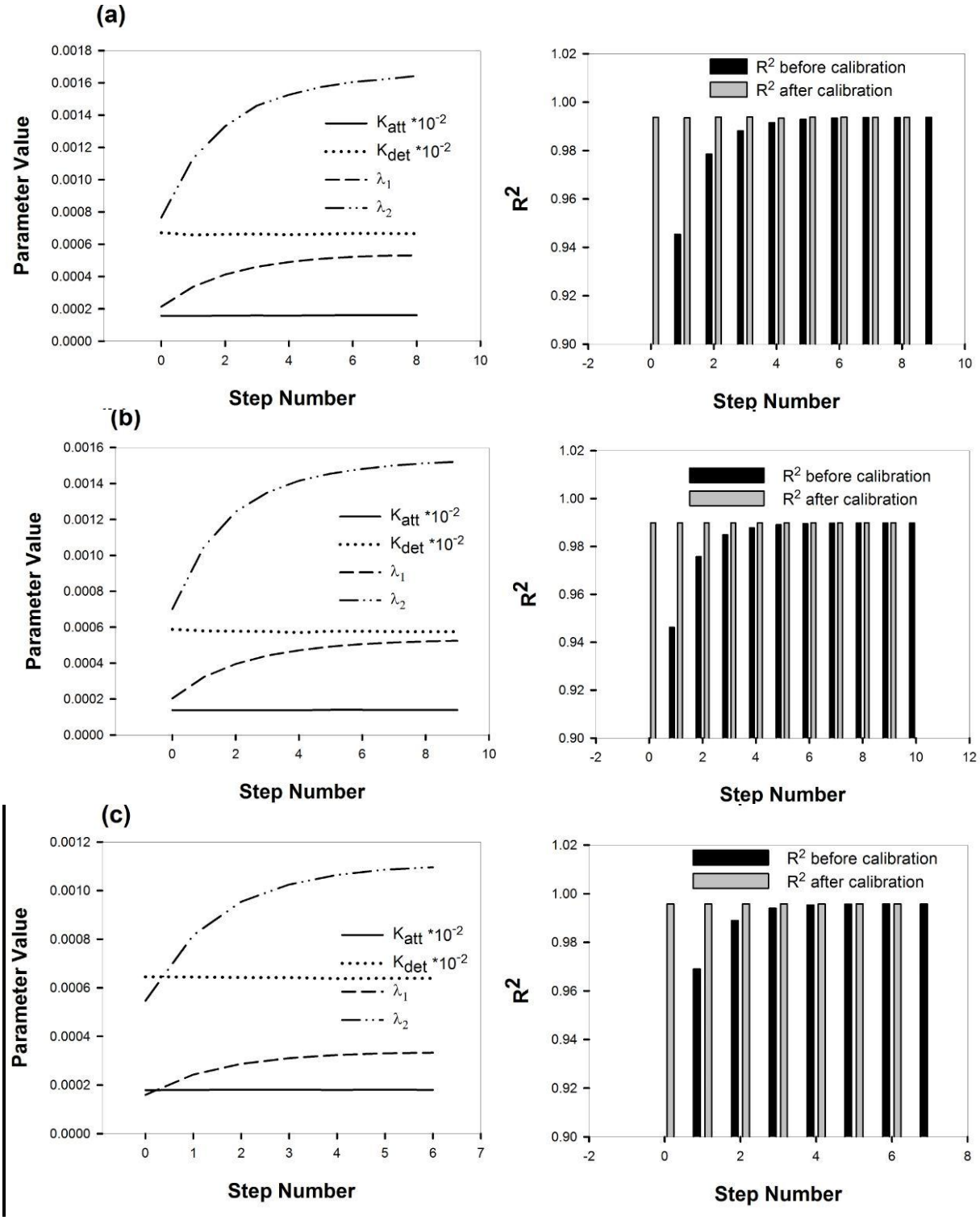

FIGURE S4. Variations in parameter values (left figures) and fitting results (right figures) during the iterative procedure for the case F2 at (a) 6 g/l, (b) 3 g/L, and (c) 1 g/L of 1–D model.

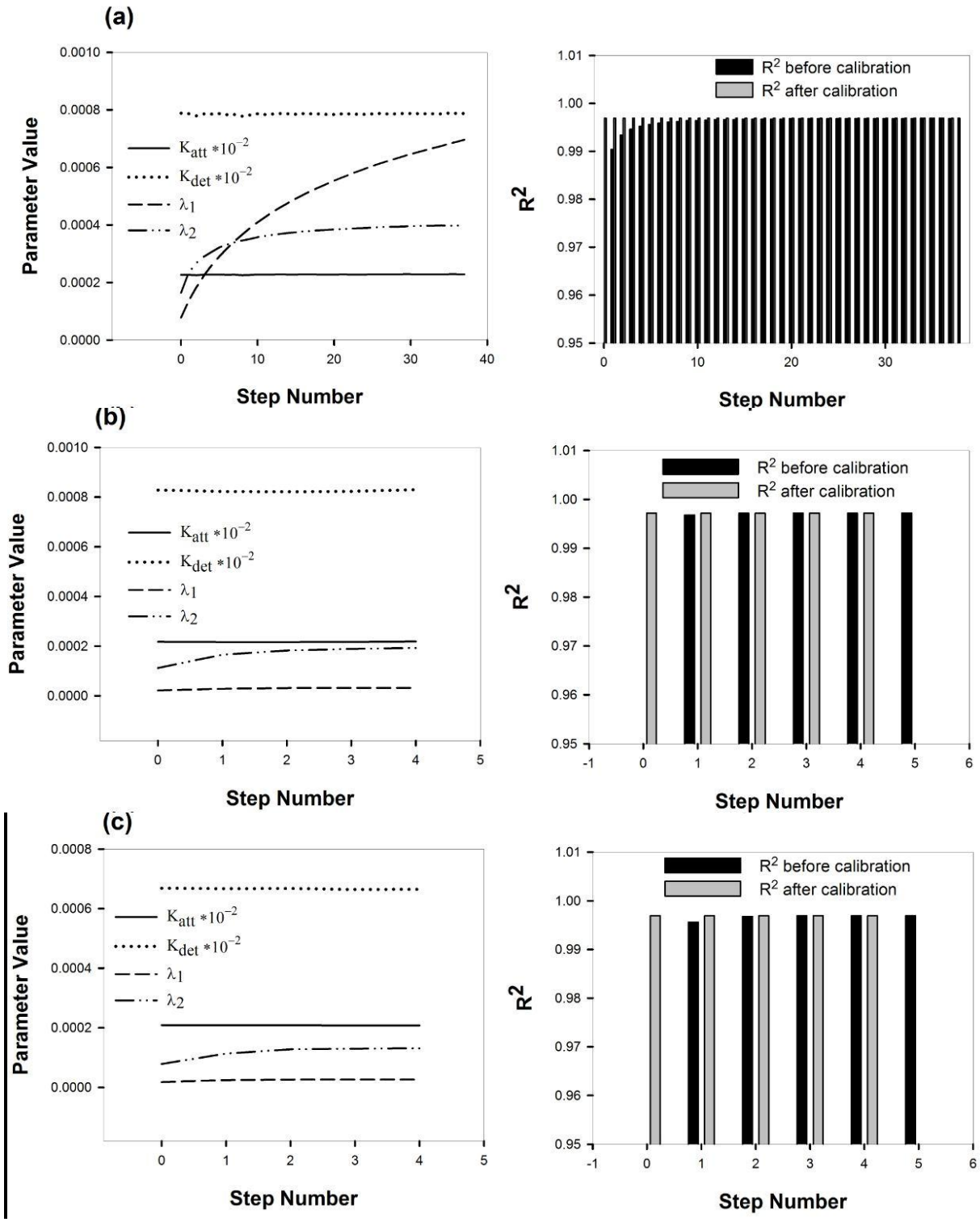

FIGURE S5. Variations in parameter values (left figures) and fitting results (right figures) during the iterative procedure for the case F3 at (a) 6 g/l, (b) 3 g/L, and (c) 1 g/L of 1–D model.

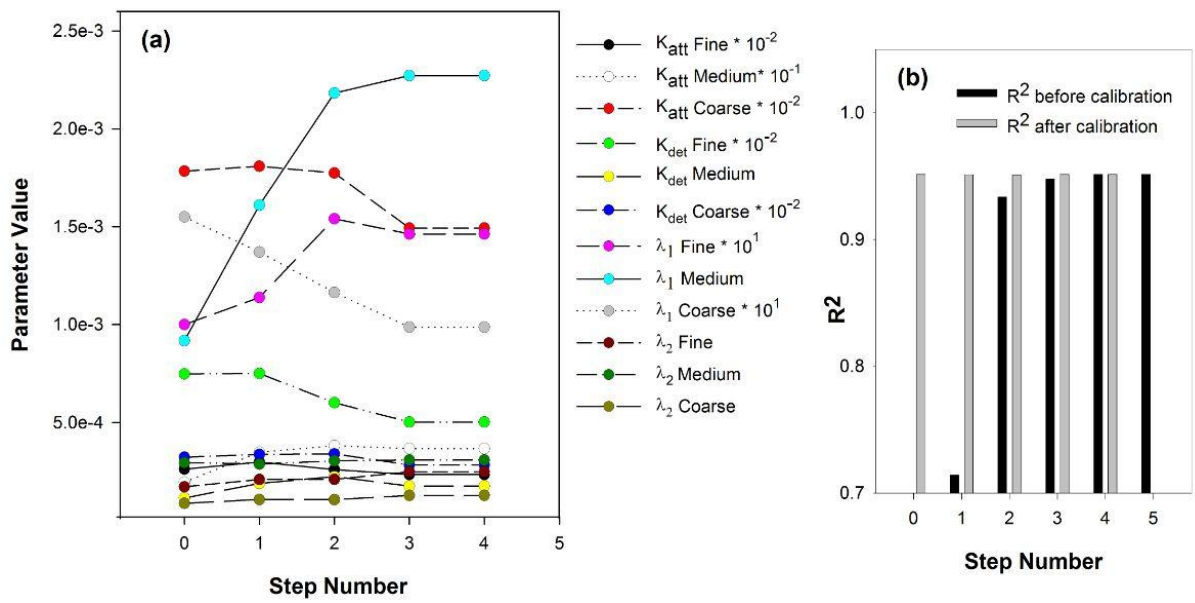

FIGURE S6. Variations in (a) parameter values and (b) fitting results during the iterative procedure for the case of the washed MRNIP2 in the 2-D model.

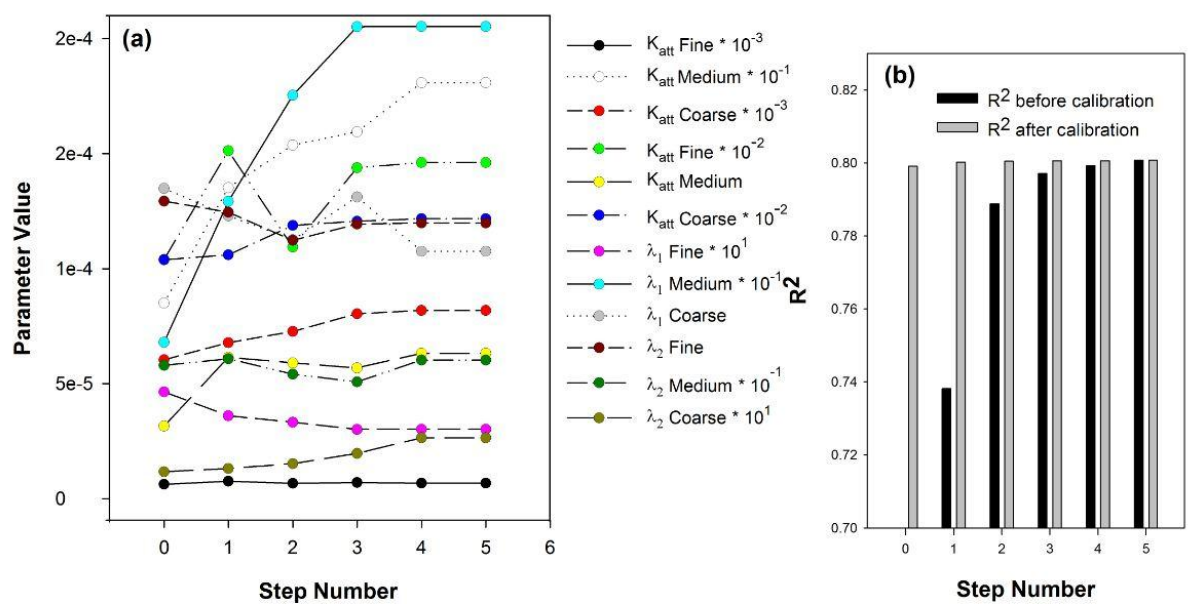

FIGURE S7. Variations in (a) parameter values and (b) fitting results during the iterative procedure for the case of the oxidized MRNIP2 in the 2-D model.

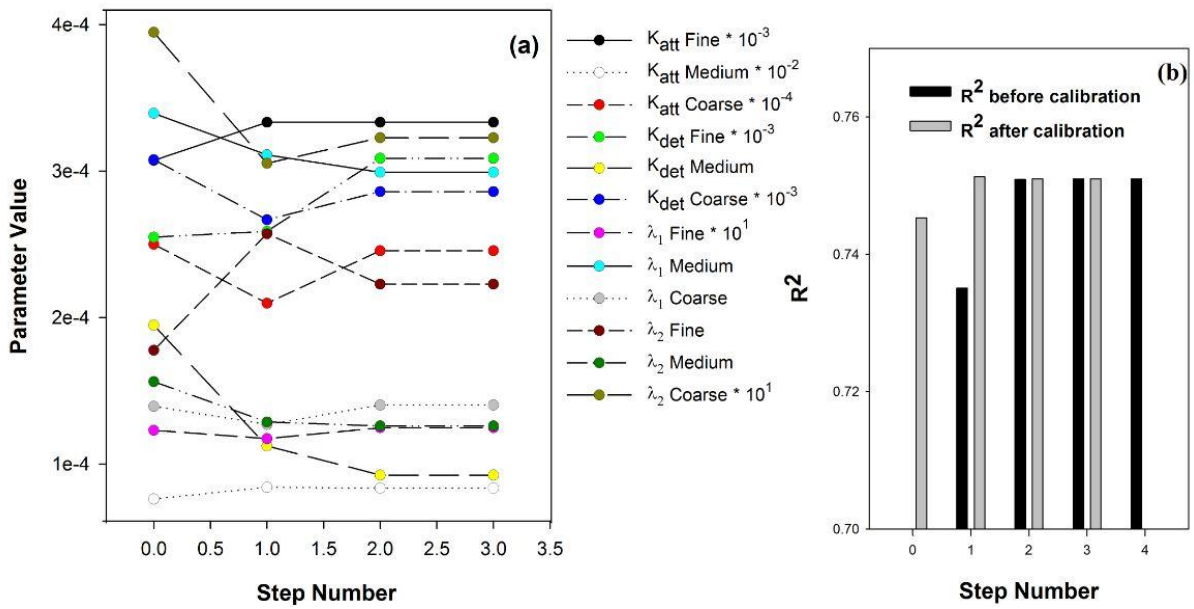

FIGURE S8. Variations in (a) parameter values and (b) fitting results during the iterative procedure for the case of the unwashed MRNIP2 in the 2-D model.

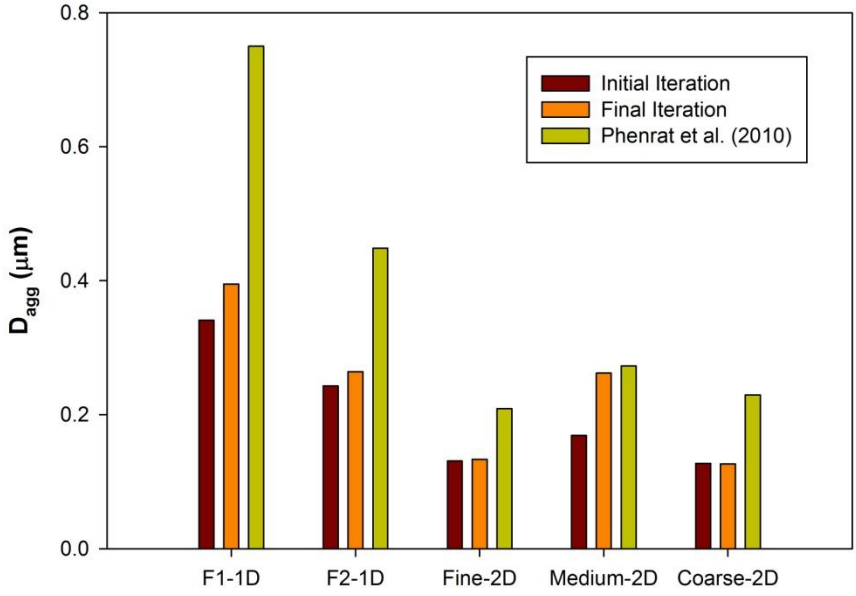

FIGURE S9. Comparison of the size (radius) of the agglomerates obtained in the initial iteration, in the final iteration, and by the empirical correlation of Phenrat et al. (Phenrat et al. 2010b) Input parameters and the results of their empirical correlation are presented in Tables S6 and S7.

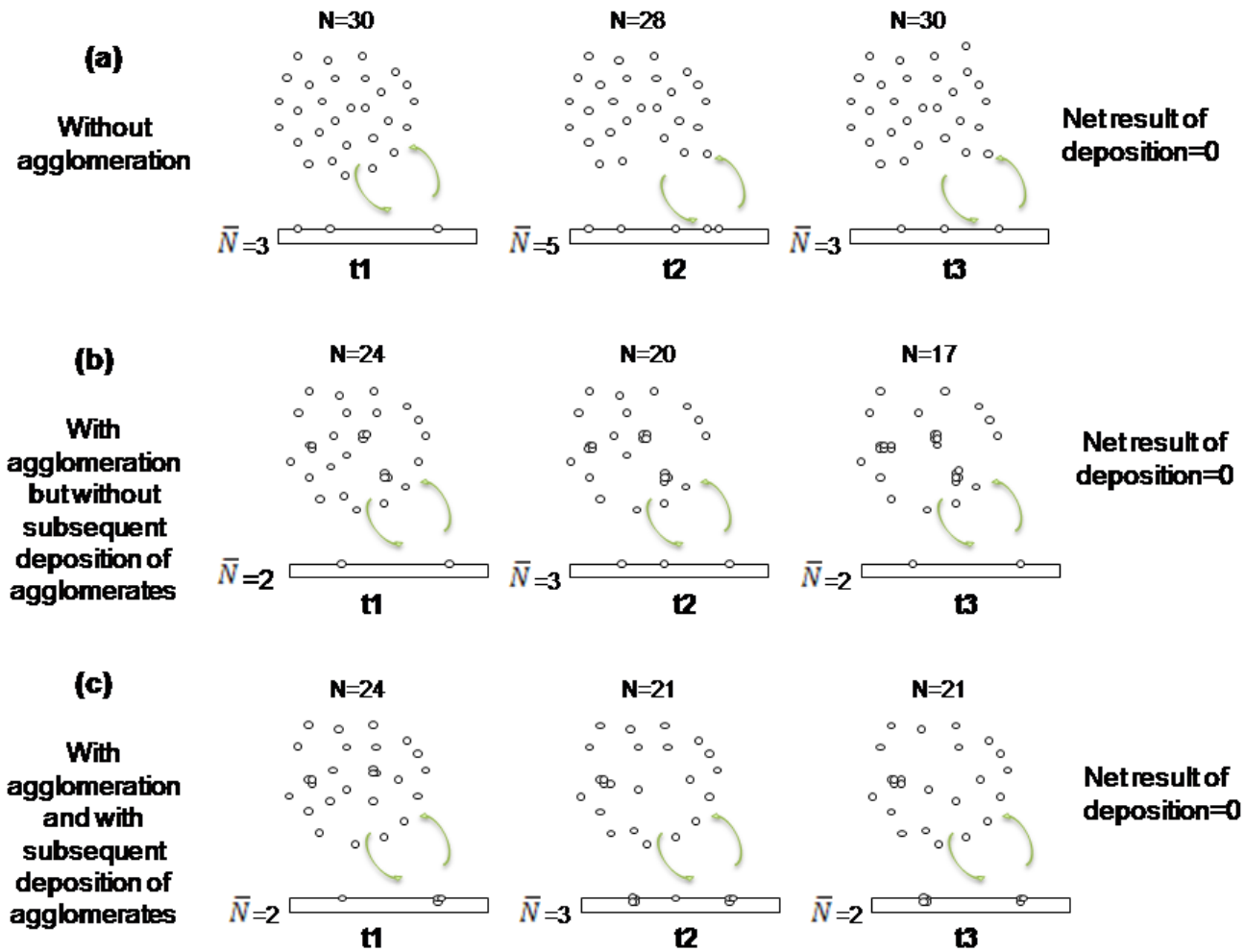

FIGURE S10. Various scenarios of the conceptual model. The numbers presented in the figure are only for enlightening purpose.

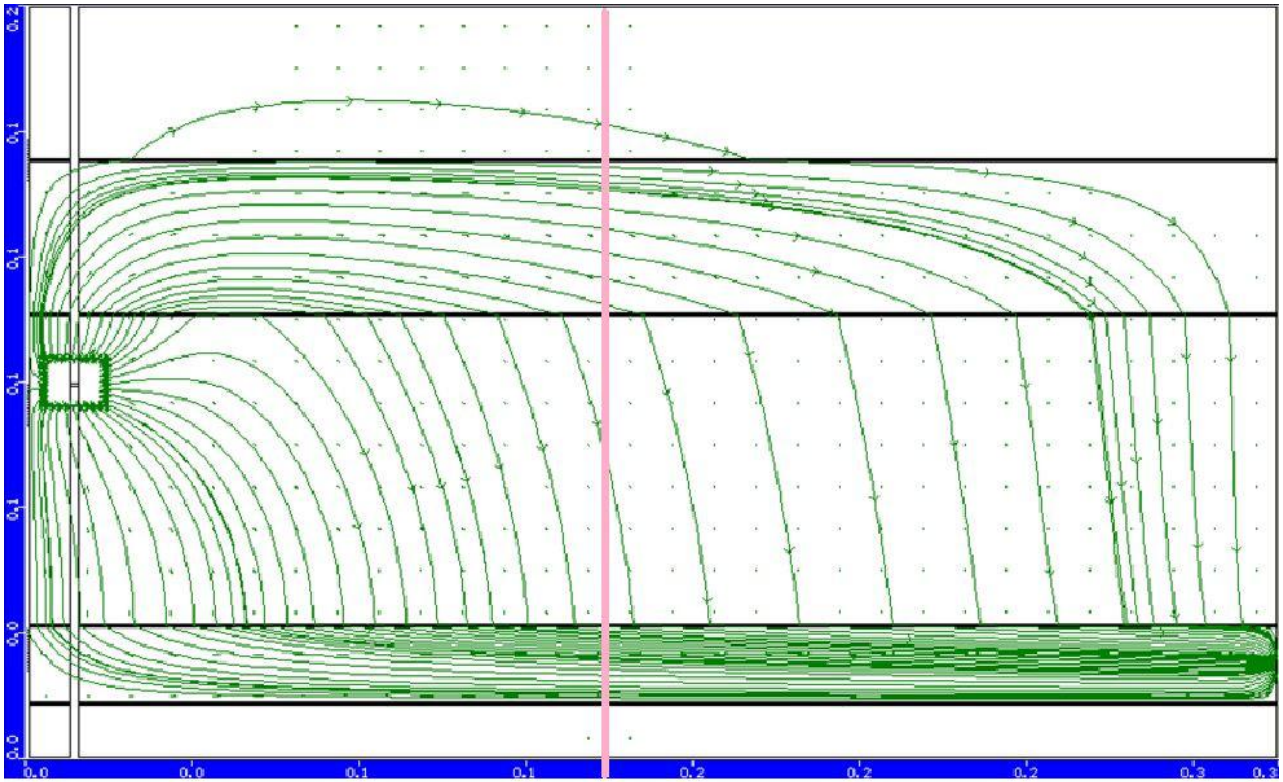

FIGUREFIGURE S11. Particle path lines obtained by the MODPATH model for calculating the weight of each layer in the averaging method.

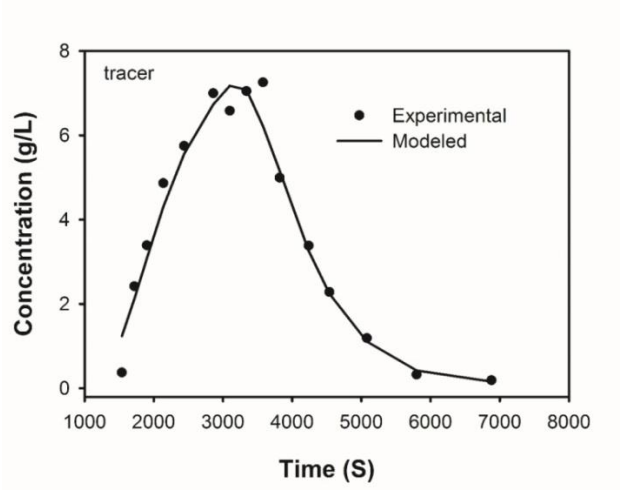

FIGURE S12. Comparison of modeled and experimental breakthrough curves of tracer data in the 2-D model.

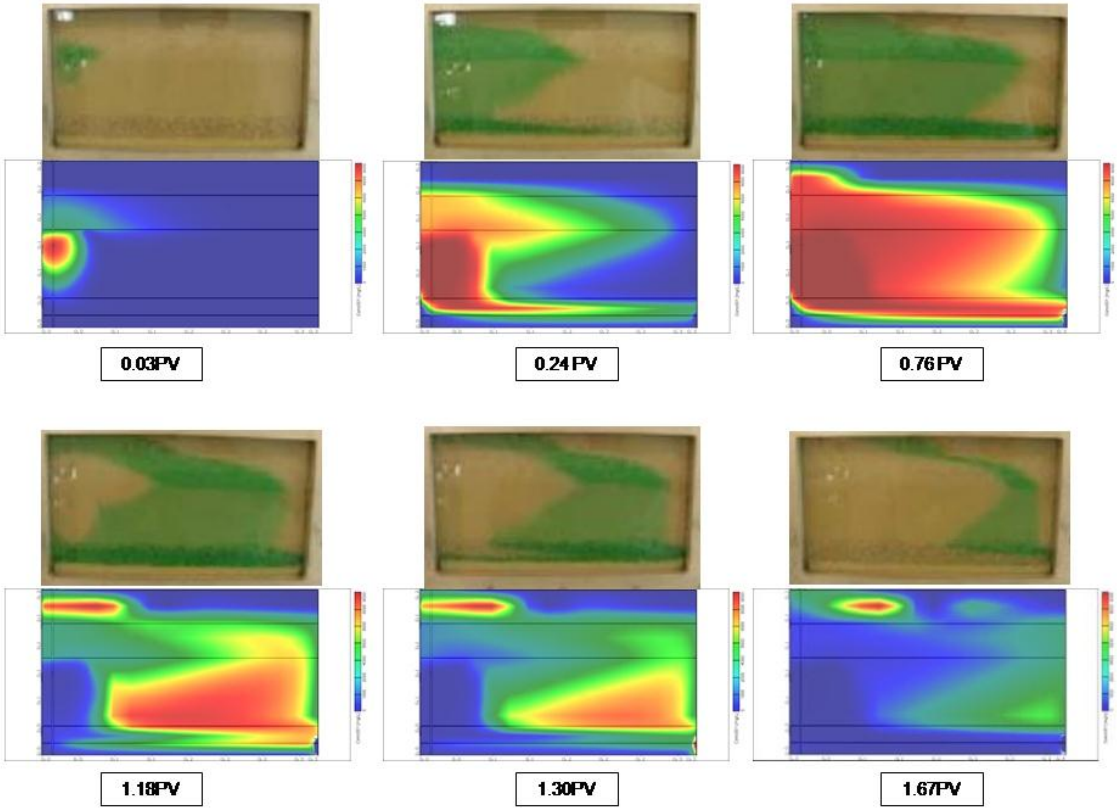

FIGURE S13. Comparison of the concentration contours of the tracer simulation results with the experimental photos.

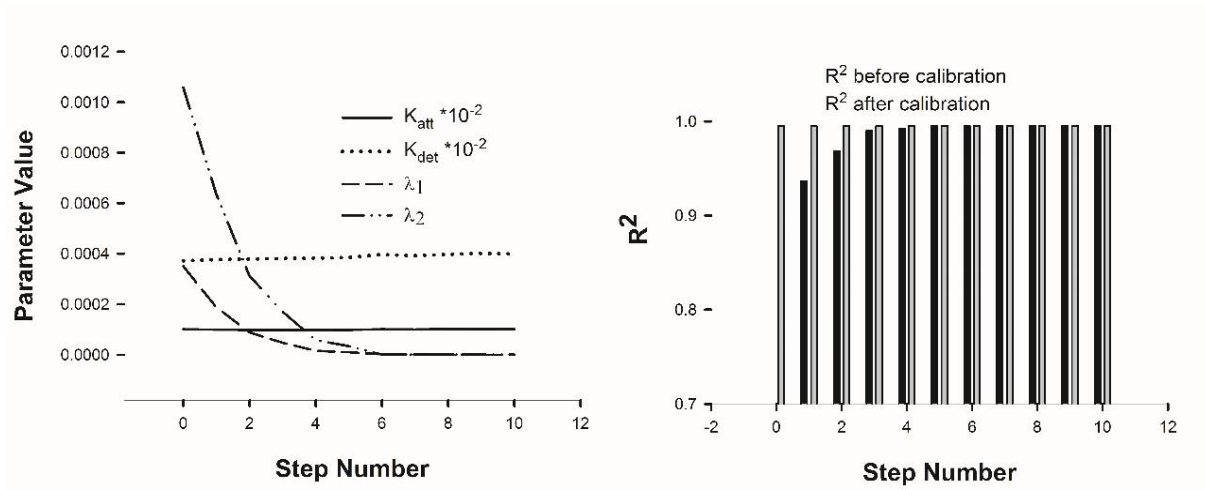

FIGURE S14. Variations in parameter values (left figures) and the fitting results (right figures) during the iterative procedure for the case of the F1 at 6 g/l when it was assumed that the C/C_0 in Eq. (7) was equal to the obtained C/C_0 from the experimental results.

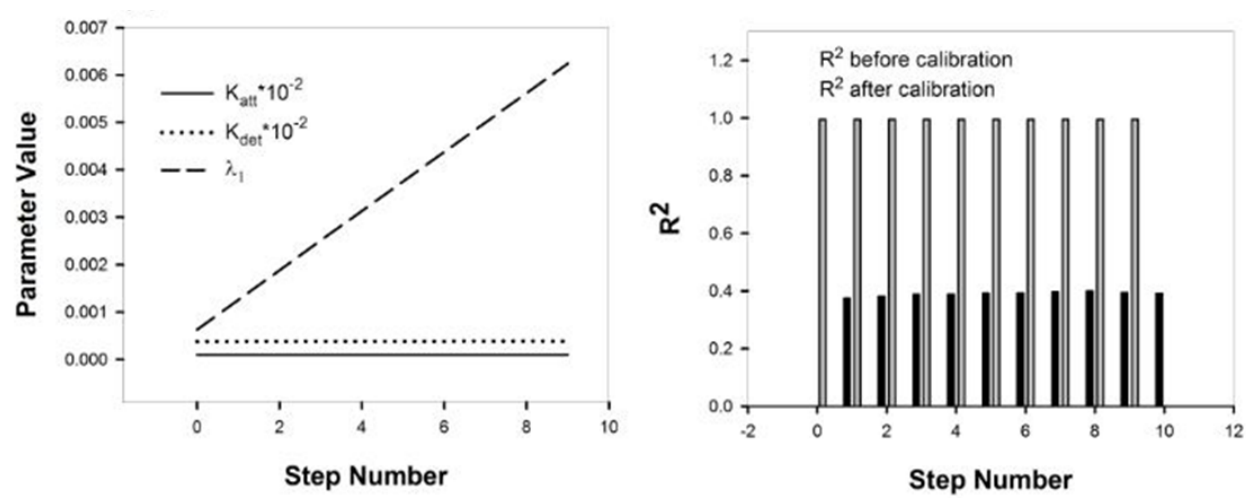

FIGURE S15. Variations in parameter values (left figure) and the fitting results (right figure) during the iterative procedure for the case F1 at 6 g/l with three parameters of K_{att}, K_{det}, and λ_1.

Literature Cited

Bradford SA, Simunek J, Bettahar M, van Genuchten MT, Yates SR (2006) Significance of straining in colloid deposition: Evidence and implications Water Resour Res 42:W12S15 doi:10.1029/2005WR004791

Fagerlund F, Illangasekare TH, Phenrat T, Kim HJ, Lowry GV (2012) PCE dissolution and simultaneous dechlorination by nanoscale zero-valent iron particles in a DNAPL source zone Journal of Contaminant Hydrology 131:9-28 doi:10.1016/j.jconhyd.2011.08.011

Harbaugh AW, Banta ER, Hill MC, McDonald MG, U.S. Geological S (2000) MODFLOW-2000: The U.S. Geological Survey Modular Ground-water Model--user Guide to Modularization Concepts and the Ground-water Flow Process. U.S. Geological Survey open-file report 00-92. U.S. Department of the Interior, U.S. Geological Survey,

Harbaugh AW, U.S. Geological S (2005) MODFLOW-2005, The U.S. Geological Survey Modular Ground-Water Model—the Ground-Water Flow Process vol 6. Modeling techniques, Section A. U.S. Geological Survey Techniques and Methods 6–A16. U.S. Department of the Interior, U.S. Geological Survey,

Hotze EM, Phenrat T, Lowry GV (2010) Nanoparticle Aggregation: Challenges to Understanding Transport and Reactivity in the Environment J Environ Qual 39:1909–1924 doi:10.2134/jeq2009.0462

Illangasekare TH, Frippiat CC, Fuˇcík R (2010) Dispersion and Mass Transfer Coefficients in Groundwater of Near-Surface Geologic Formations. Handbook of Chemical Mass Transport in the Environment. CRC Press/Taylor and Francis Group,

Kanel SR, Goswami RR, Clement TP, Barnett MO, Zhao D (2007) Two dimensional transport characteristics of surface stabilized zero-valent iron nanoparticles in porous media Environmental Science & Technology 42:896-900

Kanel SR, Goswami RR, Clement TP, Barnett MO, Zhao D (2008) Two Dimensional Transport Characteristics of Surface Stabilized Zero-valent Iron Nanoparticles in Porous Media Environmental Science & Technology 42:896-900 doi:10.1021/es071774j

Nash JE, Sutcliffe JV (1970) River flow forecasting through conceptual models part I — A discussion of principles Journal of Hydrology 10:282-290 doi:10.1016/0022-1694(70)90255-6

Parker JC, Van Genuchten T, Virginia Agricultural Experiment S (1984) Determining Transport Parameters from Laboratory and Field Tracer Experiments. Bulletin (Virginia Agricultural Experiment Station). Virginia Agricultural Experiment Station,

Pennell KD, Abriola LM, Weber WJ (1993) Surfactant-enhanced solubilization of residual dodecane in soil columns. 1. Experimental investigation Environmental Science & Technology 27:2332-2340 doi:10.1021/es00048a005

Phenrat T, Cihan A, Kim H-J, Mital M, Illangasekare T, Lowry GV (2010a) Transport and deposition of polymer-modified Fe0 nanoparticles in 2-D heterogeneous porous media: Effects of particle concentration, Fe0 content, and coatings Environmental Science & Technology 44:9086-9093

Phenrat T, Kim H-J, Fagerlund F, Illangasekare T, Lowry GV (2010b) Empirical correlations to estimate agglomerate size and deposition during injection of a polyelectrolyte-modified Fe0 nanoparticle at high particle concentration in saturated sand Journal of Contaminant Hydrology 118:152-164 doi:10.1016/j.jconhyd.2010.09.002

Phenrat T, Kim HJ, Fagerlund F, Illangasekare T, Tilton RD, Lowry GV (2009) Particle size distribution, concentration, and magnetic attraction affect transport of polymer-modified Fe0 nanoparticles in sand columns Environ Sci Technol 43:5079-5085

Pollock DW (1994) User’s Guide for MODPATH/MODPATH-PLOT, Version 3: A particle tracking post-processing package for MODFLOW, the U. S. Geological Survey finite-difference ground-water

flow model. U. S. GEOLOGICAL SURVEY, U. S. DEPARTMENT OF THE INTERIOR, Reston, Virginia

Rumbaugh JO, Rumbaugh DB (2011) Guide to Using Groundwater Vistas Version 5 Environmental Simulations Inc. (ESI), Reinholds, PA 17569, U.S.

Schijven JK, Hassanizadeh SM (2000) Removal of viruses by soil passage: Overview of modeling, processes, and parameters Crit Rev Environ Sci Technol 30:49 – 127

Schlumberger Water Services I (2011) Visual MODFLOW 2011.1 User's Manual. Kitchener, Ontario, CANADA, N2G 4Y9

Wang Y, Li Y, Fortner JD, Hughes JB, Abriola LM, Pennell KD (2008) Transport and Retention of Nanoscale C60 Aggregates in Water-Saturated Porous Media Environmental Science & Technology 42:3588-3594 doi:10.1021/es800128m

Watermark Numerical Computing & Waterloo Hydrogeologic I (1999) WinPEST User's Manual: Non-linear Parameter Estimation and Predictive Analysis Program.

Zheng C, Bennett G (2002) Applied Contaminant Transport Modeling. Wiley, New York

Zheng C, Wang P (1999) MT3DMS, A modular three-dimensional multi-species transport model for simulation of advection, dispersion and chemical reactions of contaminants in groundwater systems; documentation and user's guide US Army Corpes Engineers, Engineer Research and Development Center, Contract Report SERDP-99-1, Vicksburg, MS:202 doi:citeulike-article-id:5768548

Environmental Science & Technology

Article

pubs.acs.org/est

Electromagnetic Induction of Zerovalent Iron (ZVI) Powder and Nanoscale Zerovalent Iron (NZVI) Particles Enhances Dechlorination of Trichloroethylene in Contaminated Groundwater and Soil: Proof of Concept

Tanapon Phenrat,[*,†,‡] Thippawan Thongboot,[†,‡] and Gregory V. Lowry[§,∥]

[†]Research Unit for Integrated Natural Resources Remediation and Reclamation (IN3R), Department of Civil Engineering, Faculty of Engineering, Naresuan University, Phitsanulok, Thailand, 65000

[‡]Center of Excellence for Sustainability of Health, Environment, and Industry (SHEI), Faculty of Engineering, Naresuan University, Phitsanulok, Thailand, 65000

[§]Center for Environmental Implications of Nanotechnology (CEINT) and [∥]Department of Civil & Environmental Engineering, Carnegie Mellon University, Pittsburgh, Pennsylvania 15213, United States

Supporting Information

ABSTRACT: This study evaluates the concept of using zerovalent iron (ZVI) powder or nanoscale zerovalent iron (NZVI) particles in combination with a low frequency (150 kHz) AC electromagnetic field (AC EMF) to effectively remove trichloroethylene (TCE) from groundwater and saturated soils. ZVI and NZVI are ferromagnetic, which can induce heat under applied AC EMF. The heat generated by ZVI and NZVI induction can increase the rate of dechlorination, according to Arrhenius' equation, and increase the rate of TCE desorption from TCE-sorbed soil. Both dechlorination and TCE desorption enhance the overall TCE removal rate. We evaluated this novel concept in laboratory batch reactors. We found that both ZVI and NZVI can induce heat under applied AC EMF up to 120 °C in 20 min. Using ZVI and NZVI with AC EMF enhanced dechlorination of dissolved TCE (no soil) up to 4.96-fold. In addition to increasing the temperature by ZVI and NZVI induction heating, AC EMF increased intrinsic ZVI and NZVI reactivity, ostensibly due to accelerated corrosion, as demonstrated by the increased ORP. In a soil-water-TCE system, NZVI together with AC EMF thermally enhanced desorption of TCE from soil and increased the degradation of TCE up to 5.36-fold compared to the absence of AC EMF. For the first time, this study indicates the potential for ZVI and NZVI coupled with AC EMF as a combined remediation technique for increasing the rate and completeness of in situ cleanup of adsorbed phase contaminants.

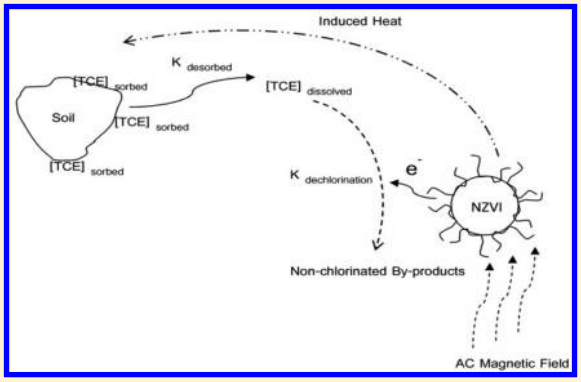

1. INTRODUCTION

In situ chemical reduction (ISCR) using zerovalent iron (ZVI)-based agents is a well-known remediation technology. In situ ZVI applications include permeable reactive barriers (PRBs) that intercept and treat the contaminant plume as it moves through the barrier,[1−6] and more recently, include injection of nanoscale zerovalent iron (NZVI) into source zones or contaminated soils.[6−15] By 2004, there were at least 120 pilot-scale and field-scale ZVI permeable reactive barriers installed.[16] By 2009, more than 45 pilot-scale and field-scale NZVI remediation tests had been conducted.[17,18] In this process, zerovalent iron (Fe^0) is oxidized by chlorinated organics (as electron acceptors), such as trichloroethylene (TCE), which are reduced to more environmentally benign byproducts, like acetylene, ethane, and ethene.[19−23] At neutral pH, Fe^0 is transformed primarily to magnetite (Fe_3O_4), but a mixture of magnetite and maghemite (Fe_2O_3) has also been reported.[24,25]

A major problem plaguing the success of NZVI is the slow rate of dissolution of TCE from nonaqueous phase liquid (NAPL)[22] or slow desorption of TCE from soil to the aqueous phase.[26,27] This is because the reaction is surface mediated; therefore, contaminants must be dissolved to transport to the NZVI surface. For this reason, the rate of TCE degradation is limited by the rate of mass transfer to the aqueous phase.[6,28] Rather, the ZVI or NZVI reacts with water to form H_2, which increases the amount of ZVI or NZVI required for remediation. Therefore, any action to enhance DNAPL dissolution or to

Received: September 14, 2015
Revised: December 8, 2015
Accepted: December 11, 2015
Published: December 11, 2015

DOI: 10.1021/acs.est.5b04485
Environ. Sci. Technol. 2016, 50, 872−880

enhance contaminant desorption can speed the reaction rate and improve the electron efficiency of the remediation.

In addition to being a reducing agent, ZVI is ferromagnetic.[29−31] Nevertheless, its magnetic property has only recently been used for enhancing the pollutant removal rate. In 1999, Jovanovic's research group first utilized the magnetic property of micron-sized Pd/ZVI particles impregnated into calcium alginate beads to make a magnetically stabilized fluidized bed (MSFB) reactor for dechlorination of *p*-chlorophenol possible under an applied DC electromagnetic field (DC MF).[32−34] However, the magnetic property of ZVI was not intentionally used to enhance the *p*-chlorophenol degradation in these studies. In 2011, Choi's research group reported that applying DC MF to ZVI can induce an oxidation reaction due to the enhanced O_2 dissolution and ZVI dissolution to Fe^{2+} for Fenton's reaction.[35] In addition, DC MF can also increase the stability of radicals by inhibiting their recombination through interaction with electron spins.[36] Recently, Guan's research group presented a series of experimental studies using superimposed weak magnetic field or premagnetization to enhance the removal efficacies of various metal and metalloid, including antimony, arsenic, chromate, copper, and selenite[37−42] by ZVI. The enhanced removal was attributed to the accelerated ZVI corrosion and the transformation of amorphous iron (hydro) oxides to lepidocrocite. During experiments, ORP was observed to have substantially decreased, whereas Fe^{2+} dissolution significantly increased after premagnetizing ZVI with DC MF. The accelerated ZVI corrosion was explained by the magneto-convection of Fe^{2+}. According to this theory, MF causes an additional convective transfer of solutes to the surface of a ferromagnetic electrode (such as ZVI) due to the difference in the magnetic susceptibility of solutes and the electrode surface[43] as well as the difference in the magnetic susceptibility of solute and solvent molecules.[44] Guan's research group conducted a simulation to illustrate that the field gradient force can accumulate paramagnetic Fe^{2+} ions along the higher field gradient at the ZVI particle surface, which creates localized galvanic couples and electromagnetic forces that stimulate the migration of ions, the breakdown of passive film, and eventually the enhancement of localized corrosion.[39,41] This phenomenon results in the higher reduction capacity of ZVI than that without DC MF. Similarly, the same field gradient force can act on paramagnetic metal ions such as Cu^{2+} to expedite Cu^{2+} adsorption on the ZVI surface.[41]

Although ferromagnetism of ZVI has recently been utilized for enhanced contaminant removal, a low frequency AC EMF (50−200 kHz) to enhance ZVI reactivity has not yet been examined. The AC EMF can potentially enhance the TCE dechlorination rate through two theoretical phenomena similar to those of DC MF, enhanced ZVI corrosion and magneto-convection of TCE to the ZVI surface. Nevertheless, AC EMF has the potential to speed up TCE remediation in groundwater and soil even better than the DC EMF via electromagnetic induction heating of ZVI and NZVI. In the medical field, magnetite nanoparticles (Fe_3O_4) are used in thermal treatments, such as magnetic assisted hyperthermia,[45] where functionalized magnetic nanoparticles target tumor cells and then they are heated by applied AC EMF to kill the cancer cells.[46] Similarly, ZVI or NZVI should be able to induce heat under an applied low frequency AC EMF. The heat generated can speed up the dechlorination reaction and can promote DNAPL dissolution or desorption of contaminants from soils. Truex et al. combined moderate-temperature subsurface electrical resistance heating (up to 50 °C) with in situ ZVI treatment in a field scale using an average power of 450 kW·h per day for a 58 m^3 treated area. They reported acceleration of TCE degradation up to four to eight times, presumably due to increasing both reaction and TCE dissolution from NAPL.[47] Electromagnetic induction heating should improve remediation in a similar way, and with less energy input. A schematic of the proposed process is shown in Figure S1 and S2 in SI (Supporting Information).

The present study evaluates the feasibility of using low frequency AC EMF (150 kHz) together with ZVI and NZVI to enhance TCE degradation in soil and groundwater. Magnetic characterization was conducted for both ZVI and NZVI. Batch experiments were conducted to evaluate the ability of ZVI and NZVI to generate heat under an applied EMF. The TCE degradation kinetics in groundwater and in soil with groundwater by ZVI and NZVI both with and without AC EMF were compared to quantify the benefits of using AC EMF.

2. MATERIALS AND METHODS

2.1. Soil and Groundwater. Soil and groundwater samples used in this study were collected from an upstream location (i.e., no TCE was detected in the area) from a contaminated site in the Map Ta Phut (MTP) Industrial Estate in Rayong Province, Thailand (see more details of sampling methods and rationales in SI). Physicochemical properties of soil including fraction of organic carbon (foc), soil texture, size distribution, and specific gravity were measured. Physicochemical properties of the groundwater including temperature, pH, ORP, conductivity, alkalinity, total organic carbon (TOC), species of cations, and anions were measured using standard analytical methods.

2.2. TCE Sorption Kinetics, Partitioning Coefficient, and Desorption Kinetics. The TCE sorption rate, sorption capacity, and desorption kinetics of MTP soil were measured by headspace measurement in serum bottles capped by Teflon Mininert valves as specified in SI. For TCE sorption experiment, each bottle contained 10 mL of headspace, 10 mL of soil slurry (4:6 of soil-to-groundwater ratio by volume), and 100 mg/L of TCE. At selected time points, a 100-μL headspace sample was withdrawn from the reactors and analyzed for TCE using GC/ECD. As no degradation byproduct was observed, the depletion in the aqueous TCE concentration was attributed to partitioning of TCE to the soil. The adsorbed TCE concentration was then calculated from mass balance.

On the other hand, desorption kinetics of TCE were studied by displacing supernatant with deionized water in the individual vials after the sorption equilibrium was achieved at 85 days of the TCE sorption kinetics experiment, then the experimental procedure continued in the same way as in the sorption kinetics experiments. The desorption kinetics were evaluated for three consecutive cycles.

2.3. ZVI, NZVI, Magnetite, and Magnetic Characterization. Two different ZVI samples were used, H150 and H200 (Hepure, Claymond, DE). Table S1 (in SI) summarizes the physical properties of H150 and H200 as obtained from the supplier. Nanofer 25 (NF25) (Nanoiron, Czech Republic) was the NZVI used. Table S2 (in SI) summarizes the physical properties of NF25 as obtained from the supplier. In addition, MRNIP, a nearly fully oxidized NZVI (Fe^0 content <5%), from Toda Corporation and magnetite nanoparticles (Fe_3O_4) (Nano

DOI: 10.1021/acs.est.5b04485
Environ. Sci. Technol. 2016, 50, 872−880

Amore, USA) were used. These particles could not dechlorinate TCE but responded to the AC EMF. All ZVI, NZVI, and magnetite particles were characterized by X-ray diffraction (XRD) and magnetic susceptibility using a vibrational sample magnetometer (VSM).

2.4. Magnetic Induction Heating (MIH) Rate of ZVI and NZVI. To investigate the rate of heating induced by ZVI and NZVI under applied AC EMF, H150, H200, NF25, MRNIP2, and magnetite suspensions were placed into the center of the induction coil of an AC EMF generator (AC EMFG) (Figure S3 in SI). The custom-made AC EMFG provided an AC EMF at the current intensity of 15 A at a frequency of 150 kHz. An infrared and contact thermometer (Fluke 561) (Fluke, Everett, WA) was used to monitor the temperature change from the induced heat. Additionally, 10 mL of ZVI, NZVI, or magnetite suspension at a particle concentration of 10 g/L (in both DI and MTP groundwater) was added to a 20 mL glass vial with a screw cap. The glass vial was inserted into an insulator prior putting into the induction coil for MIH study. The induced temperature under the applied AC EMF was monitored for 40 min or until the temperature reached 120 °C.

2.5. TCE Dechlorination in Aqueous Phase with and without AC EMF. The rate of TCE dechlorination in the aqueous phase by H150 (ZVI) and NF25 (NZVI) in DI and MTP groundwater was measured with and without applied AC EMF as fully described in SI. For the standard dechlorination study (i.e., without applied AC EMF), the TCE dechlorination rates were measured in 20 mL serum bottles capped with a Mininert closures. Each reactor contained 10 mL of headspace and 10 mL of liquid. The liquid mixture contained the suspension of either 10 g/L of NF25 or 50 g/L of H150 in either DI or MTP groundwater with the initial TCE concentration of 50 mg/L. A 100 μL headspace sample was withdrawn from the reactors at selected times and analyzed for TCE as described above for the adsorption studies. At the end of the study, a 100 μL headspace sample was withdrawn from the reactors and analyzed for dechlorination products including acetylene, ethane, and ethene. The reactors were rotated on an end-overend rotator at 30 rpm at 23 °C ± 2 °C throughout the study.

For dechlorination experiments under applied AC EMF, the experimental setup was modified by placing the insulated reactors into the center of induction coil of the AC EMFG that generated AC EMF at the current intensity of 15 A and the frequency of 150 kHz. For NF25, five cycles of electromagnetic induction heating were applied over 10 h. Each cycle was 2 h with 60 min of AC EMF application, followed by 60 min of reaction without AC EMF (i.e., cooling down). The temperature was measured by a contact IR thermometer at the end of the heating cycle. During the 60 min of reaction without AC EMF for each cycle, the insulated reactors were rotated on an end-over-end rotator at 30 rpm to allow dechlorination to take place at a gradually decreasing temperature. Finally, a 100 μL headspace sample was withdrawn from the reactors and analyzed for TCE when the temperature of the reactor was back to the room temperature. At the end of the fifth cycle, a 100 μL headspace sample was withdrawn from the reactors and analyzed for dechlorination byproducts.

A similar approach was used for H150 (ZVI). However, each cycle of reaction for H150 reactors consisted of 65 min with 5 min of AC EMF application, followed by 60 min of reaction without AC EMF. During the 60 min of reaction without AC EMF for each cycle, the insulated reactors were rotated on an end-overend rotator at 30 rpm. Due to the greater mass of H150 (50 g/L) in the reactors in comparison to NF25, the H150 reactors heated up much faster than the NF25 reactors. For this reason, we applied only a 5 min heating step for H150 reactors followed by 60 min of reaction without heating as they yielded a temperature of 80 °C, comparable to the temperature generated by NF25 reactors already.

Finally, yet importantly, in order to separate the AC EMF effect from the increasing temperature effect on TCE dechlorination rate, we conducted another set of TCE dechlorination experiments using NF25, but this time no AC EMF was applied. Nevertheless, a heating water bath was used to maintain the temperature profile for dechlorination similar to that obtained from the MIH study of NF25 with AC EMF. The difference between TCE dechlorination rates of the two cases should provide some insight into the role of AC EMF and NZVI magnetism beyond temperature effect. Moreover, to evaluate the hypothesis of enhanced TCE dechlorination via enhanced NZVI corrosion due to AC EMF, we measured ORP as a function of applied AC EMF time (at 5, 15, 30, and 60 min) for the reactors with NZVI in DI water at the previously described conditions as for TCE dechlorination. The decrease of ORP will support the possibility of enhanced NZVI corrosion hypothesis.

2.6. TCE Dechlorination for TCE Contaminated Soil and Groundwater with and without AC EMF. To assess the effect of AC EMF on the dechlorination of adsorbed TCE by NZVI, the rate of TCE degradation was measured in slurries containing soil, groundwater, and either NF25 or MRNIP2 with and without an applied EMF. In these studies, TCE is initially in equilibrium between the dissolved and soil-adsorbed phases. Without applied AC EMF, the TCE dechlorination rates were measured in 20 mL serum bottles capped with a Mininert closures. Each reactor contained 10 mL of headspace and 10 mL of TCE-contaminated soil-NZVI-groundwater slurry. To prepare the TCE contaminated soil, 20 mL reactors were filled with 8 mL of soil slurry (4:6 of MTP soil-to-groundwater ratio by volume) and 100 mg/L TCE. The reactors were equilibrated on a roller at 30 rpm at 23 ± 2 °C for 50 days. Then, a 100 μL headspace sample was withdrawn from the reactors and analyzed for TCE as described previously to determine the adsorbed mass of TCE. A 2 mL aliquot of concentrated NZVI was added to the soil/groundwater slurry to obtain the total of 10 mL of slurry with 10 g/L of NF25 or MRNIP2 together with 10 mL of headspace. The reactors were rotated on a roller at 30 rpm at 23 ± 2 °C throughout the study. At selected times, a 100 μL headspace sample was withdrawn from the reactors and analyzed for TCE. At the end of the study, a 100 μL headspace sample was withdrawn and analyzed for dechlorination byproducts including acetylene, ethane, and ethene. In addition, at the end of the study, a hexane extraction was performed by adding 5 mL of hexane to recover the remaining TCE (both dissolved and soil-sorbed phase) from the system.

An identical protocol was followed for dechlorination experiments under an applied AC EMF. However, the insulated reactors were placed into the center of the induction coil of the AC EMFG that generated an electromagnetic field at the current intensity of 15 A and the frequency of 150 kHz. Seven cycles of electromagnetic induction heating were applied in this enhanced dechlorination study, using the same procedure as

DOI: 10.1021/acs.est.5b04485
Environ. Sci. Technol. 2016, 50, 872−880

described for the reactions without soil. Hexane extraction was performed at the end of the study.

3. RESULTS AND DISCUSSION

3.1. MTP Soil and Groundwater Characteristics, TCE Partitioning, and TCE Desorption. The MTP soil and groundwater characteristics was described in SI. The TCE significantly partitioned to MTP soil (Figure S4a in SI). Moreover, K_d was 1.46 L/kg (Figure S4b in SI). Thus, according to the calculation assuming no headspace to simulate saturated subsurface, 75% of the TCE mass was adsorbed into the soil ($[TCE]_{sorbed}$ = 41 mg/kg) and 25% of the mass in groundwater ($[TCE]_{aq}$ = 25 mg/kg). According to the pseudo first order sorption kinetics (Figure.S4a in SI), the aqueous TCE removal rate via sorption is 4.95×10^{-2} day^{-1} (or 2.10×10^{-3} hr^{-1}).

As for the desorption behavior, three desorption cycles showed TCE desorption following exponential pattern to the plateau level. The pseudo first order desorption rates (Figure S5 in SI) were $11.80 \pm 5.50 \times 10^{-3}$ hr^{-1} for the first desorption cycle, $6.50 \pm 3.10 \times 10^{-3}$ hr^{-1} for the second desorption cycle, and $8.2 \pm 4.7 \times 10^{-3}$ hr^{-1} for the third desorption cycle. This suggests that slow desorption of TCE from MTP soil could limit the rate of TCE dechlorination by ZVI or NZVI.

3.2. Material and Magnetic Characteristics of ZVI and NZVI. The XRD analyses (Figure S6 in SI) confirm the existence of Fe^0 and Fe_3O_4 as the predominant phases present in all samples in this study. Nevertheless, MRNIP2 (aged NZVI) has a relatively higher fraction of Fe_3O_4 than NF25 (fresh NZVI) as expected. Each sample had unique magnetic responses under VSM test (Figure 1a), indicating differences in saturation magnetization (M_s), remanence (M_r), coercivity (H_c), and energy dissipation. Several general trends are observed and discussed in details in SI.

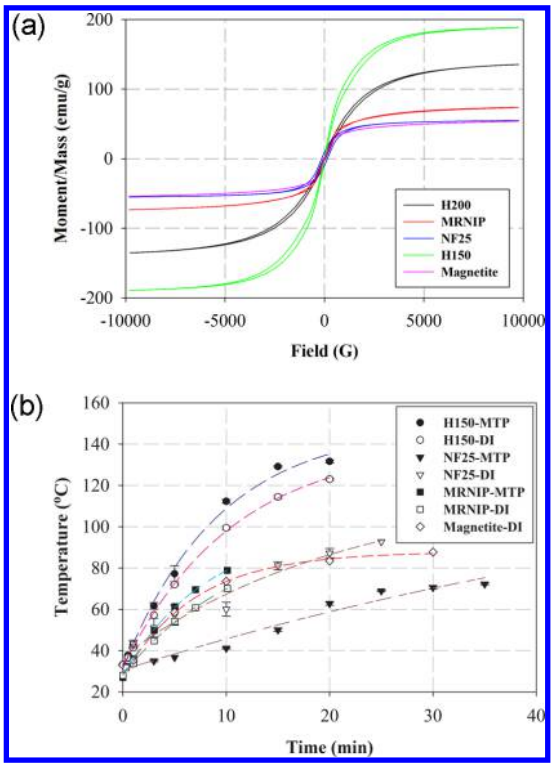

Figure 1. (a) Magnetic hysteresis behaviors of ZVI and NZVI as determined by VSM and (b) ZVI and NZVI suspension temperature increase vs AC EMF time for H150, NF25, MRNIP, and magnetite in DI and MTP groundwater.

The most important magnetic characteristic for the present study is the area under the hysteresis loop (ΔU) that represents the hysteresis loss due to the irreversible magnetization in an AC EMF. Hysteresis loss is one of three losses including eddy current loss and residual loss, which altogether generate heat during magnetic induction of magnetic particles in AC EMF. Figure S7 (in SI) enlarges the hysteresis curves (Figure 1a) from the field of 1000 to −1000 G to illustrate the hysteresis loops of each ZVI or NZVI sample. Noticeably, upon the magnetization and demagnetization cycle, magnetic particles respond irreversibly, causing hysteresis and loss of energy as heat. The degree of irreversibility, ΔU, is related to the amount of energy dissipation upon the reversal of the field. Under AC EMF, the reversal happens continuously and yields heat by energy dissipation from the particles. For a particular frequency (f) of AC EMF, heat (P) generated due to the hysteresis loss is given by eq 1.[48]

$$P = f\Delta U \tag{1}$$

The order of ΔU for ZVI and NZVI is as follows: H150 (12×10^4 emu G/g) > H200 (7×10^4 emu G/g) > NF25 (6.7×10^4 emu G/g) > MRNIP2 (5.5×10^4 emu G/g) > magnetite (4.4×10^4 emu G/g). The ΔU of ZVI and fresh NZVI are greater than aged NZVI (MRNIP2) and magnetite. These differences should result in different abilities to generate heat under an applied AC EMF.

3.3. MIH Rate for ZVI and NZVI. Under applied AC EMF, DI and MTP control experiments without ZVI or NZVI could not generate any heat. On the other hand, all ZVI and NZVI evaluated generated heat and raised the temperature of the suspension as expected (Figure 1b). In DI water, all ZVI and NZVI raised temperature of the suspension above 80 °C in less than 15 min. However, their heat induction rate constants (k_{HI}) (determined from eq 2) and maximum induced temperature increases ($\Delta T_{max} = T_{max} - T_0$) depend on their magnetic properties.

$$T = T_0 + \Delta T_{max}(1 - e^{-k_H t}) \tag{2}$$

As theoretically predicted, H150 ($K_{HI} = 9.4 \times 10^{-2}$ min^{-1} and ΔT_{max} = 109 °C in DI water) was the fastest in heating kinetics, agreeing with its highest ΔU discussed previously. In addition, H150 generated heat via hysteresis to 123 °C within 20 min. However, the heating rates of NF25, MRNIP2, and magnetite nanoparticles were similar, in line with their similar ΔU values. In DI water, NF25 ($K_{HI} = 8.9 \times 10^{-2}$ min^{-1} and ΔT_{max} = 63.9 °C in DI water) reached the maximum temperature of 92 °C in 25 min, whereas MRNIP2 ($K_{HI} = 8.6 \times 10^{-2}$ min^{-1} and ΔT_{max} = 71.6 °C in DI water) reached the maximum temperature of 86 °C in 20 min. In addition, magnetite nanoparticles ($K_{HI} = 14.4 \times 10^{-2}$ min^{-1} and ΔT_{max} = 60.6 °C in DI water) reached the maximum temperature of 84 °C in 20 min.

In general, the solution chemistry of the suspension seems to have little impact on the heating rate (Figure 1b). One exception is the NF25, where the heating rate as much lower in groundwater than in DI water ($K_{HI} = 8.9 \times 10^{-2}$ min^{-1} ΔT_{max} = 63.9 in DI vs $K_{HI} = 1.4 \times 10^{-2}$ min^{-1} and ΔT_{max} = 115.6 °C in MTP). Even after 30 min under EMF, the NF25 in MTP suspension could not exceed 80 °C like other cases discussed earlier. This is likely due to agglomeration during the

DOI: 10.1021/acs.est.5b04485
Environ. Sci. Technol. 2016, 50, 872−880

application of AC EMF. This can decrease the heat induction and energy dissipation. A similar decrease of induction heating capacity was not observed for the case of MRNIP2 (aged, polymer coated NZVI) presumably because of its higher stability against agglomeration due to a polymer coating.[49]

3.4. Dissolved TCE Dechlorination with and without AC EMF. Applied AC EMF greatly enhanced the dechlorination of dissolved TCE in DI and MTP groundwater by both NZVI (NF25) and ZVI (H150) (see Table 1 and Figure 2a).

Table 1. Mass-Normalized Pseudo First Order Rate Constants of TCE dechlorination for Various Experimental Conditions in This Study

NZVI or ZVI	type of media	heating condition	mass-normalized dechlorination rate constant (10^{-3} L/g/h)
N25	DI	none	7.10 ± 1.22
		WB	10.80 ± 1.74
		EMF	35.20 ± 4.23
N25	MTP	none	5.43 ± 0.47
		EMF	20.20 ± 3.10
N25	Soil + MTP	none	2.20 ± 0.68
		EMF	11.80 ± 1.13
H150	DI	none	0.84 ± 0.09
		EMF	1.69 ± 0.25
H150	MTP	none	1.02 ± 0.09
		EMF	1.37 ± 0.25

Without AC EMF, the mass-normalized TCE dechlorination rate constants by NF25 in DI and MTP groundwater are 7.10 ± 1.22 × 10^{-3} and 5.43 ± 0.47 × 10^{-3} L/g/h, respectively (Figure 2a and Table 1). Ionic and organic (natural organic matters) solutes in MTP groundwater appear to decrease the TCE dechlorination rate constant by a factor of 1.3 in comparison to the DI water, consistent with previous reports in the absence of AC EMF.[21] Dechlorination byproducts included ethane and ethene (Figure S8 in SI); no acetylene was observed. The opposite trend was observed for H150 (Figure S9 and Table 1), with mass-normalized pseudo first order rate constants of 0.84 ± 0.09 × 10^{-3} and 1.02 ± 0.09 × 10^{-3} L/g/h for DI and MTP groundwater, respectively. Without AC EMF, the rate constants of H150 in DI are around five to ten times smaller than the NF25 because NZVI has much larger specific surface area than ZVI, and dechlorination is a surface mediated reaction.

The application of AC EMF induced heat as previously discussed and increased the rate of TCE dechlorination compared to the absence of applied AC EMF. Interestingly, the ability of the NF25 suspension to generate heat increased with each cycle (Figure S10 in SI). This is consistent with its high remanence (M_r) and suggests that NF25 may be an effective remediation material under an applied AC EMF. The same behavior was also observed for NF25 in MTP groundwater but was less pronounced in DI water. The TCE dechlorination afforded by NF25 with AC EMF yielded the rate constants of 35.20 ± 4.23 × 10^{-3} and 20.20 ± 3.10 × 10^{-3} L/g/h for DI and MTP groundwater, respectively. This is 4.96 and 3.72 times greater than without AC EMF for DI water and MTP groundwater, respectively (Figure 2b). The enhanced

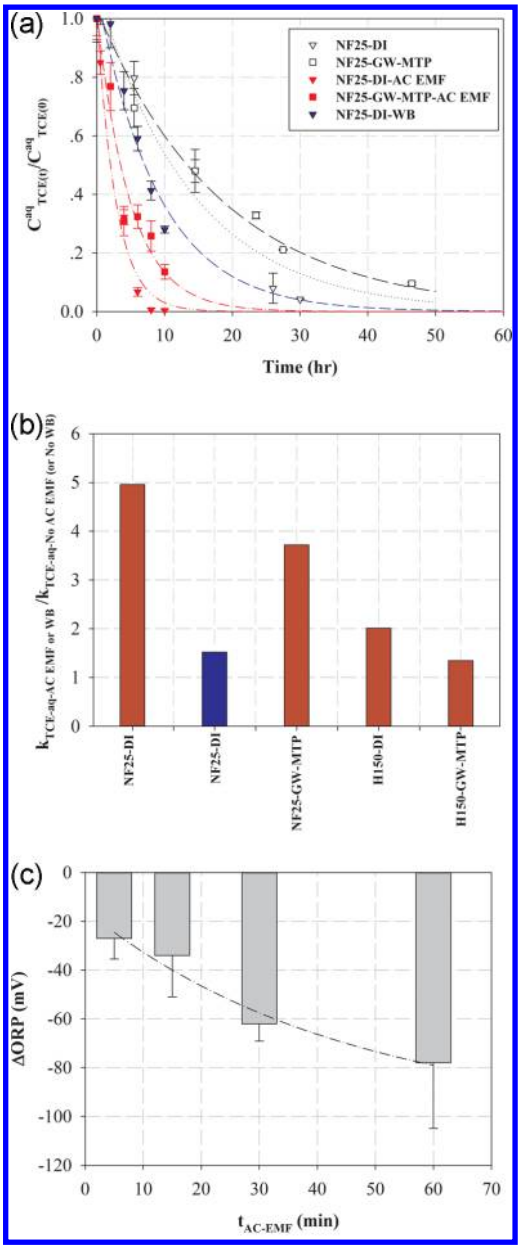

Figure 2. (a) TCE dechlorination kinetics using NF25 in DI water (triangles) and MTP groundwater (squares) with AC EMF (red symbols) and without AC EMF (white symbols) as well as NF25 in DI water heated by water bath (blue triangles). The dashed lines represent the pseudo first order modeling. (b) Summary of enhanced dissolved TCE dechlorination by NZVI and ZVI with AC EMF and water bath (WB) depicted as the ratio of the TCE dechlorination rate constant with AC EMF or WB ($k_{TCE\text{-}aq\text{-}AC\ EMF\ or\ WB}$) over the TCE dechlorination rate constant without AC EMF or WB ($k_{TCE\text{-}aq\text{-}No\ AC\ EMF\ or\ No\ WB}$) for each case. (c) The increasingly negative ORP magnitude (ΔORP) of NZVI as a function of AC EMF time ($t_{AC\ EMF}$).

dissolved TCE dechlorination rate is presumably due to the higher temperature (Arrhenius theory), magneto-convection, and enhanced ZVI corrosion, which is evaluated later in this study. Interestingly, the applied AC EMF changes the dechlorination products from ethene and ethane to acetylene in both DI and MTP groundwater (Figure S8 in SI). Considering electron consumption efficiency, the accumulation of acetylene (intermediate) instead of ethane is beneficial, as

DOI: 10.1021/acs.est.5b04485
Environ. Sci. Technol. 2016, 50, 872−880

TCE dechlorination to acetylene requires fewer electrons than degradation to ethene.

Similar to NZVI, when ZVI (H150) was placed under applied AC EMF for dissolved TCE dechlorination, it induced greater heat in every consecutive cycle. Despite the lower reactivity of ZVI compared to NZVI, application of AC EMF also increased the TCE degradation rate constants in both in DI and MTP groundwater although the increase was not as pronounced as the case of NZVI. The TCE dechlorination afforded by H150 with AC EMF yielded the rate constants of $1.69 \pm 0.25 \times 10^{-3}$ and $1.37 \pm 0.25 \times 10^{-3}$ L/g/h for DI and MTP groundwater, respectively (Figure S9 in SI). This is 2.01 and 1.34 times greater than without EMF for DI water and MTP groundwater, respectively (Figure 2b). Nevertheless, unlike NZVI, dechlorination by H150 with applied EMF yielded ethane and ethene as major byproducts in both DI and MTP groundwater (Figure S8 in SI).

According to the results discussed above, AC EMF enhances dissolved TEC dechlorination rate constants for both NZVI and ZVI. Intuitively, the enhanced reaction should be a function of electromagnetic induction time (the longer the induction time, the faster the dechlorination) and the particle concentration under the induction (the greater the particle concentration, the faster the dechlorination). Figure S11 in SI confirms this hypothesis by illustrating the linear correlation (with the slope of 0.9) between the enhanced dissolved TCE dechlorination rate constant due to EMF ($k_{\text{TCE-aq-EMF}}/k_{\text{TCE-aq-No EMF}}$) and the ratio of EMF application time ($\sum t_{\text{EMF}}$) over the total dechlorination time ($t_{\text{Dechlorination}}$) multiplied by particle concentration ($C_{\text{ZVI or NZVI}}$) for all the four cases in this study. This correlation confirms that longer EMF application time and higher concentrations of ZVI or NZVI will yield greater dechlorination rates as theoretically expected.

Additionally, we examine if the increase in dechlorination rate constants with AC EMF was due to the higher temperature alone as explained by the Arrhenius equation, or some other phenomena, such as enhanced ZVI corrosion may play some role. In order to investigate this possibility, we conducted another set of TCE dechlorination experiments using NF25 in a heating water bath to simulate the temperature profile for dechlorination obtained from the MIH study of NF25 with EMF (Figure S12 in SI). As shown in Figure 2a and Table 1, the TCE dechlorination afforded by NF25 in DI with the heating water bath yielded the rate constant of $10.80 \pm 1.74 \times 10^{-3}$ L/g/h. This is around 1.52 times greater than the TCE dechlorination rate constant of NF25 in DI without heating but still 3.26 times smaller than the TCE dechlorination rate constant of NF25 in DI with AC EMF. This suggests that besides the temperature increase, the other two phenomena (magneto-convection and enhanced ZVI corrosion) may also be enhancing the rate constant. Figure 2c supports this hypothesis by illustrating the decrease of ORP for both NZVI reactors as a function of time under AC EMF. The ORP represents the reduction capability of the system. Increasingly negative ORP indicates a greater reduction capacity of the system, (i.e., NZVI is more active in donating electrons). This finding is in good agreement with a recent study reporting the decrease of ORP of ZVI dispersion under DC MF.[39,41] Presumably, the applied AC EMF induces the field gradient force on the NZVI surface, which subsequently induces paramagnetic Fe^{2+} ions, the byproduct of NZVI oxidation, to deplete from the NZVI surface where the field gradient is low and to accumulate on the NZVI surface where the field gradient is high. This Fe^{2+} accumulation creates localized galvanic couples, which promote the breakdown of the passive iron oxide layer, which is known to decrease NZVI reactivity.[50] This local galvanic couple activity eventually enhances localized ZVI corrosion,[39,41] resulting in increasingly negative ORP magnitude and the increase of the reduction power of the system.

3.5. Sorbed TCE Dechlorination With and Without AC EMF. We investigated the influence of AC EMF on the dechlorination of TCE when it is present on both the dissolved phase and sorbed onto soil, (i.e., in a TCE presorbed soil-water system). As shown in Figure 3, the series of unfilled circles

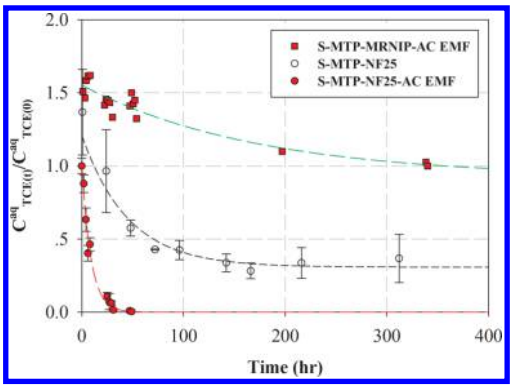

Figure 3. Dissolved TCE dechlorination kinetics in a soil-water system with preadsorbed TCE. Unfilled circles represent TCE dechlorination by NF25 without AC EMF, red circles represent TCE dechlorination by NF25 with AC EMF, and red squares represent TCE desorption from soil by (unreactive) MRNIP with AC EMF. The dashed lines represent the pseudo first order modeling.

shows the normalized dissolved TCE concentration vs time for the TCE presorbed soil-NZVI-water-headspace system without AC EMF. The dissolved TCE dechlorination rate without AC EMF was first order with a dechlorination rate constant of $2.20 \pm 0.68 \times 10^{-3}$ L/g/h, around 2.49 times smaller than the rate constant in MTP groundwater without soil. The decrease TCE dechlorination rate constant in the present of soil agrees very well with the theoretically retarded dechlorination rate constant ($k_{\text{TCE-aq-Soil}}$ in eq 3) in accordance with the retardation factor (R) due to TCE sorption to soil (eq 4). Where $k_{\text{TCE-aq}}$, ρ_b, and n are TCE dechlorination constant in groundwater without soil, bulk density of soil, and porosity, respectively.

$$k_{\text{TCE-aq-soil}} = \frac{k_{\text{TCE-aq}}}{R} \tag{3}$$

$$R = 1 + \frac{k_d \cdot \rho_b}{n} \tag{4}$$

Under the equilibrium with the k_d of 1.46 L/kg, R is calculated using eq 4 to be 7.28, and the theoretically suppressed dechlorination rate constant under the influence of TCE sorption to soil ($k_{\text{TCE-aq-Soil}}$ in eq 3) can be as low as 0.75×10^{-3} L/g/h, slightly lower than the experimentally observed rate constant.

Noticeably, without applied AC EMF, the dissolved TCE concentration did not reach zero even after 300 h of reaction. Instead, the dechlorination seemed to progress to the system where TCE in water remained constant at around 30% of the initial dissolved TCE in the system. No further decrease of dissolved TCE in the system occurred from 150 to 300 h. After

DOI: 10.1021/acs.est.5b04485
Environ. Sci. Technol. 2016, 50, 872−880

the end of the experiment, we recovered 35% by mass of the initial TCE from the reactor using hexane extraction. Additionally, 75% of the recovered TCE was sorbed onto soil, whereas 25% was dissolved in the MTP groundwater. This confirms our hypothesis that sorption and slow desorption of TCE (desorption rate constant from $6.50 \pm 3.10 \times 10^{-3}$ to $11.80 \pm 5.50 \times 10^{-3}$ hr^{-1}) slows its dechlorination rate via NZVI due to mass transfer limitation.[6,28]

This same behavior of no further dechlorination in TCE presorbed soil-NZVI-water system was previously reported by Zhang et al.[28] attributing this phenomenon to the reduced TCE availability due to sorption onto soil as well. In addition to the sorption limitation, Zhang et al. revealed that the soluble organic matter released from the soils can suppress the ZVI's dechlorination power.[28] Due to nonselective nature of reducing reaction by NZVI, which leads to its relatively short lifetime (days to couple weeks),[51] slow desorption of TCE from soil can limit the effective use of electrons in NZVI for TCE dechlorination. The NZVI might use its reducing power to transform nontargeting compounds in the soil-water system instead. This could explain no further decrease of dissolved TCE in the system from 150 to 300 h in our study and also in Zhang et al.'s study.[28]

As suggested above, rapid initial TCE desorption is essential for making the best use of NZVI's reducing power. The problem of slow TCE desorption is eliminated by the applied AC EMF. The series of red circles shows the measured dissolved phase TCE vs time in the TCE sorbed soil−water system with applied EMF. The TCE dechlorination on rate constant is higher with AC EMF than without, and unlike the absence of AC EMF, the dissolved TCE concentration goes to zero. The TCE dechlorination rate constant was $11.80 \pm 1.13 \times 10^{-3}$ L/g/h, (i.e., 5.36 times faster than the dechlorination in soil without an applied AC EMF). Nevertheless, this TCE dechlorination rate constant is still around 1.7 times smaller than the rate constant in MTP groundwater under AC EMF but without soil. The dissolved TCE was completely degraded after 31 h of reaction, and no dissolved TCE was observed over another 200 h, suggesting that the TCE degradation was completed. After the study, hexane extraction recovered only around 3% by mass of the initial TCE. This finding agrees with our conceptual model in that heat induced by electromagnetic induction of NF25 raised the temperature of the soil-water system, which enhanced TCE desorption from soil (Figure S2b in SI). Desorbed TCE was available for dechlorination and rapidly degraded by NF25. The influence of electromagnetic induction of NZVI on TCE desorption was demonstrated using the nonreactive (aged) NZVI, MRNIP. Over four MIH cycles, MRNIP generated heat and raised the temperature to around 65 °C. As a result, the dissolved TCE concentration increased to around 1.5 times of the initial concentration (red squares in Figure 3), indicating that TCE was desorbed from soil. However, allowing the system to cool to the original temperature slowly returned the TCE concentration back to its original value. The sorption rate constant was approximately 5.8×10^{-3} hr^{-1}. For the case of NF25 with AC EMF, we did not observe this because the desorbed TCE was rapidly dechlorinated at the elevated temperature.

■ ASSOCIATED CONTENT

Supporting Information

The Supporting Information is available free of charge on the ACS Publications website at DOI: 10.1021/acs.est.5b04485.

Conceptual model of plume interception by permeable reactive barrier (PRB) using zerovalent iron (ZVI), electrolytic barrier, and combined remediation using PRB (ZVI) under EMF. Schematics of contaminated groundwater and soil remediation by conventional NZVI, which relies on two-step reaction including TCE desorption from soil and TCE dechlorination at NZVI surface. Physicochemical properties of ZVI used in this study. Physicochemical properties of nanofer 25 (NF25). EMF generator (EMFG) and an induction coil (white coil) to hold vials for induction heating and EMF-enhanced dechlorination experiments. TCE sorption kinetics on MTP soil and K_d of TCE on MTP soil as determined from the slope of the graph. Physical properties of MTP soil. Physical and chemical properties of MTP groundwater. XRD of fresh NZVI (NF25) and aged NZVI (MRNIP). Byproduct distributions from TCE dechlorination using NF25 and H150 in DI and MTP with and without MIH. Temperature profiles of NF25 in DI water heated by a water bath as a function of time during five heating cycles. (PDF)

■ AUTHOR INFORMATION

Corresponding Author

*Phone: (6655) 964057; fax: ;(6655) 964002 e-mail: pomphenrat@gmail.com.

Notes

The authors declare no competing financial interest.

■ ACKNOWLEDGMENTS

This research was funded in part by (1) the National Nanotechnology Center (Thailand), a member of the National Science and Technology Development Agency, through grant number P-11-00989, (2) the Thailand Research Fund (TRF) (MRG5680129), and (3) National Research Council (R2556B070).

■ REFERENCES

(1) Comba, S.; Molfetta, A. D.; Sethi, R. A Comparison Between Field Applications of Nano-, Micro-, and Millimetric Zero-Valent Iron for the Remediation of Contaminated Aquifers. *Water, Air, Soil Pollut.* **2013**, *215* (1), 595−607.

(2) Tratnyek, P. G.; Johnson, T. L.; Scherer, M. M.; Eykholt, G. R. Remediating groundwater with zero-valent metals: Kinetic considerations in barrier design. *Groundwater Monit. Rem.* **1997**, *17*, 108−114.

(3) Matheson, L. J.; Tratnyek, P. G. Reductive dehalogenation of chlorinated methanes by iron metal. *Environ. Sci. Technol.* **1994**, *28*, 2045−2053.

(4) Ebert, M.; Kober, R.; Parbs, A.; Plagentz, V.; Schafer, D.; Dahmke, A. Assessing degradation rates of chlorinated ethylenes in column experiments with commercial iron materials used in permeable reactive barriers. *Environ. Sci. Technol.* **2006**, *40*, 2004−2010.

(5) Su, C.; Puls, W. R. Kinetics of trichloroethene reduction by zerovalent iron and tin: Pretreatment effect, apparent activation energy, and intermediate products. *Environ. Sci. Technol.* **1999**, *33* (1), 163−168.

(6) Phenrat, T.; Schoenfelder, D.; Losi, M.; Yi, J.; Peck, S. A.; Lowry, G. V., Treatability Study for a TCE Contaminated Area using Nanoscale- and Microscale-Zerovalent Iron Particles: Reactivity and Reactive Life Time. In *Environmental Applications of Nanoscale and Microscale Reactive Metal Particles*; Geiger, C. L., Carvalho-Knighton, K. M., Eds.; American Chemical Society: Washington D.C., 2010; Vol. *1027*, pp 183−202.

(7) Lowry, G. V., Nanomaterials for Groundwater Remediation. In *Environmental Nanotechnology: Applications and Impacts of Nanomaterials*; Wiesner, M. R., Bottero, J.-Y., Eds.; McGraw-Hill: New York, 2007.
(8) Tratnyek, P. G.; Johnson, R. L. Nanotechnologies for environmental cleanup. *Nano Today* **2006**, *1* (2), 44−48.
(9) Zhang, W. Nanoscale iron particles for environmental remediation: An overview. *J. Nanopart. Res.* **2003**, *5*, 323−332.
(10) Phenrat, T.; Crimi, M.; Illanagasekare, T.; Lowry, G. V., Reactive Nanoparticles for the Treatment of Chlorinated Dense Nonaqueous Phase Liquids in Soil and Groundwater. In *Nanotechnology for Environmental Decontamination*; Ram, M., Andreescu, E. S., Hanming, D., Eds.; McGraw-Hill Publisher: New York, 2011; pp 271−322.
(11) Phenrat, T.; Fagerlund, F.; Illanagasekare, T.; Lowry, G. V.; Tilton, R. D. Polymer-modified Fe0 Nanoparticles Target Entrapped NAPL in Two Dimensional Porous Media: Effect of Particle Concentration, NAPL Saturation, and Injection Strategy. *Environ. Sci. Technol.* **2011**, *45* (14), 6102−6109.
(12) Henn, K. W.; Waddill, D. W. Utilization of nanoscale zero-valent iron for source remediation - A case study. *Remediation Journal* **2006**, *16*, 57−77.
(13) Saleh, N.; Phenrat, T.; Sirk, K.; Dufour, B.; Ok, J.; Sarbu, T.; Matyjaszewski, K.; Tilton, R. D.; Lowry, G. V. Adsorbed triblock copolymers deliver reactive iron nanoparticles to the oil/water interface. *Nano Lett.* **2005**, *5* (12), 2489−2494.
(14) Sakulchaicharoen, N.; O'Carroll, D. M.; Herrera, J. E. Enhanced stability and dechlorination activity of pre-synthesis stabilized nanoscale FePd particles. *J. Contam. Hydrol.* **2010**, *118* (3−4), 117−127.
(15) Kocur, C. M. D.; Lomheim, L.; Boparai, H. K.; Chowdhury, A. I. A.; Weber, K. P.; Austrins, L. M.; Edwards, E. A.; Sleep, B. E.; O'Carroll, D. M. Contributions of Abiotic and Biotic Dechlorination Following Carboxymethyl Cellulose Stabilized Nanoscale Zero Valent Iron Injection. *Environ. Sci. Technol.* **2015**, *49* (14), 8648−8656.
(16) ITRC. *Permeable Reactive Barriers: Lessons Learned/New Directions*, #PRB-4; Inter-state Technology&Regulatory Council: Wasgington, DC, 2005.
(17) Karn, B.; Kuiken, T.; Otto, M. Nanotechnology and in Situ Remediation: A Review of the Benefits and Potential Risks. *Environ. Health Perspect.* **2009**, *117* (12), 1823−1831.
(18) Mueller, N. C.; Braun, J.; J, B.; Černík, M.; Rissing, P.; Rickerby, D.; Nowack, B. Application of nanoscale zero valent iron (NZVI) for groundwater remediation in Europe. *Environ. Sci. Pollut. Res.* **2012**, *19*, 550−558.
(19) Zhang, W.-X.; Wang, C.-B.; Lien, H.-L. Treatment of chlorinated organic comtaminants with nanoscale bimetallic particles. *Catal. Today* **1998**, *40*, 387−395.
(20) Phenrat, T.; Liu, Y.; Tilton, R. D.; Lowry, G. V. Adsorbed polyelectrolyte coatings decrease Fe^0 nanoparticle reactivity with TCE in water: conceptual model and mechanisms. *Environ. Sci. Technol.* **2009**, *43* (5), 1507−1514.
(21) Liu, Y.; Phenrat, T.; Lowry, G. V. Effect of TCE concentration and dissolved groundwater solutes on NZVI-promoted TCE dechlorination and H2 evolution. *Environ. Sci. Technol.* **2007**, *41* (22), 7881−7887.
(22) Fagerlund, F.; Illangasekare, T. H.; Phenrat, T.; Kim, H.-J.; Lowry, G. V. PCE dissolution and simultaneous dechlorination by nanoscale zero-valent iron particles in a DNAPL source zone. *J. Contam. Hydrol.* **2012**, *131* (1−4), 9−28.
(23) Arnold, W. A.; Roberts, A. L. Pathway and kinetics of chlorinated ethylene and chlorinated acetylene reaction with Fe(0) particles. *Environ. Sci. Technol.* **2000**, *34*, 1794−1805.
(24) Liu, Y.; Majetich, S. A.; Tilton, R. D.; Sholl, D. S.; Lowry, G. V. TCE dechlorination rates, pathways, and efficiency of nanoscale iron particles with different properties. *Environ. Sci. Technol.* **2005**, *39*, 1338−1345.
(25) Reinsch, B. C.; Forsberg, B.; Penn, R. L.; Kim, C. S.; Lowry, G. V. Chemical transformations during aging of zero-valent iron nanoparticles in the presence of common groundwater dissolved constituents. *Environ. Sci. Technol.* **2010**, *44* (9), 3455−3461.
(26) Werth, C. J.; Reinhard, M. Effects of Temperature on Trichloroethylene Desorption from Silica Gel and Natural Sediments. 2. Kinetics. *Environ. Sci. Technol.* **1997**, *31*, 697−703.
(27) Li, J.; Werth, C. J. Slow Desorption Mechanisms of Volatile Organic Chemical Mixtures in Soil and Sediment Micropores. *Environ. Sci. Technol.* **2004**, *38* (2), 440−448.
(28) Zhang, M.; He, F.; Zhao, D.; Hao, X. Degradation of soil-sorbed trichloroethylene by stabilized zero valent iron nanoparticles: effects of sorption, surfactants, and natural organic matter. *Water Res.* **2011**, *45* (7), 2401−2414.
(29) Phenrat, T.; Saleh, N.; Sirk, K.; Tilton, R. D.; Lowry, G. V. Aggregation and sedimentation of aqueous nanoscale zerovalent iron dispersions. *Environ. Sci. Technol.* **2007**, *41* (1), 284−290.
(30) Rosická, D.; Šembera, J. Assessment of Influence of Magnetic Forces on Aggregation of Zero-valent Iron Nanoparticles. *Nanoscale Res. Lett.* **2011**, *6*, 10.
(31) Dalla Vecchia, E.; Coisson, M.; Appino, C.; Vinai, F.; Sethi, R. Magnetic characterization and interaction modeling of zerovalent iron nanoparticles for the remediation of contaminated aquifers. *J. Nanosci. Nanotechnol.* **2009**, *9* (5), 3210−3218.
(32) Graham, L. J.; Atwater, J. E.; Jovanovic, G. N. Chlorophenol Dehalogenation in a Magnetically Stabilized Fluidized Bed Reactor. *AIChE J.* **2005**, *52* (3), 1083−1093.
(33) Graham, L. J.; Jovanovic, G. N. Dechlorination of p-chlorophenol on a Pd/Fe catalyst in a magnetically stabilized fuidized bed; Implications for sludge and liquid remediation. *Chem. Eng. Sci.* **1999**, *54* (15−16), 3085−3093.
(34) Graham, L. J.; Jovanovic, G. N. Catalytic Dechlorination of Chlorinated Hydrocarbons in a Magnetically Stabilized Fluidized Bed. *World Congr. Part. Technol.* **1998**, *3*, 2296−2307.
(35) Kim, D.-H.; Kim, J.; Choi, W. Effect of magnetic field on the zero valent iron induced oxidation reaction. *J. Hazard. Mater.* **2011**, *192*, 928−931.
(36) Brocklehurst, B. Magnetic fields and radical reactions: recent developments and their role in nature. *Chem. Soc. Rev.* **2002**, *31*, 301−311.
(37) Sun, Y.; Guan, X.; Wang, J.; Meng, X.; Xu, C.; Zhou, G. Effect of Weak Magnetic Field on Arsenate and Arsenite Removal from Water by Zerovalent Iron: An XAFS Investigation. *Environ. Sci. Technol.* **2014**, *48*, 6850−6858.
(38) Liang, L.; Guan, X.; Shi, Z.; Li, J.; Wu, Y.; Tratnyek, P. G. Coupled Effects of Aging and Weak Magnetic Fields on Sequestration of Selenite by Zero-Valent Iron. *Environ. Sci. Technol.* **2014**, *48*, 6326−6334.
(39) Liang, L.; Sun, W.; Guan, X.; Huang, Y.; Choi, W.; Bao, H.; Li, L.; Jiang, Z. Weak magnetic field significantly enhances selenite removal kinetics by zero valent iron. *Water Res.* **2014**, *49*, 371−380.
(40) Feng, P.; Guan, X.; Sun, Y.; Choi, W.; Qin, H.; Wang, J.; Qiao, J.; Li, L. Weak magnetic field accelerates chromate removal by zero-valent iron. *J. Environ. Sci.* **2015**, *31*, 175−183.
(41) Jiang, X.; Qiao, J.; Lo, I. M. C.; Wang, L.; Guan, X.; Lu, Z.; Zhou, G.; Xu, C. Enhanced paramagnetic Cu2+ ions removal by coupling a weak magnetic field with zerovalent iron. *J. Hazard. Mater.* **2015**, *283*, 880−887.
(42) Li, J.; Bao, H.; Xiong, X.; Sun, Y.; Guan, X. Effective Sb(V) immobilization from water by zero-valent iron with weak magnetic field. *Sep. Purif. Technol.* **2015**, *151*, 276−283.
(43) Waskaas, M.; Kharkats, Y. I. Magnetoconvection Phenomena: A Mechanism for Influence of Magnetic Fields on Electrochemical Processes. *J. Phys. Chem. B* **1999**, *103*, 4876−4883.
(44) Kitazawa, K.; Hirota, N.; Ikezoe, Y.; Uetake, H.; Kaihatsu, T.; Takayama, T. Magneto-convection processes observed in non-magnetic liquid−gas system. *Riken Rev.* **2002**, *44*, 156−158.
(45) Pablico-Lansigan, M. H.; Situa, S. F.; Samia, A. C. S. Magnetic particle imaging: advancements and perspectives for real-time in vivo monitoring and image-guided therapy. *Nanoscale* **2013**, *5*, 4040−4055.

DOI: 10.1021/acs.est.5b04485
Environ. Sci. Technol. 2016, 50, 872−880

(46) Bañobre-López, M.; Teijeiro, A.; Rivas, J. Magnetic nanoparticle-based hyperthermia for cancer treatment. *Rep. Prac. Oncol. Radiother.* **2013**, *18* (6), 397−400.
(47) Truex, M. J.; Macbeth, T. W.; Vermeul, V. R.; Fritz, B. G.; Mendoza, D. P.; Mackley, R. D.; Wietsma, T. W.; Sandberg, G.; Powell, T.; Powers, J.; Pitre, E.; Michalsen, M.; Ballock-Dixon, S. J.; Zhong, L.; Oostrom, M. Demonstration of Combined Zero-Valent Iron and Electrical Resistance Heating for In Situ Trichloroethene Remediation. *Environ. Sci. Technol.* **2011**, *45* (12), 5346−5351.
(48) Li, Z.; Kawashita, M.; Araki, N.; Mitsumori, M.; Hiraoka, M.; Doi, M. Magnetite nanoparticles with high heating efficiencies for application in the hyperthermia of cancer. *Mater. Sci. Eng., C* **2010**, *30* (7), 990−996.
(49) Phenrat, T.; Saleh, N.; Sirk, K.; Kim, H.-J.; Tilton, R. D.; Lowry, G. V. Stabilization of aqueous nanoscale zerovalent iron dispersions by anionic polyelectrolytes: adsorbed anionic polyelectrolyte layer properties and their effect on aggregation and sedimentation. *J. Nanopart. Res.* **2008**, *10*, 795−814.
(50) Martin, J. E.; Herzing, A. A.; Yan, W.; Li, X. Q.; Koel, B. E.; Kiely, C. J.; Zhang, W. X. Determination of the oxide layer thickness in core-shell zerovalent iron nanoparticles. *Langmuir* **2008**, *24* (8), 4329−4334.
(51) He, F.; Zhao, D.; Paul, C. Field assessment of carboxymethyl cellulose stabilized iron nanoparticles for in situ destruction of chlorinated solvents in source zone. *Water Res.* **2010**, *44* (7), 2360−2370.

DOI: 10.1021/acs.est.5b04485
Environ. Sci. Technol. 2016, 50, 872−880

Supporting Information for

Electromagnetic Induction of Zerovalent Iron (ZVI) Powder and Nanoscale Zerovalent Iron (NZVI) Particles Enhances Dechlorination of Trichloroethylene in Contaminated Groundwater and Soil: Proof of Concept

Tanapon Phenrat[1,2*], Thippawan Thongboot[1,2] , and Gregory V. Lowry[3,4]

[1]Research Unit for Integrated Natural Resources Remediation and Reclamation (IN3R), Department of Civil Engineering, Faculty of Engineering, Naresuan University, Phitsanulok, Thailand, 65000

[2]Center of Excellence for Sustainability of Health, Environment, and Industry (SHEI), Faculty of Engineering, Naresuan University, Phitsanulok, Thailand, 65000

[3]Center for Environmental Implications of Nanotechnology (CEINT) and [4]Department of Civil & Environmental Engineering, Carnegie Mellon University, Pittsburgh, PA, 15213

Submitted to

Environmental Science Technology

***Corresponding author: Tanapon Phenrat (pomphenrat@gmail.com)**

(6655)964057(ph) (6655)964002(fax)

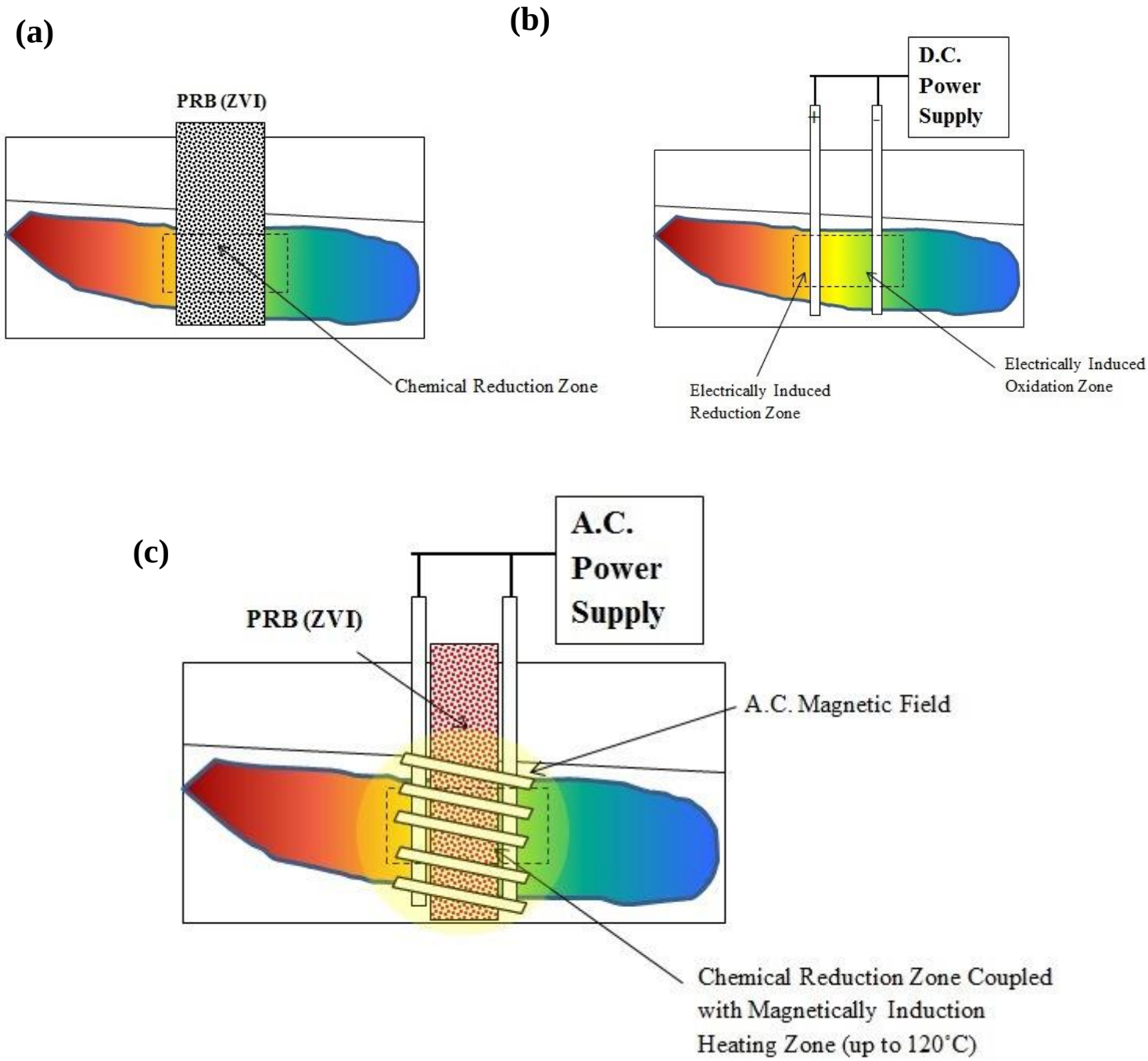

Fig. S1. Conceptual model of plume interception by (a) permeable reactive barrier (PRB) using zerovalent iron (ZVI), (b) electrolytic barrier, and (c) combined remediation using PRB (ZVI) under AC EMF

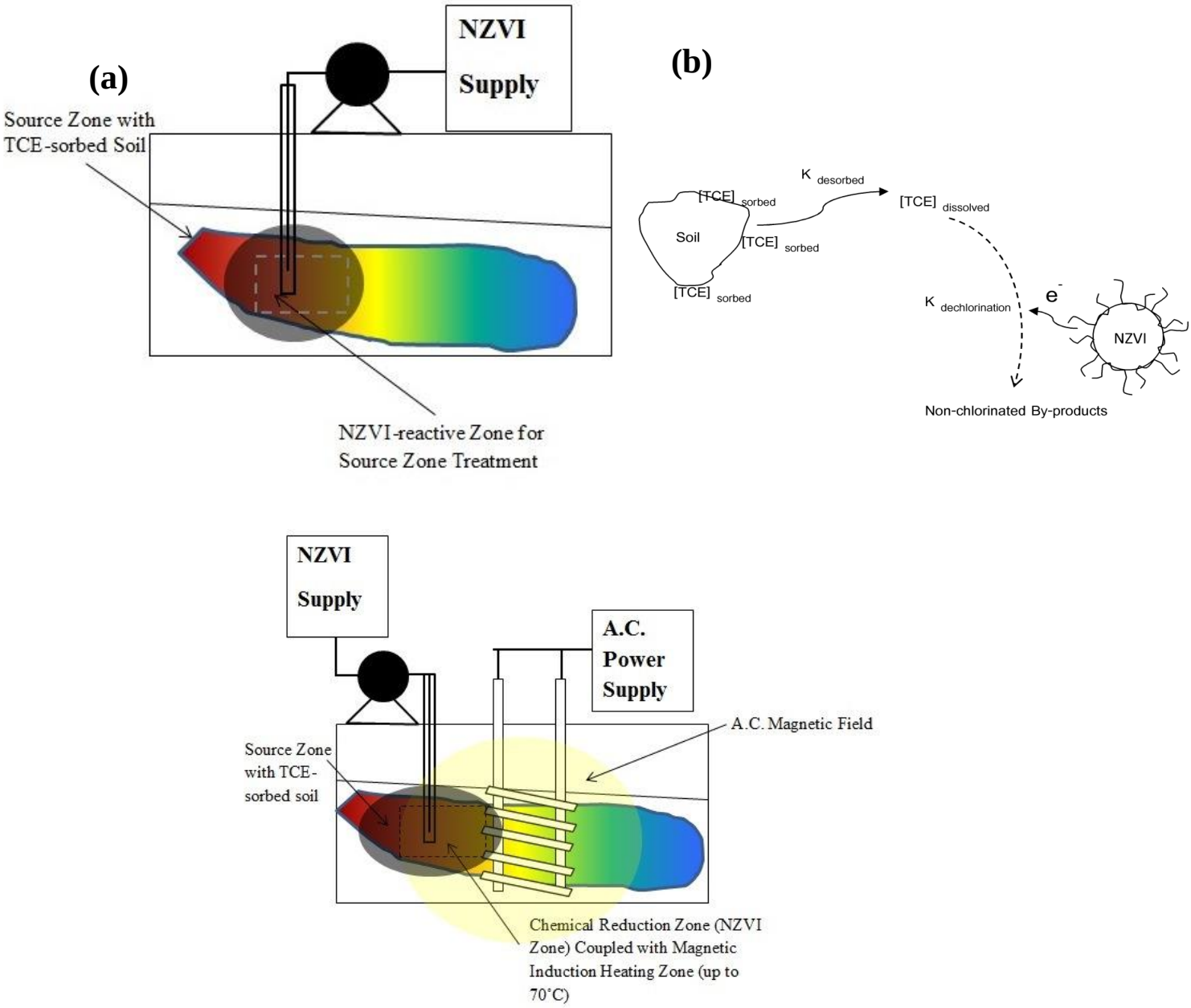

Figure S2 Schematics of contaminated groundwater and soil remediation by (a) conventional NZVI which relies on (b) two-step reaction including TCE desorption from soil and TCE dechlorination at NZVI surface, and (c) combined remediation using NZVI with AC EMF

Soil and Groundwater Samples

Soil and groundwater samples used in this study were collected from a contaminated site in the Map Ta Phut industrial park (MTP) in Rayong Province, Thailand. Groundwater and soil (3-15 meters depth) at this site is contaminated with chlorinated organics including TCE. We used a direct push technique (Geoprobe, Kansas, USA) together with a macro core soil sampler (MC) to obtain soil samples at the depth of 5 meters from an upstream (uncontaminated) region of the contaminated aquifer. We did this in order to have uncontaminated soil samples with the same physicochemical and geochemical properties as the contaminated soil. Groundwater samples were collected from a monitoring well, also upstream of the contaminated zone at a depth of 15 meters. No TCE was detected in the upstream location. We just needed the groundwater with the same geochemical condition in the site, but we would add the known concentration of TCE for the dechlorination experiments as discussed next.

TCE Sorption Kinetics, Partitioning Coefficient, and Desorption Kinetics

Before use, the soil was oven-dried. Identical reactors without TCE were also prepared as a reference. All experiments were done in duplicate. The reactors were equilibrated on a roller mixer at 30 rpm at 23 ± 2°C for 85 days. At selected time points, a 100-µL headspace sample was withdrawn from the reactors and analyzed for TCE using a 20 m Agilent J&W DB-624 capillary column on an Agilent 7820GC /ECD. At the end of the study (i.e., 85 days), a headspace sample was analyzed for TCE degradation by-products using 30 m GS-Carbonplot capillary column on an Agilent 7820 GC/FID. Measured peak area was converted to TCE concentration in the groundwater using a TCE calibration curve determined using identical reactors (20 mL

of water and 10 mL of headspace) spiked with a known mass of TCE. It was assumed that the water and air phases were in equilibrium (K_H=0.38 unitless). As no degradation by-product was observed, the depletion in the aqueous TCE concentration was attributed to partitioning of TCE to the soil. The adsorbed TCE concentration was then calculated from mass balance. To get a reliable value of the soil-water partitioning coefficient (K_d) (i.e., more than a single point isotherm), K_d was determined in identical reactors using the same mass of soil and initial TCE concentrations ranging from 12.5 mg/L to 380 mg/L. The adsorbed mass of TCE was calculated in the same way as just described.

Table S1 Physicochemical Properties of ZVI used in this Study

Type	**Size (µm) (%)**	**Chemical Composition (%)**					
		Fe	**C**	**Si**	**S**	**P**	**Mn**
HCA-150N	45-152 (90%)	92-98	3 (max)	2.5 (max)	0.15 (max)	1 (max)	0.5 (max)
H-200	45-152 (60-85%) <45 (15-40%)	93-97	1.75-4.5	1-2.5	0.01-0.15	-	-

Table S2 Physicochemical Properties of Nanofer 25 (NF25)

Physicochemical Properties of Nanofer 25 (NF25)	
Chemical composition of Fe^0	Fe(core) FeO (shell)
Content of solid phase in dispersion by weight	20%
Content Fe^0 in solid phase	≈ 85%
Other ingredients in solid phase	Fe_3O_4,FeO,C
Content of Fe^0 in dispersion by weight	17%
Crystalline structure of Fe^0	Alpha Fe
Particles morphology	spherical
Average particle size	d50 < 50nm
Particles specific surface area	>25m^2/g
Dispersion colour	black
Dispersion density	1,210 kg/m3
Fe^0 particles density	7,870 kg/m3
Fe_3O_4 density	5,700 kg/m3

Figure S3 AC EMF generator (AC EMFG) and an induction coil (white coil) to hold vials for induction heating and AC EMF-enhanced dechlorination experiments.

TCE Dechlorination in Aqueous Phase with and without AC EMF

No soil was used in these reactors. Thus, all TCE was in dissolved phase and did not experience any mass transfer limitation via desorption from soil during dechlorination. Experiments were performed in duplicate. Noticeably, here we designed the H150 reactors to contain greater amount of ZVI (i.e., 50 g/L) to compensate for its slower dechlorination rate than NZVI (i.e., the NS25 reactors). Control experiments without H150 or NF25 demonstrated that TCE loss by mechanisms other than degradation by Fe^0 was negligible (e.g., photodegradation, adsorption, and leakage). A mass balance for each case was calculated. The TCE degradation was modeled assuming a pseudo first order reaction.

The kinetics of TCE degradation under applied AC EMF was modeled assuming a pseudo first order reaction and compared with the TCE degradation rate without the applied AC EMF. Moreover, Due to the slower TCE dechlorination afforded by H150 in comparison to NF25 (i.e., ZVI vs. NZVI), we measured TCE concentration every 3 to 5 MIH cycles unlike measuring every single MIH cycle as for the case of NF25. We conducted MIH for two days for the case of H150 in comparison to 10 hours for NF25 to yield complete dechlorination of TCE.

MTP Soil and Groundwater Characteristics

The MTP soil was a dark brown clayey sand. The specific gravity was 2.53. The fraction of organic carbon was 27 g/kg (2.7%). Total organic carbon in MTP groundwater was 6.4 mg/L. The MTP groundwater was slightly acidic, pH 4.5, and had high conductivity (1,518 µS/cm) and low alkalinity (50 mg/L as $CaCO_3$). It contained both NO_3^- and SO_4^-

[2] (i.e., 16.7 and 19.9 mg/L, respectively). In addition, NO_3^- is reported to adversely affect NZVI performance. However, the adverse effect is not expected at this low NO_3^- concentration [1]

(a)

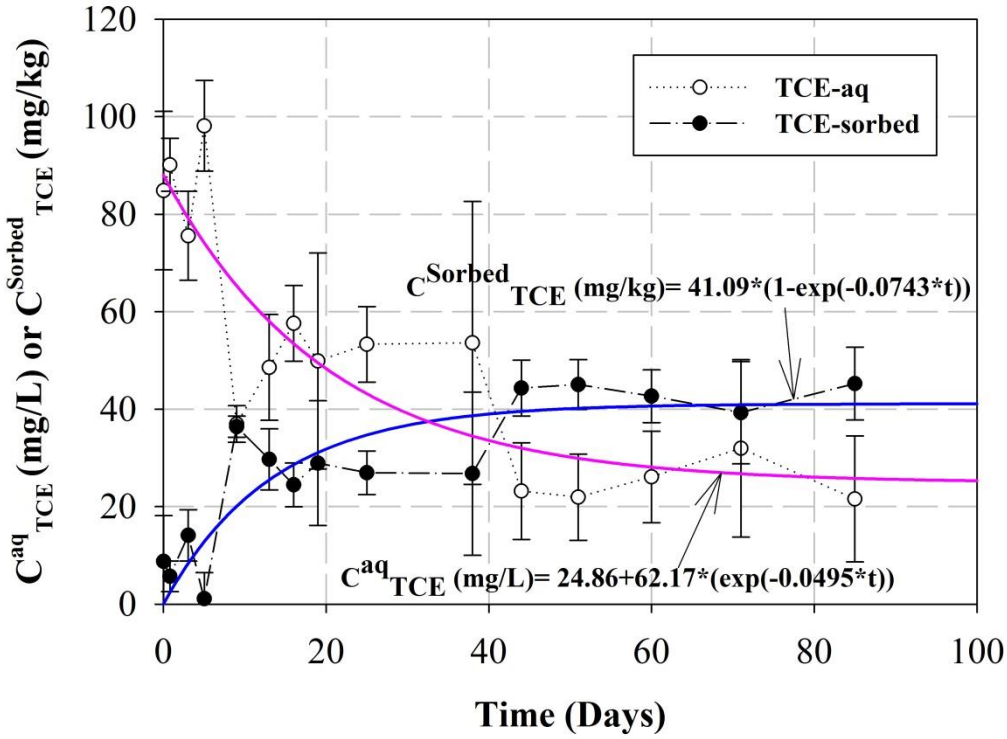

(b)

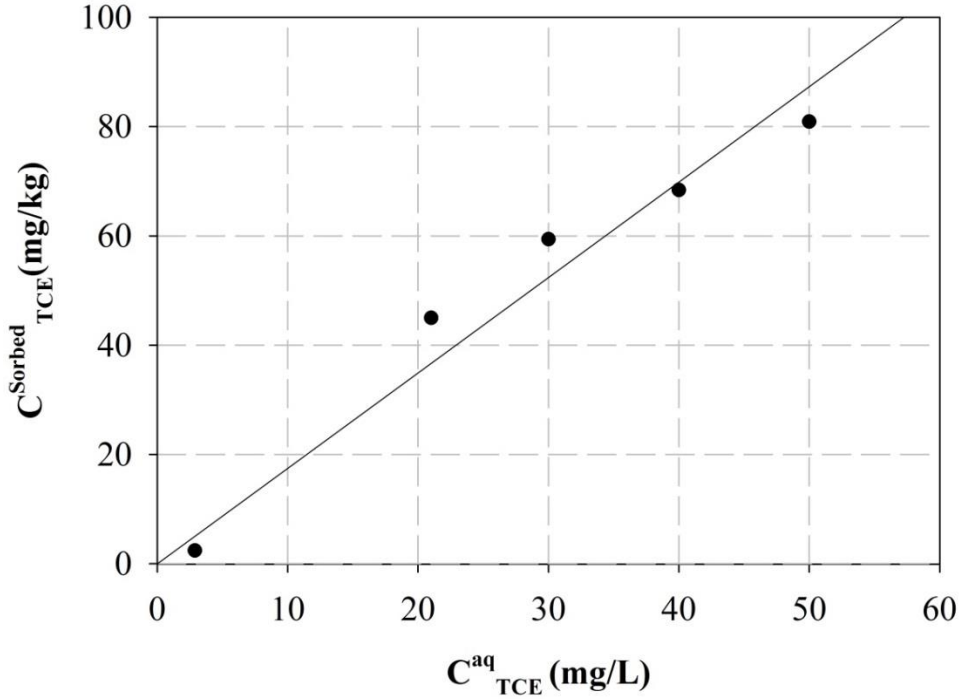

Figure S4 (a) TCE sorption kinetics on MTP soil and (b) Kd of TCE on MTP soil as determined from the slope of the graph

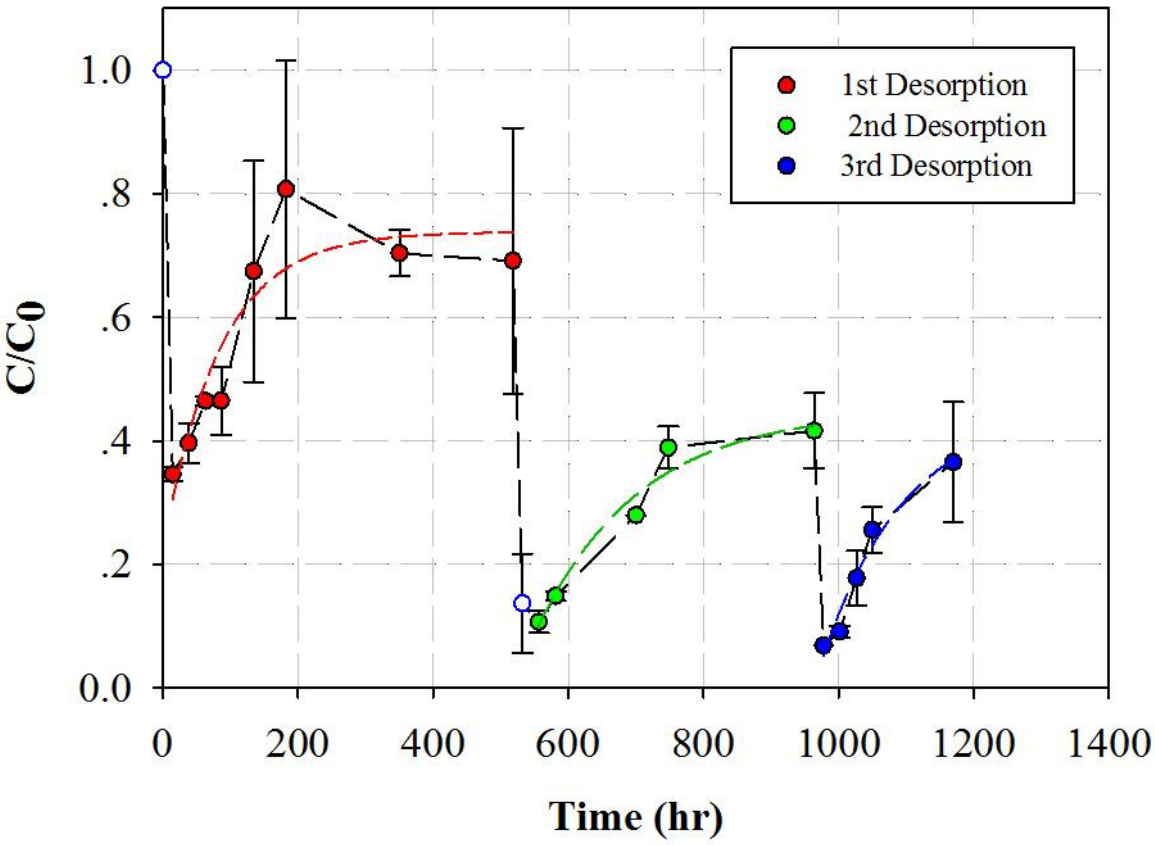

Figure S5 (a) TCE desorption kinetics involving three desorption cycles until dissolved TCE concentration reaches the plateau level for each cycle. The dashed lines represent the pseudo first order desorption modeling for each cycle.

Table S3 Physical Properties of MTP Soil

Property	Description/Vale
USC soil types	Clayey Sand
Color	Dark Brown
Specific gravity)(-)	2.53
Total Organic Carbon in Soil (g/Kg)	27.08

Table S4 Physical and Chemical Properties of MTP Groundwater

T (°C)	pH	Conductivity (µS/cm)	DO (mg/l)	ORP (MV)	TOC (mg/l)	Alk (mg/l as $CaCO_3$)	Anion/Oxyanion (mg/L)				Cation (mg/L)			
							Cl^-	NO^-_3	PO_4^{-3}	SO^{-2}_4	Na+	K^+	Mg^{2+}	Ca^{2+}
30	4.5	1,518	2.1	312	6.4	50	42.9	16.7	–	19.9	34.6	2.0	-	-

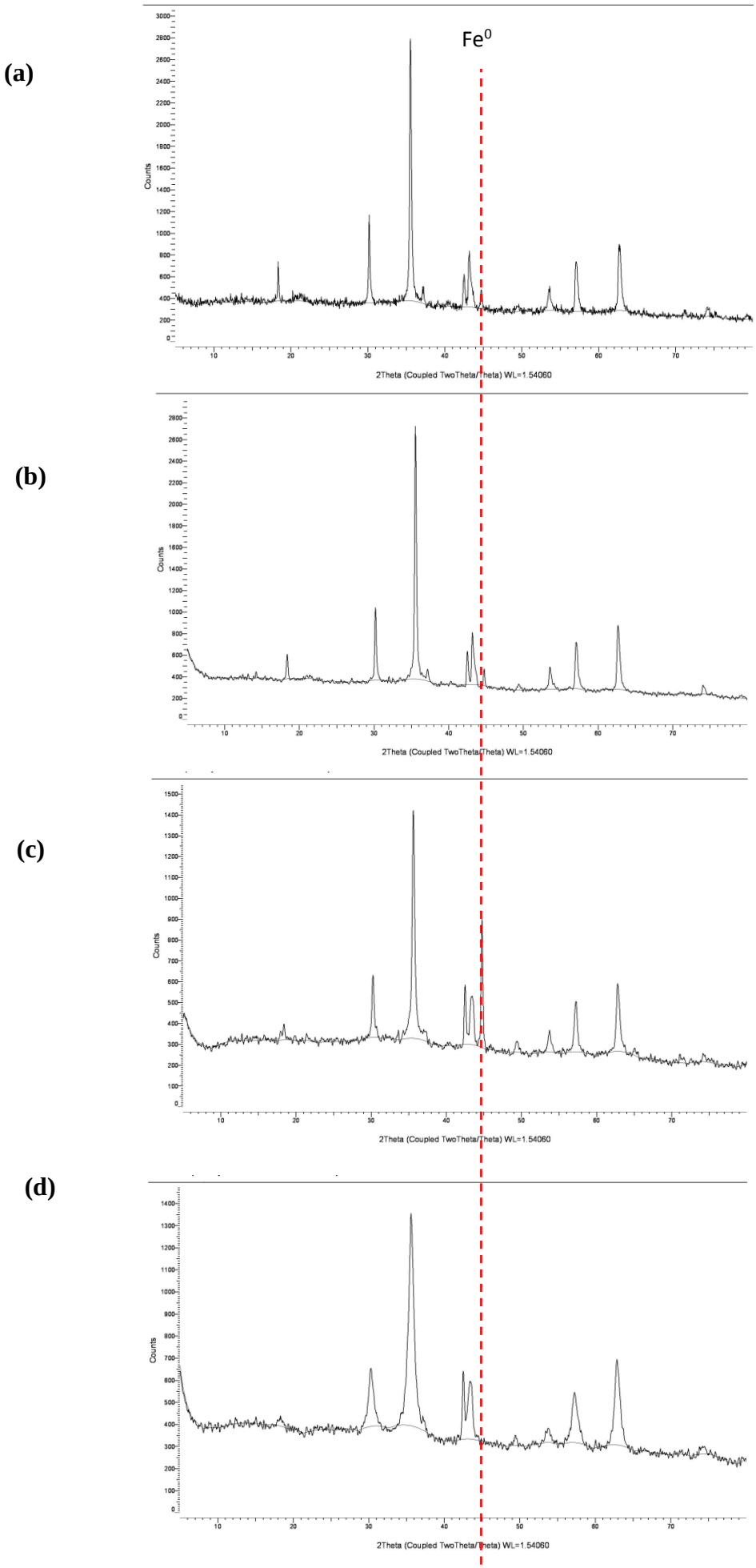

Figure S6 XRD of (a) fresh NZVI (NF25), (b) aged NZVI (MRNIP), (c) ZVI (H200), and (d) Fe_3O_4. The red dash line represents Fe^0 while the rest of the peaks are magnetite.

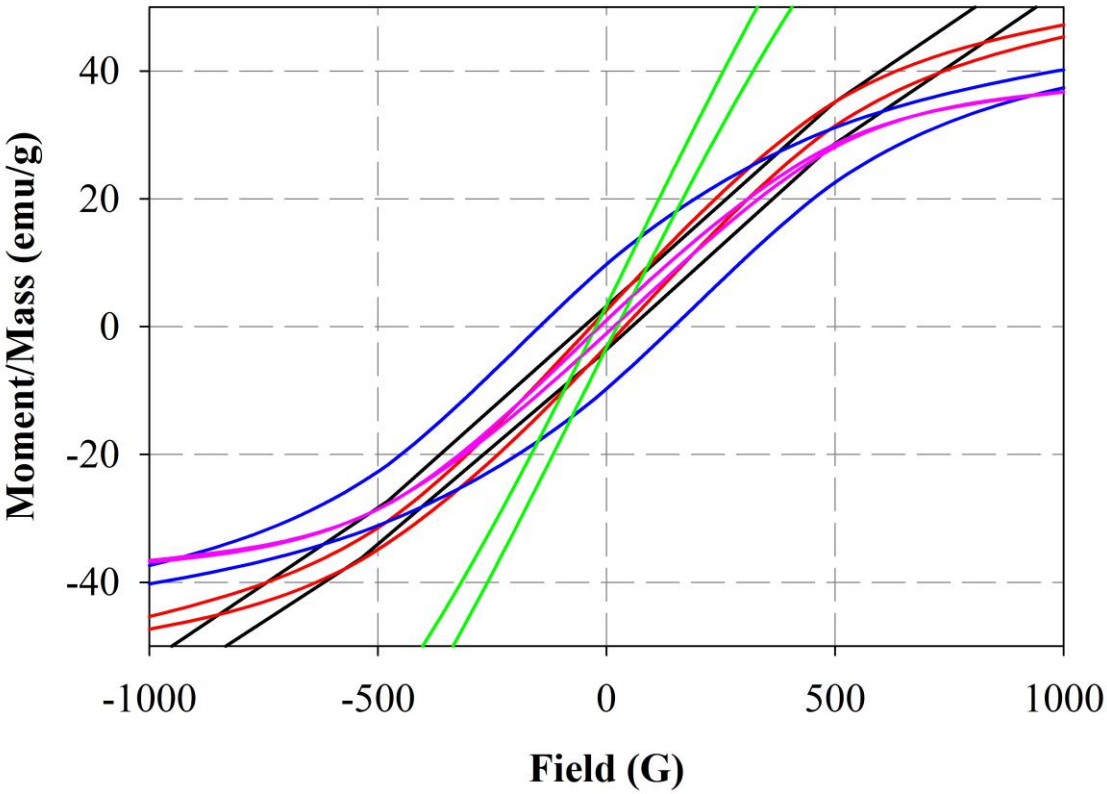

Figure S7 the enlargement of Fig.1 from the field of 1,000 to -1,000 G to illustrate the hysteresis loops of each ZVI or NZVI sample

Details of Material and Magnetic Characteristics of ZVI and NZVI

First, ZVI powder (H150 and H200) has a higher M_s (191 and 133 emu/g for H150 and H200, respectively) than NZVI (M_s of MRNIP and NF25 =74 and 55 emu/g, respectively), while magnetite nanoparticles (50 emu/g) have the lowest M_s. Due to ferromagnetism, the saturation magnetization of Fe^0 is supposed to be greater than Fe_3O_4 [2]. This agrees with findings here, and a recent study showing that oxidation of iron nanoparticles decreases M_s [3]. The remanence and coercivity of fresh NZVI (NF25) is greater than ZVI (H150 and H200), aged NZVI (MRNIP2), and magnetite, suggesting that size and oxidation of iron affects the permanence of magnetism. As shown in Fig. 1a, M_r of NF25 (11 emu/g) is greater than MRNIP2 (4 emu/g), H150 (5.5 emu/g), H200 (4 emu/g), and magnetite (1.6 emu/g). Further, M_r of NF25 is in good agreement with the value reported in the previous study [4]. Moreover, H_c of NF25 (168 G) is also substantially greater than H200 (60 G), H150 (40 G), MRNIP2 (36 G), and magnetite (36 G). This agrees with a recent study revealing that M_r and H_c decreased with the increase of particle size for multi-domain magnetic particles (particle diameter > 8-10 nm) [5].

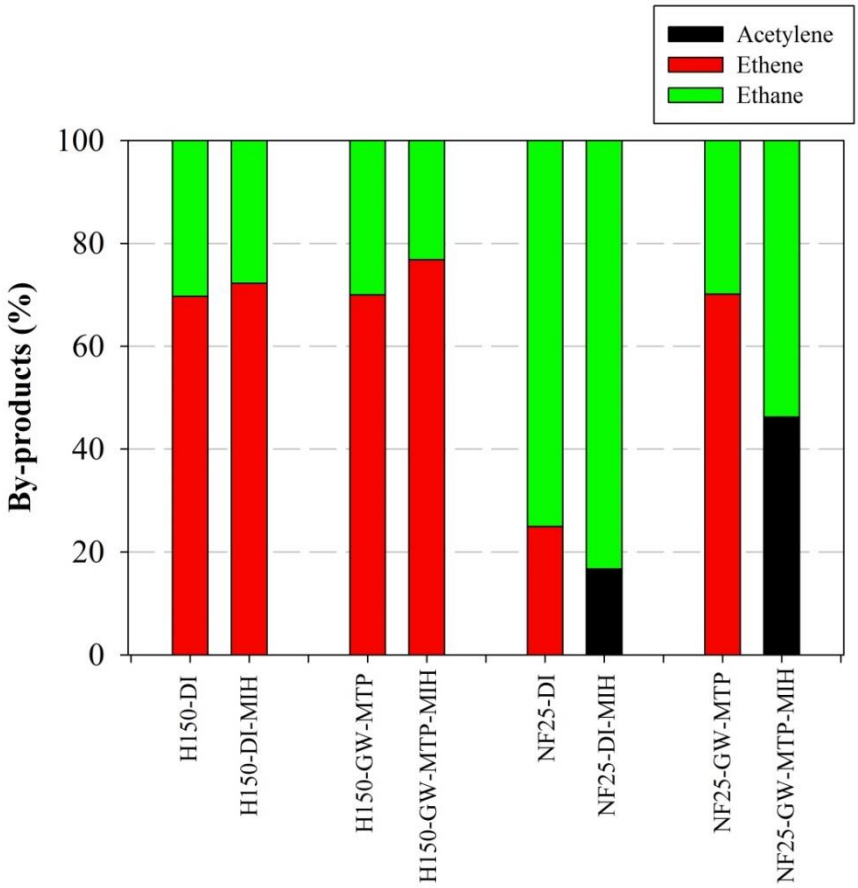

Figure S8 By-product distributions from TCE dechlorination using NF25 and H150 in DI and MTP with and without AC EMF. The mole balance of acetylene, ethene, ethane in these studies was from 93 to 108% of the initial TCE mole.

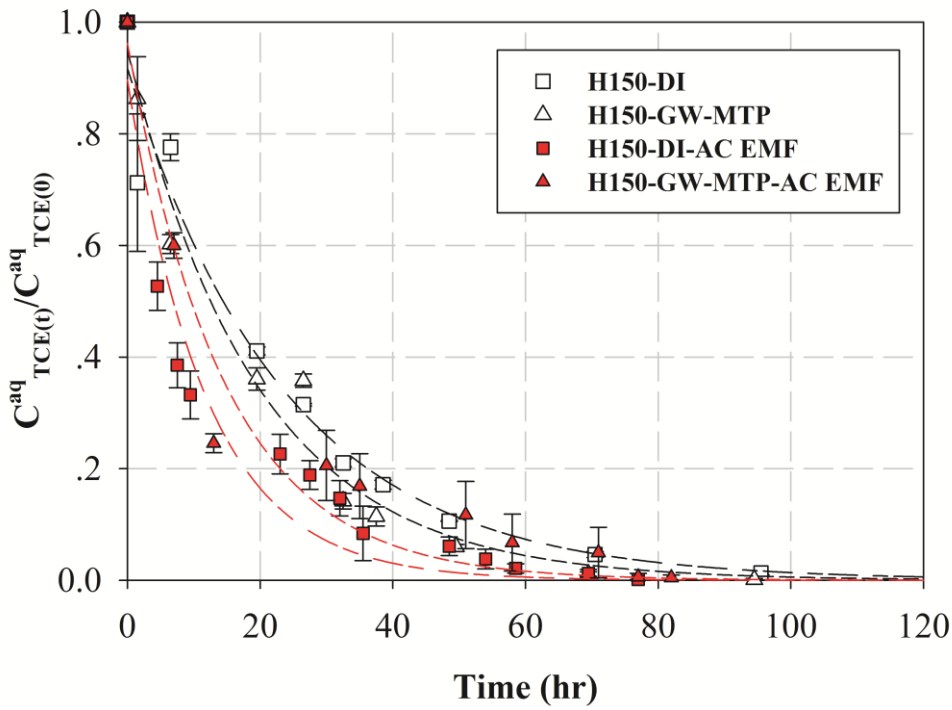

Figure S9 TCE dechlorination kinetics using H150 in DI (squares) and MTP (triangles) without AC EMF (white) and with AC EMF (red).

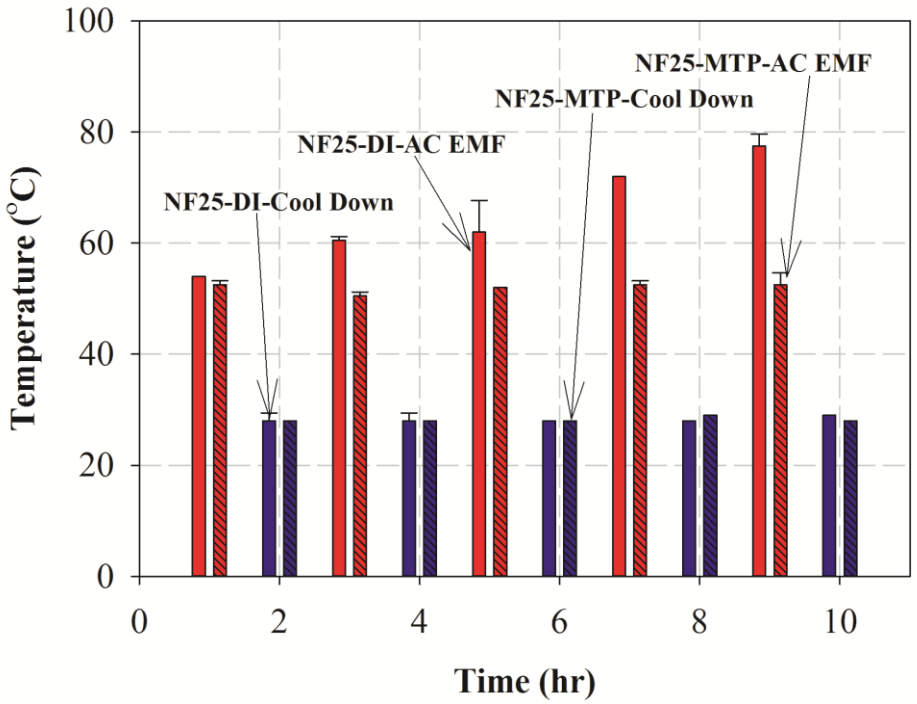

Figure S10 Temperature profiles of NF25 in DI water and MTP groundwater as a function of time during five heating cycles.

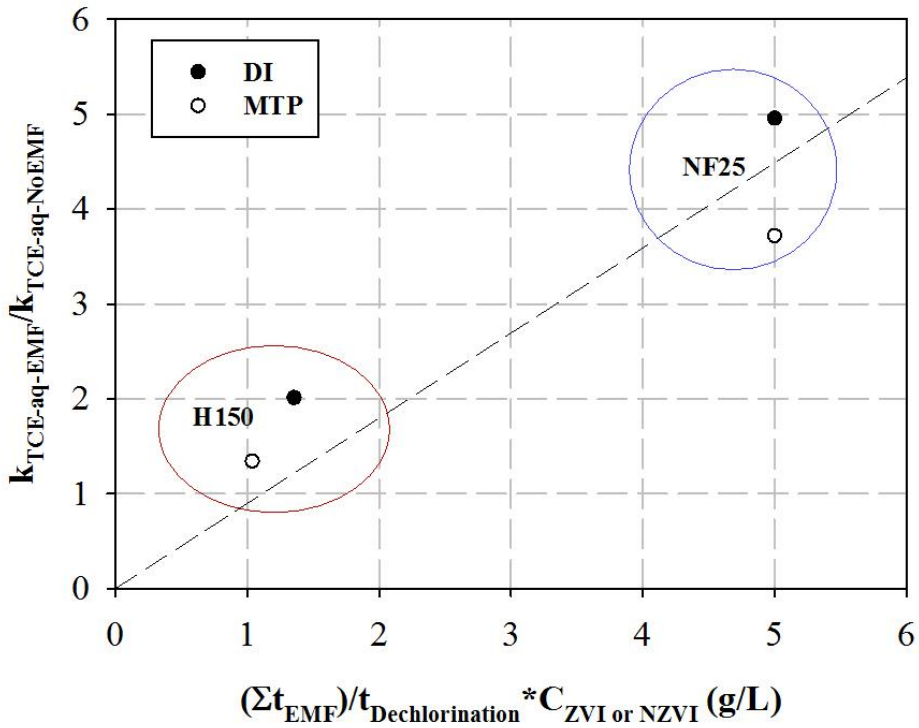

Figure S11 the linear correlation (with the slope of 0.9) between the enhanced dissolved TCE dechlorination rate constant due to AC EMF ($k_{TCE\text{-}aq\text{-}AC\ EMF}/k_{TCE\text{-}aq\text{-}No\ AC\ EMF}$) and the ratio of AC EMF application time ($\Sigma t_{AC\ EMF}$) over the total dechlorination time ($t_{Dechlorination}$) multiplied by particle concentration ($C_{ZVI\ or\ NZVI}$) for all the four cases in this study (both NF25 and H150 in DI and MTP groundwater).

TCE Dechlorination in Water Bath

In order to investigate this possibility, we conducted another set of TCE dechlorination experiments using NF25 in a heating water bath to simulate the temperature profile for dechlorination obtained from the MIH study of NF25 with EMF (Fig. S10 in SI). The simulated temperature profile over 10 hours using heating water bath is shown in Fig. S12 in SI. This 10-hour experiment consisted of five cycles of non-EMF heating. Each cycle was two hours with 60 minutes of heating with water bath at a particular temperature similar to Fig. S10 at a corresponding heating cycle, followed by 60 minutes of reaction without heating (i.e., cooling down).

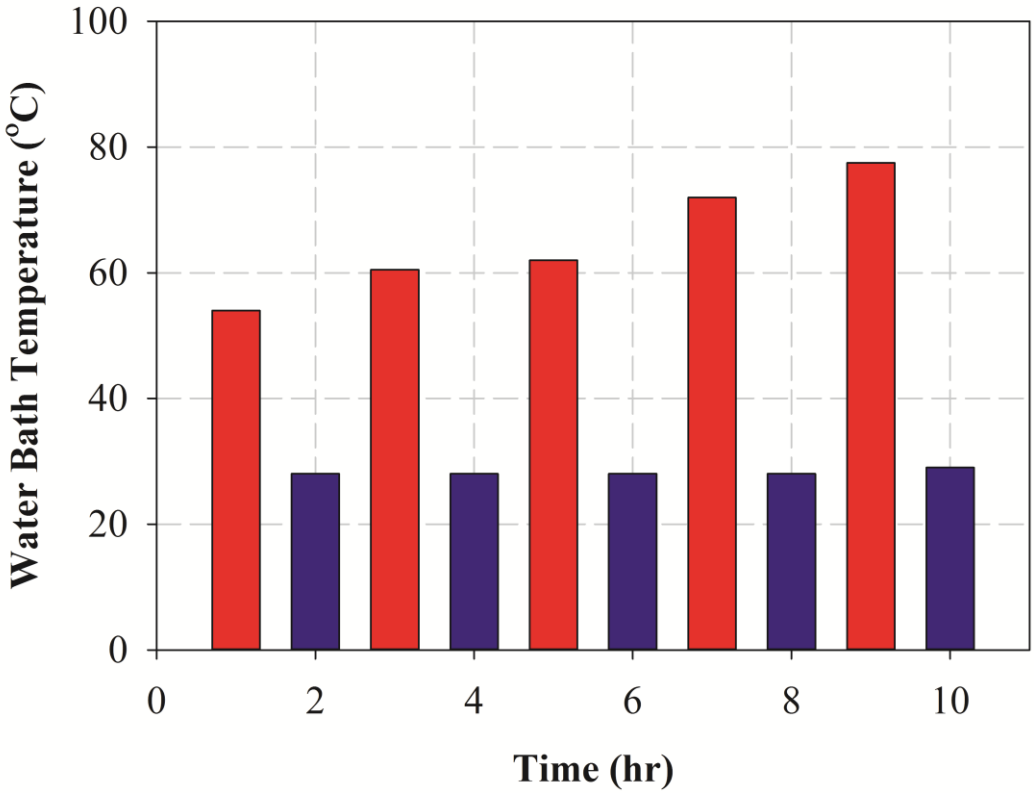

Figure S12 Temperature profiles of NF25 in DI water heated by a water bath as a function of time during five heating cycles

Reference

1. Liu, Y.; Phenrat, T.; Lowry, G. V., Effect of TCE concentration and dissolved groundwater solutes on NZVI-promoted TCE dechlorination and H2 evolution. *Environ. Sci. Technol.* **2007,** *41*, (22), 7881-7887.
2. Phenrat, T.; Saleh, N.; Sirk, K.; Tilton, R., D.; Lowry, G., V., Aggregation and sedimentation of aqueous nanoscale zerovalent iron dispersions. *Environ. Sci. Technol.* **2007,** *41*, (1), 284-290.
3. Matsuura, H.; Seto, K.; Yang, H.; Kawano, K.; Takahashi, M.; Ogawa, T., Influence of Oxidation and Size of Iron Nanoparticles on the Saturation Magnetization. *IEEE Trans. Magn.* **2008,** *44*, (11), 2804-2807.
4. Rosická, D.; Šembera, J., Assessment of Influence of Magnetic Forces on Aggregation of Zero-valent Iron Nanoparticles. *Nanoscale Res. Lett.* **2011,** *6:10*.
5. Park, J.-I.; Kang, N.-J.; Jun, Y.; Oh, S. J.; Ri, H. C.; Cheon, J., Superlattice and magnetism directed by the size and shape of nanocrystals. *Chem. Phys. Chem.* **2002,** *3*, 543-547.

ภาคผนวก 2

Delivery and Electromagnetic Induction of Foam-based Nanoscale Zerovalent Iron (NZVI) Particles as a Combined Remediation Technique for Non-Aqueous Phase Liquid (NAPL) in Unsaturated Porous Media: Proof of Concept

Journal:	*Environmental Science & Technology*
Manuscript ID	es-2016-00314f
Manuscript Type:	Article
Date Submitted by the Author:	20-Jan-2016
Complete List of Authors:	Srirattana, Supawan; Naresuan University, Civil Engineering Piaowan, Kitsanateen ; Naresuan University, Civil Engineering Lowry, Gregory; Carnegie Mellon University, Civil & Environmental Engineering Saenton, Schradh; Chiang Mai University, Geological Sciences Phenrat, Tanapon; Naresuan University, Civil Engineering

Delivery and Electromagnetic Induction of Foam-based Nanoscale Zerovalent Iron (NZVI) Particles as a Combined Remediation Technique for Non-Aqueous Phase Liquid (NAPL) in Unsaturated Porous Media: Proof of Concept

Supawan Srirattana[1,2], Kitsanateen Piaowan[1,2], Gregory V. Lowry[3,4], Schradh Saenton[5], and Tanapon Phenrat[1,2]*

[1]Research Unit for Integrated Natural Resources Remediation and Reclamation (IN3R), Department of Civil Engineering, Faculty of Engineering, Naresuan University, Phitsanulok, Thailand, 65000

[2]Center of Excellence for Sustainability of Health, Environment and Industry (SHEI), Faculty of Engineering, Naresuan University, Phitsanulok, Thailand, 65000

[3]Center for Environmental Implications of Nanotechnology (CEINT) and [4]Department of Civil & Environmental Engineering, Carnegie Mellon University, Pittsburgh, PA 15213-3890, USA.

[5] Department of Geological Sciences, Faculty of Science, Chiang Mai University, Chiang Mai, Thailand, 50200

Submitted to

Environmental Science & Technology

*Corresponding author: Tanapon Phenrat (pomphenrat@gmail.com)

(6655)964057(ph) (6655)964002(fax)

Abstract

Nanoscale zerovalent iron (NZVI) is a promising remediation agent for volatile organic compound contamination in saturated subsurface but is rarely applied for vadose zone as there are not enough water molecules in the unsaturated zone to participate in reductive dechlorination. Nevertheless, NZVI is ferromagnetic, capable of inducing heat under an applied low frequency electromagnetic field (LF-EMF), offering an opportunity to serve as a thermally enhanced remediation when combined with soil vapor extraction. In this study, we evaluated the possibility of using foam as a carrying vehicle to emplace NZVI in unsaturated porous media followed by the application of LF-EMF in laboratory batch reactors. We found that sodium lauryl ether sulfate (SLES) (3% w/w) was the best candidate for generating stable foam-based NZVI. The half-life of SLES foam-based NZVI (SLES-F-NZVI) was 173 min. The SLES-F-NZVI carried as much as 41.31 g/L of NZVI in the liquid phase of the foam, and could generate heat to raise ΔT = 77ºC in 15 min at the deposited SLES-F-NZVI =77 g/kg. Under this condition, SLES-F-NZVI together with LF-EMF enhanced TCE evaporation from TCE dense non-aqueous phase liquid (DNAPL) in unsaturated sand by 39.51 ± 6.59 times in comparison to the reactors without SLF-EMF application.

Keywords; nanoscale zerovalent iron particles; foam; unsaturated porous media; magnetic induction heating; chlorinated volatile organic compounds**;** dense non-aqueous phase liquid (DNAPL)

1. Introduction

Vadose zone contamination with chlorinated volatile organic compounds (CVOCs) is a persistent and vexing environmental problem, jeopardizing environmental quality and public health. The average half-life for CVOC abiotic transformations ranges from two months to greater than 10^{10} years[1]. CVOCs may be entrapped as dense non-aqueous phase liquid (DNAPL) residuals in pores in the vadose zone and behave as long-term sources of toxic vapor migrating to the land surface and migrating into buildings, causing vapor intrusion problems [2-4]. Additionally, CVOCs as DNALs in the vadose zone act as long-term sources of groundwater contamination by discharging CVOCs to underlying groundwater via infiltration and percolation [5, 6]. Furthermore, CVOCs can also sorb onto soil and subsequently discharge both vapor and dissolved CVOCs to contaminate soil gas and underlying groundwater [2, 3]. While cleaning up of a CVOC contaminated saturate zone comprises a variety of remedial alternatives, remediation techniques of CVOCs for the vadose zone are limited to excavation, soil vapor extraction (SVE) [7, 8], thermal enhanced SVE [9-12], and bioventing [2, 13].

In situ chemical reduction (ISCR) using nanoscale zerovalent iron (NZVI) becomes a promising groundwater remediation alternative [14-22]. Evidently, by 2009, more than 45 pilot-scale and field-scale NZVI remediation tests had been conducted [23, 24]. However, water-based NZVI is much less applicable for dechlorination of CVOCs in the vadose zone due to technical difficulties in NZVI delivery. For example, gravity may preferentially induce the migration of water-based NZVI dispersion in the vertical direction, limiting lateral transport and the radius of influence (ROI) [25]. In addition, flushing water-based NZVI dispersion in the vadose zone may cause unintended CVOC dissolution and migration to underlying aquifers,

leading to even more severe contamination. Recent studies by Zhong and Li's group from Pacific Northwest National Laboratory proposed using foam-assisted delivery of NZVI in the vadose zone to overcome these technical difficulties [25-27]. They revealed that sodium lauryl ether sulfate (SLES)-stabilized foam could transport NZVI through an unsaturated sand-packed column much better than water-based NZVI dispersion [25]. Even though the difficulties in particle delivery are solved by the foam-assisted delivery option, NZVI still faces technical difficulty in CVOC degradation, as reductive dechlorination by NZVI requires water molecules for the transformation of CVOCs to more benign by-products [18, 21, 22, 28-33]. Expectedly, the vadose zone may not have enough water molecules and may not have sufficient CVOC dissolution in pore water for substantial reductive dechlorination by NZVI. Thus, the chemical reactive nature of NZVI may not be as useful to vadose zone clean-up as it is for the saturated zone.

Nevertheless, due to its ferromagnetic properties, NZVI may still be useful for vadose zone remediation. NZVI's magnetic response under applied magnetic field has just recently been employed for remediation research. Although, in 1999, Jovanovic's research group first utilized the magnetic property of micron-sized Pd/ZVI particles impregnated into calcium alginate beads to make a magnetically stabilized fluidized bed (MSFB) reactor for dechlorination of p-chlorophenol possible under an applied DC electromagnetic field (DC MF), the magnetic property of ZVI was not intentionally used to enhance the p-chlorophenol degradation[34-36]. In 2011, Choi's research group reported that applying DC MF to ZVI can induce an oxidation reaction due to the enhanced O_2 dissolution and ZVI dissolution to Fe^{2+} for Fenton's reaction[37]. Until recently, Guan's research group presented a series of experimental studies using superimposed weak magnetic field or premagnetization to enhance the water treatment efficacies of various metal and metalloid, including antimony, arsenic, chromate, copper, and selenite[38-43] by ZVI. The enhanced removal was attributed to

the accelerated ZVI corrosion and the transformation of amorphous iron (hydro) oxides to lepidocrocite.

More importantly, ferromagnetic materials, such as Fe^0, and its oxidized ferromagnetic products including magnetite nanoparticles (Fe_3O_4) and maghemite (γ-Fe_2O_3), produce heat when subjected to a low frequency electromagnetic field (LF-EMF) (30-300 kHz). They are used in medicine for thermal treatments, such as magnetic assisted hyperthermia [44, 45], where functionalized magnetic nanoparticles target tumor cells and then are heated by applied LF-EMF to kill the cancer cells [45, 46]. Most recently, Phenrat's research group revealed that using ZVI and NZVI with applied LF-EMF enhanced dechlorination of dissolved TCE and TCE in a soil-water-TCE system up to 5-fold compared to the absence of LF-EMF, presumably due to magnetically accelerated ZVI corrosion and thermally enhanced desorption of TCE from soil[47]. For the first time, the study indicates the potential for ZVI and NZVI coupled with LF-EMF as a combined remediation technique for increasing the rate and completeness of in situ cleanup of adsorbed phase contaminants in saturated soil and groundwater.

Similarly, NZVI should be able to induce heat under an applied LF-EMF in the vadose zone as it does in the saturated zone [47]. Conceptually, coupled with SVE, the heat generated by NZVI under LF-EMF should speed up CVOC removal in the vadose zone via thermal enhancement evaporation (Fig.1). Raising chemical vapor pressures by heating soil *in situ* can decrease the remediation time and help effectively remove semi-volatile chemicals untreatable by conventional SVE. This concept is similar to that of using radio frequency heating (RFH) and microwave heating (MWH), except that RFH and MWH utilize frequencies as high as 500 kHz to 500 MHz [48, 49] and 500 MHz to 500 GHz [49, 50], respectively. In addition, a major difference between the proposed NZVI heating under LF-EMF and conventional RFH or MWH is that the LF-EMF proposed here generates heat by

electromagnetic induction of emplaced NZVI in the vadose zone, while the RFH or MWH discussed in previous studies generate heat by dielectric heating of molecules with the permanent and/or induced electric dipoles (unbalanced charges) [48-50] present in soil or pore water. For this reason, LF-EMF heating of NZVI should improve remediation efficacy in a similar way as RFH or MWH, but with less energy input. This performance is similar to the enhanced TCE dechlorination up to 8 times using combined moderate-temperature subsurface electrical resistance heating (up to 50°C) with *in situ* ZVI treatment in a field scale application [51]. Nevertheless, this novel combination of NZVI and LF-EMF has never been tested for unsaturated porous media.

The present study evaluates the feasibility of using foam-based NZVI (F-NZVI) together with LF-EMF (150 kHz) to enhance NZVI emplacement and TCE evaporation from a TCE dense non-aqueous phase liquid (DNAPL) in laboratory-scaled unsaturated porous media. The greater the enhanced TCE evaporation via magnetic induction heating (MIH) of F-NZVI, the more effective the thermally enhanced SVE. Five different surfactants were tested as F-NZVI stabilizers. Magnetic characterization was conducted for NZVI and F-NZVI. Batch and column experiments were conducted to evaluate F-NZVI stability and mobility in unsaturated porous media. The ability of F-NZVI to generate heat under an applied LF-EMF was also examined. The TCE evaporation kinetics, both with and without LF-EMF, were compared to quantify the benefits of using LF-EMF together with F-NZVI. The feasibility of this combined remediation concept is discussed based on both F-NZVI deliverability and enhanced TCE evaporation.

2. Materials and Methods

2.1. Surfactant and NZVI

Five commercially available surfactants, PEG-20 sorbitan monostearate (Tween 60), sorbitan monooleate (Span 80), Vertex Type 1 (proprietary foaming agent for lightweight cellular concrete), Vertex Type 2 (proprietary foaming agent for lightweight cellular concrete) and sodium lauryl ether sulfate (SLES) were used as foam stabilizers in this study. The first four surfactants are chemically pure while the last has active matter at around 70%. The NZVI used in this study was Nanofer 25 (NF25) (Nanoiron, Czech Republic). Table S1 (in Supporting Information (SI)) summarizes the physical properties of NF25 as obtained from the supplier. In addition, NZVI was characterized by X-ray diffraction (XRD) and magnetic properties using a vibrational sample magnetometer (VSM).

2.2. Foam generation procedure and foam characterization

The foam and F-NZVI generation procedure used in this study was described in detail in a previous study [26] (See SI and Fig.S1). This first part of the experiment controlled the surfactant concentration (1% (w/w)), NZVI concentration in the surfactant stock solution (50 g/L) and N_2 flow rate (125 mL/min) at constant values in order to determine the best type of surfactant for foam formation and stabilization. The quality of the control foam (no NZVI) and F-NZVI, the foam stability, and the bubble size distribution of the control foam and F-NZVI were determined as described in SI [27, 52]. Each experiment was conducted in duplicate.

After evaluating the best kind of surfactant for stabilizing F-NZVI (found to be SLES, as discussed in the result and discussion section), the second part of the experiment determined the optimal surfactant concentration for foam generation by generating foam using 50 g/L NZVI at various surfactant concentrations of 1, 3, 5, 7, and 9% (w/w). Then the best type of surfactant at the optimal surfactant dose was used to determine the optimal N_2 flow rate by conducting an experiment covering various N_2 flow rates of 125, 300, and 500 mL/min. For this part of the experiment, we could determine the optimal F-NZVI generating conditions.

2.3. Delivery and emplacement of F-NZVI in unsaturated sand-packed column

Only SLES-F-NZVI (F-NZVI stabilized by SLES) was used in this experiment as SLES-F-NZVI appeared to perform the best of all the five surfactants (to be discussed next). The transport experiments were performed using a cylindrical acrylic column, 16 cm in length and 2 cm in inner diameter, packed with quartz sand with an average size of 0.85 mm. The column was attached to the foam generation column (Fig.S1). Sixty pore volumes (PVs) of SLES-F-NZVI generated at the optimum generating condition (50 g/L NZVI in 3% (w/w) SLES solution at a flow rate of 1.5 mL/min and 500 mL/min N_2) was delivered into the unsaturated sand-packed column. Each experiment was conducted in duplicate. The breakthrough NZVI concentrations in SLES-F-NZVI were monitored. Furthermore, the concentration of NZVI deposited onto the unsaturated sand was determined by dissecting the sand-packed column into eight 2-cm long segments. See details of the experimental setup in SI.

2.4. Magnetic induction heating (MIH) of F-NZVI and F-NZVI emplaced on unsaturated porous media

In this experiment, the MIH capability of F-NZVI, both as free foam and foam emplaced into unsaturated porous media, under applied LF-EMF was examined. The former provides a basic understanding of how much heat free F-NZVI can be induced magnetically while the latter more realistically represents the MIH of F-NZVI for vadose zone remediation because when applied for remediation, F-NZVI will be injected and emplaced into the vadose zone, where it helps generate heat under an applied LF-EMF. Only SLES-F-NZVI as the best performing F-NZVI was investigated in this study. See the details of both experimental setups in SI.

2.5 Enhanced TCE evaporation by F-NZVI with MIH

F-NZVI coupled with MIH was evaluated for its capability to enhance TCE evaporation in a batch study. The 25 ml glass vial used in this experiment contained 2 mL of SLES-F-NZVI (generated using 100 g/L NZVI in 3% (w/w) SLES and 500 mL/min N_2) and 17.20 g of quartz sand with three different water saturations (WS) (5 %, 25 %, and 50 %) in order to evaluate the role of water saturation on enhanced TCE evaporation via F-NZVI and MIH. Pure phase TCE of 0.25 mL (or 3.5% saturation) was pipetted into the vial prior to being promptly capped with Teflon Mininert™ to prevent TCE gas leaving the reactor. The reactor was homogenized in an orbital shaker for 30 min prior to the study. Control rectors including TCE in sand without SLES-F-NZVI were made under the same set-up with the same three WS. The vial was insulated and placed into the center of the induction coil of a custom-made electromagnetic magnetic field generator (EMFG) (see SI) at 13 A and 150 kHz for MIH study for 5, 10, 15, 30, and 60 min. The temperature was measured using an infrared and a contact thermometer. TCE evaporation due to SLES-F-NZVI coupled with MIH was quantified by sampling 50 μL of headspace via a gastight syringe through the Teflon Mininert™ valve. The gas sample was analyzed for TCE and its chlorinated byproducts using a 20 m Agilent J&W DB-624 capillary column on an Agilent 7820GC/ECD. The TCE evaporation in a reactor with SLES-F-NZVI but without LF-EMF was also monitored for comparison.

3. Results and discussion

3.1. Characteristic of Foam and F-NZVI

Only three types of surfactant: SLES, Vertex Type 1, and Vertex Type 2 successfully generated foam and F-NZVI while Span 80 and Tween 60 appeared to be too sparingly soluble in water to assist foam formation. The quality of foam was very high (99.60-99.69%) both with and without NZVI for all three kinds of surfactant. At 1% (w/w) surfactant without

NZVI, SLES appeared to be the most stable (foam half-life ($t_{1/2}$) = 143 min) followed by Vertex Type 1 ($t_{1/2}$ = 130 min), and Vertex Type 2 (t1/2 = 56 min) (Fig.2a). The bubble size distribution of foam without NZVI was from 5 to 35 µm (Fig. 2b). Most of the bubble sizes for foam stabilized by Vertex Type 2 (see Fig. 2c) and SLES were 6 to 10 µm, while most of the bubble sizes for foam stabilized by Vertex Type 1 was slightly bigger, i.e. 11 to 15 µm.

Interestingly, adding NZVI into the foam did not seriously alter foam stability for both SLES-F-NZVI (NZVI foam stabilized by SLES) ($t_{1/2}$ = 140 min) and Vertext Type 1-F-NZVI ($t_{1/2}$ = 131 min), while NZVI substantially enhanced the stability of the foam stabilized by Vertex Type 2, for which $t_{1/2}$ became 112 min (Fig.2a), twice as much as without NZVI. This similar synergetic effect of nanoparticles and surfactant in foam stabilization has previously been reported [53, 54]. Fig.2d illustrates a microscopic demonstration of surfactant modified NZVI adsorption onto the foam bubble. Noticeably, black aggregates of surfactant-modified NZVI sorbed onto the surface of the foam bubble between the contact line of the two phases (gas and liquid). The accumulation of surfactant-modified NZVI on the foam surface is similar to interfacial targeting of the NAPL source zone by amphiphilic polymer-modified NZVI in saturated porous media reported in recent studies [15, 28]. The film of attached surfactant-modified NZVI on the foam bubble may increase the surface elasticity of the foam, reduce the coarsening tendency, and enhance foam stability [53]. This could explain the increased stability of Vertex Type 2-F-NZVI, mentioned previously.

Since of all three workable surfactants, SLES appeared to perform the best at 1% (w/w), we next evaluated the effect of SLES concentration (1, 3, 5, 7, and 9% (w/w)) and N_2 flow rate (125, 300, and 500 mL/min) to determine the best conditions to generate SLES-F-NZVI. As shown in Fig. S3a, at an N_2 flow rate of 125 mL/min, SLES at a concentration of 3% performed the best in terms of foam stability ($t_{1/2}$ = 173 min). Next, we evaluated the role of N_2 flow rate to determine the best N_2 flow rate which could carry NZVI modified by SLES

at 3% (w/w) the best. As shown in Fig. S3b, the greater the N_2 flow rate, the greater the concentration of NZVI in foam. At an N_2 flow rate of 500 mL/min, SLES-F-NZVI contained NZVI as much as 33.49 ± 3.72 g/L when started with an initial concentration of 50 g/L. The capability of SLES-F-NZVI at 3% (w/w) SLES and 500 mL/min N_2 on NZVI carrying was 67% of the NZVI stock solution. Consequently, this optimum SLES-F-NZVI formation was used in all of the following experiments, unless otherwise specified.

3.2. Delivery and emplacement of F-NZVI in unsaturated sand-packed column

Fig. 3a illustrates the breakthrough curve of SLES-F-NZVI generated at 50 g/L NZVI stock solution in 3% (w/w) SLES at 500 mL/min N_2 flow rate. The foam quality of SLES-F-NZVI entering the sand-packed column was 99.83%, with the liquid portion of the foam (0.17%) carrying 41.32 g/L of NZVI. Noticeably, from 5th PV to 20th PV, the breakthrough NZVI concentrations seemed to reach steady state at around 45% of the influent concentration. The unsaturated media filtered around half of NZVI carried by the foam. This finding is in good agreement with a recent study which reported that NZVI (3g/L) carried by foam generated by SLES (0.5% (w/w)) was filtered at approximately 20% by an unsaturated sand-packed column (grain diameter of 0.8-1.25 mm) [25]. Presumably, the present study generated foam at a higher NZVI concentration than Ding's study, which caused more agglomeration of NZVI in the foam (see NZVI agglomerates attached on SLES-F-NZVI in Fig. S4 in SI) and thus was filtered out by the unsaturated porous media much easier. Nevertheless, from 20th to 60th PVs, the breakthrough NZVI concentrations gradually raised to 100% transportability through the unsaturated packed bed. Presumably, after 20th PV, the moisture content in unsaturated porous media exceeded the critical moisture content (θ_{cr}) where immobilized NZVI started to be released at a rate proportional to the product of the pore water velocity and the attached particle concentration [55]. This interesting behavior was

not observed in Ding's study, in which a transport study was conducted up to only 2 PVs [25]. Possibly, the moisture content of the unsaturated sand media in their study might not have reached the critical point.

Fig. 3b illustrates the NZVI attached to the sand in the unsaturated packed column after 60 PVs. The concentration of NZVI deposited on sand decreased exponentially with the distance from the inlet, in good agreement with typical infiltration behavior of colloidal and nanoparticles in unsaturated porous media reported previously [25]. Nevertheless, the amount of deposited NZVI in this study is greater than the previous study by around 5 to 10 times because NZVI concentration in the liquid portion of SLES-F-NZVI in this study was 41.32 g/L, while the NZVI concentration in foam used a previous study was only up to 4.4 g/L [25]. We designed the NZVI emplacement in unsaturated porous media to achieve high particle concentrations because the greater the emplaced NZVI, the more effective the thermally enhanced evaporation of TCE promoted by NZVI under SLF-EMF.

3.3. Magnetic induction heating (MIH) rate of F-NZVI

3.3.1 Free F-NZVI

NZVI is ferromagnetic material with the area under the hysteresis loop (ΔU) =6.7 × 10^4 emu G/g as confirmed by XRD and VSM results (Fig. S5 and S6 as well as detailed discussion of the results in SI)[47]. Under applied SLF-EMF, the DI, SLES solution, and SLES foam control samples without NZVI could not generate any heat. However, DI and SLES solutions with NZVI as well as SLES-F-NZVI generated heat and substantially raised the temperature of the suspension, as expected (Fig. 4a). For all cases, the temperature change per (ΔT) unit mass of NZVI ($Mass_{NZVI}$) was above 65°C/g for 15 min. However, their heat induction rate constants (k_{HI}) (determined from eqn. 1) and maximum induced temperature increases (ΔT_{max} /$Mass_{NZVI}$) significantly depended on their vehicles.

$$\frac{\Delta T}{Mass_{NZVI}} = \frac{\Delta T_{Max}}{Mass_{NZVI}}(1 - e^{-k_H t}) \quad (1)$$

Interestingly, SLES-F-NZVI (K_{HI} = 29.94 × 10^{-2} min^{-1} and $\Delta T_{max}/Mass_{NZVI}$ = 380°C/g) was the fastest in term of heating kinetics, followed by NZVI in SLES solution (K_{HI} = 17.88 × 10^{-2} min^{-1} and ΔT_{max} /$Mass_{NZVI}$ = 74°C/g), and NZVI in DI water (K_{HI} = 10.14 × 10^{-2} min^{-1} and ΔT_{max} /$Mass_{NZVI}$ = 186°C/g). Noticeably, the K_{HI} of NZVI in DI water in the present study is similar to those reported in a previous study [47]. The difference of K_{HI} and ΔT_{max} /$Mass_{NZVI}$ generated by NZVI in the three different vehicles may be attributed to the specific heat capacity (C_P) of each carrying media. As DI water, SLES solution, and SLES-F-NZVI examined in this study contained the same kind of NZVI with ΔU = 6.7 × 10^4 emu G/g, the heat dissipation per unit of NZVI mass should have been the same under exactly the same LF-EMF if the carrying media did not play any role. Nevertheless, the heat dissipated to mostly air in the foam structure of SLES-F-NZVI (air = 99.83%) while the same amount of heat dissipated to water in the DI water sample and to 3% (w/w) SLES in the SLES solution sample. Since the C_P of air (1.012 J/g/C at 25ºC) is lower than the C_P of DI water (4.1813 J/g/C at 25ºC) by around a factor 4, it is comprehensible that the K_{HI} of SLES-F-NZVI was 3 times greater than that of NZVI in DI water. Similarly, ionic surfactant is known to decrease the specific heat capacity of aqueous solution at concentrations greater than the critical micelle concentration (CMC) [56]. For this reason, at 3% (w/w) SLES, which is greater than its CMC, the C_P of SLES solution is supposed to be lower than DI, resulting in faster heating kinetics and extent of NZVI in SLES solution in comparison to DI, as observed in this study. Nevertheless, the decreased C_P of 3% (w/w) SLES concentration may still be greater than that of the air in SLES-F-NZVI; this helps explain the poorer heating kinetics of NZVI in SLES solution in comparison to SLES-F-NZVI

3.3.2 F-NZVI emplaced on unsaturated porous media

SLES-F-NZVI emplaced onto unsaturated sand could also generate heat and raise the temperature under an applied SLF-EMF, but the increase of temperature was significantly lower than that of free SLES-F-NZVI based on the same foam generating conditions. For example, Fig.S7 shows the ΔT for SLES-F-NZVI deposited onto unsaturated sand at each distance from the inlet according to the NZVI emplacement profile in Fig. 3b. It should be noted that the SLES-F-NZVI in Fig.S7 was generated under the same conditions as the free SLES-F-NZVI in Fig.4a. The MIH was conducted for 5, 10, and 15 min for each sand segment. As shown in Fig.S7, for each segment, the induced ΔT slightly increased with time from 5 to 15 min. Nevertheless, ΔT ranged only from 3 to 11ºC, not sufficient for the application of thermally enhanced remediation. The much lower ΔT of deposited F-NZVI in the unsaturated porous media in comparison to the free foam is probably due to low NZVI concentration attached to the unsaturated sand. For example, the maximum NZVI concentration deposited on to the sand according to Fig.3b was only around 5 g/kg at the segment of 0 to 2 cm while the NZVI concentration in free SLES-F-NZVI was 41.32 g/L. In order to achieve a meaningful thermally enhanced vadose zone remediation, a ΔT greater than 40ºC is preferable. Consequently, we generated SLES-F-NZVI foam using 100 g/L NZVI in 3% (w/w) SLES stock solution and an N_2 flow rate of 500 mL/min and delivered it to the unsaturated pack column. After 60 PVs of delivery, the emplaced NZVI profile along the unsaturated pack sand bed was as shown in Fig. S8. Noticeably, the concentration of NZVI deposited onto the sand increased substantially, presumably due the higher NZVI concentration in SLES stock solution for foam generation, as well as the NZVI agglomeration during the foam formation which could promote NZVI filtration by unsaturated sand. However, the concentration of NZVI deposited onto the sand decreased exponentially with the distance from the inlet. The maximum NZVI deposition onto the sand was 77 g/kg at 0 to 2 cm from the inlet. With this NZVI emplacement profile in each segment, the induced ΔT

substantially increased with time from 5 to 15 min (Fig. S9) in comparison to Fig. S7. Intuitively, the greater the emplaced NZVI, the higher the increased ΔT (Fig.4b) at a particular MIH time. Promisingly, the ΔT values were 41 and 77ºC for emplaced NZVI concentrations of 22 g/kg and 77 g/kg for the unsaturated sand segment of 2 to 4 and 0 to 2 cm, respectively, after 15 min of MIH (Fig.4b). This finding suggests that in order to make SLES-F-NZVI a viable alternative induced thermal remediation agent for the vadose zone, a significant amount of NZVI, at least at a concentration of 22 to 44 g/kg, must be emplaced in the unsaturated porous media.

3.4. Enhanced TCE Evaporation by SLES-F-NZVI under SLF-EMF

Here, we evaluate the feasibility of thermally enhanced TCE evaporation using MIH of SLES-F-NZVI deposited into unsaturated porous media at the attached NZVI concentration of 77 g/kg described in the previous section. The control reactors (i.e. unsaturated sand with water saturation (WS) = 5, 25, and 50% and TCE (pure phase) saturation = 3.5% without SLES-F-NZVI) and the reactors with SLES-F-NZVI but without MIH cannot generate any heat, and the temperature remains at 25ºC over 60 min of the study. However, under an applied LF-EMF, deposited SLES-F-NZVI generated heat to achieve T from 95 to 110ºC (ΔT from 70 to 85ºC) in 15 min (Fig.5a). WS in unsaturated porous media did not obviously affect the heating kinetics of the SLES-F-NZVI reactors in SLF-EMF. Thus, the deposited SLES-F-NZVI concentration is the main governing factor.

As theoretically hypothesized, the heat generated by SLES-F-NZVI under LF-EMF substantially enhanced TCE evaporation in batch reactors. As shown in Fig. 5b (presented in log scale), the TCE concentrations in the headspace of the control reactors and SLES-F-NZVI reactors without SLF-EMF application were relatively constant over 60 min of the study, i.e.

2,236 ± 329 mg/L and 2,114 ± 465 mg/L, respectively. WS did not appear to play any obvious role in TCE evaporation in these reactors. However, TCE concentrations in the headspace of SLES-F-NZVI reactors with MIH increased sharply from 0 to 5 min MIH for WS = 25 and 50%, while it increased more gradually in the reactor with WS = 5%. After around 15 min MIH, TCE concentration in the headspace of all MIH reactors reached a similar maximum concertation of 81,504 ± 4,751 mg/L, regardless of WS. Consequently, the MIH of SLES-F-NZVI deposited in unsaturated porous media at the NZVI concentration of 77 g/kg increased TCE evaporation by 39.51 ± 6.59 times in comparison to the reactors without MIH. This proof-of-concept experiment strengthens the VOC remedial feasibility using SVE thermally enhanced by F-NZVI and LF-EMF.

Acknowledgement

This research was funded in part by (1) the Thailand Research Fund (TRF) (MRG5680129), (2) the National Nanotechnology Center (Thailand), a member of the National Science and Technology Development Agency, through grant number P-11-00989, and (3) National Research Council (R2556B070).

Figure Caption

Fig. 1 A conceptual model of delivery and electromagnetic induction of F-NZVI as a combined remediation technique for NAPL) in vadose zone.

Fig. 2 (a) Half-life ($t_{1/2}$) of foam and F-NZVI formed by three different surfactants, (b) bubble size distribution of three different types of foam, and micrograph of (c) Vertex Type 2 Foam and (d) Vertex Type 2-F-NZVI.

Fig. 3 (a) Breakthrough curve of SLES-F-NZVI over 60-PV delivery through an unsaturated sand-packed column and (b) concentration of deposited NZVI in unsaturated porous media as a function of distance from the inlet.

Fig.4 (a) MIH kinetics of SLES-F-NZVI in comparison to NZVI in DI water and SLES concentration (3% (w/w)) and (b) linear trend between deposited NZVI concentration ($C_{Attached}$-NZVI/CSand (g/kg)) and induced ΔT (ºC) at 5, 10, and 15 min MIH under 150 kHz and 13 A of EMF.

Fig. 5 (a) Heating kinetics of reactors containing unsaturated sand at WS = 5, 25, and 50% and TCE saturation =3.5% induced by SLES-F-NZVI under 150 kHz and 13 A and (b) kinetics of TCE evaporation to headspace with and without applied SLF-EMF and as a function of MIH time.

Reference

1. Barbee, G. C., Fate of Chlorinated Aliphatic Hydrocarbons in the Vadose Zone and Ground Water. *Ground Wat. Monitor. Remed.* **2007,** *14*, (1), 129-140.
2. Brusseau, M. L.; Carroll, K. C.; Truex, M. J.; Becker, D. J., Characterization and Remediation of Chlorinated Volatile Organic Contaminants in the Vadose Zone: An Overview of Issues and Approaches. *Vadose Zone J.* **2013,** *12*, (4).
3. Ronen, D.; Graber, E. R.; Laor, Y., Volatile Organic Compounds in the Saturated–Unsaturated Interface Region of a Contaminated Phreatic Aquifer. *Vadose Zone J.* **2004,** *4*, (2), 337-344.
4. Abreu, L. D. V.; Johnson, P. C., Effect of Vapor Source−Building Separation and Building Construction on Soil Vapor Intrusion as Studied with a Three-Dimensional Numerical Model. *Environ. Sci. Technol.* **2005,** *39*, (12), 4550-4561.
5. Fagerlund, F.; Illangasekare, T.; Niemi, A., Nonaqueous-phase liquid infiltration and immobilization in heterogeneous media: 1. Experimental methods and two-layered reference case. *Vadose Zone J.* **2007,** *6*, (3), 471-482.
6. Fagerlund, F.; Illanagasekare, T.; Niemi, A., Nonaqueous-phase liquid infiltration and immobilization in heterogeneous media: 2. Application to stochastically heterogeneous formations. *Vadose Zone J.* **2007,** *6*, (3), 483-495.
7. Yang , J.-W.; Cho, H.-J.; Choi, G.-Y.; Lee, S.-H., Cost-effective Monitoring for a Soil Vapor Extraction (SVE) System. A Simplified Modeling and Gas Sensor Test. *Environ. Monit. Assess.* **2001,** *70*, (1), 201-210.
8. Yoon, H.; Valocchi, A. J.; Werth, C. J., Modeling the Influence of Water Content on Soil Vapor Extraction. *Vadose Zone J.* **2003,** *2*, 368-381.
9. Michael J. Truex1, J. M. G., Jefferey G. Powers3 andKira P. Lynch, Assessment of in situ thermal treatment for chlorinated organic source zones. *Remediation J.* **2009,** *19*, (2), 7-17.
10. Nakamura, T.; Senior, C. L.; Burns, E. G.; Bell, M. D., Solar-powered soil vapor extraction for removal of dense nonaqueous phase organics from soil. *J. Environ. Sci. Health A Tox. Hazard. Subst. Environ. Eng.* **2000,** *35*, (6), 795-816.
11. Poppendieck, D. G.; Loehr, R. C.; Webster, M. T., Predicting hydrocarbon removal from thermally enhanced soil vapor extraction systems. 1. Laboratory studies. *J. Hazard. Mater.* **1999,** *69*, (1), 81-93.
12. Poppendieck, D. G.; Loehr, R. C.; Webster, M. T., Predicting hydrocarbon removal from thermally enhanced soil vapor extraction systems: 2. Field study. *J. Hazard. Mater.* **1999,** *69*, (11), 95-109.
13. Boulding, J. R.; Ginn, J. S., *Practical Handbook of Soil, Vadose Zone, and Ground-Water Contamination: Assessment, Prevention, and Remediation*. CRC Press: New York, 2003; p 728.
14. Babakhani, P.; Fagerlund, F.; Shamsai, A.; Lowry, G. V.; Phenrat, T., Modified MODFLOW-Based Model for Simulating the Agglomeration and Transport of Polymer-Modified Fe0 Nanoparticles in Saturated Porous Media. *Environ. Sci. Pollut. Res.* **2015**.
15. Phenrat, T.; Fagerlund, F.; Illanagasekare, T.; Lowry, G. V.; Tilton, R. D., Polymer-modified Fe0 Nanoparticles Target Entrapped NAPL in Two Dimensional Porous Media: Effect of Particle Concentration, NAPL Saturation, and Injection Strategy. *Environ. Sci. Technol.* **2011,** *45*, (14), 6102–6109.
16. Phenrat, T.; Cihan, A.; Kim, H.-J.; Mital, M.; Illangasekare, T.; Lowry, G. V., Transport and Deposition of Polymer-Modified Fe0 Nanoparticles in 2-D Heterogeneous Porous Media: Effects of Particle Concentration, Fe0 Content, and Coatings. *Environ. Sci. Technol.* **2010,** *44*, (23), 9086-9093.
17. Zhang, W.-X.; Wang, C.-B.; Lien, H.-L., Treatment of chlorinated organic comtaminants with nanoscale bimetallic particles. *Catal. Today* **1998,** *40*, 387-395.
18. Zhang, W., Nanoscale iron particles for environmental remediation: An overview. *J. Nanopart. Res.* **2003,** *5*, 323-332.
19. Phenrat, T.; Kim, H.-J.; Fagerlund, F.; Illangasekare, T.; Lowry, G. V., Empirical correlations to estimate agglomerate size and deposition during injection of a polyelectrolyte-modified Fe0

nanoparticle at high particle concentration in saturated sand. *Journal of Contaminant Hydrology* **2010,** *118*, (3–4), 152-164.

20. Phenrat, T.; Schoenfelder, D.; Kirschling, T. L.; Tilton, R. D.; Lowry, G. V., Adsorbed poly(aspartate) coating limits the adverse effects of dissolved groundwater solutes on Fe0 nanoparticle reactivity with trichloroethylene. *Environ. Sci. Pollut. Res.* **2015**.

21. Tratnyek, P. G.; Johnson, R. L., Nanotechnologies for environmental cleanup. *Nano Today* **2006,** *1*, (2), 44-48.

22. Fagerlund, F.; Illangasekare, T. H.; Phenrat, T.; Kim, H.-J.; Lowry, G. V., PCE dissolution and simultaneous dechlorination by nanoscale zero-valent iron particles in a DNAPL source zone. *J. Contam. Hydrol.* **2012,** *131*, (1-4), 9-28.

23. Karn, B.; Kuiken, T.; Otto, M., Nanotechnology and in Situ Remediation: A Review of the Benefits and Potential Risks. *Environ. Health Perspect.* **2009,** *117*, (12), 1823-1831.

24. Mueller, N. C.; Braun, J.; J., B.; Černík, M.; Rissing, P.; Rickerby, D.; Nowack, B., Application of nanoscale zero valent iron (NZVI) for groundwater remediation in Europe. *Environ. Sci. Pollut. Res.* **2012,** *19*, 550-558.

25. Ding, Y.; Liu, B.; Shen, X.; Zhong, L.; Li, X., Foam-Assisted Delivery of Nanoscale Zero Valent Iron in Porous Media. *J. Environ. Eng.* **2013,** *139*, (9), 1206–1212.

26. Shen, X.; Zhao, L.; Ding, Y.; Liu, B.; Zeng, H.; Zhong, L.; Li, X., Foam, a promising vehicle to deliver nanoparticles for vadose zone remediation. *J. Hazard. Mater.* **2011,** *186*, (2-3), 1773-1780.

27. Zhong, L.; Szecsody, J. E.; Zhang, F.; Mattigod, S. V., Foam Delivery of Amendments for Vadose Zone Remediation:Propagation Performance in Unsaturated Sediments. *Vadose Zone J.* **2010,** *9*, 757-767.

28. Saleh, N.; Phenrat, T.; Sirk, K.; Dufour, B.; Ok, J.; Sarbu, T.; Matyjaszewski, K.; Tilton, R. D.; Lowry, G. V., Adsorbed triblock copolymers deliver reactive iron nanoparticles to the oil/water interface. *Nano Lett.* **2005,** *5*, (12), 2489-2494.

29. Phenrat, T.; Liu, Y.; Tilton, R. D.; Lowry, G. V., Adsorbed polyelectrolyte coatings decrease Fe^0 nanoparticle reactivity with TCE in water: conceptual model and mechanisms. *Environ. Sci. Technol.* **2009,** *43*, (5), 1507–1514.

30. Liu, Y.; Phenrat, T.; Lowry, G. V., Effect of TCE concentration and dissolved groundwater solutes on NZVI-promoted TCE dechlorination and H2 evolution. *Environ. Sci. Technol.* **2007,** *41*, (22), 7881-7887.

31. Sakulchaicharoen, N.; O'Carroll, D. M.; Herrera, J. E., Enhanced stability and dechlorination activity of pre-synthesis stabilized nanoscale FePd particles. *J. Contam. Hydrol.* **2010,** *118*, (3-4), 117-127.

32. Wei, Y. T.; Wu, S. C.; Yang, S. W.; Che, C. H.; Lien, H. L.; Huang, D. H., Biodegradable surfactant stabilized nanoscale zero-valent iron for in situ treatment of vinyl chloride and 1,2-dichloroethane. *J. Hazard. Mater.* **2012,** *211-212*, 373-380.

33. Chen, M. Y.; Su, Y. F.; Shih, Y. H., Effect of geochemical properties on degradation of trichloroethylene by stabilized zerovalent iron nanoparticle with Na-acrylic copolymer. *J. Environ. Manage.* **2014,** *144*, 88-92.

34. Graham, L. J.; Atwater, J. E.; Jovanovic, G. N., Chlorophenol Dehalogenation in a Magnetically Stabilized Fluidized Bed Reactor. *AIChE J.* **2005,** *52*, (3), 1083-1093.

35. Graham, L. J.; Jovanovic, G. N., Catalytic Dechlorination of Chlorinated Hydrocarbons in a Magnetically Stabilized Fluidized Bed. *World Congr. Part. Technol.* **1998,** *3*, 2296-2307.

36. Graham, L. J.; Jovanovic, G. N., Dechlorination of p-chlorophenol on a Pd/Fe catalyst in a magnetically stabilized fuidized bed; Implications for sludge and liquid remediation. *Chem. Eng. Sci* **1999,** *54*, (15-16), 3085-3093.

37. Kim, D.-H.; Kim, J.; Choi, W., Effect of magnetic field on the zero valent iron induced oxidation reaction. *J. Hazard. Mater.* **2011,** *192*, 928-931.

38. Liang, L.; Guan, X.; Shi, Z.; Li, J.; Wu, Y.; Tratnyek, P. G., Coupled Effects of Aging and Weak Magnetic Fields on Sequestration of Selenite by Zero-Valent Iron. *Environ. Sci. Technol.* **2014,** *48*, 6326-6334.
39. Liang, L.; Sun, W.; Guan, X.; Huang, Y.; Choi, W.; Bao, H.; Li, L.; Jiang, Z., Weak magnetic field significantly enhances selenite removal kinetics by zero valent iron. *Water Res.* **2014,** *49*, 371-380.
40. Sun, Y.; Guan, X.; Wang, J.; Meng, X.; Xu, C.; Zhou, G., Effect of Weak Magnetic Field on Arsenate and Arsenite Removal from Water by Zerovalent Iron: An XAFS Investigation. *Environ. Sci. Technol.* **2014,** *48*, 6850-6858.
41. Feng, P.; Guan, X.; Sun, Y.; Choi, W.; Qin, H.; Wang, J.; Qiao, J.; Li, L., Weak magnetic field accelerates chromate removal by zero-valent iron. *J. Environ. Sci.* **2015,** *31*, 175-183.
42. Jiang, X.; Qiao, J.; Lo, I. M. C.; Wang, L.; Guan, X.; Lu, Z.; Zhou, G.; Xu, C., Enhanced paramagnetic Cu2+ ions removal by coupling a weak magnetic field with zerovalent iron. *J. Hazard. Mater.* **2015,** *283*, 880-887.
43. Li, J.; Bao, H.; Xiong, X.; Sun, Y.; Guan, X., Effective Sb(V) immobilization from water by zero-valent iron with weak magnetic field. *Sep. Purif. Technol.* **2015,** *151*, 276-283.
44. Pablico-Lansigan, M. H.; Situa, S. F.; Samia, A. C. S., Magnetic particle imaging: advancements and perspectives for real-time in vivo monitoring and image-guided therapy. *Nanoscale* **2013,** *5*, 4040-4055.
45. Lim, J. K.; Tilton, R. D.; Eggman, A.; Majetich, S. A., Design and Synthesis of Plasmonic Magnetic Nanoparticles. *J. Magn. Magn. Mater.* **2007,** *311*, 78-83.
46. Bañobre-López, M.; Teijeiro, A.; Rivas, J., Magnetic nanoparticle-based hyperthermia for cancer treatment. *Rep. Prac. Oncol. Radiother.* **2013,** *18*, (6), 397-400.
47. Phenrat, T.; Thongboot, T.; Lowry, G. V., Electromagnetic Induction of Zerovalent Iron (ZVI) Powder and Nanoscale Zerovalent Iron (NZVI) Particles Enhances Dechlorination of Trichloroethylene in Contaminated Groundwater and Soil: Proof of Concept. *Environ. Sci. Technol.* **2016,** *ASAP*.
48. Price , S. L.; Kasevich, R. S.; Johnson, M. A.; Wiberg , D.; Marley, M. C., Radio Frequency Heating for Soil Remediation. *J. Air & Waste Manage. Assoc.* **1999,** *49*, 136-145.
49. Lowe, D. F.; Oubre, C. L.; Ward, C. H., *Soil Vapor Extraction Using Radio Frequency Heating: Resource Manual and Technology Demonstration*. CRC Press: New York, 1999; p 360.
50. Falciglia, P. P.; Urso, G.; Vagliasindi, F. G. A., Microwave heating remediation of soils contaminated with diesel fuel. *J. Soils Sediments* **2013,** *13*, 1396–1407.
51. Truex, M. J.; Macbeth, T. W.; Vermeul, V. R.; Fritz, B. G.; Mendoza, D. P.; Mackley, R. D.; Wietsma, T. W.; Sandberg, G.; Powell, T.; Powers, J.; Pitre, E.; Michalsen, M.; Ballock-Dixon, S. J.; Zhong, L.; Oostrom, M., Demonstration of Combined Zero-Valent Iron and Electrical Resistance Heating for In Situ Trichloroethene Remediation. *Environ. Sci. Technol.* **2011,** *45*, (12), 5346–5351.
52. Mulligan, C. N.; Eftekhari, F., Remediation with surfactant foam of PCP-contaminated soil. *Eng. Geol.* **2003,** *70*, (3-4), 269-279.
53. Binks, B. P.; Kirkland, M.; Rodrigues, J. A., Origin of stabilisation of aqueous foams in nanoparticle–surfactant mixtures. *Soft Matter* **2008,** *4*, 2373-2382.
54. Lv, Q.; Li, Z.; Li, B.; Li, S.; Sun, Q., Study of Nanoparticle–Surfactant-Stabilized Foam as a Fracturing Fluid. *Ind. Eng. Chem. Res.* **2015,** *54*, (38), 9468–9477.
55. Saiers, J. E.; Lenhart, J. J., Colloid mobilization and transport within unsaturated porous media under transient-flow conditions. *Water Resour. Res.* **2003,** *39*, (1), 1019.
56. Kresheck, G. C., The temperature dependence of the heat capacity change for micellization of nonionic surfactants. *J. Colloid Inrterface Sci.* **2006,** *298*, 432-440.

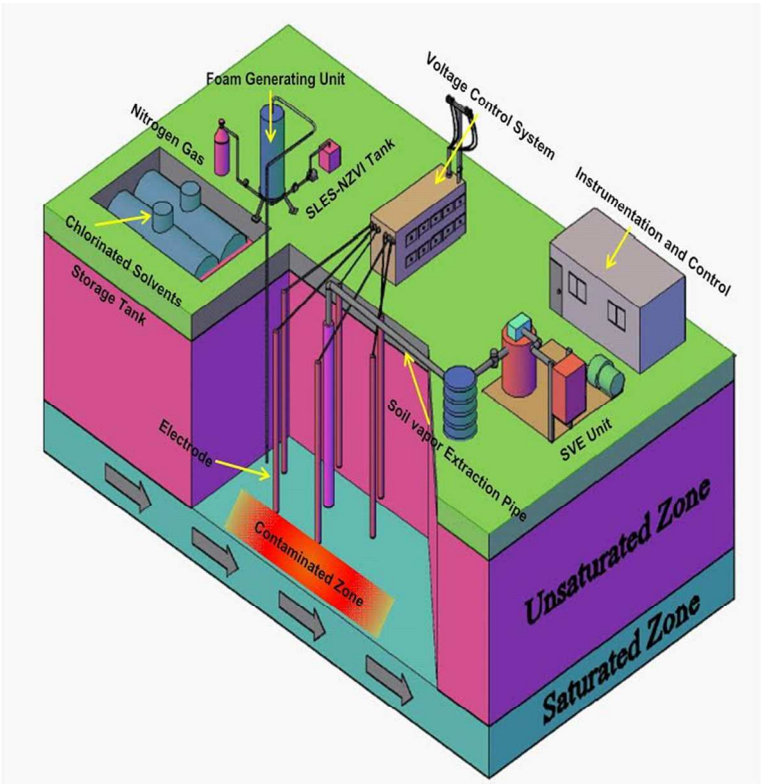

Fig. 1 A conceptual model of delivery and electromagnetic induction of F-NZVI as a combined remediation technique for NAPL) in vadose zone.
268x215mm (96 x 96 DPI)

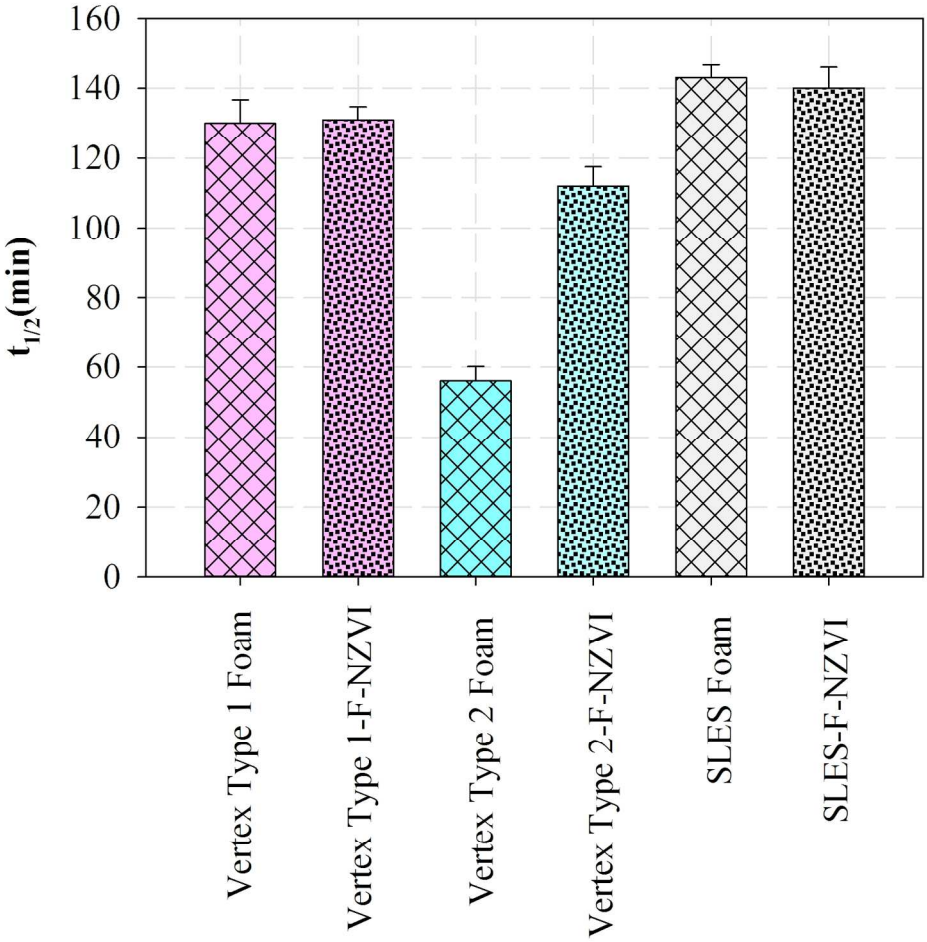

Fig. 2 (a) Half-life (t1/2) of foam and F-NZVI formed by three different surfactants
160x161mm (300 x 300 DPI)

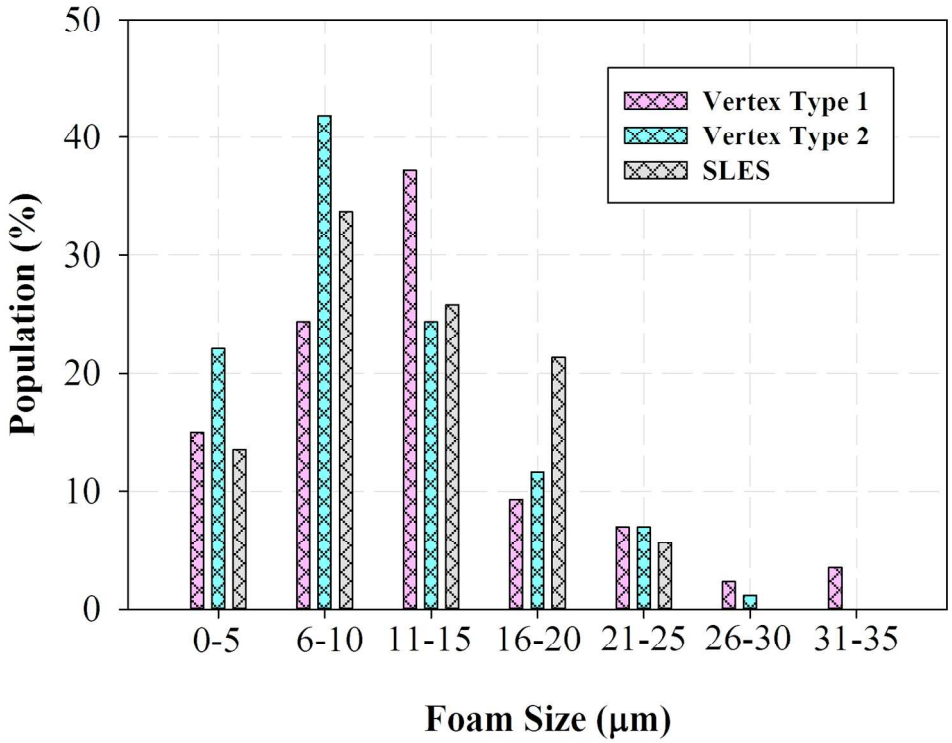

Fig. 2 (b) bubble size distribution of three different types of foam
152x124mm (300 x 300 DPI)

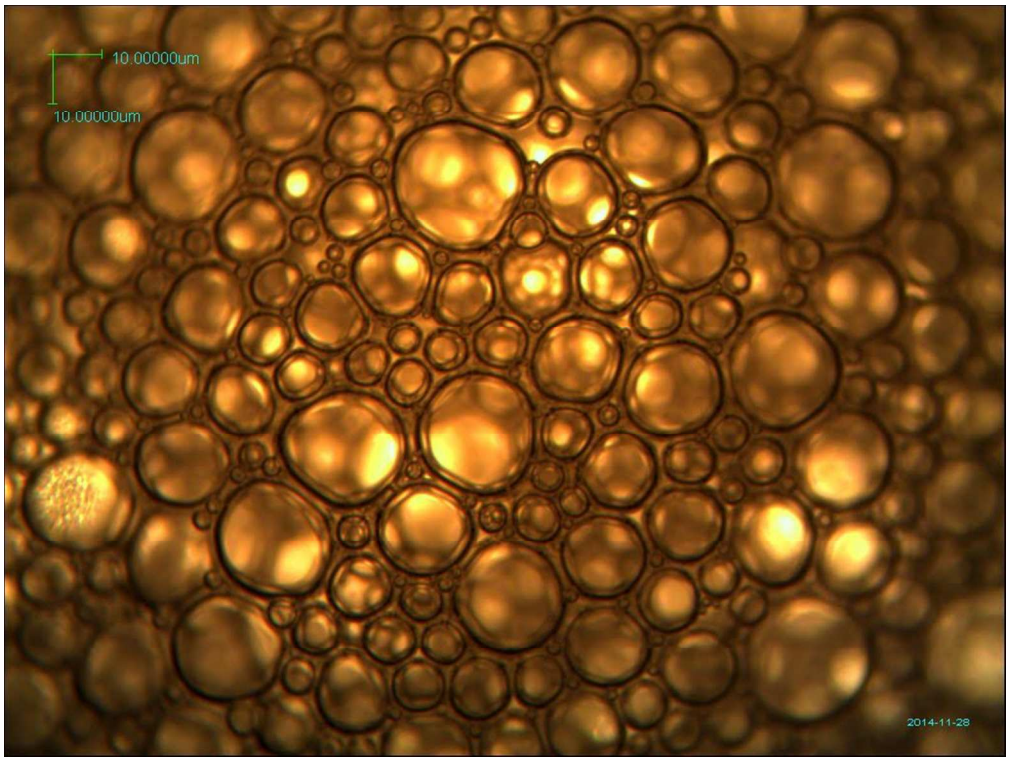

Fig. 2 micrograph of (c) Vertex Type 2 Foam
270x203mm (96 x 96 DPI)

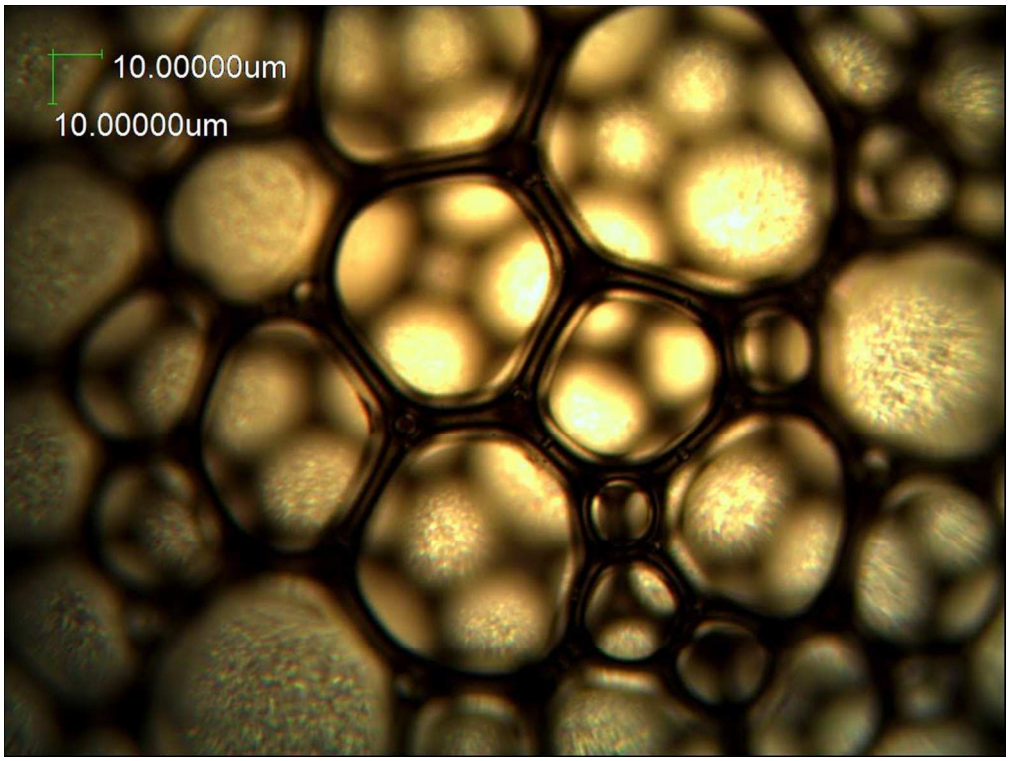

Fig. 2 (d) Vertex Type 2-F-NZVI
270x203mm (96 x 96 DPI)

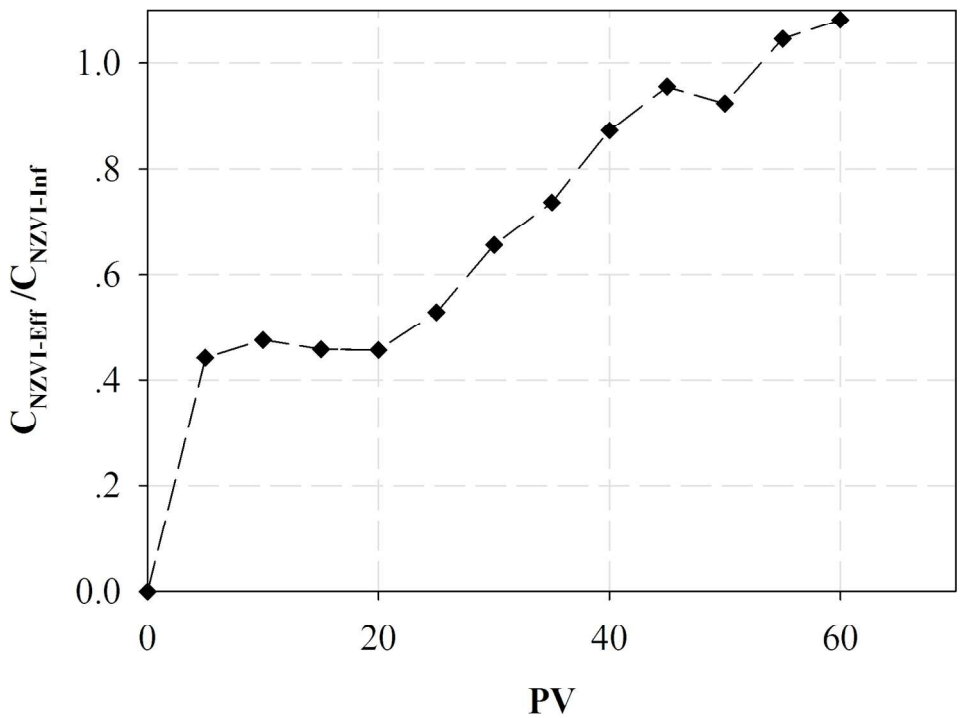

Fig. 3 (a) Breakthrough curve of SLES-F-NZVI over 60-PV delivery through an unsaturated sand-packed column
154x123mm (300 x 300 DPI)

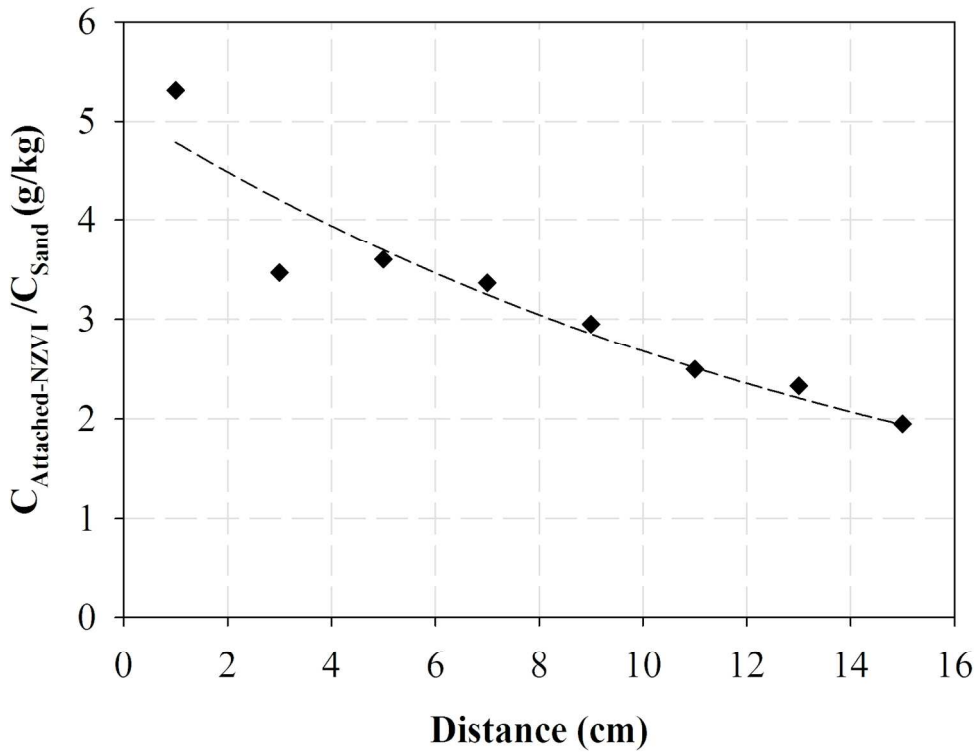

Fig. 3 (b) concentration of deposited NZVI in unsaturated porous media as a function of distance from the inlet.
150x123mm (300 x 300 DPI)

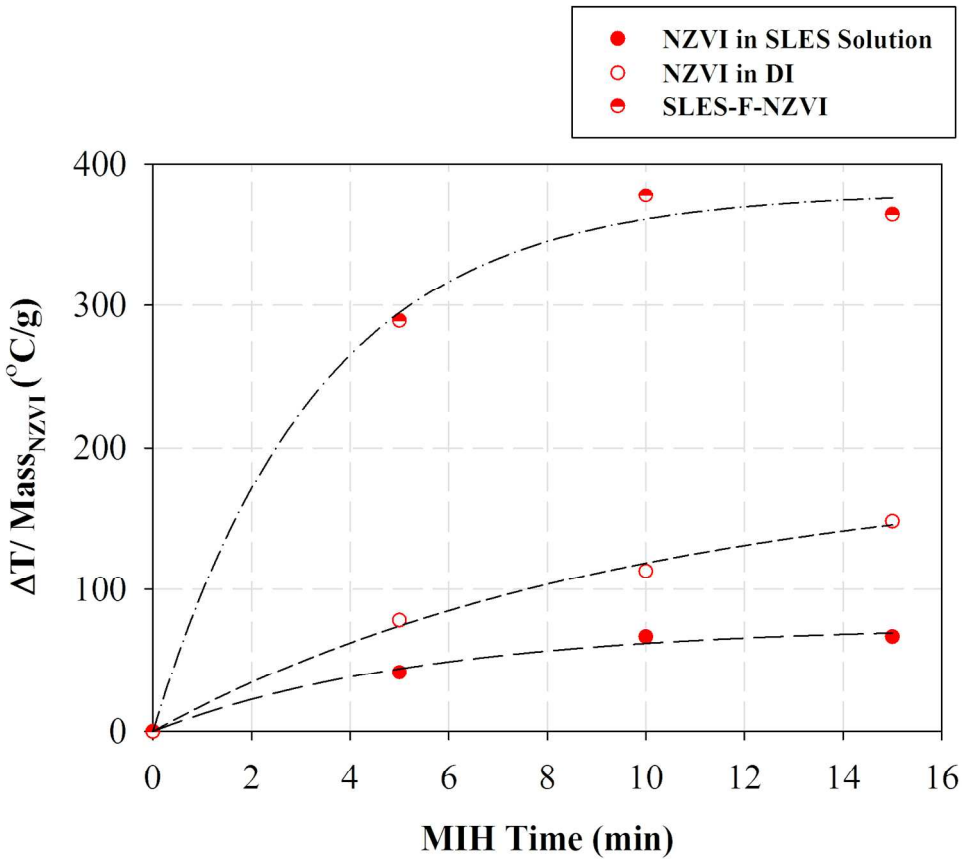

Fig.4 (a) MIH kinetics of SLES-F-NZVI in comparison to NZVI in DI water and SLES concentration (3% (w/w))
158x136mm (300 x 300 DPI)

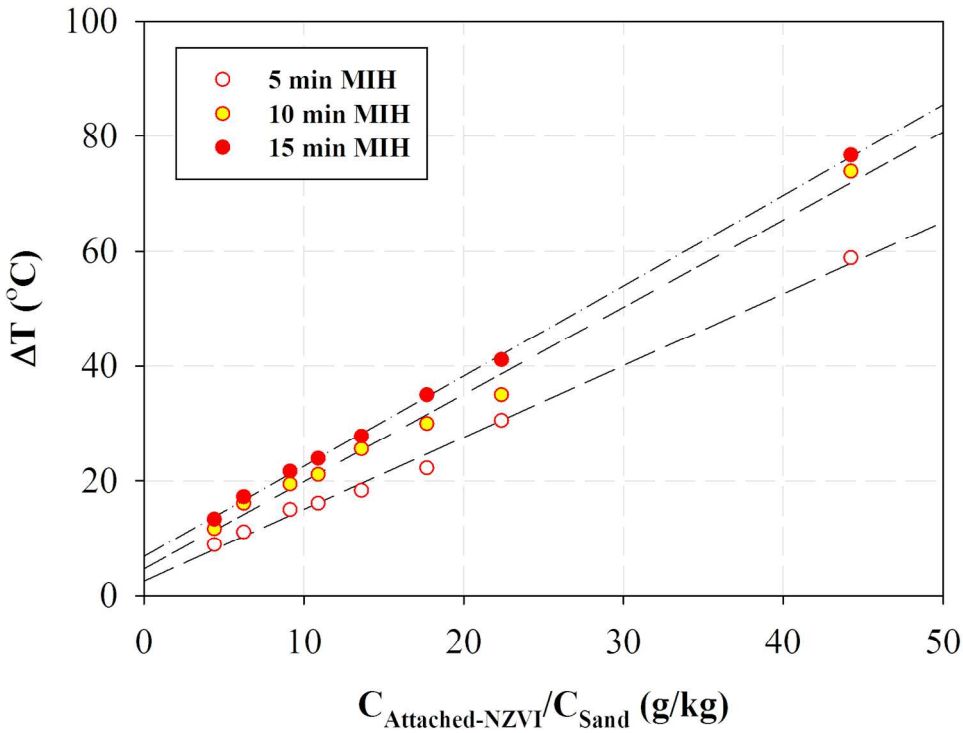

Fig.4 (b) linear trend between deposited NZVI concentration (CAttached-NZVI/CSand (g/kg)) and induced ΔT (ºC) at 5, 10, and 15 min MIH under 150 kHz and 13 A of EMF.
156x126mm (300 x 300 DPI)

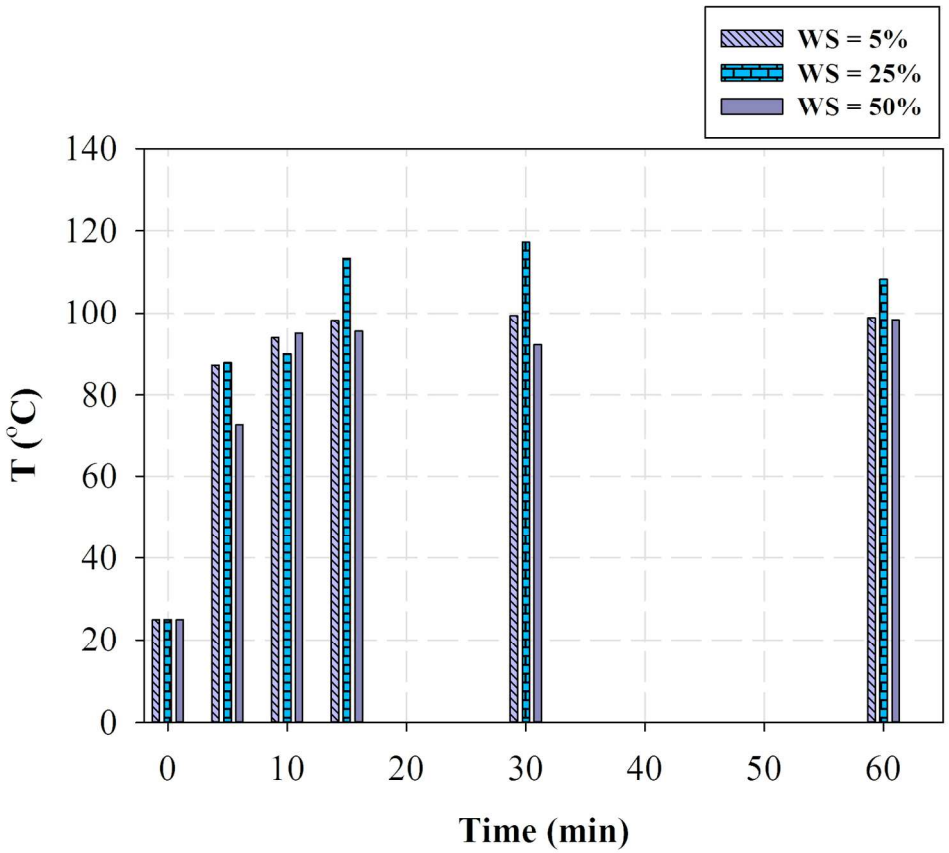

Fig. 5 (a) Heating kinetics of reactors containing unsaturated sand at WS = 5, 25, and 50% and TCE saturation =3.5% induced by SLES-F-NZVI under 150 kHz and 13 A
156x134mm (300 x 300 DPI)

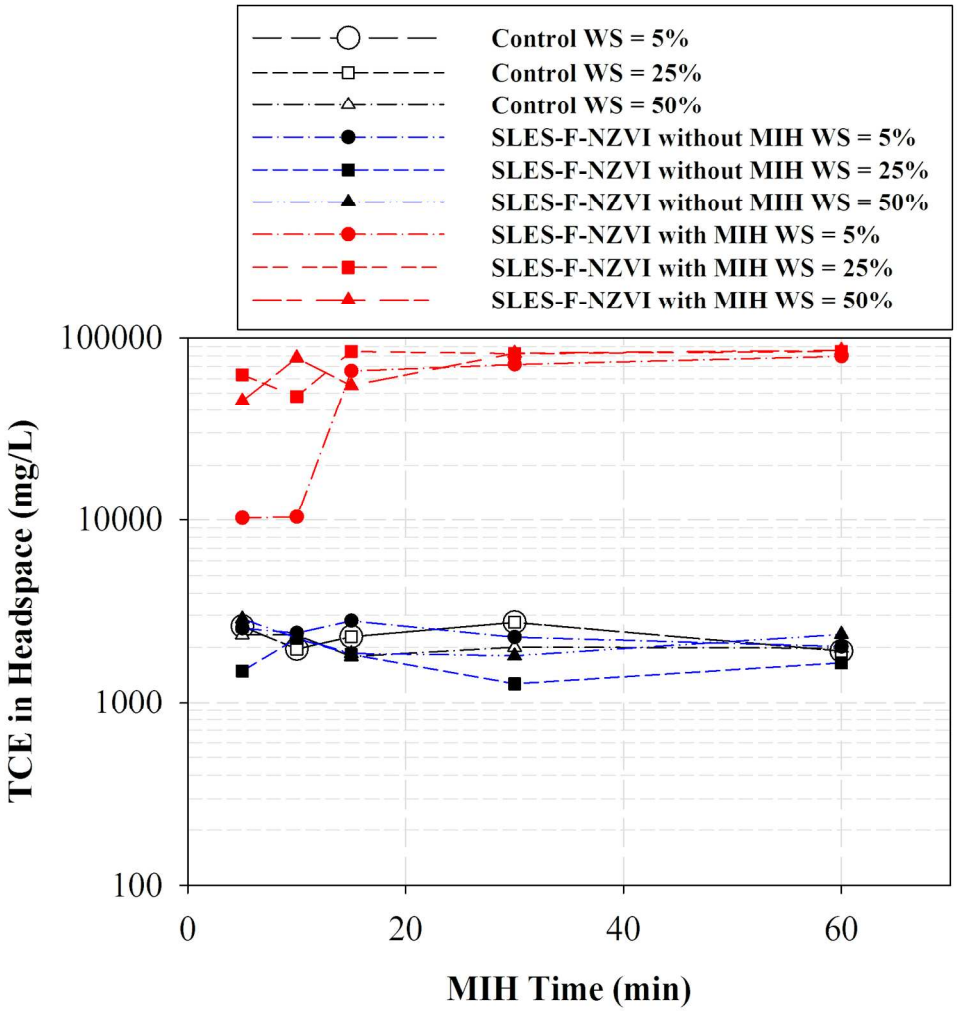

Fig. 5 (b) kinetics of TCE evaporation to headspace with and without applied SLF-EMF and as a function of MIH time.
164x166mm (300 x 300 DPI)

Supporting Information for

Delivery and Electromagnetic Induction of Foam-based Nanoscale Zerovalent Iron (NZVI) Particles as a Combined Remediation Technique for Non-Aqueous Phase Liquid (NAPL) in Unsaturated Porous Media: Proof of Concept

Supawan Srirattana[1,2], Kitsanateen Piaowan[1,2], Gregory V. Lowry[3,4], Schradh Saenton[5], and Tanapon Phenrat[1,2]*

[1]Research Unit for Integrated Natural Resources Remediation and Reclamation (IN3R), Department of Civil Engineering, Faculty of Engineering, Naresuan University, Phitsanulok, Thailand, 65000. [2]Center of Excellence for Sustainability of Health, Environment and Industry (SHEI), Faculty of Engineering, Naresuan University, Phitsanulok, Thailand, 65000. [3]Center for Environmental Implications of Nanotechnology (CEINT) and [4]Department of Civil & Environmental Engineering, Carnegie Mellon University, Pittsburgh, PA 15213-3890, USA.

[5] Department of Geological Sciences, Faculty of Science, Chiang Mai University, Chiang Mai, Thailand, 50200

Submitted to

Environmental Science & Technology

*Corresponding author: Tanapon Phenrat (pomphenrat@gmail.com)

(6655)964057(ph) (6655)964002(fax)

Table S1 Physicochemical Properties of Nanofer 25 (NF25)

Physicochemical Properties of Nanofer 25 (NF25)	
Chemical composition of Fe^0	Fe(core) FeO (shell)
Content of solid phase in dispersion by weight	20%
Content Fe^0 in solid phase	≈ 85%
Other ingredients in solid phase	Fe_3O_4,FeO,C
Content of Fe^0 in dispersion by weight	17%
Crystalline structure of Fe^0	Alpha Fe
Particles morphology	spherical
Average particle size	d50 < 50nm
Particles specific surface area	>25m^2/g
Dispersion colour	black
Dispersion density	1,210 kg/m3
Fe^0 particles density	7,870 kg/m3
Fe_3O_4 density	5,700 kg/m3

Foam and F-NZVI Generation Procedure and Characterization

Briefly, the control foam samples, i.e. foams without NZVI, were generated by first injecting approximately 5 mL of surfactant solution at a concentration of 1% (w/w) into a foam-generating column (Fig. S1) (acrylic with an i.d of 2 cm and length of 7 cm) via a peristaltic pump (Cole-Parmer Masterflex) at a flow rate of 1.5 ± 0.1 mL/min. Nitrogen gas was then introduced into the column along with solution injection at an N_2 flow rate of 125 mL/min. A 60-mesh stainless steel screen was placed at the inlet of the column to help create foam. After stable foam-generating conditions were established for 5 min, the foam was collected using test tubes 7 cm long and of 2 cm inner diameter. For the case of F-NZVI formation, the generation protocol was the same as the control foam, except that the stock solutions consisted of

50 g/L of NZVI for all five kinds of surfactant at a surfactant concentration of 1% (w/w) and an N_2 flow rate of 125 mL/min. The stock solutions were sonicated using an ultrasonic probe throughout the experiment.

To quantify the quality of the control foam and F-NZVI generated by all five surfactants, 5 ± 0.5 mL of each foam sample was collected. Ten mL methanol was used as a defoaming agent for each foam sample (Zhong et al., 2010; Shen et al., 2011). The volumes of the defoamed solutions for both control foam and F-NZVI and for each surfactant were measured using a graduated cylinder to determine the volume of the liquid component (V_l) of the foam. The difference between the total foam volume and V_l is the volume of gas in the foam (V_g). All experiments were performed in duplicate. The foam quality (F (%)) was defined by Eq.S-1 (Mulligan and Eftekhari, 2003).

$$F = \frac{Vg}{Vl + Vg} \times 100 \qquad \text{(S-1)}$$

The amount of NZVI in the liquid phase of each F-NZVI sample was quantified by separating NZVI out of the deformed solution using magnetic separation of NZVI followed by weighting of the separated NZVI after drying in an oven at 105°C for around 2 hr.

The foam stability following the same concept as the half-life of the foam was defined as the time required by the control foam and F-NZVI to reach half of its initial volume. The bubble size distributions of the control foam and F-NZVI were evaluated using a light microscope with a magnification 4×/0.01 connected to a digital camera (3.0 MP). The bubble sizes were quantified by using the S-Viewer software

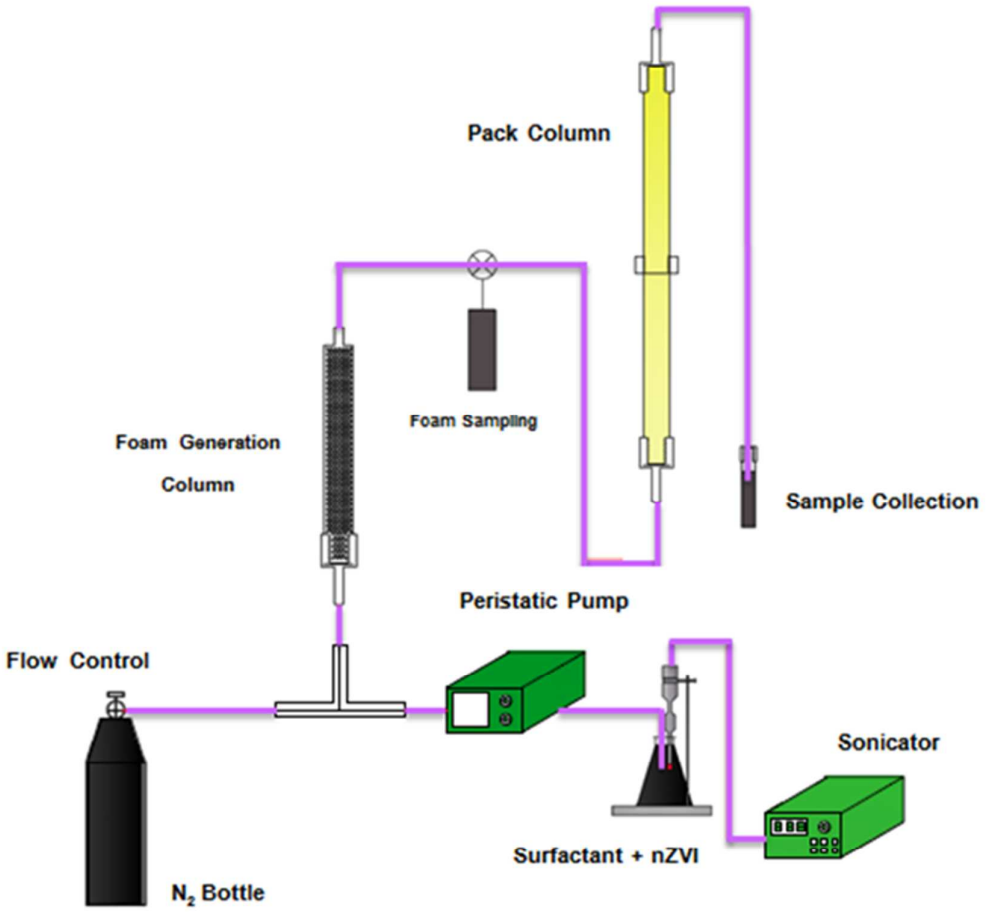

Figure S1 F-NZVI generation unit connected to an unsaturated sand-packed column for F-NZVI delivery and emplacement experiment.

Delivery and emplacement of F-NZVI in unsaturated sand-packed column

The sand (average d = 0.85 mm) was washed with DI water and dried at 105°C prior to using in the experiments. The porosity of the packed-bed sand was 0.41 ± 0.02 as determined by the gravity method. The packed columns were flushed with 3 pore volumes of 0.02 M NaCl solution prior to the study; the flushing electrolyte remaining in the columns was drained under gravity, and the columns were weighed to determine the initial water saturation (WS). Then, one pore volume (PV) of foam without NZVI was generated and flushed through the column, followed by the generation and delivery of 60 PVs of SLES-F-NZVI at the optimum generating condition (50 g/L NZVI in 3% (w/w) SLES solution at a flow rate of 1.5 mL/min and 500 mL/min N_2). The breakthrough NZVI concentrations in SLES-F-NZVI were monitored by sampling the SLES-F-NZVI at the effluent as a function of time, followed by the same procedure of foam destabilization, magnetic separation, and gravimetric determination of NZVI discussed earlier. The experiment was conducted in duplicate.

After a 60-PV experiment, the sand-packed column was dissected into eight 2-cm long segments where the sand and emplaced NZVI were removed from the segments. Retained NZVI was recovered by washing the F-NZVI and a sand mixture with 25 mL of DI water under sonication for 1 min, followed by manual vigorous shaking for a few seconds. The aqueous dispersions of NZVI washed out from the sand were decanted; NZVI was separated from the suspension by magnetic separation. The procedure was repeated 5 times for each sample until there was no more recoverable NZVI. The recovered NZVI was dried at 105°C and weighed to determine the amount of SLES-F-NZVI deposited in each unsaturated sand segment. The

percentage of emplaced F-NZVI was calculated by dividing the amount of recovered NZVI by the total amount of dried sand in each segment.

Magnetic induction heating (MIH) of F-NZVI and F-NZVI emplaced on unsaturated porous media

For free foam MIH study, a 25 mL screwed cap glass vial containing 12.5 mL of SLES-F-NZVI sample generated using 50 g/L NZVI in 3 % (w/w) SLES at an N_2 flow rate of 500 mL/min, as previously described, was placed into the center of the induction coil of a custom-made electromagnetic magnetic field generator (EMFG) (Fig. S2). The EMFG generated LF-EMF at a current density of 13 A and frequency of 150 kHz. The glass vial was inserted into an insulator prior MIH study. An infrared and contact thermometer (Fluke 561) (Fluke, Everett, Washington) was used to monitor the temperature change from the induced heat. The induced temperature under the applied LF-EMF was monitored at 5, 10, and 15 min. Each experiment was performed in duplicate. In addition to the F-NZVI, NZVI in DI water and in SLES suspension (not foam) at a particle concentration of 50 g/L were also evaluated for MIH capability, in order to compare with SLES-F-NZVI to determine if using foam as a vehicle to carry NZVI promotes or retards MIH. The MIH capability of each NZVI-carrying vehicle (DI water, SLES dispersion, and SLES foam) was defined as the temperature changes (ΔT) with respect to the amount of NZVI.

For emplaced F-NZVI, the same experimental set-up as section 2.3 was used. Delivery and emplacement of F-NZVI in an unsaturated sand-packed column was used to generate and deliver SLES-F-NZVI through an unsaturated porous media column. Sixty PVs of SLES-F-NZVI were injected in up-flow mode to emplace NZVI in the column. Then, the sand with NZVI emplacement was dissected into eight 2 cm-long

segments followed by placing each segment into the induction coil supplying LF-EMF at a frequency of 150 kHz and current density of 13 A for 15 min and recorded the temperature. The same experiment except generating F-NZVI using 100 g/L NZVI in 3% SLES (w/w) was also conducted to evaluate the effect of higher deposited NZVI concentration on ΔT in unsaturated porous media.

Figure S2 EMF generator (EMFG) and an induction coil (white coil) to hold vials for induction heating and EMF-enhanced dechlorination experiments.

(a)

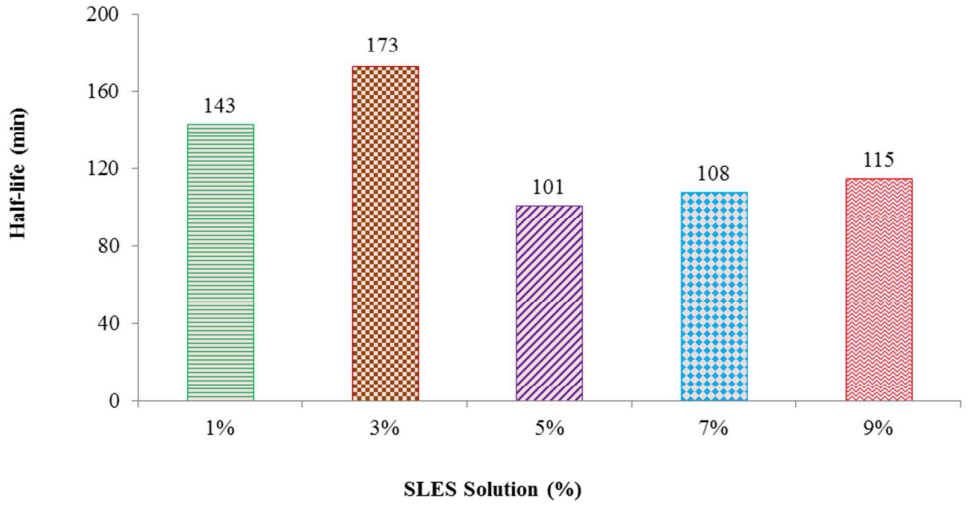

(b)

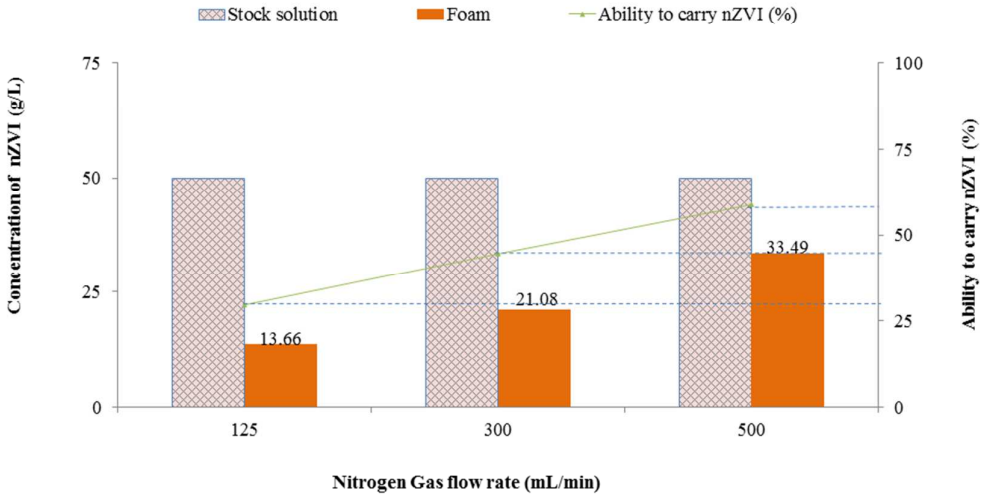

Figure S3 (a) effect of SLES concentration on foam stability and (b) effect of N_2 flow rate on F-NZVI quality and capability to carry NZVI.

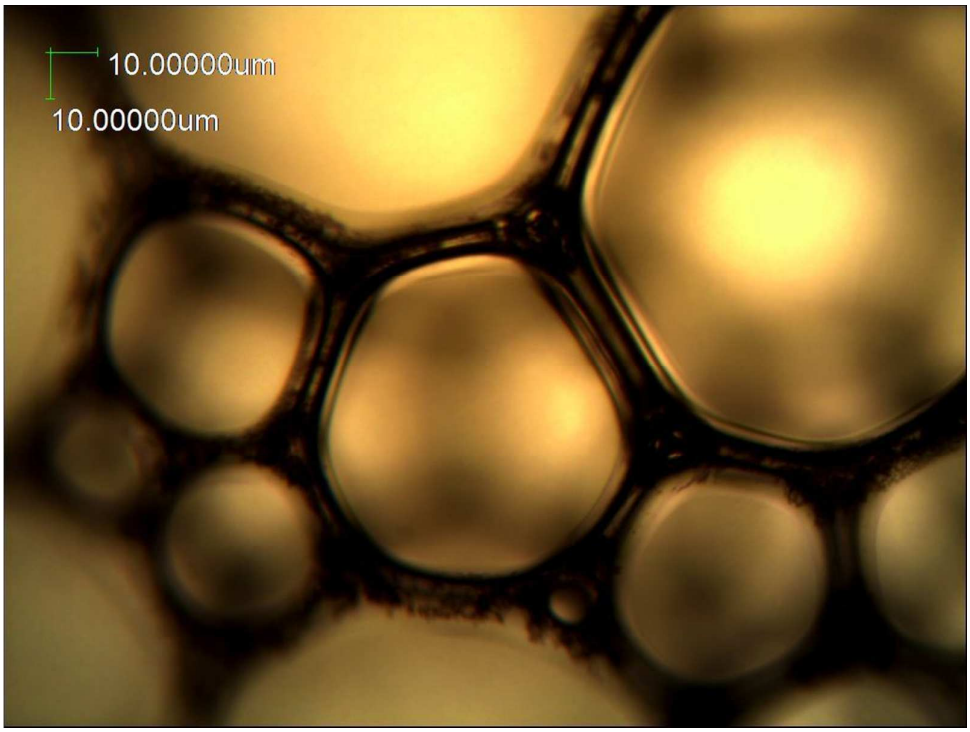

Figure S4 Micrograph of SLES-F-NZVI at 50 g/L in 3% (w/w) SLES in 500 mL/min N_2 focusing on NZVI aggregates formed on the bubble surface

Discussion on Magnetic Properties of NZVI

The XRD analysis (Fig. S5) confirmed that NZVI used in this study was predominantly Fe^0 and Fe_3O_4, both of which are magnetic. Fig. S6 illustrates NZVI magnetic responses under VSM test. The most important magnetic characteristic for the present study is the area under the hysteresis loop (ΔU) that represents the hysteresis loss due to the irreversible magnetization in EMF. Hysteresis loss is one of three losses including eddy current loss and residual loss, which altogether generate heat during magnetic induction of magnetic particles in EMF. Noticeably, upon the magnetization and demagnetization cycle, NZVI responded irreversibly, causing hysteresis and loss of energy as heat. The degree of irreversibility, ΔU, is related to the amount of energy dissipation upon the reversal of the field. Under LF-EMF, the reversal happens continuously and yields heat by energy dissipation from the particles. For a particular frequency (*f*) of LF-EMF, heat (*P*) generated due to the hysteresis loss is given by Eqn. S-2 (Li et al., 2010).

$$P = f\Delta U \qquad \text{(S-2)}$$

Based on Fig. S6, the ΔU for NZVI is 6.7×10^4 emu G/g. In addition, NZVI has a saturation magnetization of 55 emu/g. The remanence and coercivity of NZVI are 11 emu/g and 168 G, in good agreement with the values reported in a previous study (Rosická and Šembera, 2011)..

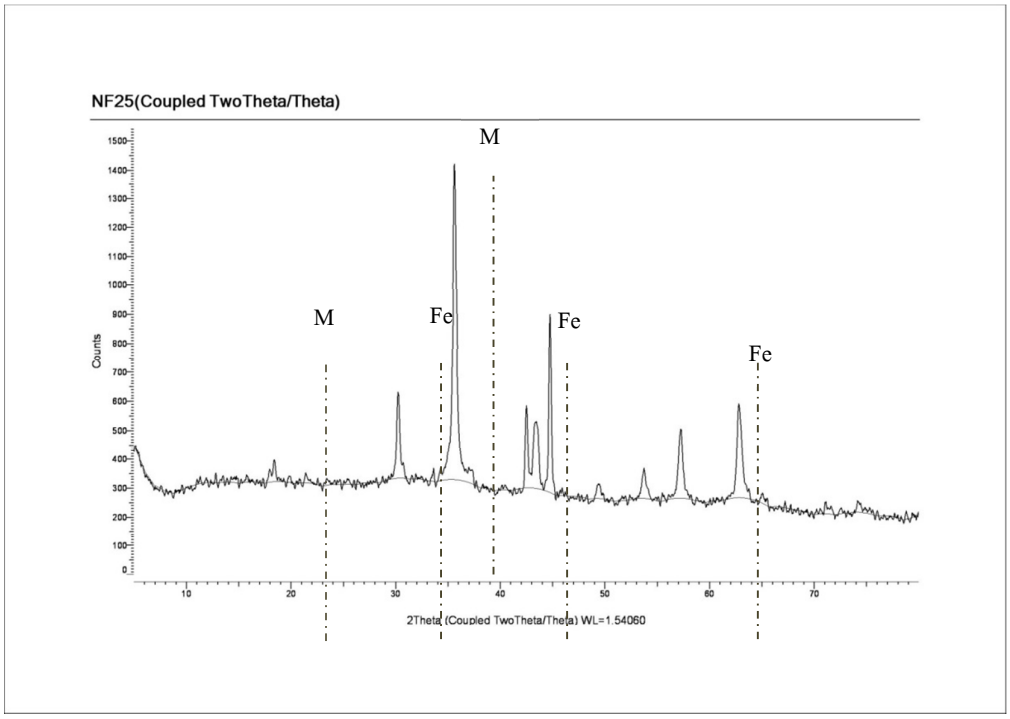

Figure S5 XRD of NZVI used in this study.

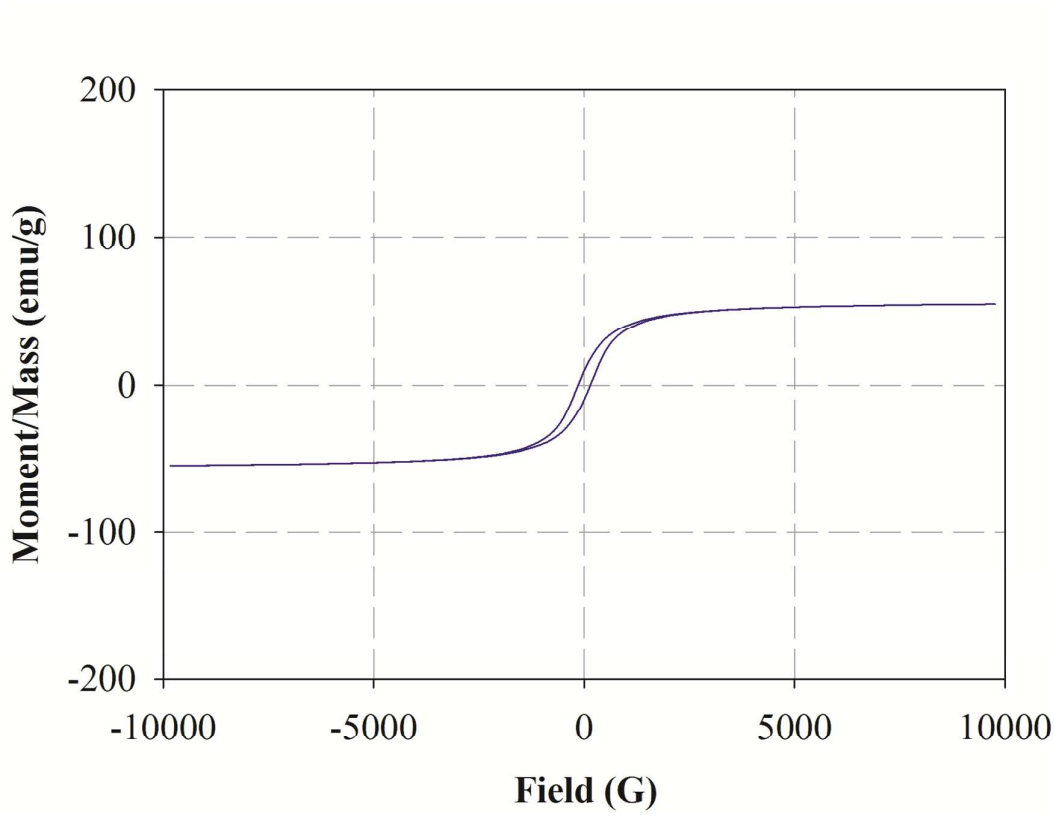

Figure S6 VSM of NZVI used in this study.

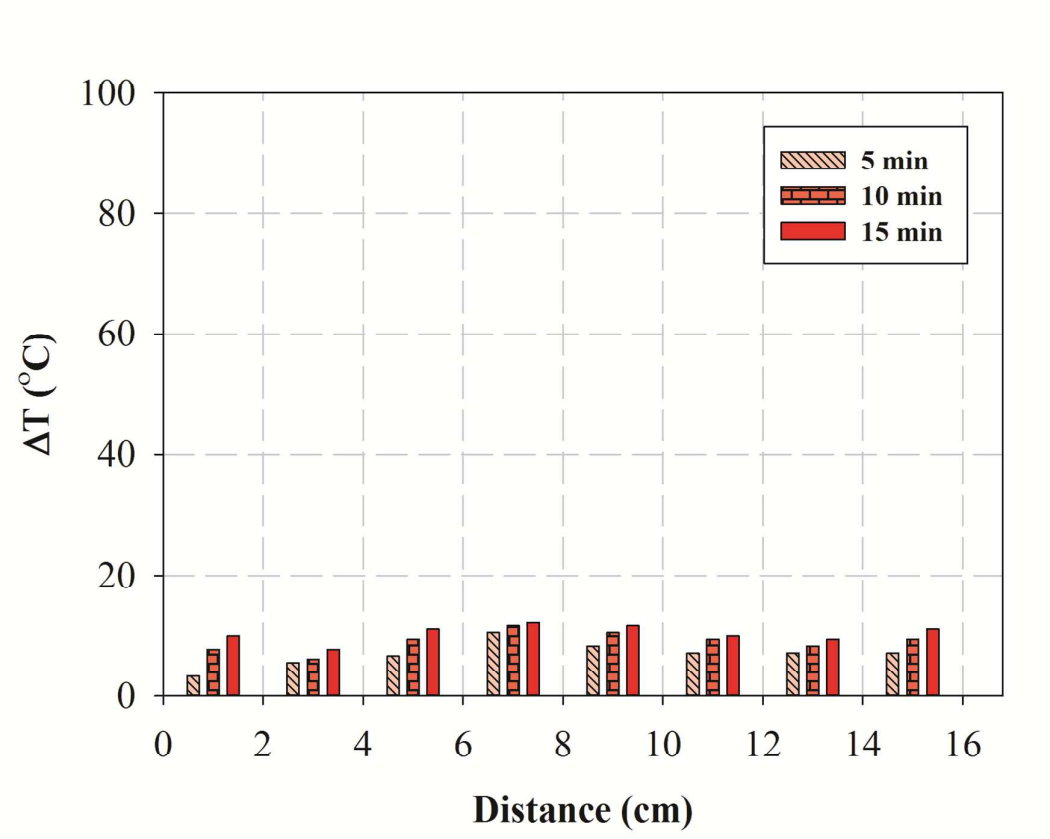

Figure S7 the ΔT for SLES-F-NZVI deposited onto unsaturated sand at each distance from the inlet according to the NZVI emplacement profile in Fig.3b.

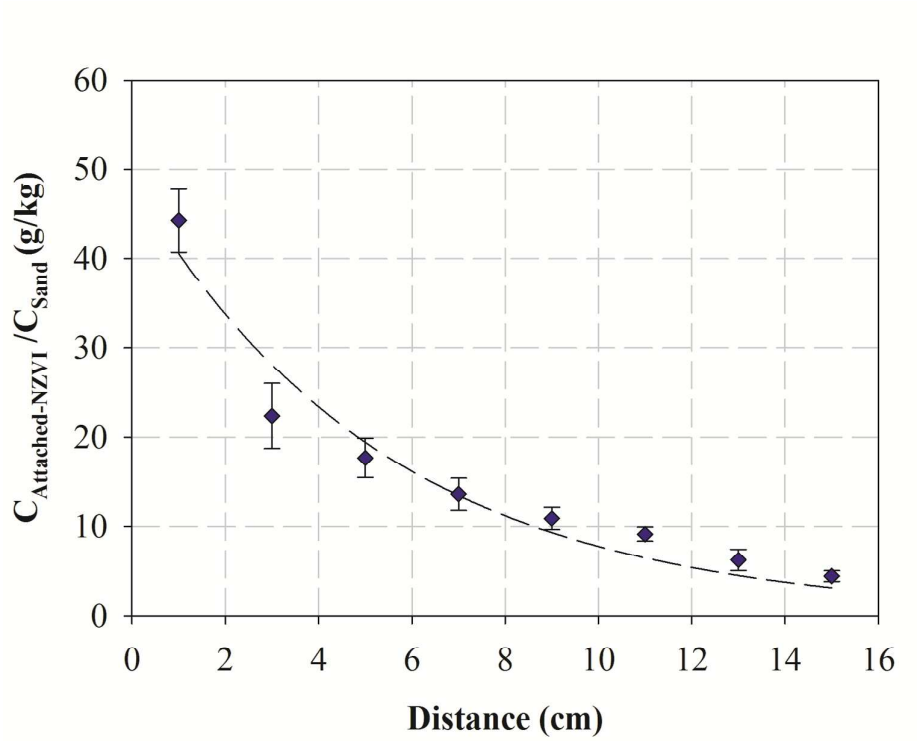

Figure S8 the emplaced NZVI profile along the unsaturated pack sand bed for 60-PV delivery of SLES-F-NZVI generated using 100 g/L NZVI in 3% (w/w) SLES stock solution and N2 flow rate of 500 mL/min

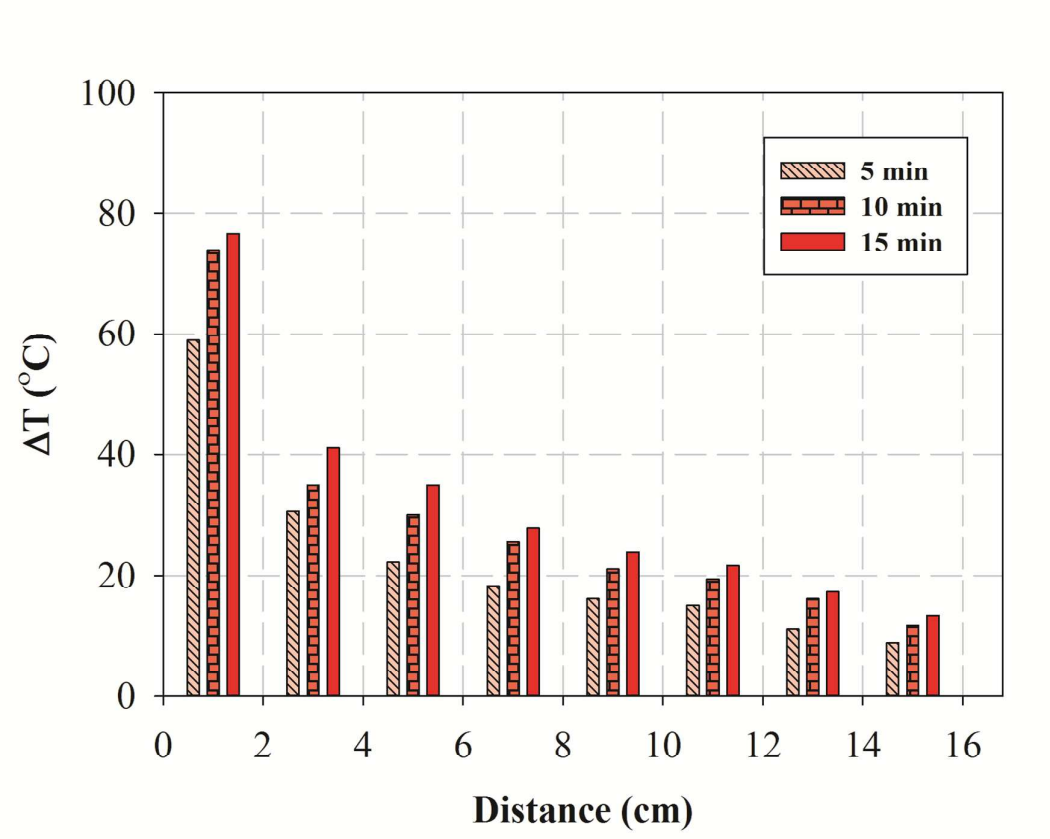

Figure S9 the ΔT for SLES-F-NZVI deposited onto unsaturated sand at each distance from the inlet according to the NZVI emplacement profile in Fig.S6.

Reference

Li, Z., Kawashita, M., Araki, N., Mitsumori, M., Hiraoka, M., Doi, M., 2010. Magnetite nanoparticles with high heating efficiencies for application in the hyperthermia of cancer. Mater. Sci. Eng. C 30, 990-996.
Mulligan, C.N., Eftekhari, F., 2003. Remediation with surfactant foam of PCP-contaminated soil. Eng. Geol. 70, 269-279.
Rosická, D., Šembera, J., 2011. Assessment of Influence of Magnetic Forces on Aggregation of Zero-valent Iron Nanoparticles. Nanoscale Res. Lett. 6:10.
Shen, X., Zhao, L., Ding, Y., Liu, B., Zeng, H., Zhong, L., Li, X., 2011. Foam, a promising vehicle to deliver nanoparticles for vadose zone remediation. J. Hazard. Mater. 186, 1773-1780.
Zhong, L., Szecsody, J.E., Zhang, F., Mattigod, S.V., 2010. Foam Delivery of Amendments for Vadose Zone Remediation:Propagation Performance in Unsaturated Sediments. Vadose Zone J. 9, 757-767.